



Politecnico  
di Bari

Department of Electrical and Information Engineering  
ELECTRICAL AND INFORMATION ENGINEERING

Ph.D. Program

SSD: ING/IND-32 - CONVERTERS, ELECTRICAL MACHINES AND  
DRIVES

**Final Dissertation**

---

# High Speed Synchronous Machines: Modeling, Design and Limits

---

by  
Gianvito Gallicchio

Supervisor:

Prof. Francesco Cupertino

*Coordinator of Ph.D Program:*

*Prof. Mario Carpentieri*

---

*XXXV Cycle - November 1st, 2019 - October 31st, 2022*



LIBERATORIA PER L'ARCHIVIAZIONE DELLA TESI DI DOTTORATO

Al Magnifico Rettore  
del Politecnico di Bari

Il sottoscritto **Galicchio Gianvito** nato a **Ceglie Messapica** il **30/03/1994**

residente a **Ceglie Messapica** in via **Calabria 44** e-mail **gianvitogalicchio@gmail.com**

iscritto al 3° anno di Corso di Dottorato di Ricerca in **Ingegneria Elettrica e dell'Informazione** ciclo **XXXV**

ed essendo stato ammesso a sostenere l'esame finale con la prevista discussione della tesi dal titolo:

**High Speed Synchronous Machines: Modeling, Design and Limits**

**DICHIARA**

- 1) di essere consapevole che, ai sensi del D.P.R. n. 445 del 28.12.2000, le dichiarazioni mendaci, la falsità negli atti e l'uso di atti falsi sono puniti ai sensi del codice penale e delle Leggi speciali in materia, e che nel caso ricorressero dette ipotesi, decade fin dall'inizio e senza necessità di nessuna formalità dai benefici conseguenti al provvedimento emanato sulla base di tali dichiarazioni;
- 2) di essere iscritto al Corso di Dottorato di ricerca in **Ingegneria Elettrica e dell'Informazione** ciclo **XXXV**, corso attivato ai sensi del "Regolamento dei Corsi di Dottorato di ricerca del Politecnico di Bari", emanato con D.R. n.286 del 01.07.2013;
- 3) di essere pienamente a conoscenza delle disposizioni contenute nel predetto Regolamento in merito alla procedura di deposito, pubblicazione e autoarchiviazione della tesi di dottorato nell'Archivio Istituzionale ad accesso aperto alla letteratura scientifica;
- 4) di essere consapevole che attraverso l'autoarchiviazione delle tesi nell'Archivio Istituzionale ad accesso aperto alla letteratura scientifica del Politecnico di Bari (IRIS-POLIBA), l'Ateneo archiverà e renderà consultabile in rete (nel rispetto della Policy di Ateneo di cui al D.R. 642 del 13.11.2015) il testo completo della tesi di dottorato, fatta salva la possibilità di sottoscrizione di apposite licenze per le relative condizioni di utilizzo (di cui al sito <http://www.creativecommons.it/Licenze>), e fatte salve, altresì, le eventuali esigenze di "embargo", legate a strette considerazioni sulla tutelabilità e sfruttamento industriale/commerciale dei contenuti della tesi, da rappresentarsi mediante compilazione e sottoscrizione del modulo in calce (Richiesta di embargo);
- 5) che la tesi da depositare in IRIS-POLIBA, in formato digitale (PDF/A) sarà del tutto identica a quelle **consegnate**/inviata/da inviarsi ai componenti della commissione per l'esame finale e a qualsiasi altra copia depositata presso gli Uffici del Politecnico di Bari in forma cartacea o digitale, ovvero a quella da discutere in sede di esame finale, a quella da depositare, a cura dell'Ateneo, presso le Biblioteche Nazionali Centrali di Roma e Firenze e presso tutti gli Uffici competenti per legge al momento del deposito stesso, e che di conseguenza va esclusa qualsiasi responsabilità del Politecnico di Bari per quanto riguarda eventuali errori, imprecisioni o omissioni nei contenuti della tesi;
- 6) che il contenuto e l'organizzazione della tesi è opera originale realizzata dal sottoscritto e non compromette in alcun modo i diritti di terzi, ivi compresi quelli relativi alla sicurezza dei dati personali; che pertanto il Politecnico di Bari ed i suoi funzionari sono in ogni caso esenti da responsabilità di qualsivoglia natura: civile, amministrativa e penale e saranno dal sottoscritto tenuti indenni da qualsiasi richiesta o rivendicazione da parte di terzi;
- 7) che il contenuto della tesi non infrange in alcun modo il diritto d'Autore né gli obblighi connessi alla salvaguardia di diritti morali od economici di altri autori o di altri aventi diritto, sia per testi, immagini, foto, tabelle, o altre parti di cui la tesi è composta.

Luogo e data **Bari, 27/12/22**

Firma

Il/La sottoscritto, con l'autoarchiviazione della propria tesi di dottorato nell'Archivio Istituzionale ad accesso aperto del Politecnico di Bari (POLIBA-IRIS), pur mantenendo su di essa tutti i diritti d'autore, morali ed economici, ai sensi della normativa vigente (Legge 633/1941 e ss.mm.ii.),

**CONCEDE**

- al Politecnico di Bari il permesso di trasferire l'opera su qualsiasi supporto e di convertirla in qualsiasi formato al fine di una corretta conservazione nel tempo. Il Politecnico di Bari garantisce che non verrà effettuata alcuna modifica al contenuto e alla struttura dell'opera.
- al Politecnico di Bari la possibilità di riprodurre l'opera in più di una copia per fini di sicurezza, back-up e conservazione.

Luogo e data **Bari, 27/12/22**

Firma



Politecnico  
di Bari

Department of Electrical and Information Engineering  
ELECTRICAL AND INFORMATION ENGINEERING

Ph.D. Program

SSD: ING/IND-32 - CONVERTERS, ELECTRICAL MACHINES AND  
DRIVES

Final Dissertation

---

# High Speed Synchronous Machines: Modeling, Design and Limits

---

by

Gianvito Gallicchio



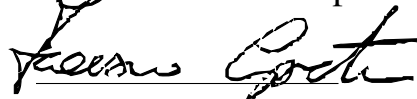
Referees:

Prof. Marco Palmieri

Dr. Simone Ferrari


Supervisor:

Prof. Francesco Cupertino



*Coordinator of Ph.D Program:*

*Prof. Mario Carpentieri*



---

XXXV Cycle - November 1st, 2019 - October 31st, 2022

# Abstract (eng)

This thesis reports the results of the three-years activities carried out during the XXXV cycle of the Ph.D. course in Electrical and Information Engineering of Politecnico di Bari.

The main goal of this work is the definition of a comprehensive design procedure for high-speed synchronous machines, including synchronous reluctance (SyR), permanent magnet assisted synchronous reluctance (PMSyR) and surface mounted permanent magnet (SPM) machines.

An original design approach is first proposed to the SyR scenario based on analytical methods and few finite element simulations capable of correcting the inaccuracies of the analytical approach. The proposed methodology takes into account both the electromagnetic, thermal and structural issues and their conflicting requirements when a high-speed design scenario is considered. In fact, magnetic non-linearities, rotor structural limitations and the rise of both stator and rotor iron losses are all considered. The adopted design approach allows achieving optimal stator and rotor geometries balancing all these competitive multi-physics aspects and keeping constant either the cooling system capability or the current density. Both silicon-iron (SiFe) and cobalt-iron (CoFe) alloys with optimized magnetic and mechanical performance are examined to assess the maximum capabilities achievable with a SyR machine technology.

The same design philosophy is then applied to the PMSyR case, when the degrees of freedom are increased by the insertion of the proper amount of PM volume within the rotor flux barriers, which is the most common design strategy used to significantly increase their performance in terms of both power density and power factor. It will be shown how a permanent magnet assisted synchronous reluctance machine can be optimized to satisfy all the electromag-



netic and structural constraints arising as the maximum operating speed increases. This will be done considering a variety PMs material, including low energy density PMs (e.g., Ferrite) and high energy density ones (e.g., rare earth materials such as NdFeB).

Finally, the SPM design case is analyzed with the same hybrid-analytical workflow, with special attention on the sleeve design as the speed increases; indeed, both thermal expansion and centrifugal forces must be accurately taken into account.

The proposed design procedure, either applied to SyR, PMSyR or SPM cases respectively, constitutes a flexible, systematic and general approach which is useful to infer design guidelines according to given assumptions and design choices.

Experimental results on four different prototypes validate the design approach.

# Abstract (it)

Questo lavoro di tesi riporta i risultati di tre anni di attività svolte durante il XXXV ciclo del corso di dottorato in Ingegneria Elettrica e dell'Informazione del Politecnico di Bari.

L'obiettivo principale del lavoro è la definizione di una completa procedura di progettazione di macchine elettriche sincrone ad alta velocità, tra cui le macchine sincrone a riluttanza pura, le macchine sincrone a riluttanza assistita da magneti permanenti e le macchine sincrone a magneti permanenti isotrope.

Un'originale metodologia di progettazione sarà prima proposta per le macchine sincrone a riluttanza; tale metodologia è basata su modelli analitici ed opportune simulazioni agli elementi finiti utili a correggere le imprecisioni dell'approccio puramente analitico. Il metodo proposto è in grado di considerare sia le problematiche elettromagnetiche che quelle termiche e strutturali, nonché i loro diversi requisiti nell'ambito di una progettazione di una macchina ad alta velocità. Infatti, la metodologia di progettazione è in grado di portare in conto sia le non-linearità magnetiche che le limitazioni strutturali e l'incremento delle perdite nel ferro di statore e rotore. L'approccio adottato permette di ottenere macchine ottimali sia da un punto statorico che rotorico, bilanciando tutti i sopracitati aspetti multifisici e mantenendo costante o la densità di corrente o il sistema di raffreddamento. Saranno esaminati differenti tipi di materiali ferromagnetici, in particolare i materiali basati sulla tecnologia a ferro-silicio (SiFe) e quelli basati sul Cobalto (CoFe), con lo scopo di individuare i limiti di potenza di una macchina a riluttanza pura.

La stessa filosofia di progettazione sarà applicata al caso di macchine a riluttanza assistita da magneti permanenti, dove l'inserimento di questi ultimi all'interno delle barriere di flusso

costituisce un ulteriore grado di libertà all'interno della progettazione; l'inserimento del giusto volume di magneti rappresenta la strategia più comune per aumentare in maniera significativa le prestazioni di un motore a riluttanza pura, sia in termini di densità di potenza che di fattore di potenza. Sarà mostrato come è possibile ottimizzare una macchina a riluttanza assistita in modo da soddisfare tutti i vincoli elettromagnetici e strutturali che insorgono quando la velocità di progetto aumenta. Tale metodologia sarà applicata considerando magneti sia a bassa (es. Ferrite) che alta (magnetite in terre rare, es. NdFeB) densità di energia.

Infine, sarà analizzato il caso delle macchine a magneti permanenti superficiali utilizzando la stessa strategia di progettazione ibrida-analitica, ponendo particolare attenzione alla progettazione della camicia di contenimento dei magneti permanenti necessaria ad alte velocità; infatti, sia il fenomeno di espansione termica che le problematiche legate alle forze centrifughe in gioco devono essere correttamente portati in conto.

La metodologia proposta, applicata alle tre tipologie di macchine, costituisce un approccio flessibile, sistematico e generale, utile per dedurre alcune linee guida di progettazione in accordo con date assunzioni e scelte di progetto.

Le considerazioni fatte saranno validate sperimentalmente su quattro diversi prototipi.

*To M.G., my star my perfect silence*

*”If your script is running properly on the first try, you’re just lucky.”*

# Acknowledgments

I would like to acknowledge all the people who have been part of this incredible journey.

First, I would like to deeply thank my supervisor, professor Francesco Cupertino, for accepting me as PhD student. His advises, technical and human skills and experience have been the motor of each project.

Then, I express my infinite gratitude to my "unofficial" co-tutors, Dr. Marco Palmieri and Dr. Mauro Di Nardo. Their guide, tutoring and the very nice small and big talks have been fundamental elements in these three years.

Thanks to professor Michele Degano and professor Chris Gerada of University of Nottingham, for the great collaboration. I hope our paths can continue to cross in the near future.

I would like to recognize the professors, researchers, laboratory technicians and company employees whom I worked with during these three years: prof. David Naso, prof. Vito Monopoli, Leo Cascella, Nicola Dell'Isola, Filippo Napoleone, Francesco Ladogana, Federica Botrugno, Giuliano Parente, Paolo Massenio, Elia Brescia and Rinaldo Consoletti. I also express my gratitude to the "ING-IND/33" colleagues for all the coffee breaks.

Thanks to my parents, my grandmother and my sister, for their support in every decision I made. I will never forget their unconditional love. Thanks to all the other family members.

A special gratitude has to be dedicated to my friends Piero, Giovanni, Roberto, Mino, Stefania and Valeria, for the good time we spent together, for the great laughs and for the trust I can give to them: this journey would have been much harder without their company.

Finally, thanks to Mariachiara. She is the most important, beautiful and meaningful part of my life.

# Contents

- Abstract (eng)** **i**
  
- Abstract (it)** **iii**
  
- Acknowledgments** **vii**
  
- Contents** **viii**
  
- List of Figures** **xiii**
  
- List of Tables** **xxiv**
  
- 1 Introduction** **1**
  - 1.1 Background on High Speed Applications . . . . . 1
  - 1.2 Electrical Machines Topologies . . . . . 5
    - 1.2.1 Synchronous reluctance machines . . . . . 6
    - 1.2.2 PM-assisted synchronous reluctance machines . . . . . 10
    - 1.2.3 Surface-mounted permanent magnet synchronous machines . . . . . 13
  - 1.3 Motivations and Goals of the Thesis . . . . . 15
  - 1.4 Structure of the Thesis . . . . . 16
  - 1.5 List of Scientific Publications . . . . . 17
    - 1.5.1 Journals . . . . . 17
    - 1.5.2 Conference Proceedings . . . . . 18

<b>2</b>	<b>Design of Synchronous Reluctance Machines</b>	<b>21</b>
2.1	Analytical design equations . . . . .	23
2.1.1	First assumptions and choices . . . . .	23
2.1.2	Main design equations . . . . .	23
2.1.3	Modeling equations . . . . .	25
2.1.4	Stator design . . . . .	26
2.1.5	Rotor design . . . . .	27
2.1.6	Inductances calculation . . . . .	29
2.1.7	Current components . . . . .	33
2.2	Limits of the analytical approach . . . . .	35
2.3	Hybrid design approach . . . . .	39
2.4	Influence of the high-speed limiting factors . . . . .	43
2.5	Results discussion . . . . .	46
2.5.1	Iron Losses influence . . . . .	47
2.5.2	Structural ribs influence . . . . .	49
2.5.3	Optimal machines . . . . .	50
2.5.4	Thermal assessment . . . . .	52
2.6	Materials selection . . . . .	54
2.6.1	Influence of the speed on the materials choice . . . . .	57
2.6.2	Analysis of the optimal designs . . . . .	60
2.6.3	Optimal geometries . . . . .	61
2.6.4	Behind the boundaries . . . . .	63
2.6.5	Thermal analysis . . . . .	66
2.7	Influence of the magnetic load . . . . .	68
2.7.1	Optimal Machines . . . . .	72
2.8	Influence of the current calculation criteria . . . . .	74
2.8.1	Analysis in the sr-mr design plane . . . . .	76
2.8.2	Performance of the maximum torque designs . . . . .	78



2.8.3	Geometries of the maximum torque designs . . . . .	80
2.9	Publications . . . . .	81
<b>3</b>	<b>Permanent Magnet assisted Synchronous Reluctance Machines</b>	<b>82</b>
3.1	Re-call and extension of the analytical design equations . . . . .	84
3.1.1	Main design equations . . . . .	84
3.1.2	Non-linear q-axis magnetic circuit . . . . .	87
3.1.3	PM design criteria . . . . .	90
3.1.4	Iterative calculation of the q-axis inductance and PM flux . . . . .	92
3.2	FE validation of the analytical model . . . . .	96
3.3	Enhancing the design approach accuracy . . . . .	99
3.4	Preliminary design considerations . . . . .	101
3.5	Effects of PM insertion at increasing speed . . . . .	104
3.5.1	Torque . . . . .	105
3.5.2	PM torque . . . . .	107
3.5.3	Reluctance torque . . . . .	108
3.5.4	Internal power factor . . . . .	110
3.6	Performance boundaries . . . . .	111
3.7	Analysis of the optimal machines . . . . .	113
3.8	Insight: PM design criteria comparison . . . . .	116
3.8.1	Performance vs speed analysis . . . . .	116
3.8.2	sr-mr plane considerations . . . . .	119
3.9	Publications . . . . .	123
<b>4</b>	<b>Surface Permanent Magnet synchronous Machines</b>	<b>124</b>
4.1	Analytical design procedure . . . . .	126
4.1.1	Stator design . . . . .	127
4.1.2	Maximum current calculation . . . . .	128
4.1.3	Rotor design: magnetic equivalent circuit . . . . .	128

4.1.4	Sleeve computation . . . . .	129
4.1.5	Iterative calculation of PM and sleeve thicknesses . . . . .	134
4.2	Design approach validation and adjustment . . . . .	135
4.2.1	Thermal performance validation . . . . .	139
4.3	High speed designs . . . . .	140
4.3.1	Airgap thickness effects . . . . .	142
4.3.2	Maximum speed effects . . . . .	143
4.3.3	Independent assessment of the high speed limiting factors . . . . .	144
4.4	Optimal designs . . . . .	146
4.4.1	Performance . . . . .	146
4.4.2	Machine geometries . . . . .	148
4.4.3	Thermal performance . . . . .	150
4.5	Publications . . . . .	151
<b>5</b>	<b>Comparison among technologies</b>	<b>152</b>
5.1	Overview on the design process . . . . .	153
5.1.1	Rotor design . . . . .	155
5.1.2	Comparison setup . . . . .	156
5.2	Performance vs speed . . . . .	157
5.3	Optimal machines analysis . . . . .	164
<b>6</b>	<b>Experimental results</b>	<b>170</b>
6.1	SyRM . . . . .	172
6.1.1	CoFe machine . . . . .	172
6.1.2	SiFe machine . . . . .	176
6.2	PMaSyRM . . . . .	181
6.2.1	Design refinement . . . . .	182
6.2.2	Experimental findings . . . . .	186
6.3	SPMM . . . . .	191

6.3.1	Selection of the final design . . . . .	191
6.3.2	Experimental findings . . . . .	192
<b>7</b>	<b>Conclusions and future work</b>	<b>198</b>
7.1	Results' summary . . . . .	198
7.2	Outlook . . . . .	203
	<b>Bibliography</b>	<b>204</b>

# List of Figures

1.1	High-speed electrical machines for the more-electric engine (Cummins) . . . . .	2
1.2	High-speed spindle (NK automation) . . . . .	4
1.3	High-speed flywheel (Williams Hybrid Power). . . . .	5
1.4	Cross-section of (a) stator (b) SyRM rotor (c) PMSyRM rotor and (c) SPM rotor. . . . .	6
1.5	Insertion of the PMs within the rotor slots of SyRMs. . . . .	11
2.1	Typical flux barriers shapes: a) circular, b) I2U and c) fluid. . . . .	23
2.2	a) Vector diagram of a SyR machine. b) Parametrization of the stator and rotor geometry. . . . .	24
2.3	Iron area considered for sizing the radial iron ribs . . . . .	28
2.4	Flux density distribution when a) the d-axis circuit is supplied. b) the q-axis circuit is supplied. . . . .	29
2.5	Rotor parametrization. . . . .	30
2.6	Subdivision of the q-axis m.m.f. . . . .	30
2.7	Magnetic equivalent circuit. . . . .	31
2.8	Iron ribs magnetic model. . . . .	32
2.9	q-axis inductance calculation by means of magnetic circuit. . . . .	34
2.10	Comparison between analytical and FE computation of torque (a, b) and internal power factor (c, d) at 1 krpm (a, c) and 50 krpm (b, d). . . . .	36
2.11	a) Ratio between analytical and FE computation of $L_{dm}$ , cross coupling effects at b) 1 krpm and c) 50 krpm. . . . .	37

2.12	Comparison between analytical and FE computation of iron losses at a) 1 krpm; b) 50 krpm. Average value of the flux density first harmonic component at 1 krpm in c) stator yoke; d) stator tooth. e) Average total bridges at 50 krpm. f) Comparison between analytical and FE computation of $L_{q-rib}$ at 50 krpm. . . . .	38
2.13	Flowchart of the FE-adjustment procedure . . . . .	40
2.14	Comparison between analytical and FE computation of torque (a, b) and $ipf$ (c, d) at 1 krpm (a, c) and 50 krpm (b, d). . . . .	42
2.15	Comparison between analytical and FE computation of the d-axis (a) and q-axis (b) magnetizing inductances, iron losses (c) and $L_{q-rib}$ (d) at 50 krpm . . . . .	43
2.16	Maximum torque (a) and internal power factor at the maximum torque (b) as a function of the speed . . . . .	45
2.17	Power as a function of the speed . . . . .	45
2.18	Optimal $sr$ (a) and $mr$ (b) as a function of the speed . . . . .	46
2.19	Constant torque loci in the plane $sr - mr$ obtained considering only the iron losses effect at: a) 1 krpm, b) 40 krpm, c) 70 krpm. . . . .	47
2.20	Constant $i_q$ (a,b,c) and $L_d - L_q$ (d,e,f) loci considering only the iron losses effect at: 1 krpm (a,d), 40 krpm (b,e), 70 krpm (c,f); constant stator core mass loci (g) and iron losses at 40 krpm (h) and 70 krpm (i). . . . .	48
2.21	Constant $ipf$ loci in the plane $sr - mr$ obtained considering only the iron losses effect at: a) 1 krpm, b) 40 krpm, c) 70 krpm. . . . .	48
2.22	Constant torque loci in the plane $sr - mr$ obtained considering only ribs effect at: a) 1 krpm, b) 40 krpm, c) 70 krpm. . . . .	49
2.23	Constant locus in the design plane $sr - mr$ obtained considering only the ribs influence at 70 krpm on a) average total ribs, b) torque decrement, c) q-axis inductance increment. . . . .	50
2.24	Constant $ipf$ loci in the plane $sr - mr$ obtained considering only iron ribs effect at: a) 1 krpm, b) 40 krpm, c) 70 krpm. . . . .	50

2.25	Optimal machines obtained considering: (a) only iron ribs, (b) only iron losses and (c) both aspects at different speeds. . . . .	51
2.26	a) Hot-spot winding and average stator iron temperatures, b) copper and stator iron losses, c) total stator losses and coolant absorbed power, as function of the speed for machines designed at constant total stator losses (Total) and constant Joule losses (Only ribs). . . . .	53
2.27	Soft magnetic materials comparison: iron losses at 1 T at different frequencies (750, 1500, 3000 Hz) as function of the yield strength; the colored scale shows the knee flux density. . . . .	55
2.28	Performance boundaries of the SyR machine technology, i.e. maximum achievable torque (a), internal power factor (b), and output power (c) as a function of the design speed for different soft magnetic materials. . . . .	58
2.29	Split (a) and magnetic ratios (b) of the optimal torque-wise machines as a function of the design speed. . . . .	60
2.30	Cross section of the optimal machines obtained for different lamination materials.	62
2.31	Constant loci obtained considering only the losses effect. Torque at: (a) 1 krpm, (b) 60 krpm, (c) 120 krpm. . . . .	64
2.32	Constant loci at 60 krpm obtained considering only the losses effect. $L_d/L_q$ (a), $i_q$ (b), $i_d$ (c), $P_{fe-st}$ (d), $P_{fe-rot}$ (e), $ipf$ (f). . . . .	64
2.33	Constant loci obtained considering only the ribs effect. Torque at: (a) 60 krpm, (b) 120 krpm; $w_{avg}$ (c), $\Delta T_{rib}$ (d), $\Delta L_{qm-rib}$ (e) and $\Delta ipf_{rib}$ (f) at 60 krpm. . .	65
2.34	a,c) Average winding and rotor temperatures, b,d) loss distribution ratios, e) total power absorbed by the cooling system of the optimal machines and f) total losses, stator total losses and cooling system power absorption for the M3 solutions. . . . .	67
2.35	BH characteristic of Hiperco 50A. . . . .	69
2.36	Torque (a) and ipf (b) as function of the speed . . . . .	70
2.37	Power as function of the speed . . . . .	70

2.38	d-axis current $i_d$ (a), q-axis current $i_q$ (b) stator iron losses (c) at the maximum torque as function of the speed . . . . .	71
2.39	$L_d$ (a), $L_q$ (b) and $L_d-L_q$ (c) at the maximum torque as function of the speed. . . . .	71
2.40	Optimal (torque wise) design variables $sr$ (a) and $mr$ (b) as function of the speed . . . . .	72
2.41	Cross sections of the optimal machines at (a,d) 20krpm, (b,e) 50krpm, (c,f) 80krpm, considering a magnetic load equal to (a,b,c) 1.2 T and (d,e,f) 1.8 T . . . . .	73
2.42	a) Average torque in the $sr - mr$ plane considering different current calculation criteria at a) 20 krpm and b) 120 krpm; b) Optimal split and magnetic ratios as function of the speed . . . . .	76
2.43	<b>Constant <math>P_{st}</math> and Constant <math>P_{tot}</math></b> scenarios at 120 krpm: a) Stator iron losses; b) $L_d-L_q$ ; c1) q-axis current; c2) rotor iron losses. . . . .	77
2.44	Maximum torque (a) and maximum power (b) as function of the speed in the 4 considered cases. . . . .	78
2.45	Total losses (a) and current density (b) as function of the speed in the 4 considered cases. . . . .	79
2.46	Optimal machines geometries. . . . .	81
3.1	Machine parametrization. . . . .	84
3.2	Vector diagram of PMaSyRMs. . . . .	85
3.3	a) q-axis magnetic equivalent circuit; b) Thévenin equivalent . . . . .	87
3.4	a) stator q-axis m.m.f. b) rotor parametrization. . . . .	88
3.5	Example of $B_{rib0}$ , $\mu_{rib-diff}$ and $\mu_{rib-app}$ identification for the iron ribs modeling. . . . .	89
3.6	Flowchart of the analytical design procedure. . . . .	94
3.7	Comparison between the analytical estimation and FE-computation of a) d-axis inductance, b) q-axis inductance and c) PM flux linkage at 80 krpm. . . . .	97
3.8	Comparison between the analytical and FE calculations of $B_{rib}$ of the a) outer barrier, b) middle barrier, c) inner barrier. . . . .	98

3.9	Comparison between the analytical estimation and FE-computation of a) torque, b) $ipf$ at 80krpm. . . . .	98
3.10	Finite element computation of a) rate between the PM flux linkage along the d-axis and q-axis, b) rate between the cross-coupling inductance and the d-axis one. . . . .	99
3.11	Comparison between the adjusted estimation and FE-computation of a) d-axis inductance, b) q-axis inductance and c) PM flux linkage at 80 krpm. . . . .	100
3.12	Comparison between the adjusted estimation and FE-computation of a) Torque, b) $ipf$ at 80 krpm. . . . .	101
3.13	Constant loci contour plot of a) total torque, b) PM torque, c) reluctance torque, d) $i_d$ , e) $i_q$ , f) $L_d - L_q$ , g) PM flux, h) PM volume and i) Needed PM volume. . . . .	102
3.14	Constant loci contour plot of a) $ipf$ and b) $ipf$ reluctance component and c) ratio between actual PM volume and needed one. . . . .	103
3.15	Constant loci contour plot of the percentage difference between the module of the total flux and its d-axis components (in p.u. of the total flux). . . . .	104
3.16	Torque function of split and magnetic ratio obtained considering three maximum speeds (40, 80, 120 krpm) for the pure SyRM and for the versions assisted by NdFeB and Ferrite magnets. . . . .	105
3.17	Reluctance ( $T_{rel}$ ) and PM ( $T_{PM}$ ) torque components of the FEaSyRMs as function of both design variables for three different speeds and locations of the maximum reluctance, PM and total torque designs. . . . .	106
3.18	Reluctance ( $T_{rel}$ ) and PM ( $T_{PM}$ ) torque components of the NDaSyRMs as function of both design variables for three different speeds and locations of the maximum reluctance, PM and total torque designs. . . . .	107
3.19	PM torque (a, d), PM flux linkage (b, e), PM volume and rotor slot volume (c, f) contours in the $sr - mr$ plane when the maximum speed is 80 kprpm for both FE- and ND-assisted machines. . . . .	108



3.20	Reluctance torque ratio (a, d), average total rib ratio (b, e), average ribs saturation ratio (c, f) contours in the $sr - mr$ plane when the maximum speed is 80 krpm for both FE- and ND-assisted machines. . . . .	109
3.21	Internal power factor contour in the $sr - mr$ plane for three different maximum speeds (40, 80, 120 krpm) for the pure SyR and the two PM-assisted versions. .	110
3.22	Ratio between the PM volume ( $V_{PM}$ ) and its required value ( $V_{PM}^*$ ) as function of both design variables for three different speeds and for both PM materials. .	111
3.23	Torque (a) and internal power factor (b) as a function of the speed of the selected designs. . . . .	112
3.24	Permanent magnets (a) and reluctance (b) torque components of the selected machines as function of the speed. . . . .	113
3.25	Power as a function of the speed of the selected designs. . . . .	114
3.26	Design variables $sr$ (a) and $mr$ (b) of the optimal SyR, FEaSyR and NDaSyR machines as function of the speed. . . . .	114
3.27	Cross section of the optimal SyR, FEaSyR and NDaSyR machines and sub-optimal SyR+ND designs at 40, 80 and 120 krpm. . . . .	115
3.28	Torque (a) and ipf (b) versus speed of the maximum torque designs . . . . .	117
3.29	Maximum power as function of the speed. . . . .	118
3.30	Optimal split (a) and magnetic (b) ratios as function of the speed; cross sections of the optimal machines at 60 krpm (c), 80 krpm (d) and 100 krpm (e) for the 3 considered scenarios. . . . .	119
3.31	Total torque (a), PM torque (b) and reluctance torque (c) for Natural compensation (1), Target ipf (2) and Torque maximization (3) design criteria at 60 krpm.	120
3.32	PM volume / available barrier volume (a), PM flux (b), average width of the rotor ribs (c) for Natural compensation (1), Target ipf (2) and Torque maximization (3) design criteria at 60 krpm. . . . .	122
4.1	Stator (a) and rotor (b) parametrization. . . . .	127

4.2	a) Flux path due to PMs; b) magnetic equivalent circuit. . . . .	129
4.3	Sleeve stress schematic view with coordinate system. . . . .	130
4.4	Maximum Von Mises stress in the sleeve as function of magnet and sleeve thicknesses at 80 krpm for a given outer rotor radius $r_r=18$ mm. . . . .	133
4.5	Maximum PM thickness as function of the sleeve thickness for different outer rotor radii at 80 krpm. . . . .	133
4.6	Iterative computation of PM height and sleeve thickness. . . . .	134
4.7	Comparison between analytical results and FE ones: a) iron losses; b) d-axis flux and c) electromagnetic torque. . . . .	136
4.8	No load (a,b) and load (c,d) peak value of the flux density within stator yoke (a,c) and stator tooth (b,d) in the $sr - mr$ plane . . . . .	137
4.9	Analytical stator iron losses (a); stator iron losses calculated using the peak value of FE-computed $B_{fe}$ at no-load (b) and load (c) conditions; actual FE iron losses (d). . . . .	138
4.10	Comparison between analytical adjusted results and FE ones: a) iron losses; b) d-axis flux and c) electromagnetic torque. . . . .	139
4.11	(a) Estimated winding average temperature, (b) ratio between iron and copper stator losses and (c) PM temperatures in the $sr$ - $mr$ plane at 40krpm. . . . .	140
4.12	Torque constant loci contour plot in the $sr - mr$ plane at (1) 40krpm, (2) 60krpm and (3) 80krpm when the airgap thickness is a) 0.5 mm, b) 1 mm, c) 1.5 mm and d) 2 mm . . . . .	141
4.13	Contour plot of PM flux (a, b, c) and q-axis current (d, e, f) when the airgap thickness is 0.5 mm (a, d), 1 mm (b, e) and 1.5 mm (c, f) at 60 krpm. . . . .	142
4.14	Contour plot of PM flux (a, b, c) and q-axis current (d, e, f), when the speed is 40 krpm (a, d), 60 kprpm (b, e) and 80 krpm (c, f) for an airgap thickness equal to 1.5 mm. . . . .	143
4.15	Optimal split (a) and magnetic (b) ratios as function of the speed. . . . .	144

4.16	Costant loci contour plot of PM flux (a, b, c), sleeve thickness (d, e, f) and stator iron losses (g, h, i) when the speed is 40 krpm (a, d, g), 60 krpm (b, e, h) and 80 krpm (c, f, i) and for an airgap thickness equal to 1.5 mm. . . . .	145
4.17	Torque (a) and power (b) as function of the speed. . . . .	147
4.18	Rotor losses of the optimal designs as function of the speed. . . . .	147
4.19	Cross section of the optimal machines at (1) 40krpm, (2) 60krpm and (3) 80krpm when the airgap thickness is a) 0.5 mm, b) 1 mm, c) 1.5 mm and d) 2 mm . . .	148
4.20	Winding (a), rotor (b), sleeve (c) and magnet (d) temperatures of the optimal designs at rated conditions. . . . .	150
5.1	Stator (a) and rotor (b,c,d) parametrizations. . . . .	154
5.2	q-axis magnetic equivalent circuit before (a) and after (b) the Thèvenin transformation. . . . .	155
5.3	Example of torque in $sr - mr$ plane for SyR (a), PMSyR (b) and SPM cases (c).156	
5.4	Power of the optimal (torque wise) designs vs speed for different airgap thicknesses and cooling system capabilities. . . . .	158
5.5	SyRM $i_d$ in the $sr - mr$ plane for a given speed (40 krpm) and cooling system capability ( $50 \text{ kW/m}^2$ ) when considering an airgap thickness equal to (a) 0.3 mm, (b) 1 mm and (c) 1.5 mm . . . . .	158
5.6	SyRM $i_q$ in the $sr - mr$ plane for a given speed (40 krpm) and cooling system capability ( $50 \text{ kW/m}^2$ ) when considering an airgap thickness equal to (a) 0.3 mm, (b) 1 mm and (c) 1.5 mm . . . . .	159
5.7	SyRM saliency ratio in the $sr - mr$ plane for a given speed (40 krpm) and cooling system capability ( $50 \text{ kW/m}^2$ ) when considering an airgap thickness equal to (a) 0.3 mm, (b) 1 mm and (c) 1.5 mm . . . . .	160
5.8	SyRM d-axis magnetizing inductance in the $sr - mr$ plane for a given speed (40 krpm) and cooling system capability ( $50 \text{ kW/m}^2$ ) when considering an airgap thickness equal to (a) 0.3 mm, (b) 1 mm and (c) 1.5 mm . . . . .	160

5.9	SyRM d-axis magnetizing inductance in the $sr - mr$ plane for a given speed (40 krpm) and cooling system capability ( $50 \text{ kW/m}^2$ ) when considering an airgap thickness equal to (a) 0.3 mm, (b) 1 mm and (c) 1.5 mm . . . . .	161
5.10	Internal power factor of the optimal (torque wise) designs vs speed for different airgap thicknesses and cooling system capabilities. . . . .	162
5.11	Rotor radius of the optimal (torque wise) designs vs speed for different airgap thicknesses and cooling system capabilities. . . . .	165
5.12	Tooth width of the optimal (torque wise) designs vs speed for different airgap thicknesses and cooling system capabilities. . . . .	166
5.13	Cross sections of the optimal SyR machines at (a,d,g) 40 krpm, (b,e,h) 60 krpm and (c,f,i) 80 krpm when the airgap thickness is (a,b,c) 0.3 mm, (d,e,f) 1 mm, (g,h,i) 1.5 mm and d) 2 mm for a cooling system capability equal to $40 \text{ kW/m}^2$ . . . . .	167
5.14	Cross sections of the optimal PMSyR machines at (a,d,g) 40 krpm, (b,e,h) 60 krpm and (c,f,i) 80 krpm when the airgap thickness is (a,b,c) 0.3 mm, (d,e,f) 1 mm, (g,h,i) 1.5 mm and d) 2 mm for a cooling system capability equal to $40 \text{ kW/m}^2$ . . . . .	168
5.15	Cross sections of the optimal SPM machines at (a,d,g) 40 krpm, (b,e,h) 60 krpm and (c,f,i) 80 krpm when the airgap thickness is (a,b,c) 0.3 mm, (d,e,f) 1 mm, (g,h,i) 1.5 mm and d) 2 mm for a cooling system capability equal to $40 \text{ kW/m}^2$ . . . . .	169
6.1	Comparison between optimal designed machine and actual prototype. . . . .	172
6.2	a) Inverter and dSpace board , b) Back-to-back motors, c) Experimental set-up layout, d) Top view of the laminations stack. . . . .	173
6.3	a) Reference and measured currents, b) measured speed, c) reference voltages, and d) measured torque transients during the experimental identification test of one d-q current combination. . . . .	175

6.4	(a,b) FE-computed torque vs experimental one a) neglecting the mechanical tolerances b) considering the mechanical tolerances; (c,d) Magnetic identification in the $i_d - i_q$ plane (a,b).	176
6.5	Experimental speed test: a) reference speed and rotor speed; b) dq reference voltages.	177
6.6	a) Von Mises stress distribution of the final rotor design, b) rotor stack prior the shaft assembly.	177
6.7	a) Section drawing of the built prototype showing the most important components, b) side view of the complete machine mounted on the bracket of the test rig.	178
6.8	Comparison between measured and FE d- and q-axis fluxes in the d-q current plane.	179
6.9	Measured and reference speeds, voltage reference and measured and reference currents during a motoring no-load test.	179
6.10	Transient and steady state acquisitions during the load test at 30 krpm in which the current module increases from 21 to 28 A.	180
6.11	Measured winding temperature during the load tests at 30 krpm compared with the estimated ones at steady state.	181
6.12	a) Full rotor parametrization, b) Von Mises stress distribution of the optimal at 80krpm.	183
6.13	Average torque and torque ripple as function of the current phase angle for the electromagnetic optimum geometry, the structural one, and the final prototype.	185
6.14	PM re-distribution FE analysis: a) PM volume of the outermost PM, b) average torque, and c) torque ripple as function of the per unit PM volumes placed in the two innermost flux barriers.	186
6.15	Design refinement evolution.	186
6.16	Top view of the rotor lamination stack before (a) and after (b) magnets and shaft insertion.	187

6.17	Experimental setup layout. . . . .	187
6.18	Scope capture while measuring the phase-to-phase voltages during the no-load test at 24 krpm. . . . .	188
6.19	Comparison between measured and FE phase-to-phase no-load voltages at 24 krpm. . . . .	189
6.20	Comparison between estimated (colored lines) and measured (dashed black lines) average torque (a) and internal power factor (b) as function of the current phase angle and for different peak current amplitudes. . . . .	189
6.21	Motoring no load test up to 50 krpm: a) speed, b) voltages, c) currents. . . . .	190
6.22	Load test at 30 krpm and the rated torque: a) duty cycles and dc-link voltage, b) phase currents, and c) torque and speed, all acquired with the control platform at 40 kHz. . . . .	190
6.23	Scope capture while measuring the phase-to-phase voltages and phase currents during the rated load test at 30 krpm. . . . .	191
6.24	Power (a) and rotor losses (b) as function of the airgap thickness at 80 and 100 krpm. . . . .	192
6.25	(a) Rotor assembly process; b) assembled rotor. . . . .	193
6.26	a) Top view of the stator laminations; b) stator after the winding assembly. . . . .	193
6.27	Experimental setup layout. . . . .	194
6.28	back emf test at 30 krpm: (a) scope capture showing the the phase-to-phase voltages during the no-load test; (b) comparison between measured and FE phase-to-phase no-load voltages. . . . .	195
6.29	Comparison between FE computed and measured torque at MTPA condition. . . . .	196
6.30	Comparison between (a) FE computed and measured power factor at MTPA condition and (b) FE computed and measured efficiency in the speed-current plane. . . . .	196
6.31	Speed test: (a) reference speed against the measured and measured-filtered ones; b) d- and q-axis voltages. . . . .	197

# List of Tables

2.1	Machine parameters . . . . .	35
2.2	Optimal machine geometrical parameters (in mm) . . . . .	51
2.3	Selected lamination materials . . . . .	57
2.4	Initial geometrical constraints and preliminary design assumptions . . . . .	57
2.5	Comparison between optimal machines . . . . .	63
2.6	Comparison between optimal machines . . . . .	73
2.7	Cooling system capability of the optimal designs. . . . .	80
3.1	Design constraints and assumptions . . . . .	96
3.2	PM characteristics . . . . .	105
3.3	PM volume ( $V_{mag}^*$ ) of the selected designs [ $\text{cm}^3$ ] . . . . .	116
4.1	Design constraints and assumptions . . . . .	135
4.2	Optimal machine geometrical parameters (in mm) . . . . .	149
6.1	Iron ribs dimensions of the optimal design [mm] . . . . .	184
6.2	Comparison between measured and FE average winding temperatures. . . . .	197

# Chapter 1

## Introduction

### 1.1 Background on High Speed Applications

High-Speed electrical machines have been investigated by several authors in the last decades, with the aim of replacing mechanically-enhanced systems which usually feature low efficiency, limited flexibility and reliability, require high maintenance and do not allow to reduce the overall envelope of the system [1, 2]. Differently, direct drive solutions without gearboxes improve all the above performance indexes. Indeed, the elimination of the gearbox leads to a more compact system with reduced size and weight, while the adoption of the power electronics clearly increases the flexibility, efficiency and reliability of the drive [3].

Several applications can benefit from this change of drive architecture, including turbochargers, mechanical turbo-compounding systems, aeroengine spools, helicopter engines, racing engines, and fuel pumps [4].

However, the concept of high-speed machines is deeply influenced by the technology issues, including the availability of high-performance materials both from a structural and magnetic points of view, manufacturing advancements, management of the thermal behavior of the drive (including the power converter) layout and the possibilities in terms of power electronics high-performance devices. Indeed, higher speeds imply higher fundamental frequency which in turn affects the switching frequency of the power converter; moreover, the rise of the centrifugal



gal forces poses challenges in terms of rotor design, while the increment of the overall losses (copper, iron and windage ones) must be taken into account so to keep the temperatures under certain limits.

Soft magnetic materials have to feature lower specific iron losses and also optimal mechanical performance as the increment of the speed necessarily implies a rise of both the iron losses and the centrifugal forces, which in turn could result in lower efficiency, thermal and structural issues. Furthermore, the selection of the most appropriate electrical steel has to also consider its magnetic characteristic (i.e. the single value BH curve characteristic) since higher saturation values imply higher machine power density [5].

The electrical machine design both in terms of electromagnetic aspects but also in terms of thermal and structural management is also directly influenced by the application. Indeed, high-speed electrical machine could either replace or complement the existing high-speed mechanical systems [4]. In the following, some examples of high-speed applications are reported.

### a. More electric engine

The adoption of electrical machines within *more electric engine* is becoming a common solution. As shown in [4], the applications could be several. Fig 1.1 reports a family of four possible high-speed electrical machines around a future engine.

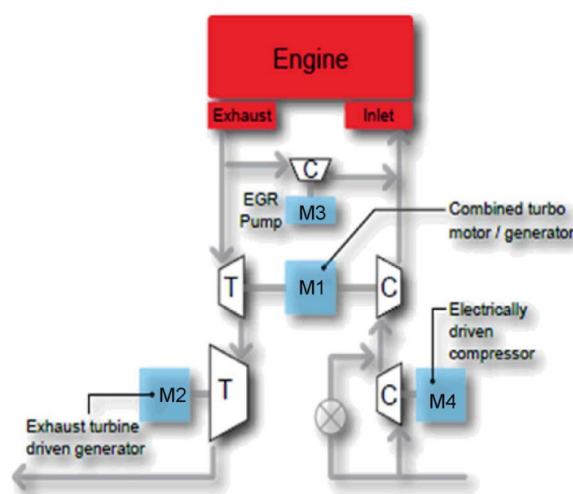


Figure 1.1: High-speed electrical machines for the more-electric engine (Cummins)

The machine M1 is placed on the same shaft as the turbine and the compressor wheels in a turbocharger, and it is used as:

- a motor to speed up the compressor to the required speed, with the aim of reducing turbo lag and improving drive-ability when there is lack of energy in the exhaust gas stream, thus reducing turbo lag and improving driveability;
- as a generator when there is excess energy in the exhaust, instead of opening a waste-gate valve to prevent shaft overspeeding.

Another high-speed machine (M2) coupled to an additional turbine can be used to improve the driveline efficiency so to extract waste heat from the exhaust gases. As an example, the recovery energy can be used to electrical loads of the vehicle or to supply a traction machine when considering a hybrid power train. Furthermore, the high-speed motor M3 can be adopted to drive an exhaust gas recirculation EGR compressor at the upstream of the turbine, thus overcoming the so-called "unfavorable pressure differential".

### **b. High-speed spindle**

The machine tool industry is also experiencing a more increasing demand on high-speed electrical machines; in such applications also the power density plays a major role.

The rotational speed range is quite large: in milling applications it depends on the processed material type varying between 6krpm for metal and 40kprpm for aluminum, while higher rotational speeds are reached when considering ultraprecision grinding applications [6]. Fig. 1.2 show a commercial example of high-speed spindle featuring a speed range between 20 and 200 krpm [7]

### **c. Gas Compressor**

The use of electric motor to drive compressors is clearly a common adopted procedure, but in the last decades the availability of new high-speed motor technologies, which include the



Figure 1.2: High-speed spindle (NK automation)

adoption of magnetic bearings, have increased the popularity of such solution. Indeed, magnetic bearings allow the elimination of the gearbox which in turn determines safety, efficiency, availability, reduced operation and maintenance costs increments, resulting in an environment-friendly compressor drives [8].

#### **d. Flywheel Energy Storage Systems**

The mechanical energy storage using a rotating flywheel is a common adopted solution to recover energy. An electric motor is used to store the electrical energy. The latter spins the flywheel leading to the conversion from electrical energy to mechanical one; in a dual way, the conversion from mechanical to electrical energy allows to perform the energy recover using the same electric motor.

Traditionally, such flywheels feature low rotational speed, low power and energy densities, whereas new concept flywheels can reach higher speeds and can out-compete NiMH batteries which are typical embedded within hybrid vehicles [4] albeit the energy density is lower. However, when considering short-time operations (e.g. power assist hybrid electric vehicle), high-speed flywheel allows a more compact solution, higher efficiency, longer lifetime, and a wider operating temperature range [9]. A commercial example of high-speed flywheel is reported in Fig. 1.3.



Figure 1.3: High-speed flywheel (Williams Hybrid Power).

## 1.2 Electrical Machines Topologies

From the previous section, it follows that high-speed applications could require different machine specifications which in turn include the power density, power factor, low cost, wide speed range, and so on.

According to the above needs, it is possible to identify several machine topologies and a first macrodistinction can be made between synchronous and asynchronous ones. The first can be also divided into isotropic (e.g. surface permanent magnet synchronous motors) and anisotropic machines (e.g. synchronous reluctance machines with and without permanent magnets, switched reluctance machines, etc.), whereas induction motors represent the most adopted asynchronous ones.

This thesis will be focused on the design of synchronous machines. In particular, three machine topologies will be analysed.

1. Synchronous Reluctance Machines (SyRMs), since they feature high efficiency, low cost and good power density.
2. Permanent Magnet assisted Synchronous Reluctance Machines (PMaSyRMs), since they can improve the main drawbacks of SyRM namely the low power factor and high torque ripple.
3. Surface mounted Permanent Magnet synchronous Motor (SPMMs), since they represent the gold-standard in terms of efficiency, power factor, power density.

The three machines basically share the stator (Fig. 1.4a) which hosts a three phase winding and it is slotted, whereas a different rotor design (Fig. 1.4b, c and d for SyRM, PMaSyRM and SPM respectively) characterizes each machine topology. In the following, the state of the art of

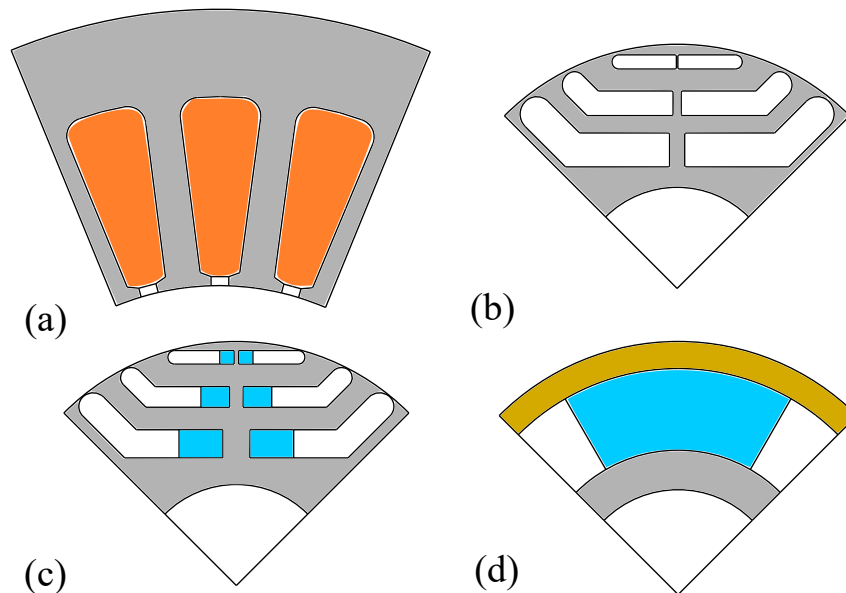


Figure 1.4: Cross-section of (a) stator (b) SyRM rotor (c) PMaSyRM rotor and (c) SPM rotor.

these three machine types will be investigated, thus highlighting the opportunity and challenges of each machine design.

### 1.2.1 Synchronous reluctance machines

Synchronous reluctance machines have attracted increasing attention in several sectors, especially automotive and industry. In the latter, i.e. mainly for low-medium speed applications, SyR machines allow a considerable volume reduction and/or an improvement of the operational efficiency compared to induction motors (IM) [10, 11]. Along with higher efficiency (when compared to IMs), simple rotor construction and absence of permanent magnets are further advantages which make SyR machines a valuable alternative also in the automotive sector. Despite these advantages, high torque ripple and low power factor are the most important drawbacks of this machine topology.

**a. Design challenges**

A lot of research effort has been dedicated to overcome the above reported issues mainly focusing on the rotor design [12–15], which represents the greatest challenge as it involves many degrees of freedom and complex phenomena [16, 17]. Important contributions to the analytical modelling of SyR machines are reported in [18–21]. The fast resolution of the analytical models comes at the cost of the accuracy of the performance prediction. The main assumptions of these models are a simplification of the rotor geometry and linearity of the iron materials. The latter, in some cases, could lead to imprecise prediction mainly due to the complex relation between flux and current [22]. The cross-coupling effects are particularly relevant in SyR machine therefore they must be considered for an accurate prediction of the torque required in the design stage and/or control purpose [23]. An interesting attempt to fully include the saturation effect within an analytical model has been reported in [24] and used in [25] to characterize the machine behavior also in case of rotor eccentricity. Although interesting, this approach does not allow to define a set of design-oriented equations aimed at identifying the performance trade-offs via a reduced number of design variables as in [26]. The latter, along with [27], proposes a comprehensive design procedure (including both stator and rotor) that, under certain assumptions (including the linearity of soft magnetic materials), allows to identify the trade-offs involved in the design of a low speed SyR machine. This set of analytical design equations has been extended in [28] in order to eliminate the hypothesis of linearity of the magnetic materials and so improve the accuracy of the predicted performance. The proposed method uses few finite element simulations carried out on an extremely restricted subset of design solutions, in order to take into account the inevitable non-linearities affecting the SyR machine performance. In general, the design procedure of SyR machine is usually divided in two steps: first an analytical (or hybrid) model is used to carry out a preliminary design; then a Finite Element Analysis (FEA) is employed to fine-tune the design accounting for the aspects disregarded in the first stage. For low speed application, this second design refinement stage is mainly electromagnetic.

**b. High-speed scenario: structural iron ribs and iron losses**

As the speed increases, the above second phase also includes several mechanical FEAs aimed at designing the so-called iron bridges (or ribs) to guarantee that the rotor maximum Von Mises stress is below the material yield limit [29]. Indeed, if these structural strengthening iron bridges are widened in order to ensure the rotor integrity at high speed, then the electromagnetic performances quickly deteriorate. As the speed increases, the conflicting requirements between electromagnetic and structural performance pose severe design challenges. In order to optimize the electromagnetic performance while guaranteeing the rotor integrity, several multi-physics design approaches have been proposed. In [30, 31], it has been shown that, if a FE-based optimization is adopted, then dividing the design procedure in two steps, i.e., the electromagnetic design followed by a mechanical design, is beneficial for both computational effort and performance of the final solution [32, 33]. In [34], an analytical model has been extended to include the effect of the radial iron ribs on the electromagnetic performance with the aim of assessing analytically the maximum power capability of SyR machines as function of the speed. All these studies, whether based on computational expensive FE automatic design approach, or based on simplified analytical models, have been carried out considering a given stator design. In other words, all these works mainly focus on the rotor design, effectively designing the stator disregarding the effect on the rotor structural behavior (e.g. choice of the split ratio). By doing so, also the balance between magnetic and electric loads is a-priori selected during the stator design without evaluating its effect on the overall performance.

As the speed increases, also the iron losses become a further limiting factor to consider during the design of a high speed SyR machine. This is a common challenge when designing high speed machines. Indeed, as the maximum speed increases, a different cooling system has to be designed to dissipate the higher iron losses. However, if the total losses are kept constant during the comparative design exercise, by decreasing the Joule losses quota as the iron losses rise, then the cooling system can be maintained unchanged leading to a comparison on a fair basis.

Clearly, the iron losses as well as the overall performance are deeply influenced by the soft magnetic material: different material present different magnetic, mechanical and thermal properties which in turn play a key role in the machine design.

**c. Material selection: a compromise choice**

The ever increasing variety of soft magnetic materials in terms of chemical compositions, manufacturing processes and thermal treatments makes the electrical machine design a challenging task [35]. The material selection is particularly important when designing high power density electrical machines where the constituent materials are pushed to the working limits in order to maximize their exploitation [36]. Indeed, transportation applications in the aerospace sector require impressively high power density levels in order to compete with the mechanical counterparts [37]. Similar challenges are faced by the automotive industry [38], although the electrical machine requirements are different.

Non-oriented cold-rolled carbon steel with different silicon content (SiFe) and alloys with different ratio of cobalt-iron (CoFe) are the main soft magnetic material families commercially available in a wide range of lamination thicknesses and thermal treatments [39]. The first one covers the majority of the market share while the second is mainly used in high power density applications given its higher cost (about one order of magnitude) and higher saturation flux density [40]. Along with the latter, magnetic permeability, iron losses and mechanical strength are the main performance indexes affecting the material selection.

Clearly, the soft magnetic material choice depends on the considered electrical machine topology and related needs. Regarding high-speed electrical machines, permanent magnet synchronous machines, induction motors and switched reluctance topologies could benefit from the adoption of high grade or thin gauge SiFe or CoFe materials [36,41,42]. The iron losses at the maximum operating frequency and the saturation flux densities are the main performance factors driving the choice of the soft magnetic material to be adopted. The yield strength also plays a fundamental role when designing high speed induction machines or interior permanent



magnet synchronous with laminated rotor back iron [43,44]. Regarding electrical machines for transportation applications, the material selection is also influenced by the maximum torque-speed profile along with the operating cycle [45–47].

Indeed, the driving cycle defines the material choice correctly balancing the competitive needs of having high saturation level, low iron losses and high yield strength [48]. The soft magnetic material selection is particularly challenging when designing high-speed electrical machines featuring complex rotor structure such as Synchronous Reluctance (SyR) machines. The conflicting requirements between the rotor structural integrity at high speed and the electromagnetic and thermal performances severely influence the design process including the soft magnetic material selection [33,49,50]. A comparative study of low-speed SyR machines with different grades of SiFe has been reported in [51] mainly assessing the efficiency aspects of the material choice. A FE-based design optimization procedure has been presented in [52] where the authors evaluate the SyR maximum power capability as function of the speed for different soft magnetic materials. Another interesting attempt to include the structural aspects within the design workflow has been presented in [34]. A linear analytical model based on the magnetic equivalent circuits has been used to identify the maximum power capability of SyR machines as function of the maximum design speed. Although these two studies attempt to assess the effect of the structural limitation on the electromagnetic performance, they both consider a fixed stator design and current density disregarding the thermal impacts of the increased iron losses. It follows that a fair comparison between soft magnetic material should consider both the stator and rotor design within the design process and should be capable of including the thermal and structural issues in a correct way.

### **1.2.2 PM-assisted synchronous reluctance machines**

The performance of synchronous reluctance machines can be improved inserting permanent magnets (PMs) within the rotor slots [53–55], as graphically shown in Fig. 1.5. When the performance improvement is medium-low, the resulting machine is usually called permanent

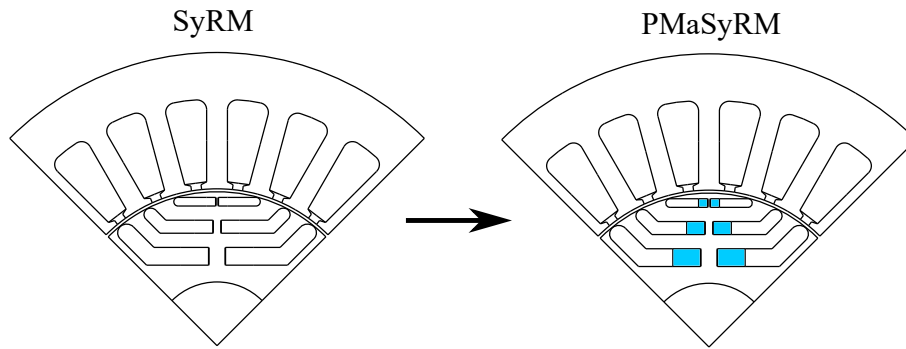


Figure 1.5: Insertion of the PMs within the rotor slots of SyRMs.

magnet assisted synchronous reluctance machine otherwise - when dominant - it falls within the realm of the interior permanent magnet synchronous machines [56, 57]. The differentiation between these two machine types is definitely vague and open to interpretation [58, 59]. It can be either related to the torque contribution quotas as stated above or to the design process [60]. In fact, the latter can be performed either designing a SyRM and then adding the PMs with a given criterion or considering both torque contributions at the same time [61] or considering only the PM torque in the first instance neglecting the reluctance component.

The design process of the resulting electrical machine (hereafter called permanent magnet assisted synchronous reluctance machine) is far from being standardized as it involves multiple design choices with conflicting results [62]. The design task becomes even more challenging when the application requires high speed operations due to the increased complexity added by the rotor structural design [63, 64].

Two main strategies have been proposed in recent years to design PMaSyRMs. The first one divides the design process into two or more steps [60] while the other approach treats the electrical machine as a unique device [65].

With the first design approach, both stator and rotor geometries are identified following the design rules of SyRMs, thus disregarding the effect of the permanent magnet assistance [66]. After this first stage, the effects of the PM insertion are evaluated with analytical or finite element tools. In particular, the PM quantity is dictated by the adopted design criterion, i.e. obtain either the widest constant power speed range or the maximum torque increment [58, 67]

subject to the constraints imposed by the demagnetization phenomena [68]. The distribution of the PMs within the rotor flux barriers is instead selected so to reduce the harmonic content of the resulting airgap flux density and consequently the torque ripple. Also this design step can be carried out analytically, as elegantly reported in [69], or by finite element method [70], which has the advantage of including all the secondary phenomena within the analysis (e.g. localized rotor saturation and slot harmonics effects). When designing PMSyRMs for high speed applications, a further mechanical design step must be considered to determine the iron rib dimensions and distribution required to guarantee the rotor structural integrity at the maximum speed [33].

On the contrary, the second design philosophy treats the PMSyRM as a unique device thus the PM electromagnetic and structural effects are considered from the initial stage. This approach has been implemented either with the aid of a simplified equivalent magnetic circuit [65] or by brute force FE-based design optimization [71]. In the first case, the hypothesis of linearity of the magnetic materials and the fact that the cross-saturation effect is neglected represent the main drawbacks. On the contrary, the FE-design optimization approach is very accurate but computationally more expensive than the analytical one. Albeit its high accuracy, FE-based optimization of multi-objective problems with a very wide research space often leads to sub-optimal solutions depending on the given time frame [30]. Indeed, unless a powerful computational cluster is available, dividing the research space and so the design procedure into several steps could lead to better results [32].

Although the comprehensive analytical design approach presented in [68, 72] is effective, at least as preliminary design stage to be followed by a FE refinement, it does not consider the permanent magnet influence on the stator design and neglects the soft magnetic material non-linearity. An interesting attempt to consider part of the non linearity effect has been proposed in [73] where the saturation of the main flux path is considered with the aid of a non-linear magnetic equivalent circuit. For high speed applications, when the dimensions of the rotor iron ribs become relevant, also the saturation of the high reluctance flux path plays a leading role in determining the machine performance. Indeed, the estimation of the q-axis inductance and

of the PM flux linkage assuming a certain saturation level of the iron ribs loses accuracy as the speed increases, i.e. as the rib dimensions increase. Indeed, the PM insertion into the rotor flux barriers complicates both structural and electromagnetic aspects. In fact, the PM increases the rotor mass to be sustained by the iron ribs and the presence of the latter non-linearly affects the machine performance, i.e. PM flux linkage and q-axis inductance.

The non-negligible thickness of the iron ribs poses also challenges regarding the analytical evaluation of the machine performance, which in turn depends on PM flux, inductances and stator magneto-motive force. It follows that an accurate analytical method should be capable of considering the main non-linearities of the magnetic circuit in order to correctly size the amount of PMs to insert within the flux barriers. Based on the performance index of interest, it is possible to identify three main criteria for the PM sizing:

- *Natural compensation*: the PMs dimensions are selected so to maximize the constant power speed range.
- *Target ipf*: the PMs dimensions are selected so to reach a pre-defined internal power factor.
- *Torque maximization*: the PMs dimensions are chosen with the aim of maximizing the average torque.

Therefore, the main challenge for PMSyRM is the definition of a design procedure suitable for high speed operations fully considering the effect of the PM presence and without neglecting the interaction between the structural targets of having iron ribs and their non-linear electromagnetic behavior.

### 1.2.3 Surface-mounted permanent magnet synchronous machines

Permanent Magnets Synchronous Machines (PMSMs) constitute a widespread solution for those applications requiring high torque density, efficiency and power factor especially when

high strength magnets made of rare earths are adopted [74–76]. Indeed, they out-compete induction motors in terms of efficiency, torque density, dynamic and thermal behaviors [77,78], while they guarantee higher power factor and lower torque ripple when compared to synchronous reluctance machines. Based on the permanent magnets arrangement, PMSMs can be divided into surface mounted ones and interior permanent magnet ones. PMs are attached to the outer surface of the rotor in the first case, whereas they are embedded within the rotor core in the latter. Since rare earth materials present high compressive strength and low tensile strength, they can barely withstand centrifugal forces due to high rotational speeds; therefore a retaining sleeve can be required to guarantee the rotor integrity especially in case of surface mounted PMSMs [79]. Such sleeve pre-stresses the material to compensate the centrifugal force at high speed operation [79]. This leads to two major drawbacks: firstly, the magnetic airgap becomes wider, with a consequent reduction of the average torque; secondly, depending on its composition, the sleeve can increase the total losses or can worsen the heat extraction from the rotor structure. In fact, sleeves can be made of non-magnetic metallic materials (e.g. stainless steel, titanium alloy, inconel) or composite ones (i.e. carbon fiber reinforced plastic). The former facilitate the heat removal from the rotor thanks to their superior thermal conductivity, but are prone to higher eddy current losses due to their good electrical conductivity; the latter show an enhanced weight to strength ratio but present opposite features in terms of thermal and electrical conductivity with respect to metallic sleeves [79, 80].

As well as for SyRM and PMSyR, also in the SPM case the other high-speed challenge is represented by the thermal management due to the increment of all loss components. Indeed, it affects the choices of the soft magnetic material (silicon-steel or cobalt-iron alloys), the wire type (random or litz wire) and the cooling system.

In literature, several works have addressed the design of high speed PMSMs. A typical approach starts with a pure electromagnetic design, which neglects the influence of the sleeve, aimed at obtaining the main machine parameters [81,82]; then, a mechanical parametric study [80, 83, 84] is performed to evaluate the rotor stress, size the sleeve and refine the final design. Other approaches consider the electromagnetic and structural designs within the same

workflow, either using simplified analytical models [85, 86] or more sophisticated approaches based on finite element analysis (FEA) [87–89]. It is worth to highlight that most of these approaches, analytical or FE-based, either start with a given stator design or do not consider the sleeve sizing within the electromagnetic design routine or do not keep the total losses constant when comparing different geometries. Indeed, a systematic design approach should be able to consider both the electromagnetic, thermal and structural needs within the same workflow and allow to assess the performance boundaries as the maximum speed increases.

### **1.3 Motivations and Goals of the Thesis**

The aim of this thesis is to present a comprehensive and systematic design approach for high speed synchronous machines, capable of taking into account the full definition of both stator and rotor geometries considering the limitation introduced by the rotor structural behavior and thermal constraints of the adopted materials, the electromagnetic targets, the cooling system and temperature limitations.

The design exercise is first applied for SyRMs, by introducing a set of analytical design equations based on the definition of only two independent design variables and some assumptions and constraints; the limits of such analytical model, which include saturation/cross-saturation and iron losses estimation, are then highlighted and overcome by a "adjustment" procedure capable of correctly consider all the machine non-linearities and thermal and structural limitations.

Then, the hybrid design approach is used for investigate:

- the performance boundaries as the design speed increases for a given SyRM outer envelope and selected materials, with the aim of quantify, model and separate the influence of structural and thermal limitations ;
- the influence of different types of soft ferromagnetic materials in order to assess the maximum power capability of this machine topology as function of the design speed; by doing so, it is possible to fairly assess the SyR performance boundaries achievable with

the considered materials;

- the tradeoffs involved when selecting the iron flux density (i.e. the magnetic load) to be used during the SyR machine design when adopting a Co-Fe alloy as the speed increases;
- the effects of adopting different stator current calculation criteria on the performance of SyRMs for several maximum speeds, especially from a electromagnetic and thermal point of view.

Then, the design methodology is extended to the PMSyRM scenario, where the PM insertion criterion within the rotor slots constitutes a further degree of freedom in the rotor design as the PM can be used to improve either the constant power speed range, the power factor or the average torque. The analytical equations and the adjustment procedure are properly modified so take into account the presence of the permanent magnets by improving the magnetic equivalent circuit and magnetic non-linearities correction. Then, three different PM insertion design criteria are compared and finally one of them is used for further investigation and for the machine prototyping.

Finally, the design philosophy is modified so to correctly account for the SPM rotor design which clearly needs a different approach if compared to a reluctance machine scenario. Also in this case, the thermal and structural limiting influences are investigated.

## 1.4 Structure of the Thesis

The thesis has been organized as follows.

- The second chapter is dedicated to the SyRMs design and fully describe the adopted design procedure, the materials selection and magnetic load influence and the effects of considering different thermal choices in terms of maximum current calculation.
- The third chapter deals with the PMSyRMs scenario and, after brief re-call of the analytical model, describes the influence of the PM within the design workflow both from an

electromagnetic and structural point of view also comparing different PM materials.

- The SPM case is therefore analyzed in the fourth chapter, where the influence of designing a retaining sleeve is deeply investigated also for different airgap thickness.
- A final comparison among technologies is reported in chapter 5, thus highlighting the main topology differences in terms of performance and optimal geometries.
- The sixth chapter reports the results of several experimental tests on 4 different prototypes, with the aim of validating the design approach.
- Finally, the main conclusion are drawn in the final chapter.

## 1.5 List of Scientific Publications

### 1.5.1 Journals

1. G. Gallicchio *et al.*, "Surface Permanent Magnet Synchronous Machines: High Speed Design and Limits," in *IEEE Transactions on Energy Conversion* (Early Access).  
doi: 10.1109/TEC.2022.3225224
2. M. Di Nardo, G. Gallicchio *et al.*, "High Speed Permanent Magnet Assisted Synchronous Reluctance Machine - Part II: Performance Boundaries," *IEEE Transactions on Energy Conversion* vol. 37, no. 4, pp. 2567-2577, Dec. 2022.  
doi: 10.1109/TEC.2022.3176383
3. G. Gallicchio *et al.*, "High Speed Permanent Magnet Assisted Synchronous Reluctance Machines - Part I: A General Design Approach," in *IEEE Transactions on Energy Conversion* vol. 37, no. 4, pp. 2556-2566, Dec. 2022.  
doi: 10.1109/TEC.2022.3176382
4. M. Di Nardo, G. Gallicchio *et al.*, "High-Speed Synchronous Reluctance Machines: Materials Selection and Performance Boundaries," in *IEEE Transactions on Transportation*



*Electrification*, vol. 8, no. 1, pp. 1228-1241, March 2022.

doi: 10.1109/TTE.2021.3109452

5. G. Gallicchio *et al.*, "High Speed Synchronous Reluctance Machines: Modeling, Design and Limits," in *IEEE Transactions on Energy Conversion*, vol. 37, no. 1, pp. 585-597.

doi: 10.1109/TEC.2021.3086879

6. E. Grasso, M. Palmieri, R. Mandriota, G. Gallicchio, F. Cupertino, M. and Nienhaus (2021). Influence and compensation of the stator flux on the direct flux control sensorless technique for PMSMs. *The Journal of Engineering*, 2021(6), 334-347.

doi: 10.1109/10.1049/tje2.12039

7. G. Gallicchio, M. D. Nardo, M. Palmieri and F. Cupertino, "Analysis, Design and Optimization of Hysteresis Clutches," in *IEEE Open Journal of Industry Applications*, vol. 1, pp. 258-269, 2020.

doi: 10.1109/OJIA.2020.3042884

8. G. Gallicchio, M. Palmieri, M. Di Nardo, and F. Cupertino, "Fast Torque Computation of Hysteresis Motors and Clutches Using Magneto-static Finite Element Simulation," *Energies*, vol. 12, no. 17, p. 3311, Aug. 2019.

doi:10.3390/en12173311

## 1.5.2 Conference Proceedings

1. G. Gallicchio, M. Palmieri, F. Cupertino, M. Di Nardo, M. Degano and C. Gerada, "Permanent Magnets Assistance Design Methods of High-Speed Synchronous Reluctance Machines," *2022 IEEE Energy Conversion Congress and Exposition (ECCE)*, 2022, pp. 1-8.

doi: 10.1109/ECCE50734.2022.9947998

2. G. Gallicchio, M. Palmieri, F. Cupertino, M. Di Nardo, M. Degano and C. Gerada, "Design Methodologies of High Speed Synchronous Reluctance Machines," *2022 Interna-*

- tional Conference on Electrical Machines (ICEM)*, 2022, pp. 448-454.  
doi: 10.1109/ICEM51905.2022.9910624
3. G. Gallicchio, M. Palmieri, F. Cupertino and M. Di Nardo, "Influence of the Cost Function on the Optimal Design of Magnetic Hysteresis Couplings," *2022 International Conference on Electrical Machines (ICEM)*, 2022, pp. 1-7.  
doi: 10.1109/ICEM51905.2022.9910938
4. O. Korman, M. Di Nardo, M. Degano, C. Gerada, G. Gallicchio and F. Cupertino, "On the Pole Pair Selection of Synchronous Reluctance Machines for Traction Applications," *2022 International Conference on Electrical Machines (ICEM)*, 2022, pp. 448-454.  
doi: 10.1109/ICEM51905.2022.9910687
5. G. Gallicchio, M. Palmieri, F. Cupertino, M. Di Nardo, M. Degano and C. Gerada, "Influence of the Magnetic Load on High Speed Synchronous Reluctance Machines Design," *IECON 2021 – 47th Annual Conference of the IEEE Industrial Electronics Society*, 2021, pp. 1-6.  
doi: 10.1109/IECON48115.2021.9589972
6. G. Gallicchio, M. Palmieri, F. Cupertino and M. Di Nardo, "On the Radial Scalability of Magnetic Hysteresis Couplers," *2021 IEEE Workshop on Electrical Machines Design, Control and Diagnosis (WEMDCD)*, 2021, pp. 119-124.  
doi: 10.1109/WEMDCD51469.2021.9425669
7. G. Gallicchio, M. Palmieri, F. Cupertino and M. Di Nardo, "Optimal Design of Magnetic Hysteresis Couplers," *2021 IEEE Workshop on Electrical Machines Design, Control and Diagnosis (WEMDCD)*, 2021, pp. 131-136.  
doi: 10.1109/WEMDCD51469.2021.9425644
8. M. Palmieri, G. Gallicchio and F. Cupertino, "An Automated Design Procedure for the Power Density Optimization of IPM machines," *2020 IEEE International Conference on*

*Power Electronics, Drives and Energy Systems (PEDES)*, 2020, pp. 1-6.

doi: 10.1109/PEDES49360.2020.9379355

9. G. Gallicchio, M. Palmieri, E. Grasso, M. Nienhaus and F. Cupertino, "Inductances Computation Using Finite Element Analysis for PMSM Sensorless Control," *2020 IEEE International Conference on Power Electronics, Drives and Energy Systems (PEDES)*, 2020, pp. 1-6.

doi: 10.1109/PEDES49360.2020.9379864

10. G. Gallicchio, M. Palmieri and F. Cupertino, "Comparison Between PM Motors for an Aircraft E-pump Drive," *2020 IEEE International Conference on Power Electronics, Drives and Energy Systems (PEDES)*, 2020, pp. 1-6.

doi: 10.1109/PEDES49360.2020.9379506

## **Chapter 2**

# **Design of Synchronous Reluctance**

## **Machines**

This chapter describes the procedure adopted for the design of synchronous reluctance machines considering both low and high speed design scenarios. The design philosophy is based on the analytical approach first reported in [27], which reduces the problem complexity by the definition of only two independent design variables. The accuracy of such design approach has been improved by means of an adjustment procedure aiming at correctly estimate the performance of the machine candidates as a function of the two independent design variables.

The high speed limiting design factors, namely structural and iron losses, are included within a set of design equations, in order to assess their impact on the overall performance and the geometry of the optimal design solutions. After introducing the extended set of design equations in section 2.1, its limits are reported in section 2.2 along with a methodology to improve its accuracy in section 2.3. The influence of both high speed limiting design aspects are then deeply investigated in sections 2.4 and 2.5. The material and magnetic load selections are investigated in sections 2.6 and 2.7, while comparison among current calculation criteria (affecting the thermal performance) is shown in section 2.8.

For the sake of reducing the complexity of the high-speed design and since the final application is a continuous-duty one, the base speed and the maximum speed are considered to be

equal, therefore the flux weakening region is not investigated.

## 2.1 Analytical design equations

### 2.1.1 First assumptions and choices

The design methodology adopted in this thesis is based on the definition of two independent design variables, with the aim of reducing the design complexity if some reasonable assumptions, rules and preliminary design choices are adopted. Indeed, the design of synchronous reluctance machines is a challenging task since it involves a lot of degree of freedom which include the shape, orientation and position of the flux barriers.

Several possibilities can be adopted for the shape of the flux barriers: circular, "I2U" and "fluid" shapes (see Fig. 2.1) are generally adopted. In this thesis, the "I2U" shape is hereafter considered. Most of the considerations which will be shown could be surely extended to other barriers shapes as well.

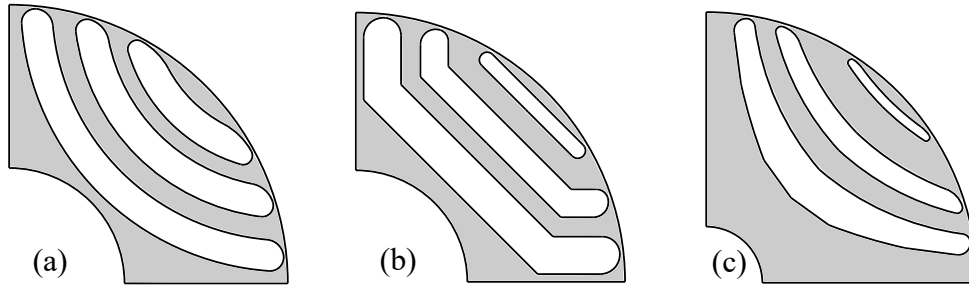


Figure 2.1: Typical flux barriers shapes: a) circular, b) I2U and c) fluid.

Other assumptions include the number of pole pairs which is set to 2 as it is a common choice in high-speed applications since an increment of the pole pairs would lead to a raise of the iron losses which could be significant during high-speed operations, and the winding layout which is a single-layer distributed winding for all the designs. Concentrated winding will not be investigated since the winding layout is not one of the topic of this thesis.

### 2.1.2 Main design equations

Torque and power factor can be expressed as functions of two independent variables: split ratio ( $sr$ ), defined as the ratio between the outer rotor radius ( $r_r$ ) and the outer stator radius ( $r_s$ ) as

reported in (2.1) and (2.2)

$$sr = \frac{r_r}{r_s} \quad (2.1)$$

and the magnetic ratio ( $mr$ ), which is the ratio between the airgap flux density ( $B_g$ ) and the iron flux density ( $B_{fe}$ ) as in (2.2)

$$mr = \frac{B_g}{B_{fe}} \quad (2.2)$$

The remaining geometrical parameters, all depicted in Fig. 2.2a, can be expressed in terms of these two quantities via physical and geometrical considerations [28]. It follows that both

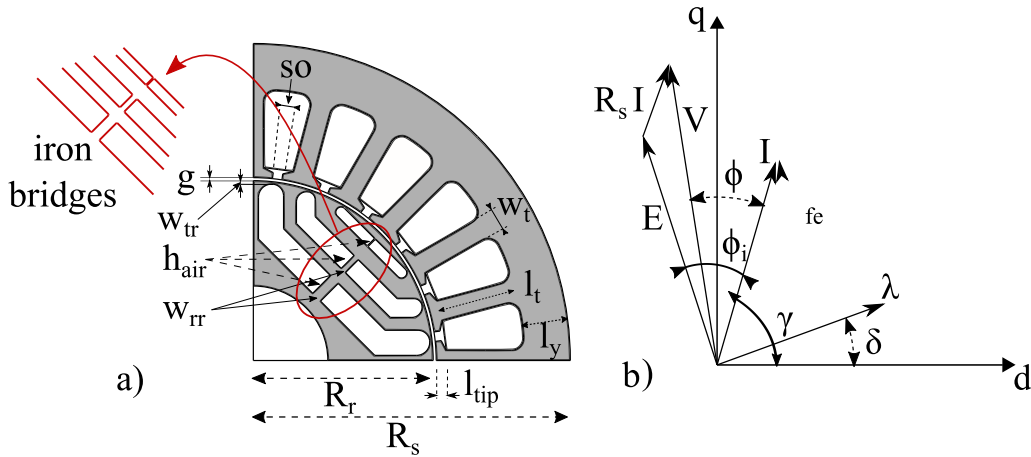


Figure 2.2: a) Vector diagram of a SyR machine. b) Parametrization of the stator and rotor geometry.

the machine geometry and the performance can be expressed as function of the  $sr$  and  $mr$  thus leading to the definition of a design plane in which several machine candidates are compared and the trade-offs between electromagnetic, thermal and structural needs can be evaluated.

In general the main performance indexes are torque and power factor which present different shape over the  $sr - mr$  plane: indeed, the combination of  $sr - mr$  which optimizes the torque does not necessarily coincide with the one maximizing the power factor. In fact, the power factor depends only on the inductances, while the torque depends on both inductances and capability of the machine to produce the stator magneto-motive force (m.m.f) and flux, which in turn depends on the geometry and on the constraints imposed during the design (e.g. external radius, electrical loading, current density, total losses, etc.). The hypotheses underlying this set

of design equations can be summarized as follows.

- The stator outer radius ( $r_s$ ) and axial length ( $l_{fe}$ ) are fixed.
- The permeability of the iron materials composing the stator and rotor core and the stator teeth is assumed to be infinite; therefore, the machine design is treated as a linear problem.
- The power dissipation capability of the cooling system is fixed, which means that the ratio between machine total losses and external surface available for the heat exchange ( $k_{cool}$ ) is given. This would lead to fair comparison since all the machine of the design plane can share the same cooling system.
- The flux density  $B_{fe}$  within each stator and rotor part is preliminary chosen.

### 2.1.3 Modeling equations

The torque produced by an electrical motor (a SyR motor in this case) can be expressed, in its general form, as follows:

$$T = \frac{3}{2}p(\lambda_d i_q - \lambda_q i_d) \quad (2.3)$$

where  $p$  is the number of pole pairs,  $i_d$  and  $i_q$  are d-axis and q-axis currents, whereas  $\lambda_d$  and  $\lambda_q$  are d-axis and q-axis flux linkages. This torque equation refers to the d-q reference frame reported in Fig. 2.2, whereas the d-axis and the q-axis are the lower and higher reluctance ones respectively. The fluxes of (2.3) can be written so to highlight the inductance contribution as follows:

$$\lambda_d = L_{dd}i_d + L_{dq}i_q \quad (2.4)$$

$$\lambda_q = L_{dq}i_d + L_{qq}i_q \quad (2.5)$$

In (2.4) and (2.5)  $L_{dq}$  is the term which takes into account the cross-coupling effects (usually neglected in the analytical design), and  $L_{dd}$  and  $L_{qq}$  are the d- and q-axis inductances, sum of



the magnetizing and leakage components:

$$L_{dd} = L_{dm} + L_s \quad (2.6)$$

$$L_{qq} = L_{qm} + L_s + L_{q-rib} \quad (2.7)$$

where  $L_s$  is the leakage inductance, equal for both axis, and  $L_{q-rib}$  is the additional leakage inductance due to the flux short circuited via the iron ribs.

From the vector diagram at steady state depicted in Fig. 2.2b, the internal power factor  $ipf$ , i.e. the cosine of the angle between the induced voltage  $E$  and the current vector  $I_m$ , can be deduced:

$$ipf = \cos(\phi_i) = \sin(\gamma - \delta) \quad (2.8)$$

where  $\gamma$  and  $\delta$  are the current and the flux phase angles, respectively.

It follows that accuracy of the torque and power factor calculations depends on the inductances estimations which in turn are function of the machine design.

The latter includes the stator and rotor designs which in turn depend on the  $sr - mr$  combination. It will be shown that the split ratio mainly affect the rotor radius, while the magnetic ratio deeply influences the thickness of the stator and rotor iron parts (stator yoke and tooth, rotor flux guides).

### 2.1.4 Stator design

The design of the stator can be performed once the flux per pole is defined. Dealing with synchronous reluctance machines and adopting the d-q reference frame reported in 2.2b, the d-axis can be considered as the "strong" one since most of the flux is produced by the fictitious d-axis coils.

The flux per pole can be therefore defined as follows:

$$\phi_p = 2r_r l_{fe} B_g / p \quad (2.9)$$

where  $B_g$  is assumed to be produced only by the d-axis current, whose mathematical expression will be reported in the following. According to (2.9) the tooth width ( $w_t$ ) and stator yoke thickness ( $l_y$ ) can be sized imposing the desired iron flux density  $B_{fe}$ :

$$l_y = \frac{\pi r_s}{2 p} sr \cdot mr \quad (2.10)$$

$$w_t = \frac{2\pi r_s}{6qp} sr \cdot mr \quad (2.11)$$

where  $q$  is the number of slots per pole per phase. The tooth length follows by geometrical considerations:

$$l_t = r_s - r_r - l_y - l_{ts} \quad (2.12)$$

By imposing a certain shape for the slot (which include the slot opening  $so$ , tooth shoe height  $l_{ts}$  etc), it is possible to compute the slot area  $A_{slots}$  and the end-winding length  $l_{ew}$  as follows:

$$A_{slots} = \frac{6 \cdot q \cdot p \cdot l_t}{2} \cdot \left[ \frac{2\pi(sr \cdot r_s + g + l_{ts})}{6 \cdot q \cdot p} + \frac{2\pi(sr \cdot r_s + g + l_t)}{6 \cdot q \cdot p} - 2w_t \right] \quad (2.13)$$

$$l_{ew} = 2l_t + \left( sr \cdot r_s + \frac{l_t}{2} \right) \frac{\pi}{p} \quad (2.14)$$

leading to the definition of the stator design. In (2.13)  $g$  is the airgap thickness.

### 2.1.5 Rotor design

Regarding the rotor geometry design, the following rules/assumptions [27] are adopted.

- Uniform distribution of the equivalent rotor slots:

$$\Delta\alpha^i = \frac{2\pi}{n_r} \quad \text{for } i = 1, 2, \dots, n \quad (2.15)$$

where  $n_r$  is the numbers of the equivalent rotor slots and  $n$  the number of flux barriers.

- Flux barriers sharing the same permeance:

$$P_b = \frac{\mu_0 S_b^i}{h_a^i} = K \quad \text{for } i = 1, 2, \dots, n \quad (2.16)$$

where  $S_b^i$  and  $h_a^i$  are the  $i^{\text{th}}$  barrier surface and height, respectively.

- Total iron thickness along the q-axis equal to the stator yoke thickness.

The above rules allow to fully define the rotor, including the flux barriers height and surface. The last rotor parameters are the structural iron bridges whose design can be correctly performed using a structural FEA coupled to an optimization algorithm [29] or adopting a parametric approach. Indeed, given the complexity of the rotor structural behaviour, the design of the iron bridges, i.e. the selection of their thickness, positions and orientation along the barrier constitute a challenging design aspect. However, a simplified analytical formulation considering only the steady state centrifugal force  $F_c^i$  is commonly used [29, 90] to estimate the total iron bridge ( $w_r^i$ ) of the  $i^{\text{th}}$  barrier:

$$w_r^i = \frac{k_s F_c^i}{\sigma_s l_{fe}} = \frac{k_s}{\sigma_s l_{fe}} m_{fg}^i R_{fg}^i \Omega^2 \quad (2.17)$$

where  $k_s$  is a safety factor,  $\sigma_s$  is the yield strength of the rotor lamination,  $m_{fg}$  is the sum of the flux guide masses which has to be sustained by the  $i^{\text{th}}$  iron bridge,  $R_{fg}$  is the center of gravity of the same mass, and  $\Omega$  is the mechanical speed. The calculated rib thickness increases going from the outermost to the innermost flux barrier because the mass which must be sustained increases in the same direction as shown in Fig. 2.3.

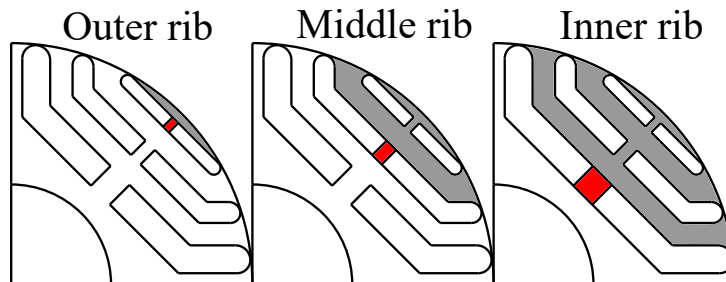


Figure 2.3: Iron area considered for sizing the radial iron ribs

### 2.1.6 Inductances calculation

The stator magneto-motive force can be divided into two components, namely the d-axis and q-axis ones. When only the d-axis circuit is supplied, the flux path within the machine would resemble the one reported in Fig. 2.4a. It is worth to notice that the rotor magnetic potentials are

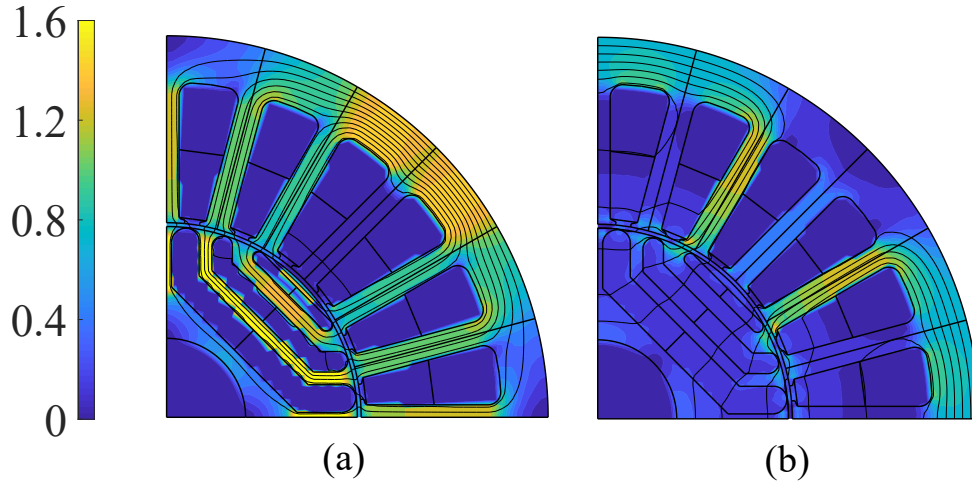


Figure 2.4: Flux density distribution when a) the d-axis circuit is supplied. b) the q-axis circuit is supplied.

zero in that condition, therefore the d-axis inductance can be calculated according to following well-known equation:

$$L_{dm} = \frac{\pi}{2} \mu_0 k_w \left( \frac{N_s}{p} \right)^2 \frac{sr \cdot r_s l_{fe}}{k_c g} \quad (2.18)$$

where  $k_w$  is the winding factor,  $N_s$  the turns' number in series per phase,  $k_c$  the Carter's coefficient and  $\mu_0$  the vacuum permeability.

Differently, as shown in Fig. 2.4b, the rotor islands react to the q-axis m.m.f, therefore each rotor island would assume a different magnetic potential. A common approach [27] for the q-axis flux computation starts by dividing the m.m.f. into two parts: its averaged value along the rotor periphery with internals equal to the rotor pitches ( $\Delta\alpha^i$  in Fig. 2.5) also called *staircase function*  $f(\alpha)$ , and the remaining part of the m.m.f.  $c(\alpha)$  as shown in Fig. 2.6.

The latter component leads to generation of the so-called circulating flux which accounts for the flux which does not cross the rotor barriers, while the first one generates the flow-through component that is the flux flowing between one rotor island to the next one. The circulating

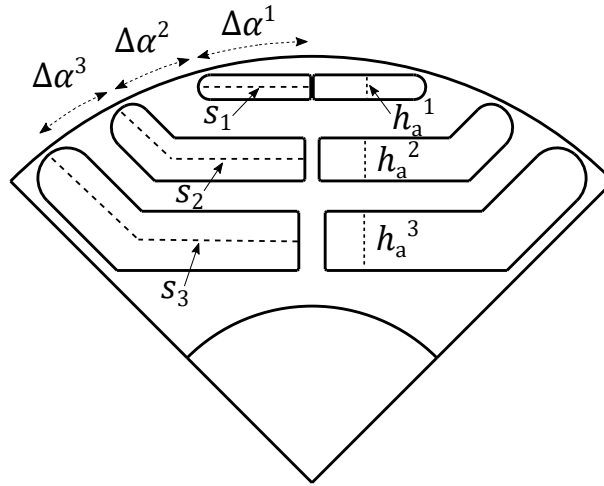


Figure 2.5: Rotor parametrization.

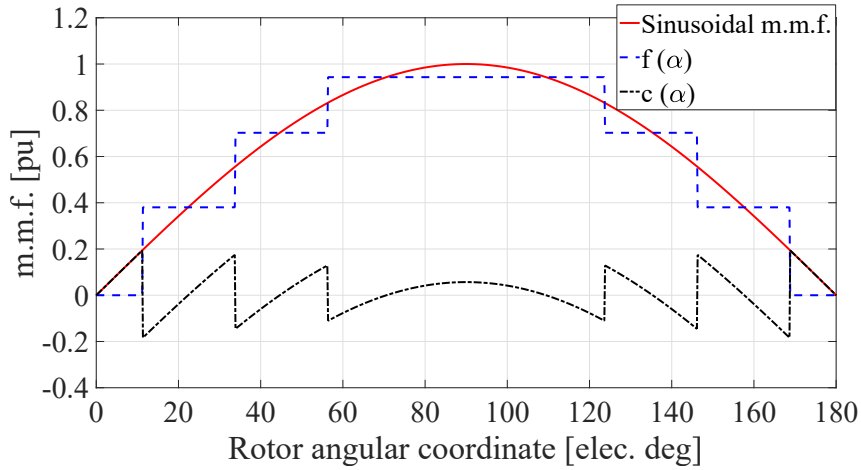


Figure 2.6: Subdivision of the q-axis m.m.f.

inductance component can be calculated as in (2.19) in p.u. of the d-axis base inductance [27]:

$$\frac{L_{qm-c}}{L_{dm}} = \left( 1 - \frac{4}{\pi} \sum_{k=1}^n f_i^2 \Delta\alpha_i \right) \quad (2.19)$$

where  $f_i$  are the step values of the staircase function.

With the aim of correctly computing the main flux q-axis inductance, a simplified calculation (which neglects the iron ribs influence) can be adopted:

$$\frac{L_{qm-f}}{L_{dm}} = \left( \frac{4}{\pi} \frac{pk_c g}{sr \cdot r_s} \sum_{k=1}^n \frac{s_i}{h_a^i} \Delta f_i \right) \quad (2.20)$$

where  $s_i$  and  $h_a^i$  are the flux barriers surface (in p.u. of the axial length) and thickness respectively, while the leakage inductance due to the flux shunted via iron ribs can be computed using (2.21).

$$L_{q-rib} = \frac{4}{\pi i_q} N_s k_w w_{avg} l_{fe} B_{sat} \quad (2.21)$$

where  $B_{sat}$  is predefined saturation value of the iron ribs and  $w_{avg}$  is the ribs average value. The increment of the q-axis inductance due to the increment of the thicknesses of the structural iron bridges clearly leads to a bigger  $\lambda_q$  caused by the additional flux portion flowing via the iron ribs which in turn implies a loss of torque and power factor. Indeed, the torque is proportional to the difference between the d- and q-axis inductances which decreases as the iron ribs become wider.

This kind of q-axis calculation approach is effective when applied to low-medium speed scenarios, since the structural iron ribs are smaller enough to be considered equally saturated, while it loses accuracy when applied to very high-speed scenarios.

In such cases, the equivalent magnetic circuit reported in Fig. 2.7 can be adopted.

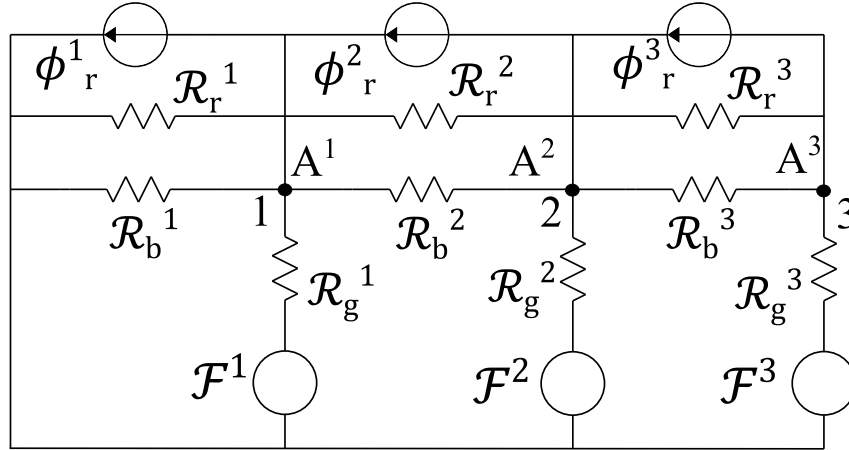


Figure 2.7: Magnetic equivalent circuit.

The stator m.m.f. is modeled by the three m.m.f. generators  $F^1$ ,  $F^2$  and  $F^3$ , while the flux barriers are taken into account by the reluctances  $R_b^1$ ,  $R_b^2$  and  $R_b^3$ , as in (2.22) and (2.23):

$$F^i = \frac{3k_w N_s I_{max}}{\pi p} \cdot f^i \quad \text{for } i = 1, 2, \dots, n \quad (2.22)$$

$$R_b^i = \frac{1}{P_b^i} \quad \text{for } i = 1, 2, \dots, n \quad (2.23)$$

The airgap m.m.f. drops are taken into account with the reluctances  $R_g^1$ ,  $R_g^2$  and  $R_g^3$  expressed as in (2.24):

$$R_g^i = \frac{g}{\mu_0 \cdot \Delta\alpha^i \cdot r_r \cdot l_{fe}} \quad (2.24)$$

As the influence of the iron ribs becomes non-negligible as the maximum speed increases, the flux generators  $\phi_r^1$ ,  $\phi_r^2$  and  $\phi_r^3$  in parallel with the reluctances  $r_r^1$ ,  $r_r^2$  and  $r_r^3$  are used to correctly model the iron ribs effects, which can be calculated by (2.25):

$$\phi_r^i = B_{rib0}^i \cdot w_r^i \cdot l_{fe} \quad , \quad R_r^i = \frac{h^i}{\mu_{rib}^i \cdot \mu_0 \cdot w_r^i \cdot l_{fe}} \quad (2.25)$$

where  $B_{rib0}^i$  and  $\mu_{rib}^i$  are defined by the ribs working point  $B_{rib}^i$  on the rotor B-H curve (as graphically explained in Fig. 2.8).

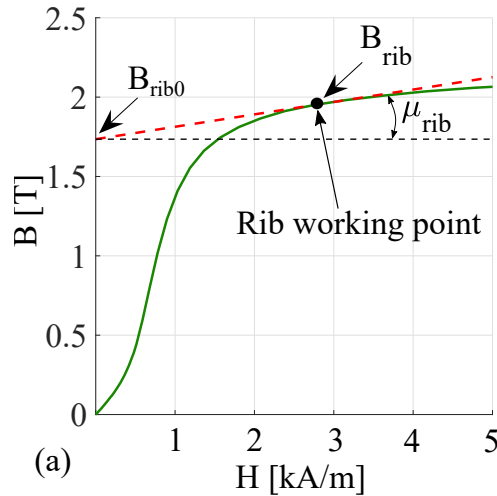


Figure 2.8: Iron ribs magnetic model.

The resolution of such magnetic circuit can be performed applying the nodal-voltage method at the nodes 1, 2 and 3 leading to the calculation of the unknown rotor magnetic potentials  $A^1$ ,  $A^2$  and  $A^3$ . A correct calculation of the latter depends on the accuracy of the ribs magnetic models (i.e.  $B_{rib0}$  and  $\mu_{rib}$ ) which in turn depends on the rotor material BH curve and ribs width (which influences the saturation level). Therefore, an iterative procedure has to be adopted, in

which the ribs magnetic model is updated according to the  $A^i$  calculation at each iteration until the convergence is reached.

Such procedure (summarized in the flowchart shown in Fig. 2.9) consists in following steps:

- stator and rotor design for  $sr - mr$  combination, including tooth and yoke width and rotor flux barriers definition;
- ribs magnetic model definition imposing a reasonable saturation value (e.g. 2 T);
- resolution of the magnetic circuit by applying the nodal-voltage method thus leading to the calculation of the actual flux density within the iron ribs;
- updating the irob ribs magnetic model if the  $B_{rib}$  error does not lie within a predefined threshold;
- final resolution of the magnetic circuit and calculation of the airgap flux density waveform;
- calculation of the q-axis inductance by integrating the airgap flux density over the pole pitch and dividing by the q-axis current.

It is worth to notice that such resolution needs the q-axis current knowledge.

### 2.1.7 Current components

The d-axis current component can be inferred from the Ampere's law (when  $i_q = 0$ ):

$$i_d = \frac{\pi k_{cg}}{3 \mu_0} \frac{p}{k_w N_s} B_g \quad (2.26)$$

The q-axis component can be calculated knowing  $i_d$  and the maximum current  $I_{max}$ :

$$i_q = \sqrt{I_{max}^2 - i_d^2} \quad (2.27)$$



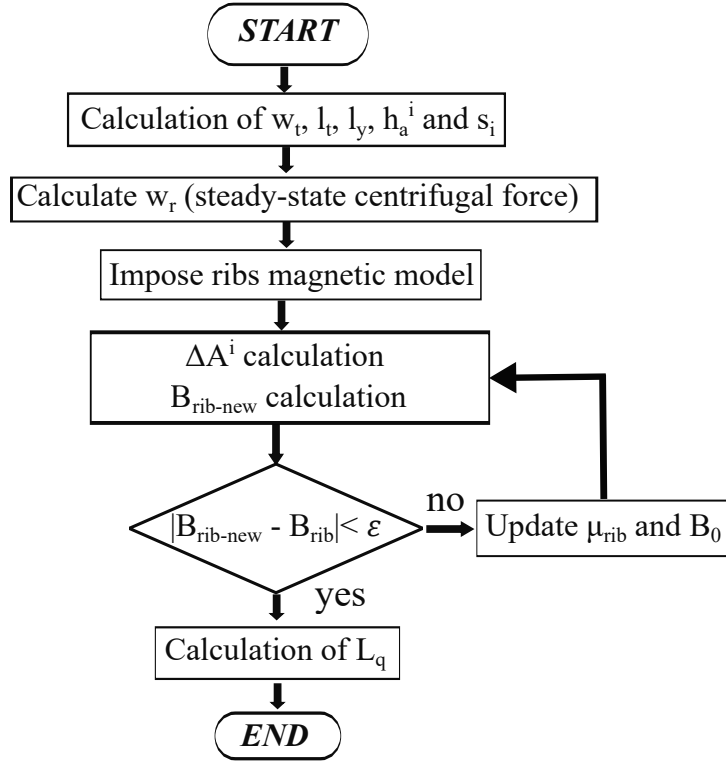


Figure 2.9: q-axis inductance calculation by means of magnetic circuit.

Considering the motor geometrical dimensions and the correlation between cooling capability  $k_{cool}$ , total losses  $P_t$  (2.28), and phase resistance  $R_{ph}$  (2.29), the maximum current value  $I_{max}$  is calculated as in (2.30).

$$P_t = 2\pi r_s l_{fe} k_{cool} = P_j + P_{fe} = 3R_{ph} I_{max}^2 + P_{fe} \quad (2.28)$$

$$R_{ph} = 3N_s^2 \frac{2\rho_{cu}(l_{fe} + l_{ew})}{k_{fill} A_{slot}} \quad (2.29)$$

$$I_{max} = \frac{1}{3N_s} \sqrt{\frac{k_{fill} A_{slots}}{2\rho_{cu}(l_{fe} + l_{ew})} (2\pi r_s l_{fe} k_{cool} - P_{fe})} \quad (2.30)$$

In (2.29)  $k_{fill}$  is the imposed slot fill factor and  $\rho_{cu}$  is the copper resistivity, while in (2.28)  $P_{fe}$  are the stator iron losses and  $P_j$  the Joule ones. For low-speed operations of SyR machines, iron losses are negligible with respect to the Joule ones, and can be disregarded in the  $I_{max}$  computation [27, 28]. Conversely, considering a design scenario at constant stator losses, the iron losses become significant as the speed increases, thus reducing the value of  $I_{max}$ . The iron

loss ( $P_{fe}$ ) can be estimated considering the Steinmetz equation as in (2.31):

$$P_{fe} = k_{fe} M_{fe} [k_h f^\alpha B_{fe}^\beta + k_e (f B_{fe})^2] \quad (2.31)$$

where  $k_{fe}$  is a correction factor (usually between 1-2),  $M_{fe}$  is the iron mass,  $k_h$  and  $k_e$  are the hysteresis and the eddy current coefficients,  $\alpha$  and  $\beta$  are exponential coefficients for the frequency and flux density, respectively, and  $f$  is the electrical frequency. This formulation neglects the harmonic losses and assumes that the whole stator iron shares the same flux density level over one electrical period.

## 2.2 Limits of the analytical approach

Considering the set of assumptions and constraints reported in Table 2.1, and using the design equations described in the previous section, the dependencies of torque and power factor from the split and magnetic ratio are analyzed by means of contour plots in the  $sr - mr$  design plane.

Table 2.1: Machine parameters

Parameter	Value	Units
Outer stator radius	26.2	mm
Stack length	50	mm
Pole pair	2	/
Cooling capability	37000	W/m <sup>2</sup>
Stator yoke flux density	1.9	T
Stator tooth flux density	2.1	T
Airgap thickness	0.25	mm
Lamination material	Vacodur 49	//
Yield strength	390	MPa

With the aim of evaluating the accuracy of the analytical design formulations, all the ma-

chine designs in the  $sr - mr$  plane have been FE-simulated both at low (1krpm) and high speed (50krpm). Fig. 2.10 reports a comparison between the analytical and the FEA results in terms of average torque and internal power factor in the  $sr - mr$  plane. Both torque and power factor

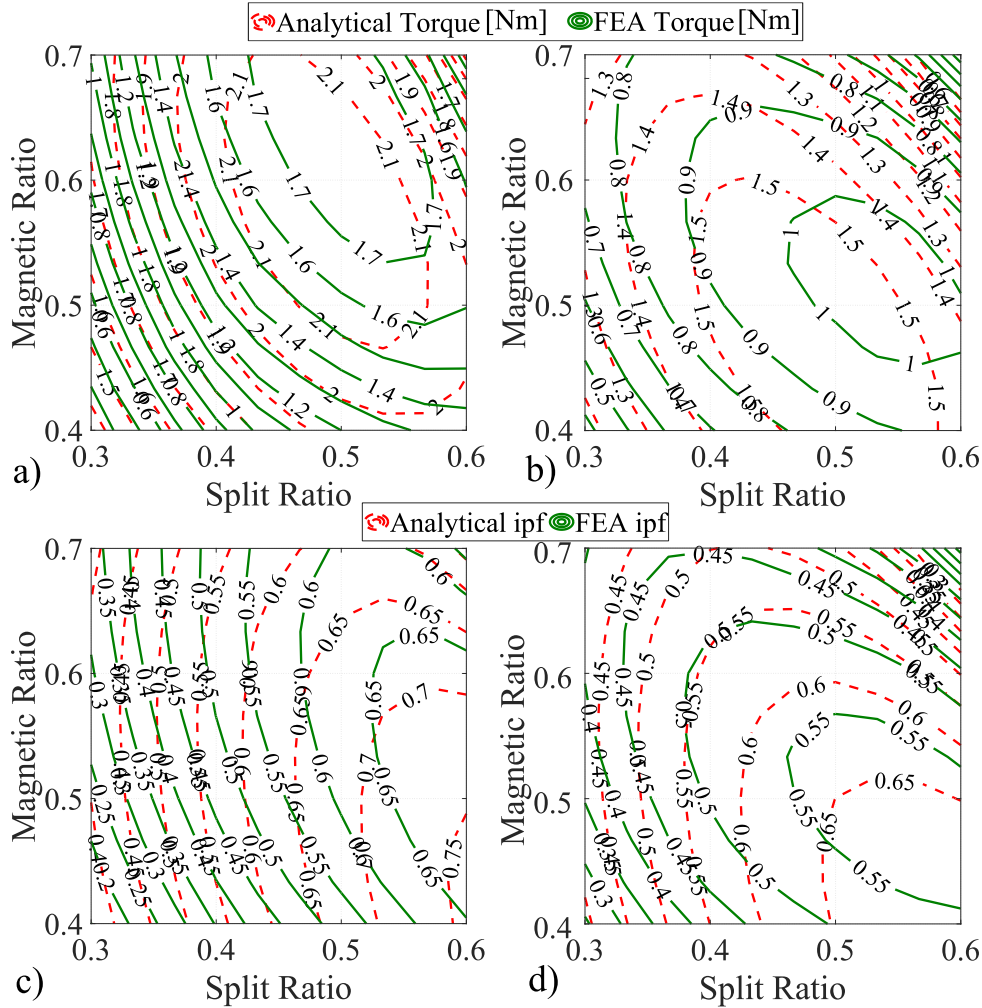


Figure 2.10: Comparison between analytical and FE computation of torque (a, b) and internal power factor (c, d) at 1 krpm (a, c) and 50 krpm (b, d).

show relevant errors for low and high speed, although in the latter case the discrepancy is much higher.

Low speed designs, Fig. 2.10a and 2.10c, exhibit error that can be ascribed to:

- the saturation of the d-axis flux path (affecting  $L_d$ ), which has been ignored in the analytical design stage since the iron permeability has been assumed to be infinite,
- the cross-coupling effect (expressed by the term  $L_{dq}$ ), which has also been ignored during

the analytical performance estimation.

While for high speed designs (Fig. 2.10b and 2.10d):

- the mismatch between the analytical and FE-computed iron losses
- the approximation in the  $L_{q-rib}$  computation

are further sources of error in the torque and power factor predictions. To confirm these causes of mismatch, further investigations are reported hereafter for each source of error. Fig. 2.11a shows the ratio between the analytical and FE calculation of  $L_{dm}$ , which is the d-axis saturation factor. The latter is higher for design solutions with low split and magnetic ratios, which correspond to the region where the torque error is higher. Fig. 2.11b and 2.11c report the ratio between  $L_{dq} \cdot i_q$  and  $L_{dd} \cdot i_d$ , which quantifies the cross-coupling in the design plane for both low and high speeds. This term has been FE-evaluated adopting the frozen permeability approach

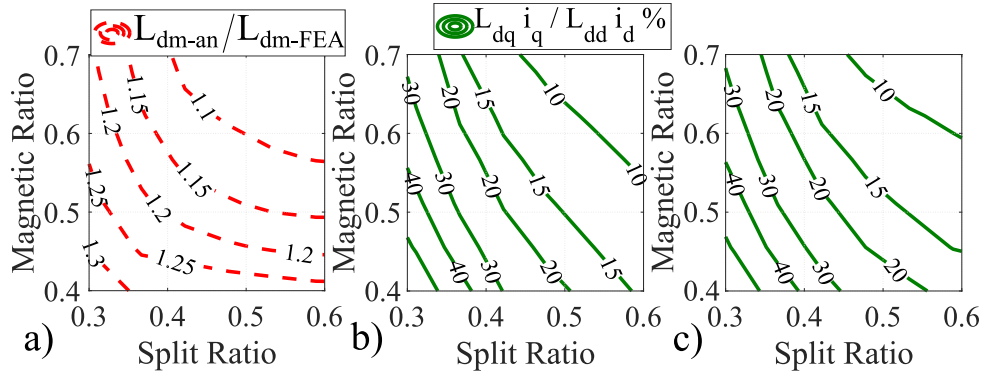


Figure 2.11: a) Ratio between analytical and FE computation of  $L_{dm}$ , cross coupling effects at b) 1 krpm and c) 50 krpm.

reported in [91, 92]. As expected, in the design plane region where the cross coupling is more pronounced, the torque and power factor error is higher. At the higher speed, the cross-coupling terms are slightly higher with respect to the lower speed due to the increment of the iron area in common to both d- and q-axis fluxes.

Regarding the iron losses, the analytical estimation clearly does not match with the FE computation, both in terms of numerical values and contour shape, as shown in Fig. 2.12a and 2.12b. This mismatch is due to the non uniform distribution of the stator iron flux density

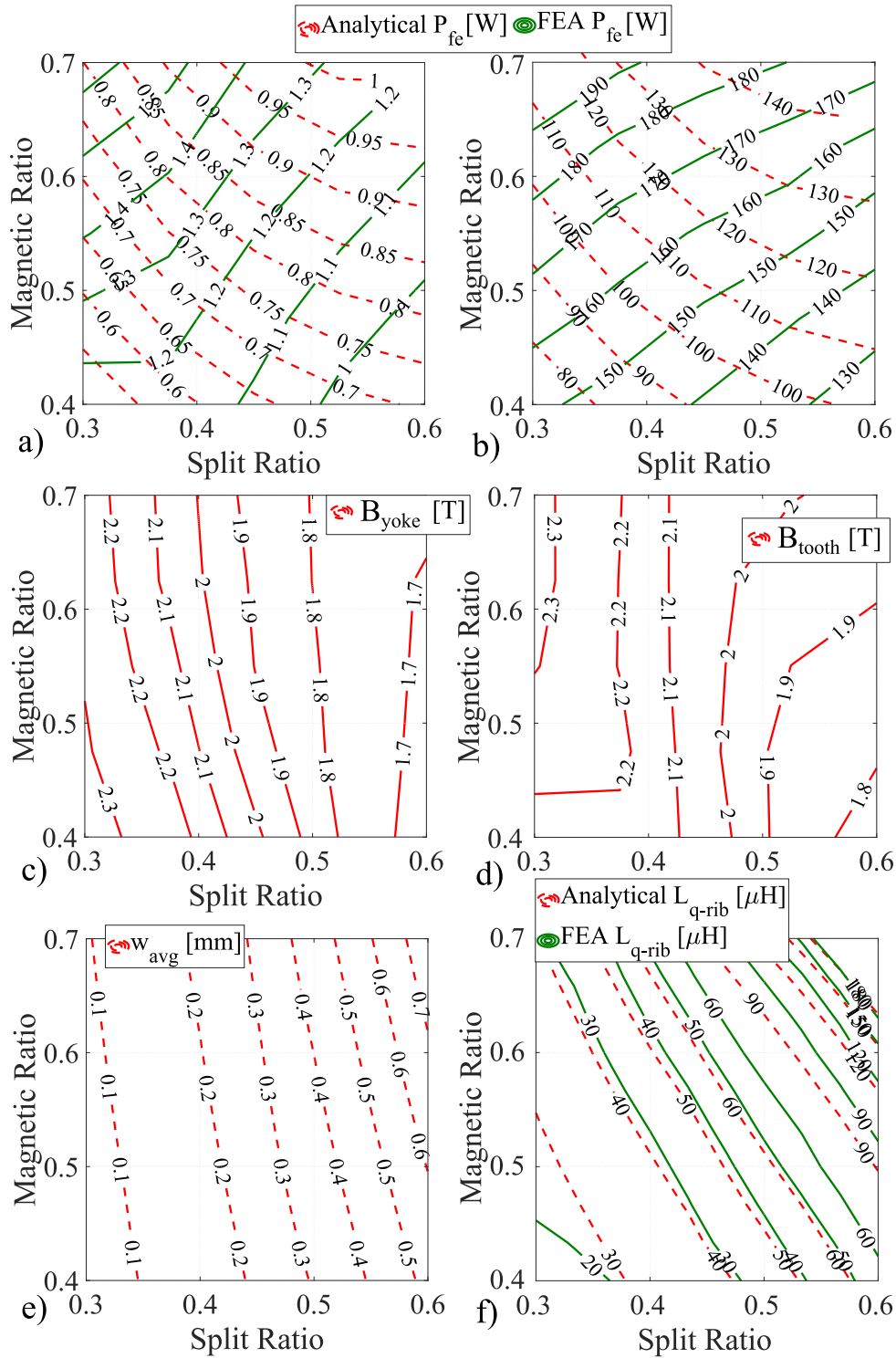


Figure 2.12: Comparison between analytical and FE computation of iron losses at a) 1 krpm; b) 50 krpm. Average value of the flux density first harmonic component at 1 krpm in c) stator yoke; d) stator tooth. e) Average total bridges at 50 krpm. f) Comparison between analytical and FE computation of  $L_{q-rib}$  at 50 krpm.

over the full  $sr - mr$  plane as reported in Fig. 2.12c and 2.12d. These pictures show the first harmonic of the stator yoke and tooth flux densities (at 1 krpm) extracted from the FEAs. Fig. 2.12e and 2.12f confirm that approximating the increment of the q-axis inductance proportional to the average total bridge is acceptable being similar the contour shapes of  $w_{avg}$  and  $L_{q-rib}$  FE calculated. Despite a qualitative match, there is a difference between analytical and FE inductance increment. The FE calculation of the q-axis inductance due to the iron ribs presence has been performed by difference between the q-axis inductance at the design speed and the one obtained at zero speed for each  $sr - mr$  combination.

## 2.3 Hybrid design approach

The downsides analyzed in the previous section are clearly due to the several approximations of the analytical model and could be easily overcome performing a FEA for each design solution in the  $sr - mr$  plane. However, this becomes unreasonably expensive from a computational point of view and would nullify the advantage of using an analytical formulation in first instance. An interesting solution to this problem has been proposed in [28], where the authors FE-evaluate the design solutions at the corners of the  $sr - mr$  plane. Using the FE-calculated values of the flux linkages, it is possible to adjust the analytical fluxes estimation and so torque and power factor. Although effective, this procedure does not allow to discern the root cause of the discrepancies between the analytical and FE results. In addition, it neglects the effect of the iron losses on the overall performance. In the following, a comprehensive procedure is proposed which is able to adjust the analytical-FE mismatch due to the saturation effects, increased iron losses and iron ribs incurring at high speeds. With the implemented iterative FE-adjustment algorithm, the causes of the discrepancies between analytical and FE results can be separately quantified. The flowchart shown in Fig. 2.13 summarizes the proposed approach which consists of the following steps.

- The analytical design is performed for all  $sr - mr$ .

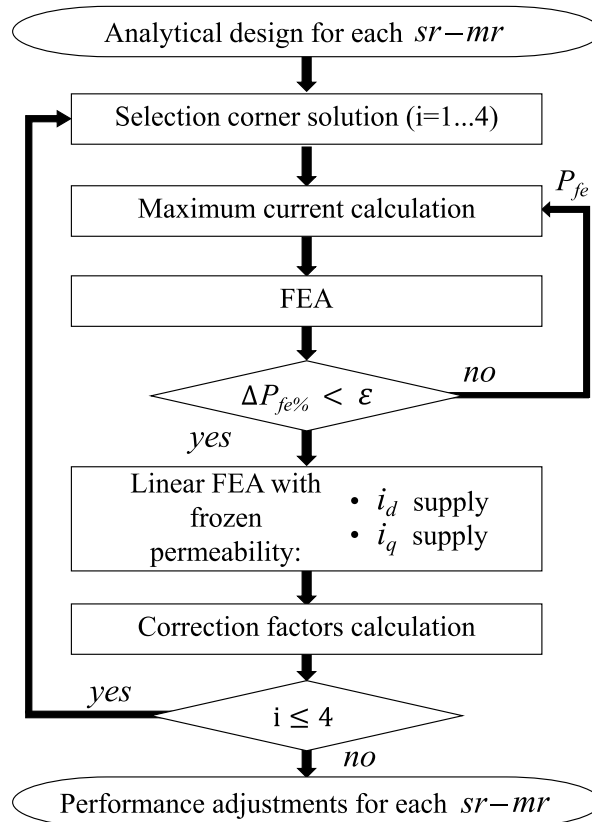


Figure 2.13: Flowchart of the FE-adjustment procedure

- For each corner solution of the  $sr - mr$  plane, the maximum current is calculated and a transient FEA is carried out so to calculate the iron losses. The latter are compared with the previous values used for the maximum current calculation. If the relative error lies within a predefined threshold, the algorithm proceeds to the next step, otherwise a further FEA is performed updating the iron loss value for the maximum current computation.
- Once the correct  $i_d, i_q$  currents are known, two linear FEAs are carried out with the permeability frozen to the values obtained from the previous non-linear FE simulation. By supplying only d- or q-axis current component is then possible to split both d- and q-axis inductances into two components (e.g.  $L_{dd}$  and  $L_{dq}$ ), allowing the full characterization of the cross coupling term and the saturation effect. The slot leakage inductance is also calculated as the difference between the inductance, estimated with the flux linkage, and the integration of the airgap flux density.

- After the two linear FEAs are performed, five corrections factors are evaluated:  $k_{Pfe}$ ,  $k_{Ldm}$ ,  $k_{Lq}$ ,  $k_{Ldq}$  and  $k_{Ls}$  accounting for the modelling error of the iron losses, saturation and cross-saturation, and q-axis inductance of the iron ribs.
- Once this iterative procedure is performed for each corner solutions, then the correction factors are extended to the full  $sr - mr$  plane using a linear interpolation.

Torque and internal power factor values can be then re-calculated according to the following equations:

$$T_{adj} = \frac{3}{2}p[(k_{Ldm}L_{dm}i_d + k_{Ldq}L_{dq}i_q)i_q - (k_{Ldq}L_{dq}i_d + k_{Lq}(L_{qm} + L_{q-rib})i_q)i_d] \quad (2.32)$$

$$ipf_{adj} = \sin \left[ \arctan \left( \frac{i_q}{i_d} \right) - \arctan \left( \frac{(k_{Lq}(L_{qm} + L_{q-rib}) + k_{Ls}L_s)i_q + k_{Ldq}L_{dq}i_d}{(k_{Ldm}L_{dm} + k_{Ls}L_s)i_d + k_{Ldq}L_{dq}i_q} \right) \right] \quad (2.33)$$

The application of this FE-adjustment procedure is shown in Fig. 2.14 in terms of torque and internal power factor contours in the  $sr - mr$  plane for two different speeds (1 and 50 krpm). It is worth underlining the good agreement between the analytical adjusted results and the FEA ones. In terms of torque, the average error is approximately 1.7% over the whole  $sr - mr$  plane. The maximum torque error is about 20% and it is always located away from the maximum torque or power factor designs which is the area of final interest. A lower error is experienced by the  $ipf$  with an average value of 0.7% over the whole  $sr - mr$  plane and a maximum of about 10%. The good agreement at low speed is due to the adjustment of the modeling errors of both magnetizing inductances ( $L_{dm}$ ,  $L_{qm}$ ) and the neglected saturation and cross saturation phenomena (acting on  $L_{dm}$ ,  $L_{dq}$  respectively). These aspects are corrected via the coefficients  $k_{Ldm}$ ,  $k_{Lqm}$  and  $k_{Ldq}$ . Fig. 2.15a and 2.15b underline the good agreement between the adjusted and the FEA magnetizing inductances while Fig. 2.11b reports the cross-coupling effect in the whole  $sr - mr$  plane. When considering high speed designs, the influence of the modelling error of the iron losses and iron ribs inductance becomes more relevant therefore their adjustment is fundamental to improve the performance estimation accuracy. Fig. 2.15c reports an evident improvement of the iron losses estimation compared to the pure analytical approach shown in



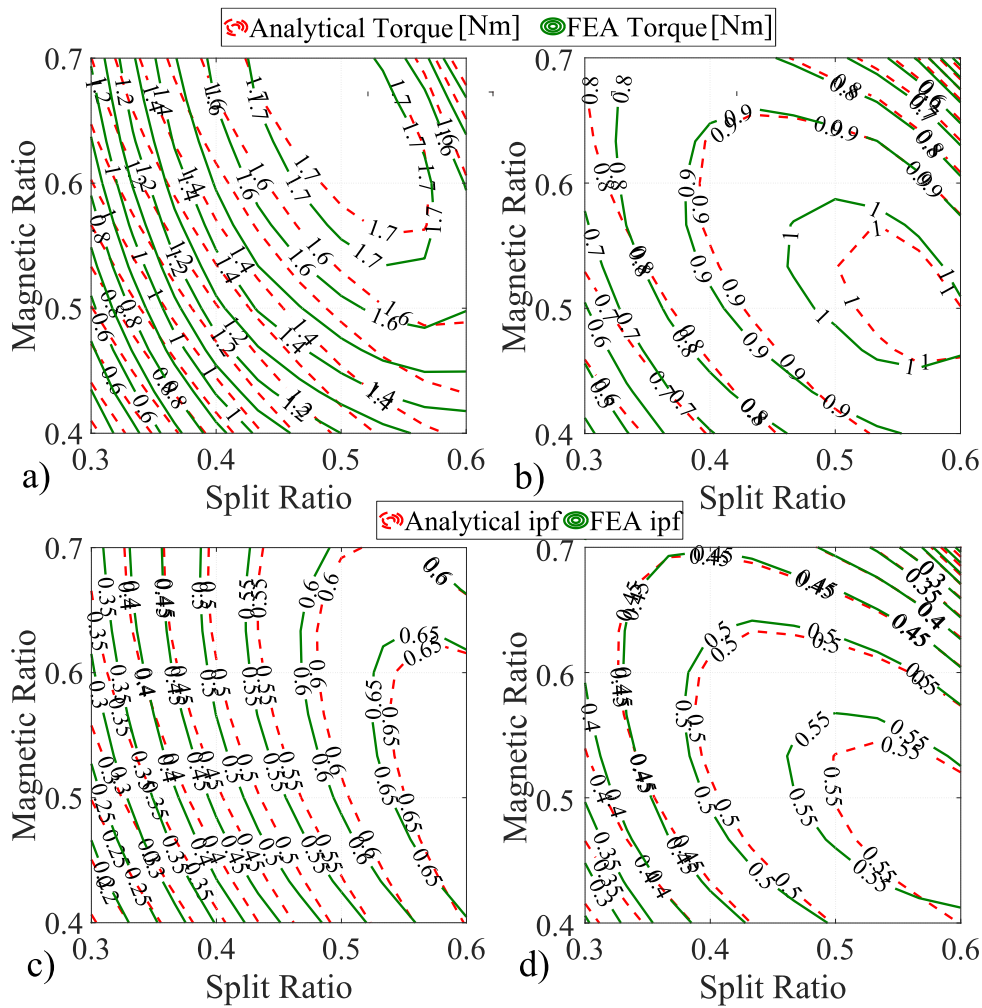


Figure 2.14: Comparison between analytical and FE computation of torque (a, b) and *ipf* (c, d) at 1 krpm (a, c) and 50 krpm (b, d).

Fig. 2.12a,b. Fig. 2.15d confirms that the proposed iterative procedure allows bridging the gap between analytical and FE estimated q-axis inductance increment due to the iron ribs shown in Fig. 2.12f.

The computational time required to perform the above described procedure lies between 10 and 30 minutes according to the number of iron losses iterations and to the specifications of the workstation adopted for the simulations.

It is worth to underline that selecting the corners' machines is just an option. Indeed, 4 different and symmetric machines can be simulated to perform the magnetic model adjustment as well, especially when the design plane present unfeasible corners' machines.

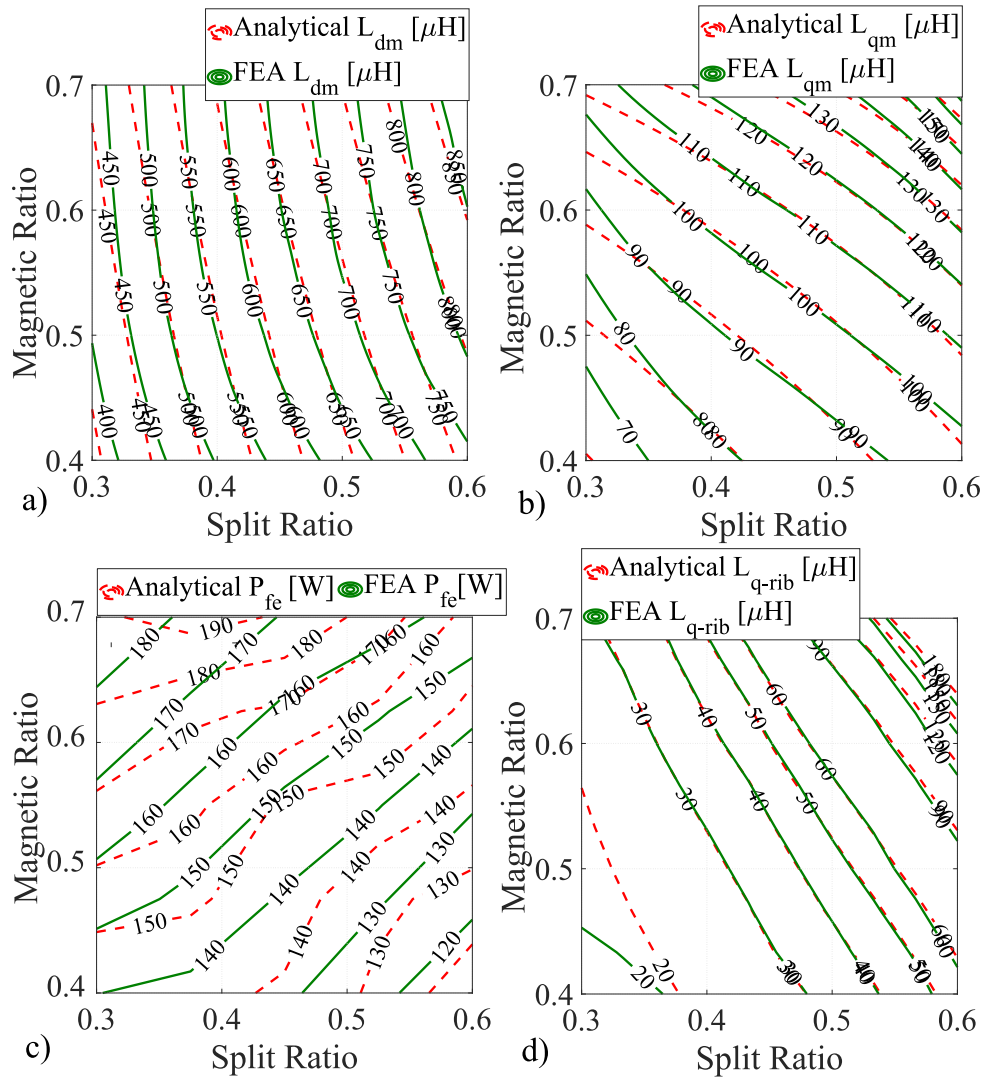


Figure 2.15: Comparison between analytical and FE computation of the d-axis (a) and q-axis (b) magnetizing inductances, iron losses (c) and  $L_{q-rib}$  (d) at 50 krpm

## 2.4 Influence of the high-speed limiting factors

Although the errors between the analytically estimated performance and the FE ones are not null, the good qualitative match of the contour shapes allows using the presented design approach to draw general design guidelines for high speed SyR machines. In this section, the described design procedure is applied to the machine whose main dimensions and design assumptions are reported in Table 2.1 and considering different maximum design speeds. As the speed increases, analyzing torque and power factor contours changes and how the optimal performance decreases, as well as how the optimal geometry evolves is deemed to be very

interesting. In particular, the following workflow is hereafter adopted:

1. for each considered speed, the proposed hybrid design routine is applied and the torque and ipf contours in the plane  $sr - mr$  are evaluated;
2. for each speed, the average torque is chosen as main performance index and the maximum torque solution is selected from the design plane  $sr - mr$ ; this choice is not univocal since machines maximizing other performance indexes (e.g. ipf) or a particular geometrical quantity (e.g. tooth length over tooth width ratio) could be preferred as well;
3. once point 1 and 2 have been performed for each speed, it is possible to assess the performance of the maximum torque designs in terms of power, power factor, optimal design variables and optimal geometries as function of the rotational design speed. It follows that, for each design speed, there will be a unique selected solution featuring a certain geometry and performance.

The outlined design routine also consents to separately analyze the effect on the performance due to the increased iron ribs and iron losses incurring at high speeds. Fig. 2.16 depicts the maximum torque and the power factor in the same operating condition as a function of the speed for three different cases:

1. ignoring the iron losses in the maximum current computation in eq. (2.30) (blue line);
2. ignoring the structural limitation, i.e. neglecting the iron rib thickness and the relative q-axis inductance increment (red line);
3. considering both high speed limiting design aspects (green line).

As expected, both optimal torque and power factor decrease as the speed increases when both limiting design factors are considered. The torque reduction from the lowest to the highest speed is about 66% while the power factor reduction is much lower, i.e. circa 33% (almost halved). As the speed increases, both iron losses and structural ribs negatively affect the torque, with the first one having a bigger impact. Conversely, the  $ipf$  is improved by the effect of

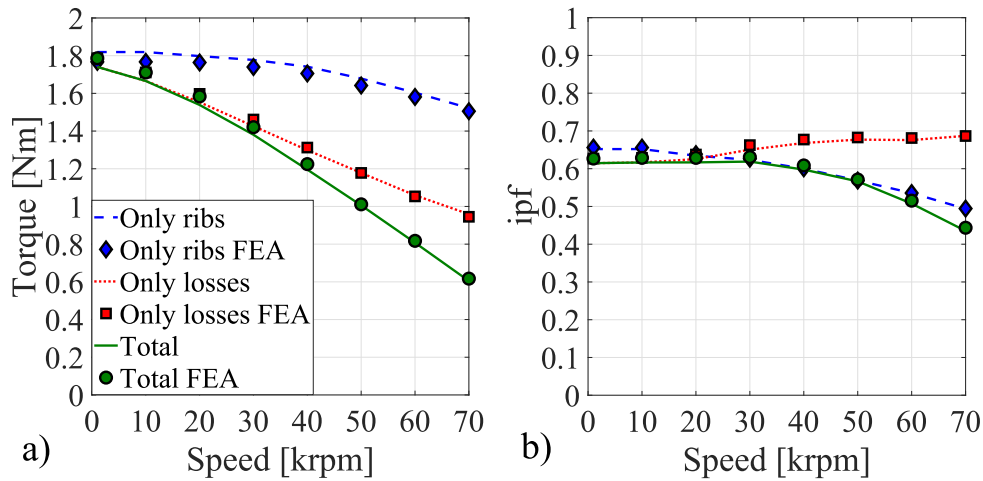


Figure 2.16: Maximum torque (a) and internal power factor at the maximum torque (b) as a function of the speed

iron losses whereas it is reduced by the presence of iron ribs. The latter effect prevails on the first one and so the *ipf* globally decreases. If the (total) torque reduction is less than the speed increment, then the mechanical output power obviously increases, as shown in Fig. 2.17, otherwise above a certain speed, the output power decreases. Above this threshold speed, it is not convenient to further increase the operating speed, so the maximum power capability of the SyR machine is reached. Fig. 2.17 also reports the maximum mechanical power achievable

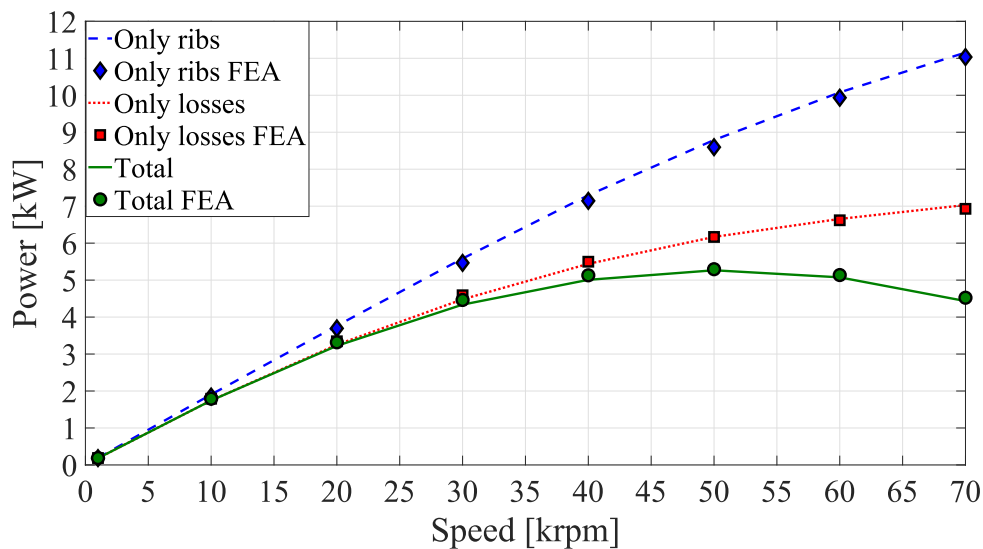


Figure 2.17: Power as a function of the speed

considering the iron ribs and iron losses effects separately. It is worth to underline that the

maximum power point when considering only the structural limitation is higher with respect to the case where both structural and total loss constraints are considered. Fig. 2.16 and 2.17 also report the performance of the optimal machines evaluated via FEAs (shown with the markers). An excellent agreement is evident and this indirectly validates the proposed design approach.

Fig. 2.18 reports the optimal design variables (i.e  $sr$  and  $mr$ ) as a function of the speed. The split ratio slightly increases with the speed while the magnetic ratio monotonically decreases when both limiting design factors are taken into account. When the latter are considered sepa-

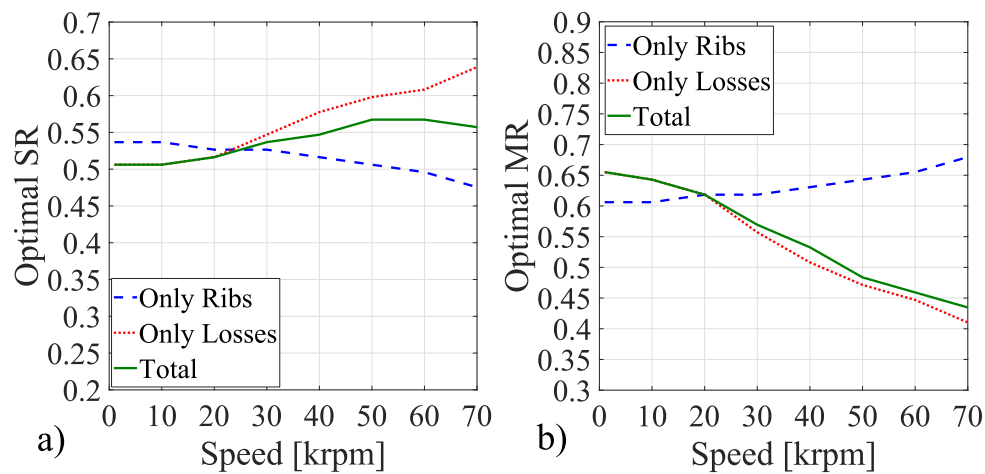


Figure 2.18: Optimal  $sr$  (a) and  $mr$  (b) as a function of the speed

rately, the rise of the iron losses causes an increment of the optimum split ratio and a decrement of the optimal magnetic ratio. Conversely, the same design variables show the opposite behaviour if only the ribs effect is considered. Therefore, as the speed increases, the combination of these two effects slightly increases the split ratio, whereas reduces the magnetic ratio.

## 2.5 Results discussion

In order to investigate in detail the trends shown in Fig. 2.16 and 2.18, in the following torque and power factor loci in the design plane for three different speeds are analyzed. Such results are obtained considering the influence of iron losses and iron ribs separately.

### 2.5.1 Iron Losses influence

Fig. 2.19 shows three constant torque loci calculated considering only the effect of the stator iron losses. It is clear that the maximum torque designs (■ @ 1krpm, ● @ 40krpm, ◆ @

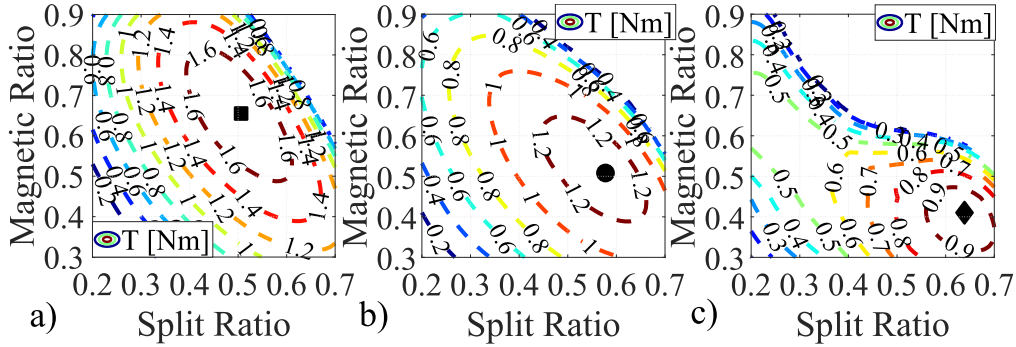


Figure 2.19: Constant torque loci in the plane  $sr - mr$  obtained considering only the iron losses effect at: a) 1 krpm, b) 40 krpm, c) 70 krpm.

70krpm) move towards the bottom-right side of the design plane and so the optimum (torque wise) split ratio increases whereas the optimum magnetic ratio decreases. This trend is caused by the reduction of the q-axis current. In fact, the maximum torque location is the compromise among the competitive needs of maximizing the magnetic anisotropy ( $L_d - L_q$ ), the magnetizing current  $i_d$  and the q-axis current  $i_q$ . The first two ( $L_d - L_q$  and  $i_d$ ) do not depend on the speed if the iron ribs effect is neglected, whereas the third one ( $i_q$ ) depends on the slot areas (unaffected by the speed) and the iron losses. As the speed increases, the iron losses rise reduces the q-axis current component, as shown in Fig. 2.20a, 2.20b and 2.20c. Consequently, the influence in the torque generation ( $(L_d - L_q)i_d i_q$ ) of the q-axis current weakens and the maximum torque design moves towards the maximum magnetic anisotropy, i.e. higher split ratio and low magnetic ratio, as also shown in Fig. 2.20d, 2.20e and 2.20f. The iron losses contours for 40 and 70 krpm along with the stator iron mass contour are reported in Fig. 2.20g, 2.20h and 2.20i. Since the iron stator surface does not change with the speed, Fig. 2.20g also reports the maximum torque design for each considered speed. The maximum torque design moves towards the zone of the design plane with lower stator iron surface and so lower iron losses which in turn means higher q-axis current and bigger slots area. The increment of the  $ipf$  corresponding to the maximum

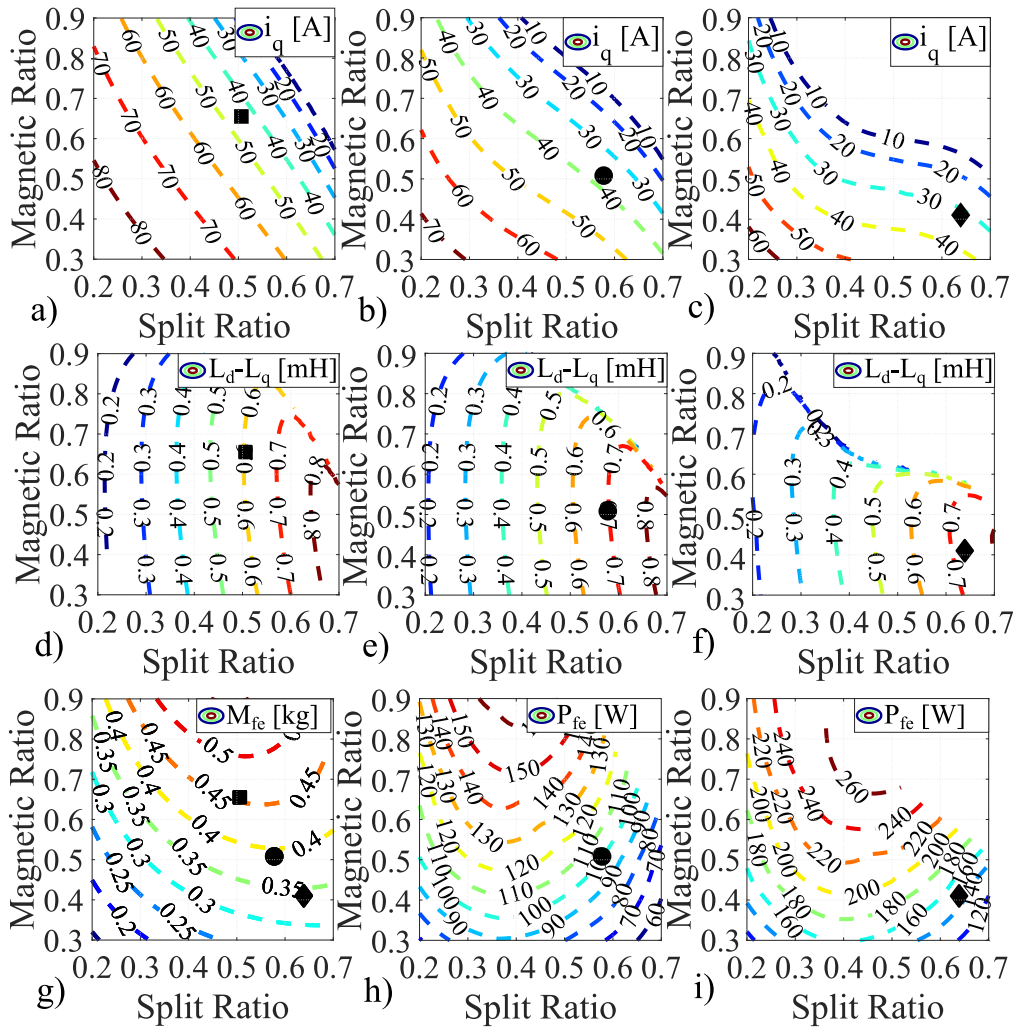


Figure 2.20: Constant  $i_q$  (a,b,c) and  $L_d - L_q$  (d,e,f) loci considering only the iron losses effect at: 1 krpm (a,d), 40 krpm (b,e), 70 krpm (c,f); constant stator core mass loci (g) and iron losses at 40 krpm (h) and 70 krpm (i).

torque design can be easily explained considering Fig. 2.21. The constant  $ipf$  loci are slightly

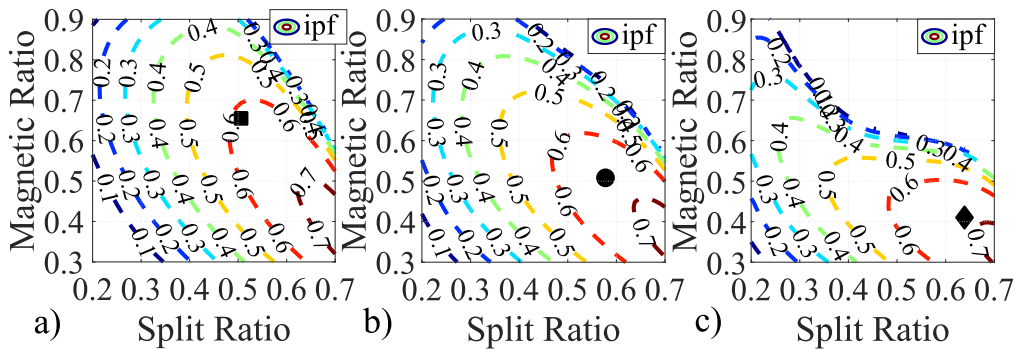


Figure 2.21: Constant  $ipf$  loci in the plane  $sr - mr$  obtained considering only the iron losses effect at: a) 1 krpm, b) 40 krpm, c) 70 krpm.



affected by iron losses and, since the direction of the maximum torque designs corresponds to the direction towards higher magnetic anisotropy, also the  $ipf$  increases.

## 2.5.2 Structural ribs influence

Fig. 2.22 reports the constant torque loci obtained considering only the iron ribs effect for three different speeds (1, 40 and 70 krpm). The maximum torque designs (■ @ 1krpm, ● @ 40krpm,

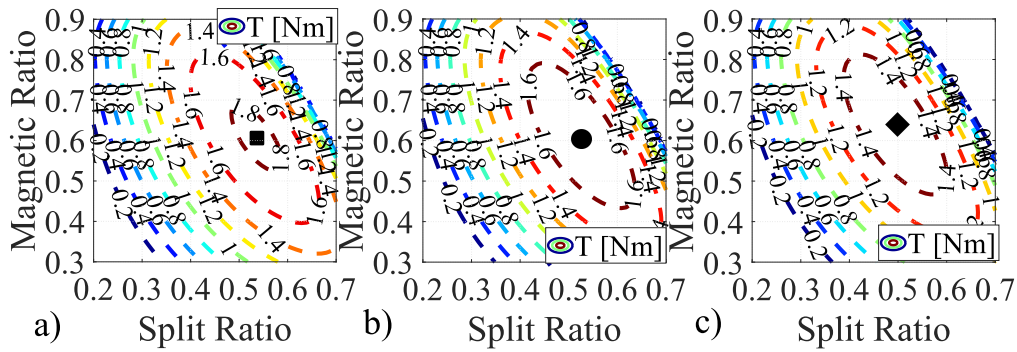


Figure 2.22: Constant torque loci in the plane  $sr - mr$  obtained considering only ribs effect at: a) 1 krpm, b) 40 krpm, c) 70 krpm.

◆ @ 70krpm) slightly move towards the top-left corner of the design plane because in the same direction the average total bridge  $w_{avg}$  decreases (as also shown in Fig. 2.18). In fact, lower split ratio  $sr$  implies lower rotor radius and so lower centrifugal forces which reduce the required rib  $w_{avg}$ , as reported in Fig. 2.23a.

Fig. 2.23b and 2.23c report the percentage variations of torque (decrements) and q-axis inductance (increment) with respect to the design with no ribs. It is worth noticing that the influence of the iron ribs is heavier on the q-axis inductance than on the torque; in fact, for a given couple of design variables  $sr$  and  $mr$ ,  $\Delta L_{q-rib}\%$  is higher than  $\Delta T_{rib}\%$ . This behaviour can be justified analyzing eq. (2.21), which highlights that  $L_{q-rib}$  is proportional to  $w_{avg}$  and inversely proportional to  $i_q$ ; while  $w_{avg}$  increases going from the bottom-left to the upper-right corner of the design plane (Fig. 2.23a), the q-axis current increases in the opposite direction (as shown in Fig. 2.20b), therefore  $i_q$  intensifies the effect of  $w_{avg}$  in the  $L_{q-rib}$  increment. The high increase of the q-axis inductance causes a significant power factor drop as reported in Fig.



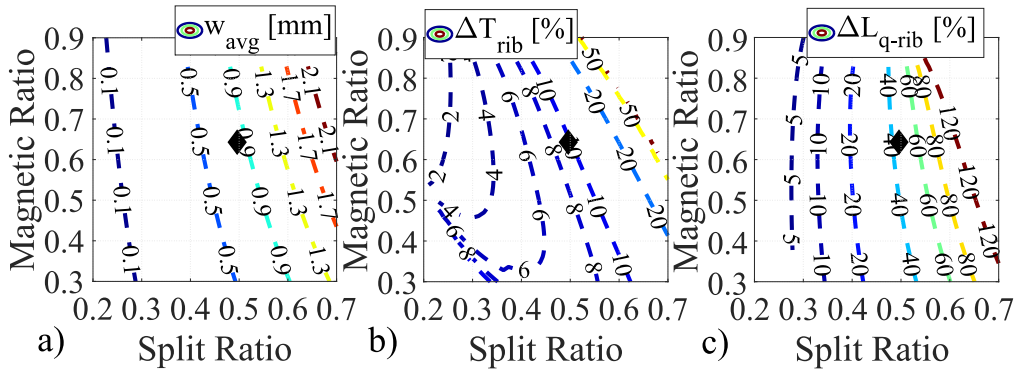


Figure 2.23: Constant locus in the design plane  $sr - mr$  obtained considering only the ribs influence at 70 krpm on a) average total ribs, b) torque decrement, c) q-axis inductance increment.

2.16b.

Although the shape of the constant  $ipf$  loci does not change significantly with the speed (as shown in Fig. 2.24), its value is greatly reduced. It can be stated that the ribs presence affects the power factor more than the torque.

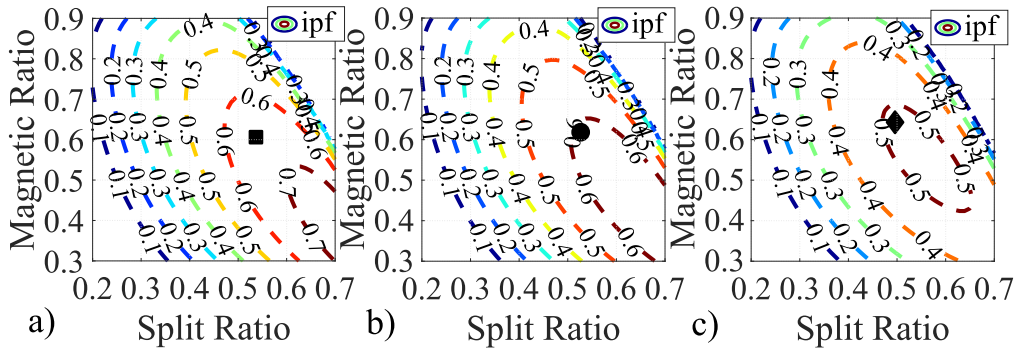


Figure 2.24: Constant  $ipf$  loci in the plane  $sr - mr$  obtained considering only iron ribs effect at: a) 1 krpm, b) 40 krpm, c) 70 krpm.

### 2.5.3 Optimal machines

Fig. 2.25a, 2.25b and 2.25c report the rated flux density distribution of the optimal machines obtained considering separately the influence of iron ribs (a), the iron losses (b) and both limiting phenomena (c) for 4 different speeds (1, 20, 50 and 70 krpm).

The considerations described in the previous two sections are visually confirmed especially regarding the split ratio. Regarding the magnetic ratio, this affects the dimensions of stator

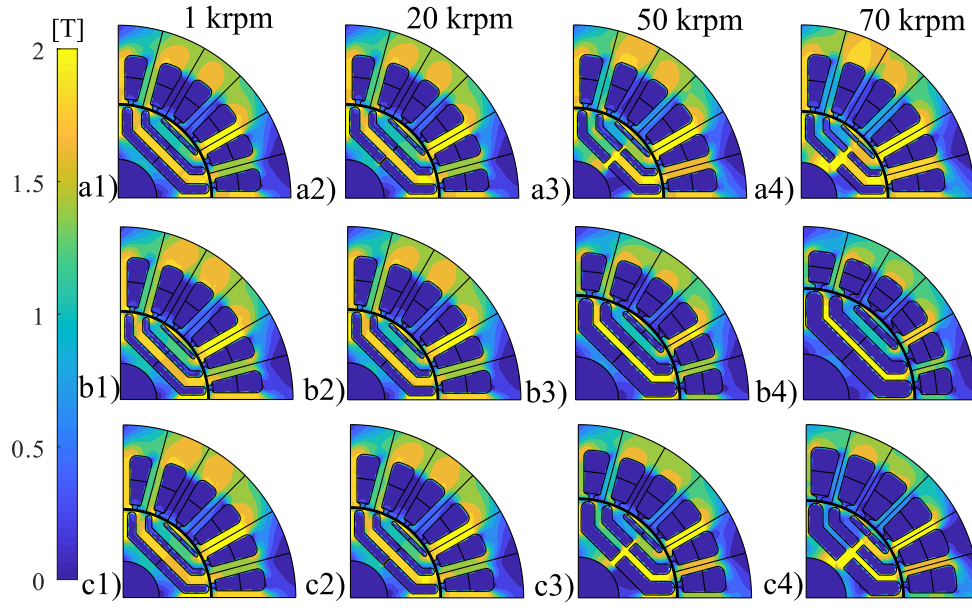


Figure 2.25: Optimal machines obtained considering: (a) only iron ribs, (b) only iron losses and (c) both aspects at different speeds.

teeth and yoke and rotor flux guides (and so flux barrier thicknesses). Table 2.2 reports the main geometrical parameters of the optimal machines. Analysing both Fig. 2.25 and Table 2.2, the following considerations can be done.

Table 2.2: Optimal machine geometrical parameters (in mm)

Design	Variable	1 krpm	20 krpm	50 krpm	70krpm
<b>Only ribs</b>	$w_t$	2.01	2.00	1.97	1.96
	$l_y$	4.45	4.44	4.37	4.36
	$h_{air-3}$	1.53	1.53	1.43	1.30
	$h_{air-2}$	1.11	1.11	1.04	0.94
	$h_{air-1}$	0.64	0.64	0.59	0.54
<b>Only loss</b>	$w_t$	2.05	1.97	1.74	1.61
	$l_y$	4.54	4.37	3.86	3.58
	$h_{air-3}$	1.28	1.43	2.22	2.62
	$h_{air-2}$	0.93	1.04	1.61	1.90
	$h_{air-1}$	0.53	0.59	0.92	1.09
<b>Total</b>	$w_t$	2.04	1.97	1.69	1.49
	$l_y$	4.54	4.37	3.75	3.31
	$h_{air-3}$	1.28	1.43	2.06	2.20
	$h_{air-2}$	0.93	1.04	1.49	1.59
	$h_{air-1}$	0.53	0.59	0.86	0.91

1. The width of the flux barriers increases with the speed if only the iron losses are taken into account, whereas a quasi-constant trend can be inferred when only the effect of iron ribs is considered.
2. Similar considerations can be drawn for the tooth width. The reduction of the optimal magnetic ratio depicted in Fig. 2.18b (for the total and only losses cases) reduces the airgap flux density, i.e. the flux per pole and so the required tooth width for a fixed flux density  $B_{fe}$ . Conversely, being the magnetic ratio almost constant, if only the iron ribs effect is considered, also the tooth width of the optimal machine does not change significantly. Similar trends are experienced by the stator yoke thickness.

These considerations are clearly dependent on the selected lamination material which influences the balance between structural and iron losses effects.

It is important to underline that machines obtained considering only the losses influence do not represent a real case, since the structural iron ribs are necessary to guarantee the rotor integrity under high-speed operations. Conversely, the results obtained neglecting the effects of iron losses can be considered feasible high-speed machine designs. In fact, the higher iron losses can be effectively managed (within reasonable limit) improving the cooling system capability as the speed increases.

In any case, the optimal geometry identified with the proposed design approach needs a structural FE refinement stage. The location and distribution of the iron ribs along the barriers need to be optimized keeping the total iron bridge thickness per barrier as close as possible to the analytical estimated values. By doing so, the average torque would not change being not affected by the ribs position along the barrier but mainly by their thickness [93].

#### **2.5.4 Thermal assessment**

The proposed design procedure imposes the total stator losses to be constant, therefore the Joule losses (always calculated at 130°C) are reduced as the iron losses increase with the design speed. This assumption allows to use the same cooling system for the whole set of designed machines

therefore leading to a comparison on a fair basis. Although the optimal machines have the same total stator losses, they feature different loss distributions, therefore the machine thermal behaviour is envisaged to change as the design speed increases. In fact, machines with higher Joule losses experience higher winding temperatures as these are more difficult to be extracted with respect to the stator iron losses. These considerations are confirmed by the green lines in Fig. 2.26a reporting the hot-spot winding and average stator iron temperatures calculated with the commercial suite [94] for the optimal machines. Fig. 2.26b shows the trends of the Joule and stator iron losses.

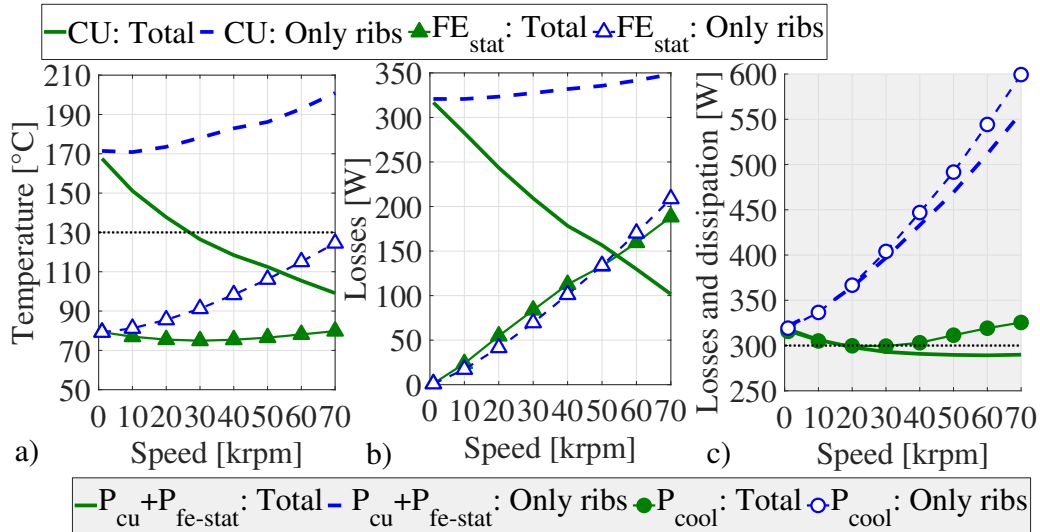


Figure 2.26: a) Hot-spot winding and average stator iron temperatures, b) copper and stator iron losses, c) total stator losses and coolant absorbed power, as function of the speed for machines designed at constant total stator losses (Total) and constant Joule losses (Only ribs).

On the contrary, if only the Joule losses are considered constant during the design procedure (dotted blue lines in Fig. 2.26b), the overall stator losses increase with the design speed as a consequence of the increased iron losses, leading to a rise of the winding temperature as depicted by the blue dotted lines in Fig. 2.26a. The rise of the winding temperature when constraining only the Joule losses is not massive due to the important increment of the power absorbed by the coolant as shown in Fig. 2.26c. Adopting a constant stator losses scenario guarantees obtaining more conservative designs being the winding temperature always within reasonable margin and the coolant absorbed power invariant as the design speed increases (green

marked line in Fig. 2.26c).

## 2.6 Materials selection

In the last section a CoFe alloy has been adopted for both the stator and rotor laminations, with both good mechanical and magnetic properties; however, the performance and optimal geometry of a high speed SyR machine heavily depends on the selected soft magnetic material. In fact, specific iron losses  $p_{fe}$  and yield strength  $\sigma_s$  are intrinsic characteristics of the material affecting the decrement of the performance as the speed increases: the former reduces the maximum current, whereas the latter increases the q-axis inductance. Obviously, it is possible to achieve the best performance adopting a material with low specific iron losses and high yield strength. Unfortunately, materials with high  $\sigma_s$  generally present high specific iron losses and viceversa. Indeed, high mechanical strength is achieved by reducing the grain size of the material which in turn increases the iron losses [95]. Therefore, the choice of the lamination material is the result of a comparative study in which materials with different magnetic and mechanical properties are analyzed. The best solution, i.e. the one which guarantees the maximization of the output power for a defined rotor speed, will depend on the material characteristics.

Fig. 2.27 reports a comparison in terms of yield strength, saturation flux density and iron losses of some commercially available grades of SiFe (●, ★, ▼, ■) and CoFe (▲ and ◆) under their respective trade names. The iron losses have been calculated with a modified Steinmetz model (eq. (2.31)) with the coefficients fitted with the data provided by the manufacturers [96–99]. The saturation flux density is considered as the point where a 5% flux density improvement corresponds to a 50% increment of the magnetic field.

Common SiFe steels (● in Fig. 2.27), such as M250 and M330 with 0.35/0.5mm lamination thickness are usually used in medium-high performance volume-manufactured machines [100] thanks to their medium electromagnetic and mechanical characteristics. Reducing the lamination thickness (from the more common range 0.35-1mm to 0.1-0.2mm) of standard SiFe alloys (with Si content around 3%) is a commonly adopted approach to lower the eddy current losses

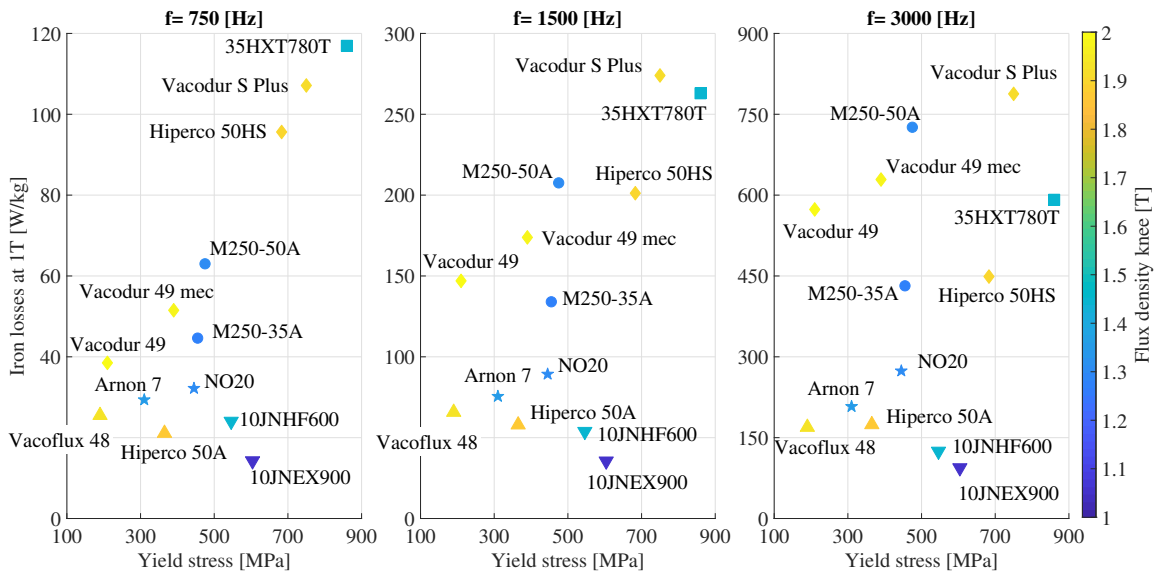


Figure 2.27: Soft magnetic materials comparison: iron losses at 1 T at different frequencies (750, 1500, 3000 Hz) as function of the yield strength; the colored scale shows the knee flux density.

(e.g. NO10, NO20, Arnon 7, ★ in Fig. 2.27). Reducing the lamination thickness is a less expensive way leading to higher flux densities with respect to the option of increasing the Si content even though it slightly complicates the assembly process [39]. It is well known that the silicon (Si) addition to the carbon steel increases the electric resistivity and the mechanical hardness at the cost of a lower saturation flux density and permeability [101]. The maximum Si content has been historically limited to 3.5% by manufacturing considerations since higher percentages make the alloy more brittle and hard and so difficult and expensive to produce. In the last decade, this challenge has been overcome thanks to the adoption of tailored manufacturing processes such as chemical vapor deposition [102] and diffusion annealing [103] (e.g. 10JNEX900 and 10JNHF600, ▼ in Fig. 2.27) pushing the maximum Si content up to 6.5% [104]. Extremely high yield strength (above 800 MPa) has been achieved with special production techniques (e.g. dislocation strengthening [105]), at the cost of increased iron losses (e.g. 35HXT780T, ■ in Fig. 2.27).

The cobalt content makes the CoFe alloys more expensive than the SiFe contender but allows higher saturation flux densities. In general, CoFe alloys have lower yield strength with respect to SiFe (i.e. Vacoflux 48, Vacoflux 50 and Hiperco 50A, ▲ in Fig. 2.27). This metric can be

improved by lowering the Co content (e.g. Vacoflux 17, Hiperco 27) or by adding small percentage of vanadium and/or by additional alloying the material with niobium (Hiperco 50HS, Vacodur 49 and Vacodur S Plus, ♦ in Fig. 2.27), all at the cost of higher iron losses and lower saturation levels [100]. However, the most important leverage to control the trade-off between mechanical and electromagnetic performance of CoFe alloys is the annealing process. Lower annealing temperatures decrease the grain sizes leading to higher yield strength and lower electromagnetic properties (e.g. Hiperco 50HS, Vacodur 49 mec, Vacodur S Plus in Fig. 2.27). By doing so, stators and rotors can be manufactured from the same material and then be subject to different heat treatments in order to achieve a magnetically optimized stator and a rotor with a higher yield strength. It is worth to underline that the cutting process of laminated materials worsens the electromagnetic performance [106]. However, SiFe alloys could and are usually used without expensive post manufacturing thermal treatments, which would restore part of this magnetic property deterioration [107]. On the contrary, for CoFe alloys, the annealing process is indispensable to obtain the desired magnetic and mechanical characteristics [39].

The above considerations reveal the rationale behind the manufacturers' common choices of adopting SiFe alloys, with standard Si content, in low-medium power density applications and/or high volume electrical machines production. On the contrary, CoFe alloys are relegated to niche applications (e.g. aerospace and motor sport) where the higher power density benefit, allowed by the higher saturation levels, outweighs the higher cost [37].

Analysing Fig. 2.27, it is already possible to envisage the lack of an absolute winner, i.e. a soft magnetic material outperforming the others for every design speed. In fact, the relative vertical positions of the considered materials change as the frequency increases.

With the aim of analysing a wide range of materials, five different steel grades have been investigated for the comparative study shown in the next sections: a common SiFe grade (M250-35A), a high performance SiFe having low iron losses and good mechanical performance (10JNHF600), a SiFe alloys with outstanding yield strength (35HXT780T) and two CoFe alloys (Hiperco 50A, Hiperco 50HS). Table 2.3 summarizes the stator-rotor sets of materials considered: three combinations feature the same materials for both stator and rotor, while

the other two have materials optimized magnetically for the stator and mechanically for the rotor.

With the aim of performing a fair comparison, the analysis will be carried out considering also the rotor iron losses in the  $I_{max}$  calculation.

Table 2.3: Selected lamination materials

<b>Name</b>	<b>Stator (S)</b>	<b>Rotor (R)</b>	<b>Thickness (S/R)</b>
M1	M250-35A	M250-35A	0.35 / 0.35 mm
M2	10JNHF600	10JNHF600	0.1 / 0.1 mm
M3	10JNHF600	35HXT780T	0.1 / 0.35 mm
M4	Hiperco 50A	Hiperco 50A	0.15 / 0.15 mm
M5	Hiperco 50A	Hiperco 50HS	0.15 / 0.15 mm

### 2.6.1 Influence of the speed on the materials choice

The design procedure described in section 2.3 is applied in the following for the machine parameters reported in Table 2.4. Several maximum speed requirements (from 0 to 120 krpm) and

Table 2.4: Initial geometrical constraints and preliminary design assumptions

<b>Parameter</b>	<b>Value</b>	<b>Units</b>
Outer stator radius	30	mm
Stack length	30	mm
Pole pair	2	/
Barrier angle at the airgap	16.87, 28.12, 39.38	deg.
Cooling capability	50000	W/m <sup>2</sup>
Airgap thickness	0.25	mm

the material combinations listed in Table 2.3 are explored. In order to maximize the magnetic exploitation of each material, all the machines have been designed considering iron flux densities (stator and rotor yokes and stator teeth) proportional to the flux density at the knee of the



respective BH curve. In particular, the stator and rotor yokes flux densities have been set equal to the knee flux density, whereas the stator tooth one is assumed to be 20% higher.

Fig. 2.28a reports the torque of the optimal designs in the  $sr - mr$  planes for each design speed and for all the considered soft magnetic materials. Fig. 2.28b shows the power factor of the same designs. It is worth to underline that the optimal design for a given speed and combination magnetic materials is hereafter considered as the one providing the maximum torque in the plane  $sr - mr$ . Clearly, another design solution in the plane  $sr - mr$  can be

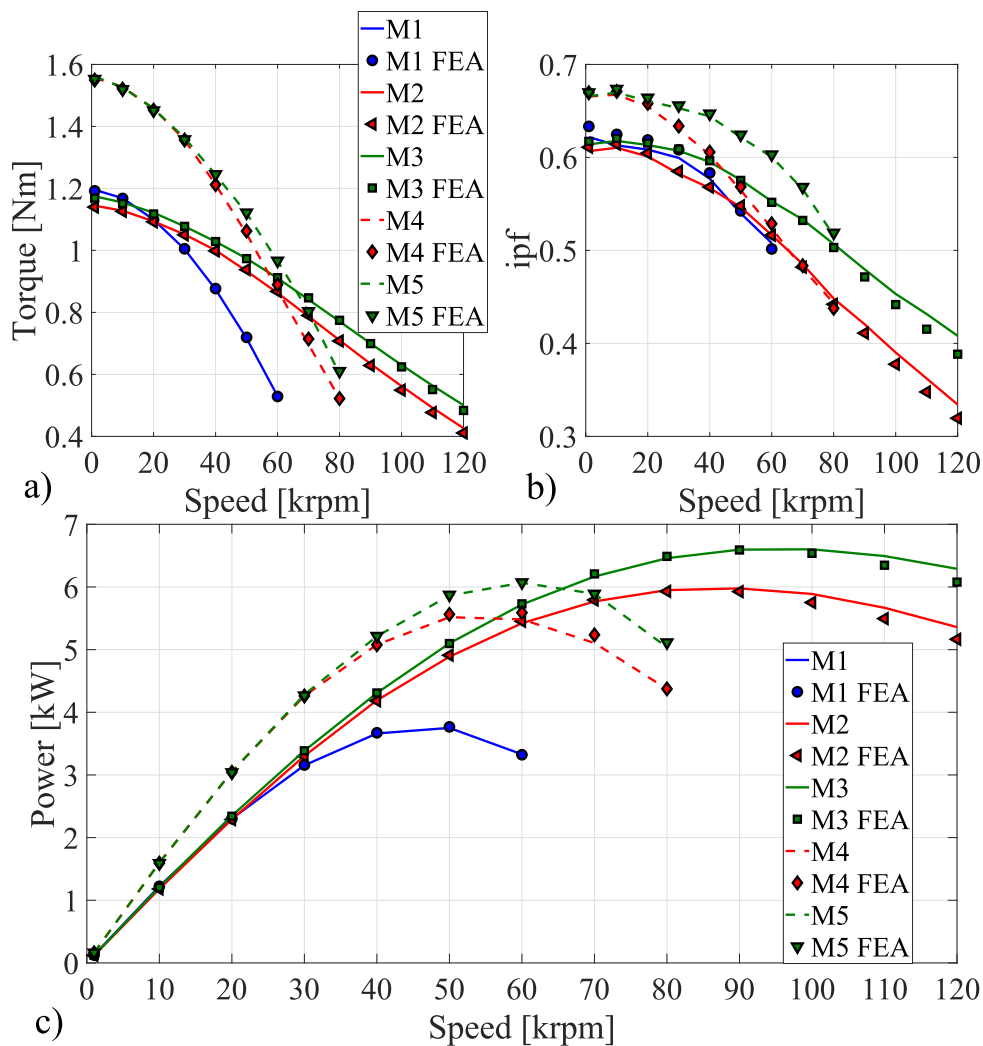


Figure 2.28: Performance boundaries of the SyR machine technology, i.e. maximum achievable torque (a), internal power factor (b), and output power (c) as a function of the design speed for different soft magnetic materials.

chosen (e.g. the one providing the maximum internal power factor). However, the maximum

torque selection criterion has been adopted because the aim of this comparative design exercise is to assess the performance boundaries of SyR machine topology in terms of output power as function of the speed and magnetic materials.

Fig. 2.28a and b show the good match between the performance estimated with the proposed method and the FEA-calculated ones. As expected, torque and power factor decrease with the speed regardless of the alloy type.

All SiFe materials combinations start from the same torque values but, the standard one (M1) deteriorates with a higher rate with respect to the other two (M2, M3). On the contrary, the power factor of the optimal machines featuring the standard SiFe (M1) has a similar trend to the one achieved with the high grade SiFe (M2). Adopting SiFe alloy with optimized mechanical property on the rotor (M3) allows to improve both performance indexes but mostly the power factor. These improvements are even more evident for higher speeds.

CoFe steels outperform the SiFe contenders only up to a certain speed. It is worth to underline that the CoFe machines deteriorates more quickly than the SiFe ones both torque and power factor wise. Indeed, considering machines at 1 and 80 krpm, M2 (M3) torque worsens about 38% (34%) while M4 (M5) 66% (61%). Similarly, the power factor decrements are about 26% and 17% for M2 and M3 and circa 33% and 22% for M4 and M5, respectively. The adoption of alloys with higher saturation levels, e.g. CoFe, leads to a higher q-axis flux leakage due to the structural ribs with respect to the SiFe cases. This is the main cause of the bigger rate of performance decrement of CoFe alloys with respect to the SiFe ones. Fig. 2.28c reports the maximum output power as a function of the speed for all materials. Each considered material combination features a threshold speed above which it is not convenient to further increase the speed as a mean to push the output power and so the volumetric power density for a given cooling system. This threshold speed is clearly higher when adopting high performance SiFe alloys; for M1 this speed limit is 50 krpm, for M2 and M3 is about 90 krpm while M4 and M5 reach 50 and 60 krpm, respectively. The maximum output power is also approximately 10% higher when using high performance SiFe alloys (e.g. M2-6kW, M4-5.5kW) with respect to the CoFe ones. The adoption of standard SiFe allows reaching a maximum power 30% smaller than the more

performing high grade SiFe M2. As previously stated, CoFe alloys outperform the SiFe ones up to a certain speed, circa 55 or 65 krpm (considering M4 and M5 respectively). The power gain is maximum around 40 krpm and it is about 17%. Above this speed, the power improvement decreases until it becomes negative around 55 and 65 krpm after which SiFe alloys are definitely more convenient. Adopting alloys with optimized mechanical performance for the rotor (e.g. M3 and M5) allows to improve the output power of almost 10% for both SiFe and CoFe alloys. This improvement is more evident at high speed levels where the iron ribs dimensions become significant and have a major effect on the overall performance.

### 2.6.2 Analysis of the optimal designs

The comparative design exercise, reported in the previous section, shows that the maximum speed requirement is crucial for the selection of the soft magnetic materials.

The optimal machine geometries change as the speed increases and vary according to the selected soft magnetic materials. In fact the location of the maximum torque design in the plane  $sr - mr$  (highlighted with the marker in Fig. 2.28a2) changes with the speed and consequently also the optimal geometry changes. Fig. 2.29a and 2.29b report the split and the magnetic ratios of the torque-wise optimal machines as function of the speed. Their global trends are not

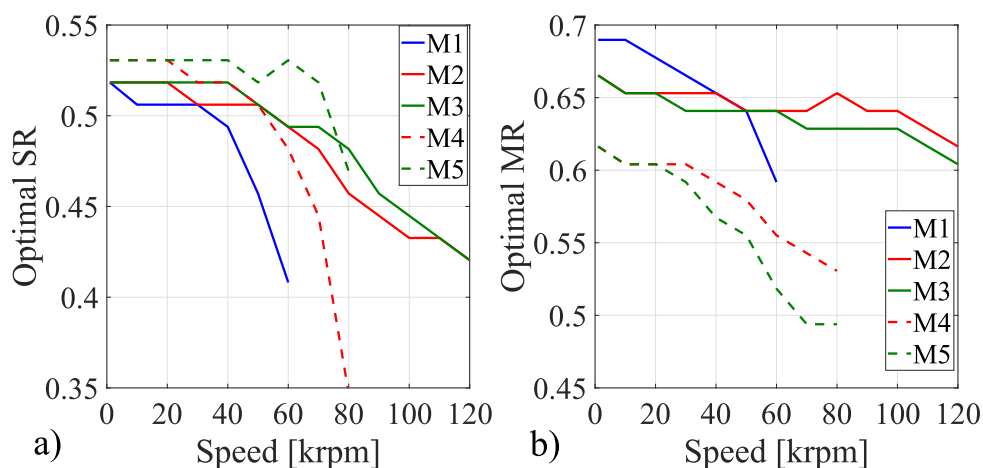


Figure 2.29: Split (a) and magnetic ratios (b) of the optimal torque-wise machines as a function of the design speed.

affected by the chosen lamination material. In fact, both design variables decrease as the speed

increases but the rate of decrement depends on the materials.

In the next sub-section, the optimal geometries are analyzed in details while in the sub-section 2.6.4 the rationale behind these trends is investigated separately evaluating the effects of the iron losses and iron ribs increments. A thermal assessment of the selected machines is finally reported in the sub-section 2.6.5.

### 2.6.3 Optimal geometries

In Fig. 2.30, the cross sections of the optimal machines at four different speeds (20, 40, 80 and 120 krpm) and their flux density distribution at the rated condition are reported. As the speed increases the rotor radius always decreases, but machines featuring rotor materials with low yield strength (e.g. M2 and M4) present smaller rotors with respect to M3 and M5. Similarly, the decrement of the optimal magnetic ratio implies the reduction of the stator tooth ( $w_t$ ) and yoke ( $l_y$ ) as well as the rotor flux guide dimensions as reported in Table 2.5. This decrement is again less pronounced when adopting a rotor lamination material with optimized mechanical performance.

It is worth to underline that the selected optimal solutions for certain speeds and material combinations are definitely unconventional given the low split ratio and the high tooth length. These particular geometries could lead to manufacturing challenge, but from the electromagnetic point of view they provide the maximum torque. Selecting another solution in the  $sr - mr$  plane, e.g. geometries with conventional proportions (and so smaller tooth length), would surely be sub-optimal given their lower torque production capability.

Table 2.5 also reports the average torque, the iron losses including the stator and rotor ones ( $P_{fe-rot}$ ), the torque reduction due to the iron ribs and the maximum current reduction due to the iron losses. For each material combination, both percentage variations ( $\Delta T_{rib}$ ,  $\Delta I_{max}$ ) are calculated in relation to the respective values of the low speed designs (1000 rpm).

The iron losses in CoFe machines are always higher compared to the high performance SiFe ones (e.g. M2 and M3). At high speed, 80 krpm, this aspect heavily affects the average torque,

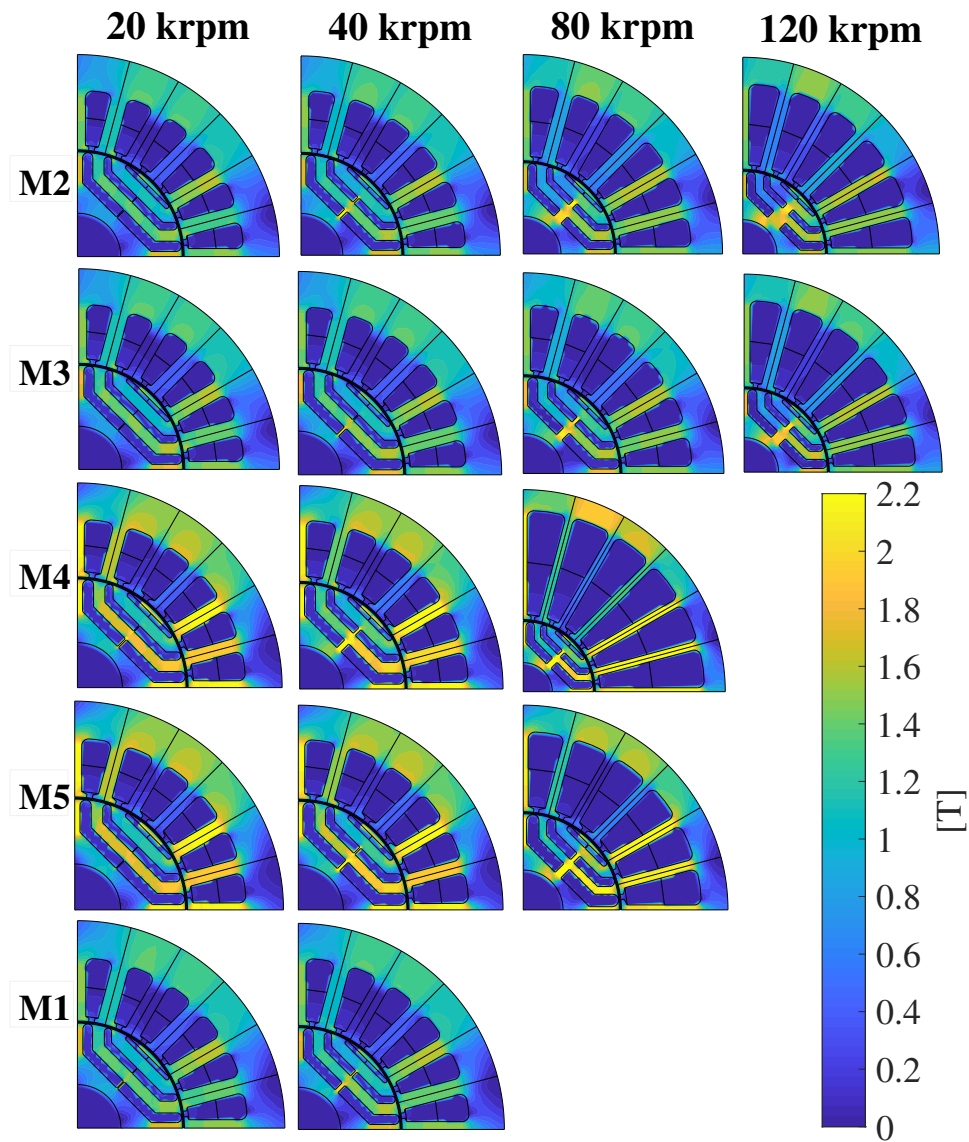


Figure 2.30: Cross section of the optimal machines obtained for different lamination materials.

via the reduction of the maximum current  $\Delta I_{max}$  (see eq.(2.30)). However, at 40 krpm, the higher knee flux density of the CoFe steel compensates the reduction of the stator current due to the iron losses rise and so the torque is higher with respect to the corresponding SiFe machines. It is also worth to notice that although the CoFe alloys have lower yield strengths, the torque reductions due to the iron ribs ( $\Delta T_{rib}$ ) are smaller with respect to the SiFe ones. This is mainly due to the fact that the optimal CoFe machines have a lower rotor radius.

Table 2.5: Comparison between optimal machines

Speed	Variable	M1	M2	M3	M4	M5
40 krpm	$T$ [Nm]	0.87	1.00	1.03	1.21	1.25
	$P_{fe-st}$ [W]	87.7	36.1	36.0	56.7	53.6
	$P_{fe-rot}$ [W]	17.7	2.79	10.1	16.4	26.5
	$\Delta T_{rib}$ [%]	3.1	2.8	2.2	4.3	2.4
	$\Delta I_{max}$ [%]	20.7	7.01	8.40	13.81	15.22
	$w_t$ [mm]	2.28	2.33	2.34	1.93	1.89
	$l_y$ [mm]	5.06	5.18	5.21	5.10	5.00
	$h_{air-3}$ [mm]	1.45	1.48	1.47	1.62	1.76
	$h_{air-2}$ [mm]	1.05	1.08	1.14	1.17	1.28
	$h_{air-1}$ [mm]	0.60	0.62	0.55	0.67	0.73
	80 krpm	$T$ [Nm]	-	0.71	0.77	0.52
$P_{fe-st}$ [W]		-	86.9	84.2	175.5	159.5
$P_{fe-rot}$ [W]		-	6.38	16.8	14.1	35.3
$\Delta T_{rib}$ [%]		-	11.2	8.2	6.2	7.2
$\Delta I_{max}$ [%]		-	18.1	19.7	42.5	44.1
$w_t$ [mm]		-	2.11	2.14	1.16	1.46
$l_y$ [mm]		-	4.68	4.75	3.06	3.85
$h_{air-3}$ [mm]		-	1.34	1.50	1.52	1.82
$h_{air-2}$ [mm]		-	0.97	1.09	0.91	1.32
$h_{air-1}$ [mm]		-	0.56	0.62	0.52	0.76

### 2.6.4 Behind the boundaries

In this sub-section, the trends shown in Fig. 2.29 and so the optimal geometries are justified analysing the constant torque and power factor loci in the design plane  $sr-mr$  for three different rotor speeds separately considering the structural and iron losses limiting factors. For the sake of brevity, only the most performing material combination above 65 krpm (i.e. M3) is shown and discussed as the others behave in a similar manner.

Fig. 2.31a, 2.31b and 2.31c show the constant torque loci calculated considering only the effect of the iron losses for three different speeds (1, 60, 120 krpm). As the speed increases, the maximum torque designs (■ @ 1 krpm, ● @ 60 krpm, ◆ @ 120 krpm) move towards the bottom-right side of the  $sr-mr$  plane, therefore the optimum split ratio increases whereas

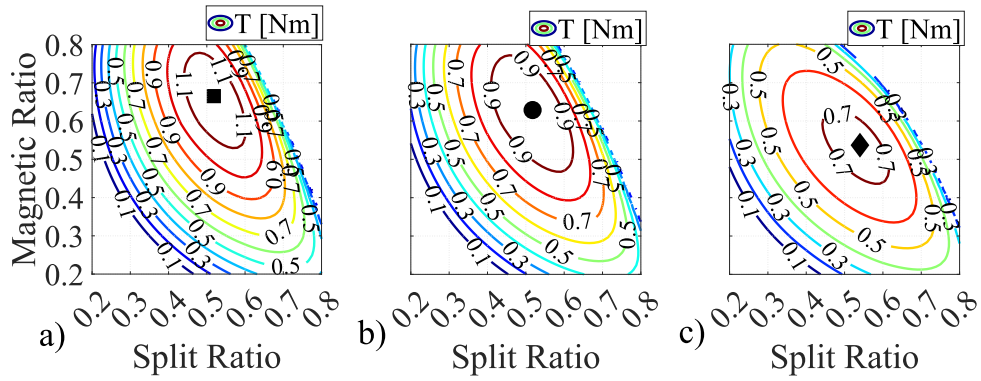


Figure 2.31: Constant loci obtained considering only the losses effect. Torque at: (a) 1 krpm, (b) 60 krpm, (c) 120 krpm.

magnetic ratio decreases. This trend can be explained considering that the maximum torque location is a compromise between the needs of maximizing the machine anisotropy ( $L_d/L_q$ , Fig. 2.32a), the magnetizing current  $i_d$  (Fig. 2.32b) and the q-axis current  $i_q$  (Fig. 2.32c). For

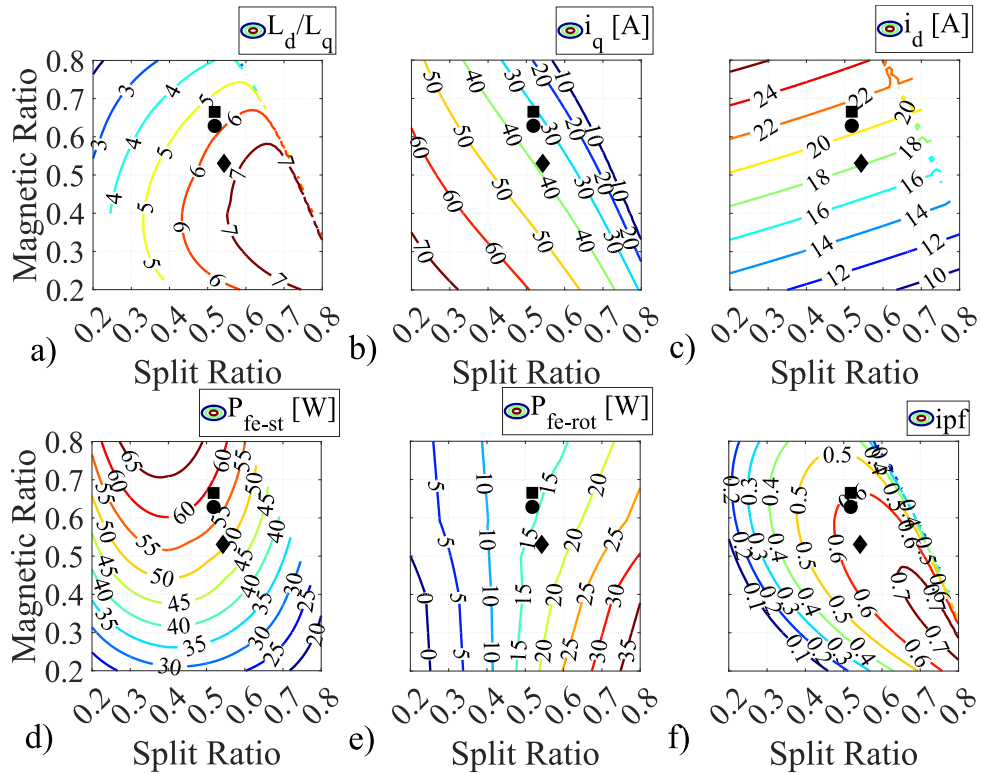


Figure 2.32: Constant loci at 60 krpm obtained considering only the losses effect.  $L_d/L_q$  (a),  $i_q$  (b),  $i_d$  (c),  $P_{fe-st}$  (d),  $P_{fe-rot}$  (e),  $ipf$  (f).

sake of brevity, Fig. 2.32 reports the contours only at 60 krpm together with the maximum torque locations for all the three speeds (1, 60 and 120 krpm). Indeed, the  $L_d/L_q$  and  $i_d$  are

speed independent when the iron ribs are neglected while the q-axis current  $i_q$  is affected by the iron losses and so by the speed. As the speed increases, the higher iron losses lead to a q-axis current reduction (although the contour shape of  $i_q$  is not affected). Therefore, the maximum torque design moves towards the area of the design plane with lower stator and rotor iron losses (reported in Fig. 2.32d, e) and higher magnetic anisotropy (see Fig. 2.31a). Along the same direction, the internal power factor increases as shown in Fig. 2.32f because it follows the saliency ratio improvement.

Fig. 2.33a, and 2.33b report the constant torque loci obtained considering only the iron ribs effect for two different speeds (60 and 120 krpm). As the speed increases, the maximum

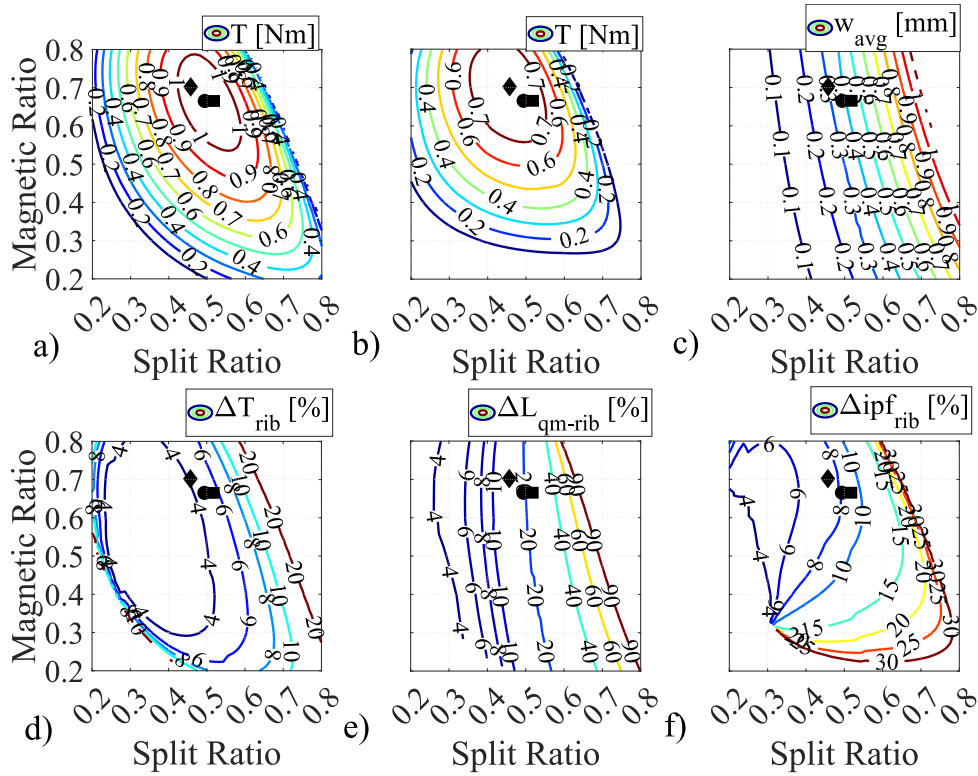


Figure 2.33: Constant loci obtained considering only the ribs effect. Torque at: (a) 60 krpm, (b) 120 krpm;  $w_{avg}$  (c),  $\Delta T_{rib}$  (d),  $\Delta L_{qm-rib}$  (e) and  $\Delta ipf_{rib}$  (f) at 60 krpm.

torque designs move towards the left because the lower the split ratio the lower the average total bridge  $w_{avg}$ , as reported in Figs. 2.33c for the 60 krpm case. In fact, lower rotor radius implies lower centrifugal forces, which reduce the iron rib thicknesses. It is worth to underline that the influence of the iron rib thickness is heavier on the q-axis inductance than on the torque as



shown in Fig. 2.33d and 2.33e. The latter report the percentage variations of torque and q-axis inductance worsening always for the 60 krpm case with respect to the design with no ribs. The high increase of the q-axis inductance causes a significant power factor drop, as reported in Fig. 2.33f.

This analysis allows drawing the following considerations.

- The presence of the structural iron ribs reduces the optimal split ratio and increases the optimal magnetic ratio since this design direction allows to minimize  $\Delta L_{q-rib}[\%]$  and so  $\Delta T_{rib}[\%]$ .
- The effect of the iron losses is that the optimum location moves toward the bottom-right of the design plane (i.e. higher split ratio and lower magnetic ratio) because in the same direction the magnetic anisotropy increases and the stator iron losses decreases.
- When both iron losses and structural ribs are considered in the design exercise, the trends of the optimal split and magnetic ratios are a compromise between their competitive effects and so depend on the considered magnetic materials (as reported in Fig. 2.29).

### 2.6.5 Thermal analysis

The comparative design exercise among different lamination materials has been carried out considering the same total losses equal to the maximum capability of the cooling system. This assumption guarantees that the thermal behaviours of the designed machines are approximately the same avoiding the need of redesigning a new cooling system for each motor. The total loss has been imposed considering the winding Joule loss at a given temperature (i.e. 130°C) throughout the whole design process and independently from the lamination material. Although the total loss is kept constant, machines featuring the same constituent materials but different geometries (i.e. different  $sr, mr$ ) or machines featuring different materials have a diverse loss distribution (copper, stator and rotor iron losses). Consequently, the temperature distribution of the compared optimal machines will not be exactly the same even though the total loss has been

kept unchanged.

Indeed, machines with higher Joule losses experience higher winding temperatures as these are more difficult to be extracted with respect to the stator iron losses. Fig. 2.34a reports the winding temperatures of the optimal machines calculated with the commercial suite [94] considering an external spiral water jacket as cooling system (whose details will be reported in the next section). Fig. 2.34b depicts the ratio between the Joule loss and the total stator losses.

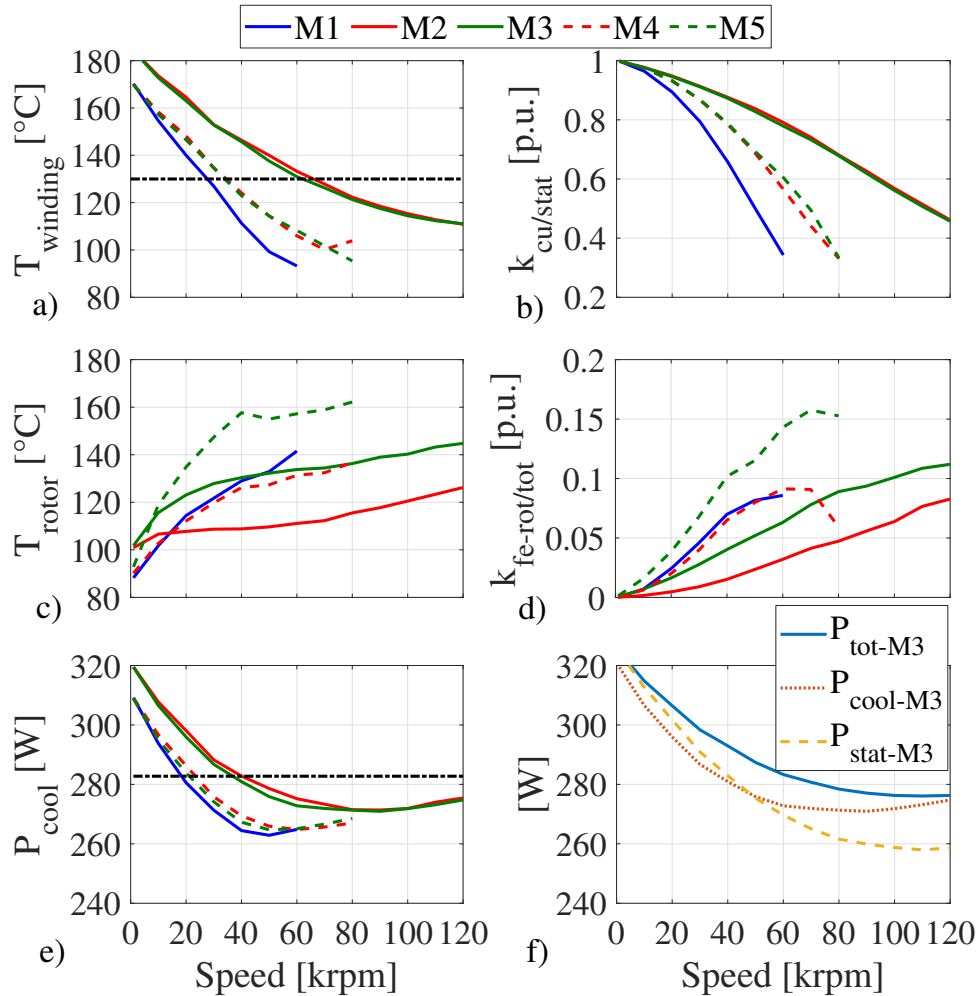


Figure 2.34: a,c) Average winding and rotor temperatures, b,d) loss distribution ratios, e) total power absorbed by the cooling system of the optimal machines and f) total losses, stator total losses and cooling system power absorption for the M3 solutions.

As expected, designs with higher Joule to iron loss ratio exhibit higher winding temperature.

In addition, machines designed with CoFe alloys (M4, M5) have lower copper losses with respect to the SiFe ones (M2, M3) and so they feature a lower winding temperature rise.

Fig. 2.34c and d show the rotor temperature and the ratio between the rotor iron loss and the total losses, respectively. Machines with mechanically optimized rotor material (M3 and M5) pay the price of higher rotor iron losses and therefore worse rotor temperature (compared to M2 and M4). Comparing solutions designed with CoFe and SiFe, the former definitely lead to higher rotor temperatures given their higher rotor iron losses.

Fig. 2.34e outlines the power absorbed by the cooling system for all material combinations along with the one considered during the design process (black dotted line). It can be noticed that the dissipated losses deviate from the initial value due to the different winding temperature rise, leading to different Joule losses at thermal steady state. In any case, this deviation is within 10% confirming that the comparison is performed on a fair basis as the cooling system is suitable to cover all the considered machines.

Last sub-figure (Fig. 2.34f) reports the loss absorbed by the cooling system for the material combination M3 along with its stator and total losses. Up to a certain speed (approximately 50 krpm) the losses absorbed by the coolant almost equal the total stator losses, while above this speed the cooling system dissipates also part of the rotor iron losses. This confirms that the calculation of the maximum current with eq.(2.30), considering also the rotor iron losses, is a conservative approach suitable for designing machines for a wide range of maximum speeds.

## 2.7 Influence of the magnetic load

The latter material comparison analysis has been performed keeping constant the magnetic load (i.e.  $B_{fe}$ ) regardless the design speed: indeed,  $B_{fe}$  has been set to be as close as possible to the knee point of the material B-H characteristic in order to fully exploit the adopted soft magnetic material. However, as the speed increases, designing SyR machines with a lower value of iron flux density could be beneficial given the consequent lower iron losses.

The purpose of this section is to investigate the tradeoffs involved when selecting the iron flux density to be used during the SyR machine design when adopting a Co-Fe alloy.

The initial geometrical constraints and preliminary design assumptions are reported in Table

2.4. The stator and rotor laminations are composed by CoFe alloys namely Hiperco 50A and Hiperco 50HS, respectively. The former presents excellent magnetic performance, whereas the latter features high yield strength due to the different annealing process.

With the aim of maximizing the power capability the procedure is applied for several speeds from 1 krpm to 90 krpm and for four different values of the magnetic load  $B_{fe}$ , which determines the working point of the stator yoke and teeth. The B-H curve of the stator lamination steel is reported in Fig. 2.35, along with four markers highlighting the considered working points of the stator yoke. Torque and power factor contours for each speed are then calculated

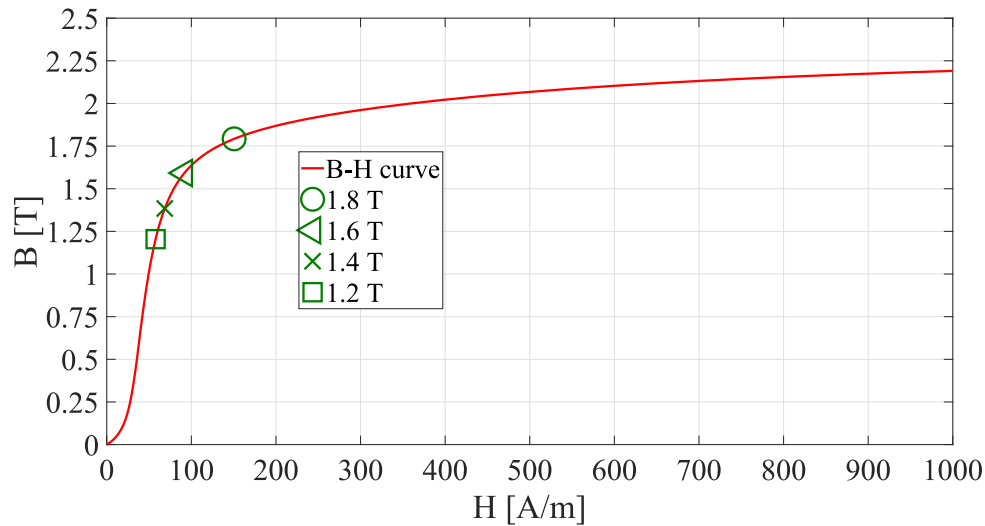


Figure 2.35: BH characteristic of Hiperco 50A.

in their respective  $sr - mr$  plane. From the latter, the maximum torque design is chosen in order to evaluate the maximum power capability as a function of the speed and the selected magnetic load.

Fig. 2.36a and 2.36b reports the maximum torque and the internal power factor of the maximum torque designs as a function of the speed for four different magnetic loads: 1.8 T, 1.6 T, 1.4 T and 1.2 T, whereas the output power is reported in Fig. 2.37.

As expected, the structural and thermal limiting factors negatively affect both torque and internal power factor, whatever magnetic load is chosen. It is worth to underline that the higher value of  $B_{fe}$  provides the best performance (torque wise) up to 60 krpm. Above this speed, reducing the magnetic load to 1.6 T at 70krpm, 1.4 T at 80krpm and 1.2 T at 90krpm clearly

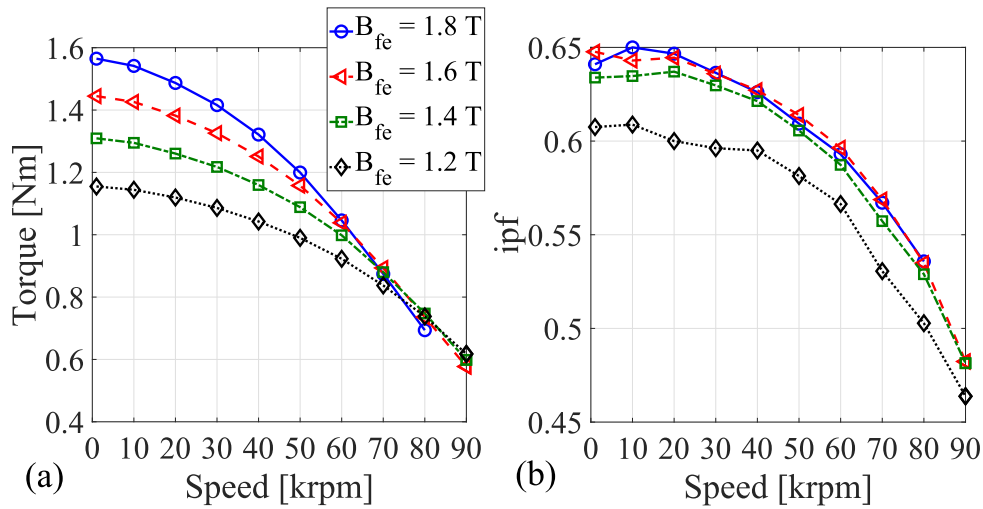


Figure 2.36: Torque (a) and ipf (b) as function of the speed

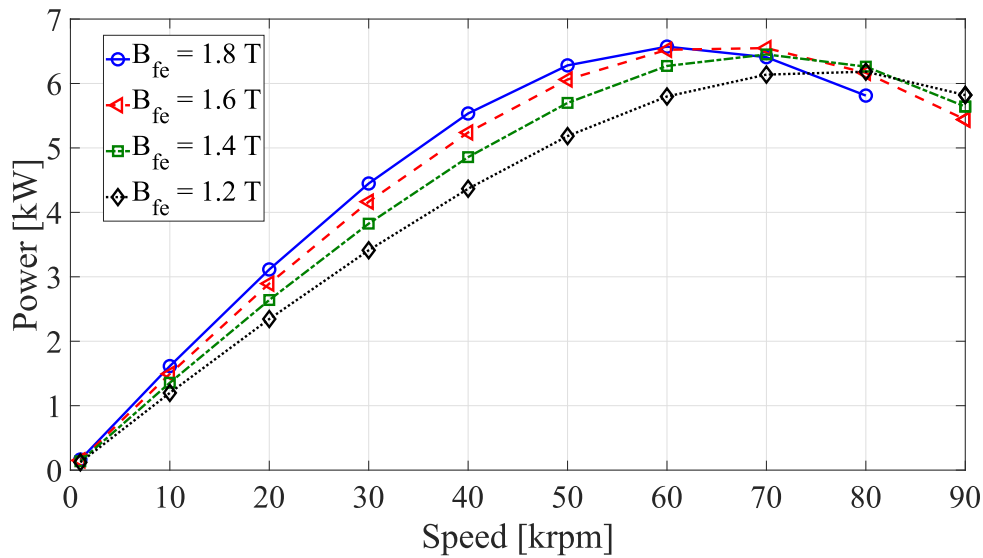


Figure 2.37: Power as function of the speed

leads to a performance improvement. In other words, each case features a threshold speed above which it is not convenient to further increase the speed, since the output power will decrease. This threshold speed can be increased by reducing the magnetic load as shown in Fig. 2.37 although it comes at the cost of a slightly lower maximum power.

The reason of this behavior can be inferred analysing Fig. 2.38 and 2.39. The first one reports the d- and q-axis currents and the iron losses of the optimal designs as function of both speed and magnetic load while the second shows the d- and q-axis inductances and their difference.

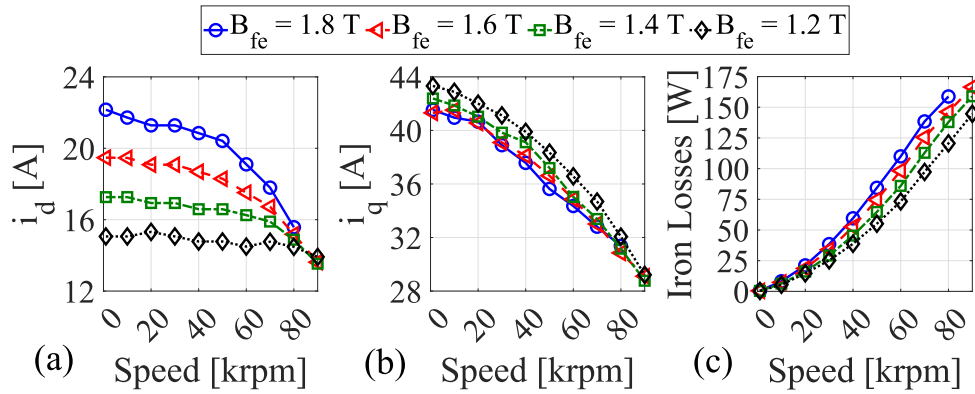


Figure 2.38: d-axis current  $i_d$  (a), q-axis current  $i_q$  (b) stator iron losses (c) at the maximum torque as function of the speed

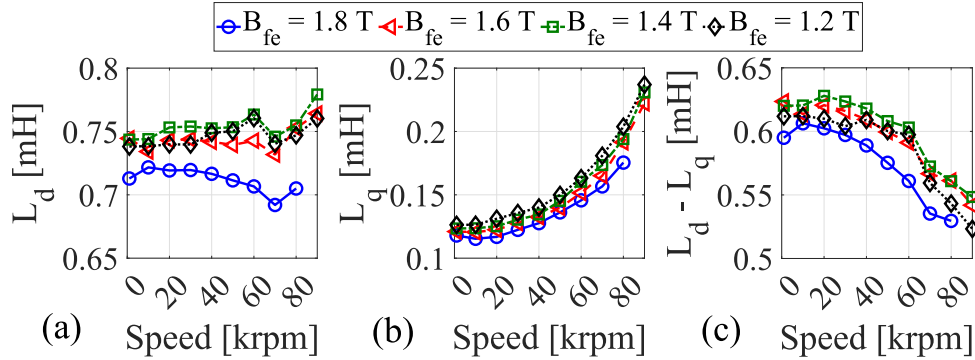


Figure 2.39:  $L_d$  (a),  $L_q$  (b) and  $L_d - L_q$  (c) at the maximum torque as function of the speed.

Clearly, the rise of the iron losses is more pronounced when adopting a high magnetic load. As an example, at 80krpm the stator iron losses are 160 W when  $B_{fe} = 1.8$  T and 120 W when  $B_{fe} = 1.2$  T. As a consequence, in the first case the q-axis current reduction is higher with respect to the latter case.

Regarding the d-axis current, high iron flux densities obviously require higher magnetizing currents; the reduction of this current components with the speeds is mainly ascribed to the different location of the maximum torque design in the  $sr - mr$  plane.

As expected, the d-axis inductance is almost independent from the speed and increases as the iron flux density decreases (up to a certain point until the unsaturated value is reached). The q-axis inductance drastically increases with the speed due to the increment of the iron bridge dimension. It also increases as iron flux density decreases due to the higher ribs-shunted fluxes.

The trends of both inductances leads to a decrement of their difference and to an improve-

ment when the magnetic load is lower.

Before 60krpm, adopting a high value of iron flux density is beneficial since the influence of the current reduction due to the iron losses is not a preponderant phenomenon in the torque generation. Conversely, as the speed increases, the q-axis current reduction is more pronounced so it is preferable to select a lower iron flux density which also allow a higher inductances difference.

Regarding the internal power factor of the maximum torque designs, it always increases with the magnetic load even after 60krpm as shown in Fig. 2.36b. This is clearly due to the lower rib-shunted fluxes ascribed to the higher iron flux density.

### 2.7.1 Optimal Machines

The design variables (split and magnetic ratio,  $sr - mr$ ) of the optimal (torque wise) design are shown in Fig. 2.40 while the cross sections of the optimal geometries at three different speeds (20, 50 and 80 krpm) and their flux density maps are shown in Fig. 2.41.

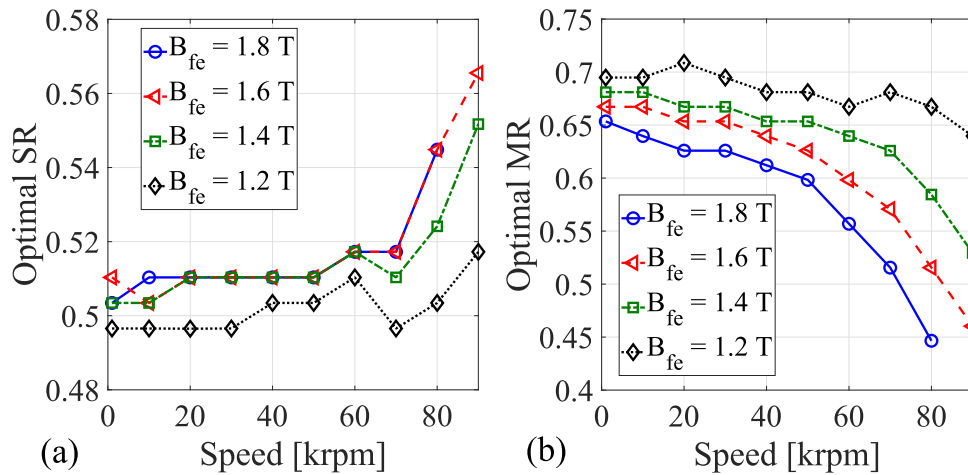


Figure 2.40: Optimal (torque wise) design variables  $sr$  (a) and  $mr$  (b) as function of the speed

Fig. 2.41a, 2.41b and 2.41c report the optimal machines obtained considering the lowest magnetic load (i.e 1.2 T), whereas the highest magnetic load case (i.e 1.8 T) cross-sections are reported in Fig. 2.41d, 2.41e and 2.41f. Table 2.6 reports torque, iron losses, rotor radius, tooth and back iron thickness of the considered optimal machines.

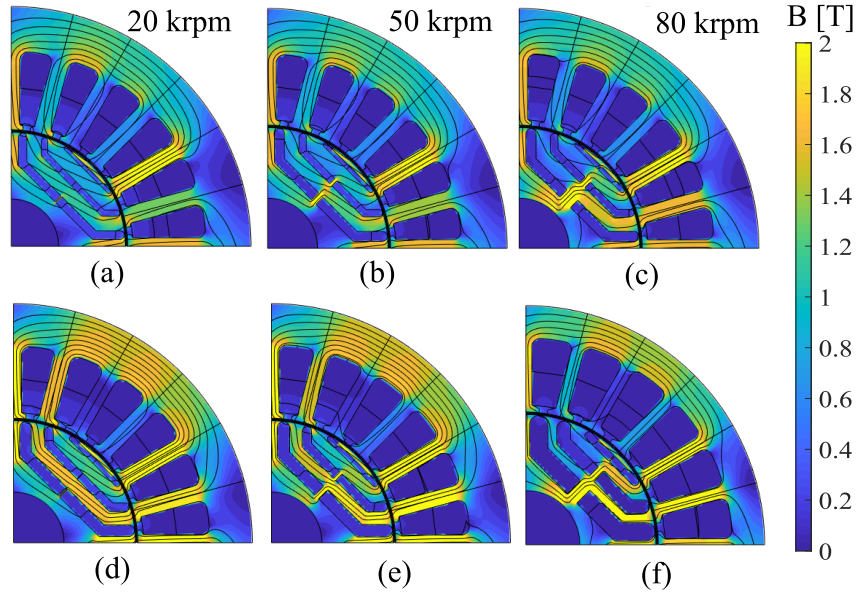


Figure 2.41: Cross sections of the optimal machines at (a,d) 20krpm, (b,e) 50krpm, (c,f) 80krpm, considering a magnetic load equal to (a,b,c) 1.2 T and (d,e,f) 1.8 T

Table 2.6: Comparison between optimal machines

Speed	Variable	$B_{fe} = 1.2T$	$B_{fe} = 1.8T$
<b>20 krpm</b>	$T$ [Nm]	1.10	1.49
	$P_{fe-st}$ [W]	15	21
	$R_r$ [mm]	14.3	15.3
	$l_y$ [mm]	5.6	5.31
	$w_t$ [mm]	2.11	2.01
<b>50 krpm</b>	$T$ [Nm]	0.98	1.20
	$P_{fe-st}$ [W]	55	84
	$R_r$ [mm]	15.1	15.3
	$l_y$ [mm]	5.7	5.07
	$w_t$ [mm]	2.15	1.92
<b>80 krpm</b>	$T$ [Nm]	0.74	0.68
	$P_{fe-st}$ [W]	120	160
	$R_r$ [mm]	15.1	16.3
	$l_y$ [mm]	5.6	4.04
	$w_t$ [mm]	2.11	1.52

Analysing both Fig. 2.40 and 2.41 and Table 2.6, the following considerations can be drawn.



- The rotor radius is slightly affected by the speed (up to 60krpm) whatever the magnetic load is imposed and slightly decreases as the iron flux density decreases.
- The optimal magnetic ratio decreases with the speed and with high value of iron flux density.
- The relationship between the stator tooth thickness ( $w_t$ ) and the speed is dependent by the selected iron flux density. When the latter is small,  $w_t$  remains almost constant, whereas it decreases for higher  $B_{fe}$  values. The same considerations can be extended to the stator yoke thickness ( $l_y$ ).
- The flux density contour plots highlight the accuracy of the hybrid analytical design approach, since the actual value of the iron flux density is on average equal to the one imposed during the design exercise.

## 2.8 Influence of the current calculation criteria

In this section, the hybrid design approach has been used to compare different current calculation criteria for several maximum speeds ranging from 1 krpm to 120 krpm considering the machine parameters listed in Table 2.1. Several criteria can be adopted to determine  $I_{max}$  and this choice greatly influences the machine electromagnetic and thermal performance.

Indeed, the selection of such criteria is particularly important when analysing several machine designs as it defines the common base for the comparative exercise. In particular, the maximum current can be calculated constraining either the current density (**Constant-J**) or the Joule losses (**Constant-P<sub>j</sub>**), or the stator losses (**Constant-P<sub>st</sub>**) or the total machine losses (**Constant-P<sub>tot</sub>**).

In the first design scenario,  $I_{max}$  can be calculated as:

$$I_{max} = \frac{J \cdot k_{fill} \cdot A_{slot}}{z_q} \quad (2.34)$$

where  $z_q$  is the number of conductors per slot.

Conversely, the current formulation changes if a constant loss  $P^*$  (which can be either Joule, or stator or total) is considered. In particular, starting from the relationship (2.35) it is possible to define all the constant loss criteria:

$$P^* = 3 \cdot R_{ph} \cdot I_{max}^2 + P_{fe-st} + P_{fe-rot} \quad (2.35)$$

Hence, considering the **Constant- $P_j$**  criterion, the iron losses terms are set to zero, therefore the maximum current is easily calculated by (2.36):

$$I_{max} = \sqrt{\frac{P^*}{3 \cdot R_{ph}}} \quad (2.36)$$

On the contrary, (2.37) or (2.38) have to be adopted if the design criteria **Constant- $P_{st}$**  or **Constant- $P_{tot}$**  are selected:

$$I_{max} = \sqrt{\frac{P^* - P_{fe-st}}{3 \cdot R_{ph}}} \quad (2.37)$$

$$I_{max} = \sqrt{\frac{P^* - P_{fe-st} - P_{fe-rot}}{3 \cdot R_{ph}}} \quad (2.38)$$

where the stator iron losses can be analytically estimated and FE-tuning using the procedure described in sections 2.1 and 2.3.

In particular, for each speed and current calculation criterion, the torque as function of both design variables  $sr - mr$  are determined. Then, the maximum torque solutions are compared as the maximum speed increases both in terms of performance and geometries. All four different current calculation criteria described in the previous section have been investigated, namely: **Constant- $P_j$** , **Constant- $P_{st}$** , **Constant- $P_{tot}$**  and **Constant- $J$** . In the first three scenarios  $P^*$  has been set to 280 W, while in the last case  $J$  has been fixed to 23 A/mm<sup>2</sup>.  $P^*$  and  $J$  have been selected so to obtain the same current density when considering a low speed design (i.e 1 krpm).

### 2.8.1 Analysis in the $sr - mr$ design plane

Fig. 2.42 reports the constant torque loci in the  $sr - mr$  plane at 20 krpm and 120 krpm considering the four current calculation criteria. Analysing these figures, it can be deduced that

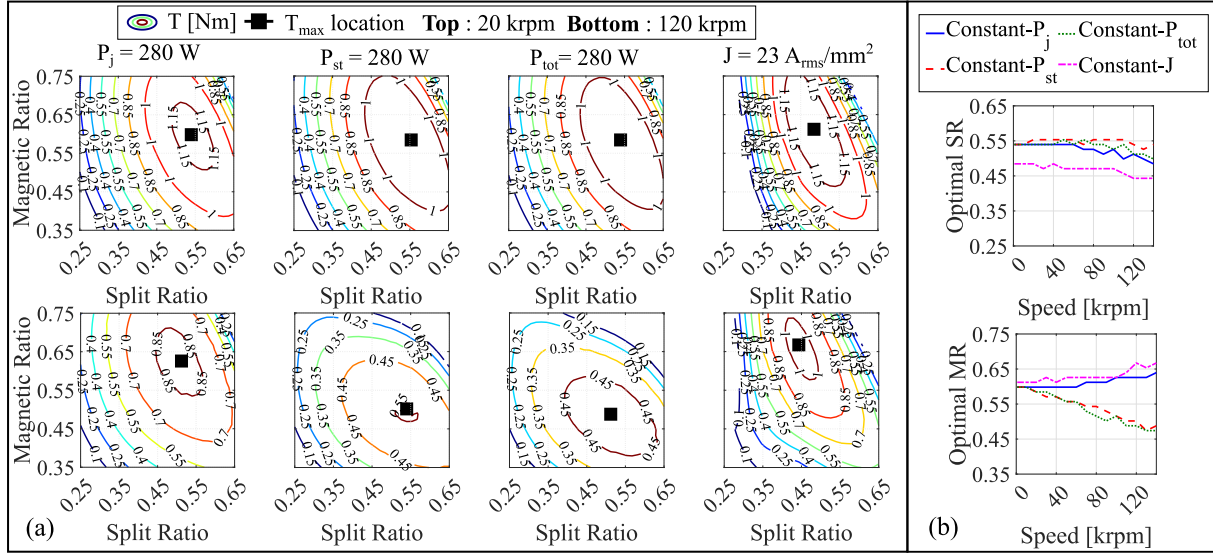


Figure 2.42: a) Average torque in the  $sr - mr$  plane considering different current calculation criteria at a) 20 krpm and b) 120 krpm; b) Optimal split and magnetic ratios as function of the speed

the maximum torque location is not affected by the current calculation method when designing SyRMs with a maximum speed relatively low (i.e.  $< 20$  krpm in this case study). Indeed, the constant losses scenarios share almost the same contour shape while the constant current density one leads to a slightly different contour behaviour.

As the speed increases, the effects of the current calculation methods become more evident as both torque contour and position of the maximum torque solution change. The latter are identified by the  $sr - mr$  values reported in Fig. 2.42b as function of the speed.

The maximum torque location is defined by the compromise between the competitive needs of maximizing the magnetic anisotropy ( $L_d - L_q$ ), the d-axis current ( $i_d$ ) and the q-axis current ( $i_q$ ) as shown in Fig. 2.43a, b and c. The latter show the three factors defining the torque contour in the  $sr - mr$  plane for **Constant- $P_j$**  current calculation criterion at 20 krpm. The first one ( $L_d - L_q$ ) depends on the speed via the iron rib dimension, the second one ( $i_d$ ) is speed

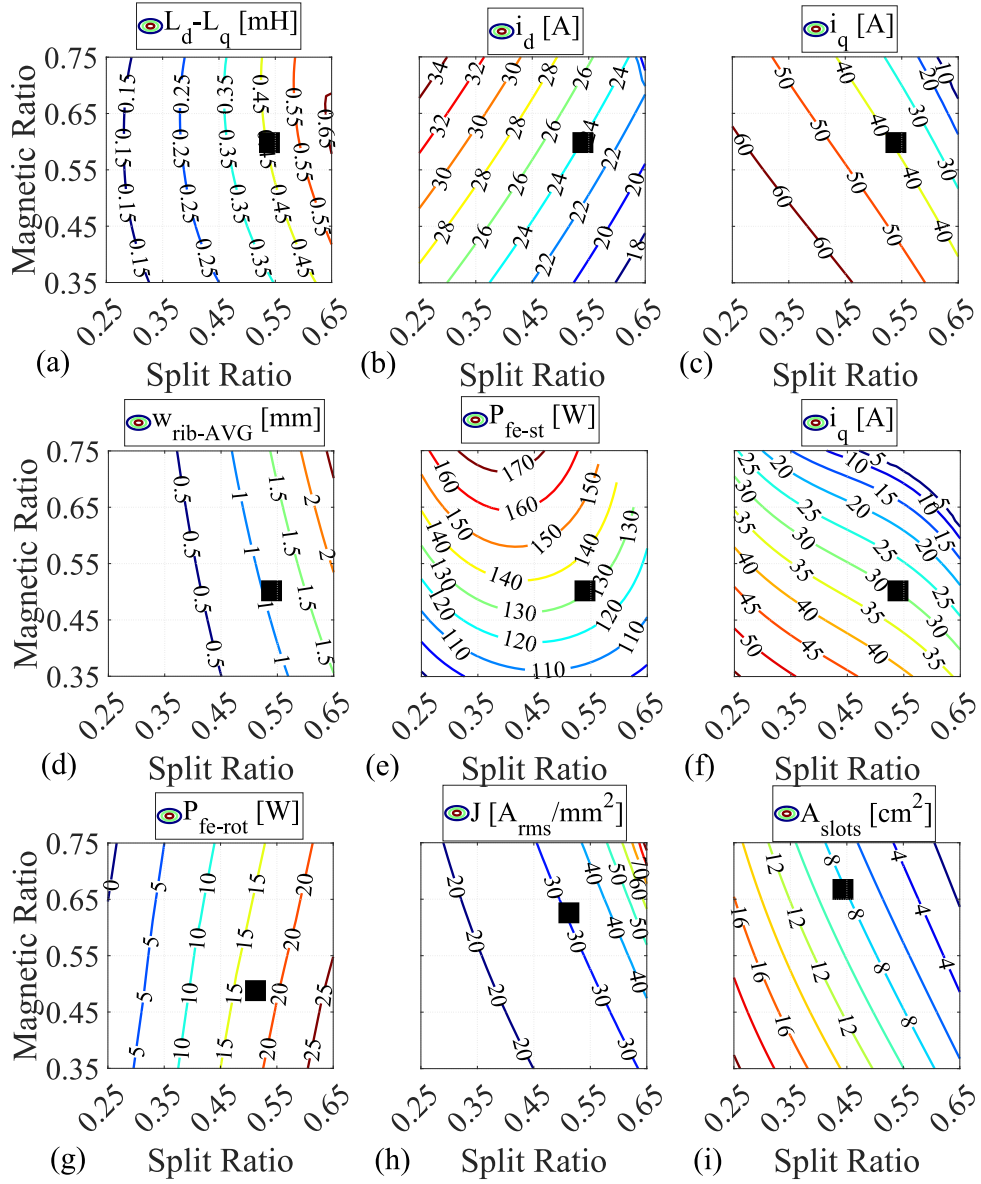


Figure 2.43: **Constant  $P_{st}$**  and **Constant  $P_{tot}$**  scenarios at 120 krpm: a) Stator iron losses; b)  $L_d-L_q$ ; c) q-axis current; c2) rotor iron losses.

independent while the last one ( $i_q$ ) is related to the speed via the stator and rotor iron losses if these are included in the calculation of the maximum current ( $I_{max}$ ).

Adopting a **Constant- $P_j$**  scenario, the maximum torque location for high maximum speed moves towards higher  $mr$  and slightly lower  $sr$  since in this direction the iron ribs dimensions decrease and so the related torque drop as shown in Fig. 2.43d in terms of average rib ( $w_r$ ).

When also the stator iron losses are included within the current calculation (**Constant- $P_{st}$**  criterion), as the maximum speed increases, the optimal magnetic ratio decreases while the split

ratio remains constant. The maximum torque design moves towards the zone of the design plane with lower stator iron losses (lower  $mr$ ) which in turn means higher q-axis current and so higher torque as shown in Fig. 2.43e and f.

Including the rotor iron losses in the current calculation (**Constant- $P_{tot}$**  criterion) leads to a slight reduction of the optimal split and magnetic ratios respect to the values obtained with the **Constant- $P_{st}$**  scenario for the same speed as in this direction the rotor iron losses decrease as shown in Fig. 2.43g.

When applying a constant current density design approach (**Constant- $J$** ), the torque contour plot resembles the constant Joule loss scenario as the maximum torque location as the maximum speed increases moves more prominently towards higher  $mr$  and lower  $sr$ .

## 2.8.2 Performance of the maximum torque designs

Fig. 2.44a and 2.44b shows the maximum torque and the maximum power as function of the speed for the four considered current calculation criteria. The FE evaluated performance are

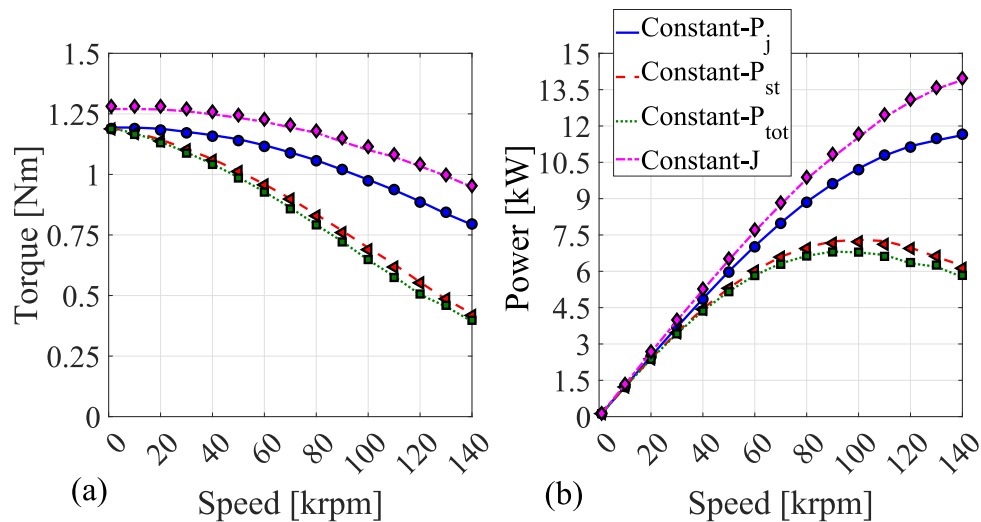


Figure 2.44: Maximum torque (a) and maximum power (b) as function of the speed in the 4 considered cases.

reported in the same figure with the markers showing an excellent agreement with the predicted values. Clearly, the most conservative approach (i.e. **Constant- $P_{tot}$** ) leads to the worst performance. The application of the **Constant- $P_{st}$**  criterion leads to similar results (i.e the maximum

power increment is about 5%) since the rotor iron losses are quite smaller than the stator ones. Conversely, when the Joule losses or the current density are kept constant, the maximum performance significantly increase when considering high-speed SyR machines.

It is worth to underline that keeping constant the total losses leads to designs that can share the same cooling system, whereas a more powerful cooling layout should be adopted when using the others current calculation criterion. Indeed, the total losses of the optimal machine obtained adopting the **Constant- $P_j$**  and the **Constant- $J$**  criteria considerably increases with the maximum speed as reported in Fig. 2.45a.

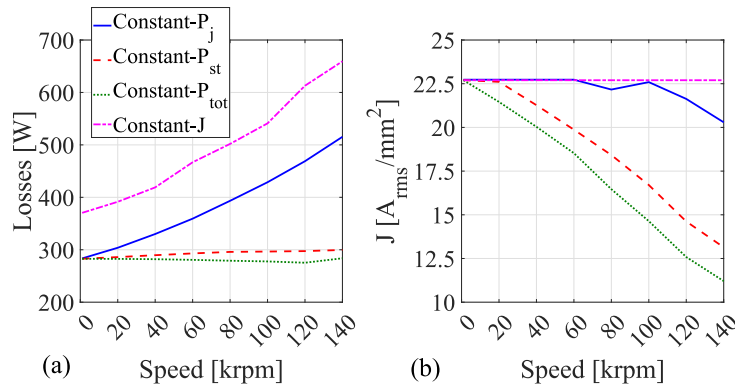


Figure 2.45: Total losses (a) and current density (b) as function of the speed in the 4 considered cases.

This aspect can be surely neglected when designing low speed machines since the influence of the iron losses is minimal from both electromagnetic and thermal point of views. Differently, as the speed increases, the increment of the iron losses force the designer either to reduce the stator current or to increase the cooling system capability. In other words, the current density has to decrease with the speed if the total loss has to be kept constant as shown in Fig. 2.45b.

A possible figure of merit characterizing the cooling system capability is the ratio  $k_j$  between the losses to be dissipated and the stator external surface ( $S_{st}$ ):

$$k_j = \frac{P_{tot}}{S_{st}} \quad (2.39)$$

Table 2.7 reports the value of  $k_j$  of the optimal torque designs for three different speeds and the

four current calculation criteria. The increment of the speed leads to a  $k_j$  increment except for the most conservative criteria (**Constant- $P_{tot}$**  and **Constant- $P_{st}$** ). Only in these case, all the designs can share the same cooling system independently from the speed. Conversely, adopting the **Constant- $J$**  (or the **Constant- $P_j$** ) criterion leads to a design at 120krpm requiring a cooling system approximately 53% more powerful respect to the one required at 20krpm.

Although the **Constant- $P_{tot}$**  and **Constant- $P_{st}$**  current calculation criteria seem to lead to the same result, the former leads to optimal designs with lower rotor iron losses and so better thermal performance as shown in Table 2.7.

Table 2.7: Cooling system capability of the optimal designs.

Speed	$k_j[\text{kW}/\text{m}^2](P_{\text{fe-rot}}[\text{W}])$			
	Const. $P_j$	Const. $P_{st}$	Const. $P_{tot}$	Const. $J$
20 krpm	54 (3.4)	51 (3.4)	50 (3.2)	70 (4)
80 krpm	70 (16.2)	52 (14.5)	50 (12.5)	89 (19.7)
120 krpm	83 (24.4)	53 (17.4)	50 (14.2)	108 (29.5)

### 2.8.3 Geometries of the maximum torque designs

Fig. 2.46 reports the cross sections of the optimal machines at 20, 80 and 120 krpm for each design criterion. The insights reported in the previous subsection can be visually observed. On one hand it can be noticed that the airgap radius (directly influenced by  $sr$ ) always decreases with the speed except for the **Constant- $P_{st}$**  design scenario. On the other hand, the magnetic ratio influences the flux guides and stator teeth width. Indeed, the decrement of  $mr$  with the speed in the constant stator and total losses cases leads to machine configurations with higher flux barriers width and lower teeth width. Differently, the magnetic ratio increases with the speed in the constant Joule losses and constant current density scenarios, therefore the machine configurations is characterized by large teeth and flux guides.

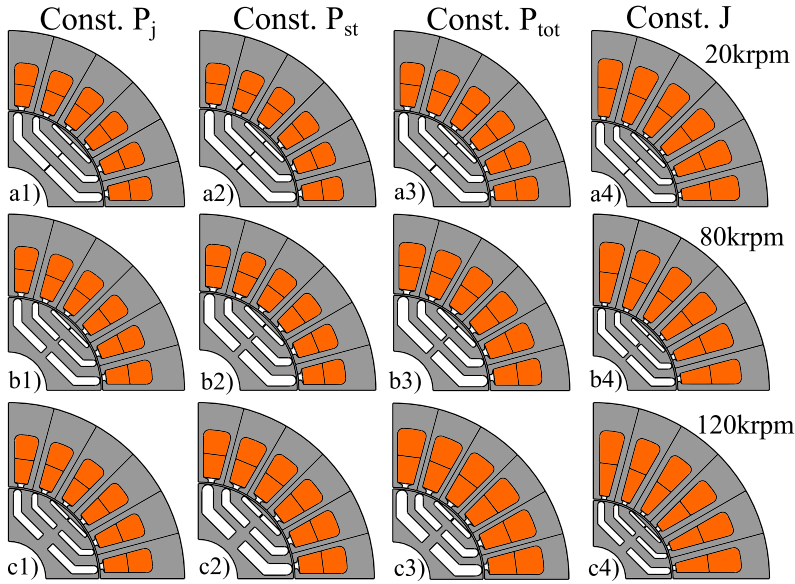


Figure 2.46: Optimal machines geometries.

## 2.9 Publications

The results presented in this chapter have been published by the author in [108], [109] [110], [111] and [112].



## Chapter 3

# Permanent Magnet assisted Synchronous Reluctance Machines

In this chapter, the equations as well as the design methodology used for the SyRM scenario are briefly re-called and extended to the PMSyRM case, suitable for high speed operations fully considering the effect of the PM presence and without neglecting the interaction between the structural targets of having iron ribs and their non linear electromagnetic behaviour. Indeed, the analytical performance prediction, used during the design, is enhanced by the calculation of the PM flux linkage and q-axis inductance with a non-linear lumped-parameters magnetic circuit capable of taking into account the saturation of the structural iron ribs leading to the correct sizing of the PMs which guarantee a specified performance requirement. The proposed design approach allows to define both stator and rotor geometries, which can be then FE-refined prior the manufacturing.

The study is to use the proposed approach in order to:

- design several machines having different operating speeds ranging from 1 to 140krpm;
- consider the effect of different PM types, e.g. Ferrite and NdFeB magnets, with respect to the SyR designs;
- evaluate the effectiveness of adding the PMs once both stator and rotor geometries are

---

defined;

- analyse how and why the optimal performance changes as the maximum speed increases;
- analyse the optimal geometries obtained considering different speeds, magnet grades and design choices.

Also in this chapter the base speed and the maximum speed are considered to be equal, therefore the flux weakening region is not investigated.

### 3.1 Re-call and extension of the analytical design equations

As for SyRM, torque and power factor are expressed as functions of two per-unit variables: the split ratio  $sr$  and the magnetic ratio  $mr$ , for a given outer envelope ( $r_s$  and  $l_{fe}$  are fixed as well as the magnetic load  $B_{fe}$ ).

The remaining geometrical parameters, all depicted in Fig. 3.1, are therefore expressed in terms of these two independent quantities, allowing to fully define the machine geometry for a given outer envelope. In the next two subsections, first the main equations used to analytically

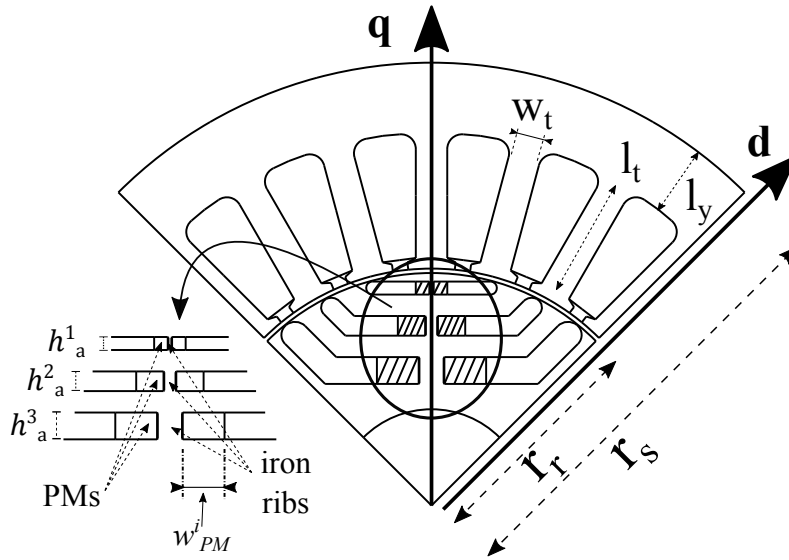


Figure 3.1: Machine parametrization.

estimate torque and power factor are recalled, then the non-linear q-axis equivalent magnetic circuit is described. The third subsection outlines different PM design criteria, while in the last part the iterative procedure required to calculate both PM flux linkage and q-axis inductance is described.

#### 3.1.1 Main design equations

The torque produced by PMSyRMs can be expressed, in its general form, as follows:

$$T = \frac{3}{2} \cdot p \cdot (\lambda_d \cdot i_q - \lambda_q \cdot i_d) \quad (3.1)$$

while the internal power factor, defined by the sine of the angular displacement between the current and flux linkage vectors (Fig. 3.2), can be written as:

$$ipf = \sin \left[ \arctan \left( \frac{i_q}{i_d} \right) - \arctan \left( \frac{\lambda_q}{\lambda_d} \right) \right] \quad (3.2)$$

As for the SyRM design, for a given couple of independent design variables ( $sr$ ,  $mr$ ), the d-

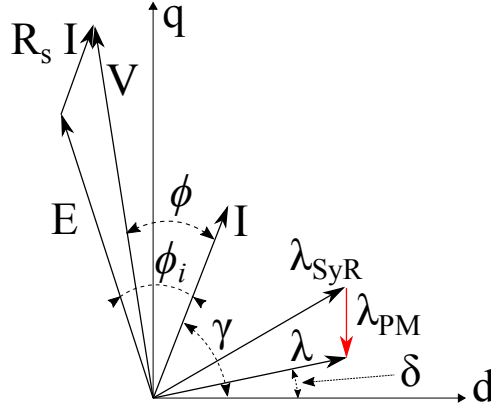


Figure 3.2: Vector diagram of PMSyRMs.

axis flux per pole is defined ( $2 \cdot r_r \cdot l_{fe} \cdot B_g/p$ ), therefore the tooth width ( $w_t$ ) and stator yoke radial thickness ( $l_y$ ) can be evaluated imposing the iron flux density  $B_{fe}$ .

The complete rotor geometry, except for the PM dimensions, can be defined still following the rules reported in [27]. On one hand, the barriers angular positions (in electrical degrees) at the airgap can be calculated so to obtain a uniform distribution of the equivalent rotor slots and imposing barriers having the same permeance and the total iron thickness along the q-axis equal to the stator yoke thickness. It is worth to underline that the above rotor design choices (which are just one option) allow minimizing the torque ripple [113]. Indeed, uniform distribution of the equivalent rotor slots and barriers with equal permeance allow obtaining a direct proportionality between the stator and rotor m.m.f. so to minimize their harmonic interaction, if the local saturation effects and the influence of different tangential ribs thicknesses are neglected.

Dealing with PMSyRMs, if the PM height is imposed equal to the flux barrier one, the only remaining degree of freedom is the PM width  $w_{PM}$ .

The current components are calculated imposing the airgap flux density ( $B_g$  and so the

magnetic ratio  $mr$ ) and the cooling system. In fact, the d-axis current can be inferred according to the Ampère's law (2.26).

Conversely, the q-axis current can be computed knowing the maximum current  $I_{max}$  which can be calculated imposing the cooling capability  $k_{cool}$  as in (3.3):

$$I_{max} = \frac{1}{3N_s} \sqrt{\frac{k_{fill} A_{slots}}{2\rho_{cu}(l_{fe} + l_{ew})} (2\pi r_s l_{fe} k_{cool})} \quad (3.3)$$

As just described, for a given split and magnetic ratio, it is possible to calculate the current components once the iron flux density  $B_{fe}$  and the cooling system  $k_{cool}$  are defined. In order to estimate both torque and power factor the flux linkages  $\lambda_d$  and  $\lambda_q$  need to be accurately calculated. In the PMSyRM case, the latter can be written as:

$$\lambda_d = (L_{dm} + L_s)i_d + L_{dq}i_q - \lambda_{PM-d} \quad (3.4)$$

$$\lambda_q = L_{dq}i_d + (L_{qm} + L_{q-rib} + L_s)i_q - \lambda_{PM-q} \quad (3.5)$$

where the inductance terms have been defined in chapter 2 while  $\lambda_{PM-d}$  and  $\lambda_{PM-q}$  are the d- and q-axis fluxes produced by the PMs. Both  $L_{dq}$  and  $\lambda_{PM-d}$  terms are neglected in the analytical design because they can only be accurately estimated by means of FE analysis. On the contrary, many analytical formulations are available in literature to calculate the leakage inductance  $L_s$  [114]. The d-axis magnetizing inductance can be still calculate using (2.18), whereas a different approach has to be used to calculate the q-axis one.

Indeed, the q-axis equivalent circuit adopted in the previous chapter is here modified so to account for the PMs presence. Such magnetic circuit also accounts for the non linear behaviour of the iron ribs.

It is worth to underline that the stator and rotor geometrical parameters are calculated disregarding the permanent magnets flux. This is clearly valid for SyRM; however, when designing PMSyRMs, this assumption remains valid as long as the PM flux linkage does not substantially affect the total flux. This detail will be discussed thoroughly in the following.

### 3.1.2 Non-linear q-axis magnetic circuit

As already explained in the first chapter of this thesis, when only the d-axis current is applied the rotor magnetic potentials are zero, therefore the d-axis flux and inductance can be easily calculated. Differently, if only the q-axis component of the stator m.m.f. is considered, the rotor iron segments assume different magnetic potentials thus the rotor magnetically reacts to the applied stator m.m.f.. The no-load flux linkage due to the PMs and the q-axis inductance can be calculated solving the equivalent magnetic circuit reported in Fig. 3.3a for a rotor with 3 barriers per pole. The magnetic circuit resembles the one reported in Fig. 2.7, Indeed, also in this case the m.m.f generators  $F^1$ ,  $F^2$  and  $F^3$  stand for the q-axis stator magneto-motive forces averaged along the periphery of the rotor with intervals equal to the rotor pitches  $\Delta\alpha^i$  as shown in Fig. 3.4. The reluctances related to the airgap paths can be calculated for the  $i^{\text{th}}$  equivalent

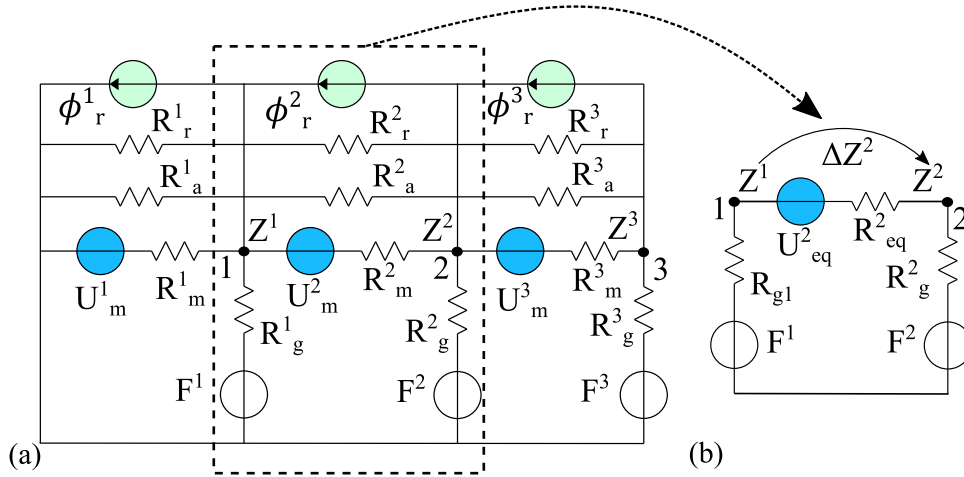


Figure 3.3: a) q-axis magnetic equivalent circuit; b) Thévenin equivalent

circuit branch as in (2.24).

Differently for the pure SyRM case, the PMs are represented by the series of the m.m.f. generators  $U_m^i$  and the reluctances  $R_m^i$  which can be both calculated for the  $i^{\text{th}}$  barrier as:

$$U_m^i = B_{rem} \cdot w_{PM}^i \cdot l_{fe} \cdot R_m^i \quad (3.6)$$

$$R_m^i = \frac{h_{PM}^i}{\mu_{PM} \cdot \mu_0 \cdot w_{PM}^i \cdot l_{fe}} \quad (3.7)$$

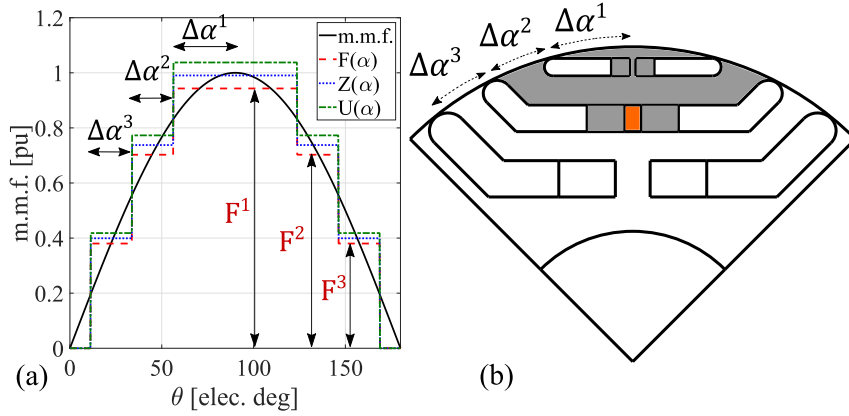


Figure 3.4: a) stator q-axis m.m.f. b) rotor parametrization.

where  $B_{rem}$  is the residual flux density of PM material which is set to zero when designing SyRM and  $\mu_{PM}$  is the relative permeability of the PM. The remaining part of the barrier is taken into account by the reluctances  $R_a^i$  equal to:

$$R_a^i = \frac{h_a^i}{\mu_0 \cdot w_a^i \cdot l_{fe}} \quad (3.8)$$

being  $h_{PM}^i$ ,  $h_a^i$ ,  $w_{PM}^i$ ,  $w_a^i$  the heights and the widths of  $i^{\text{th}}$  PM and flux barrier, respectively. Although a different choice is possible, in this work the PM height  $h_{PM}^i$  is considered equal to the flux barrier one  $h_a^i$ .

The structural iron ribs are modeled with flux generators  $\phi_r^i$  in parallel with the reluctances  $R_r^i$  which can be both calculated as in (2.25), whereas its width is calculated according to the simplified formulation which accounts for the steady-state centrifugal force as in (2.3) which has to consider also the PM mass.

The iron rib permeability  $\mu_{rib-diff}^i$  and the flux density  $B_{rib0}^i$  both depend on the rib working point  $B_{rib}^i$  on the non-linear B-H curve of the rotor soft magnetic material as depicted in Fig. 3.5. Indeed, they are defined by the line tangent to the point  $B_{rib}^i$  which can be expressed as:

$$B_{rib}^i = B_{rib0}^i + \mu_{rib-diff}^i \cdot H_{rib}^i \quad (3.9)$$

from which it is possible to calculate both  $\phi_r^i$  and  $R_r^i$  required to solve the equivalent magnetic

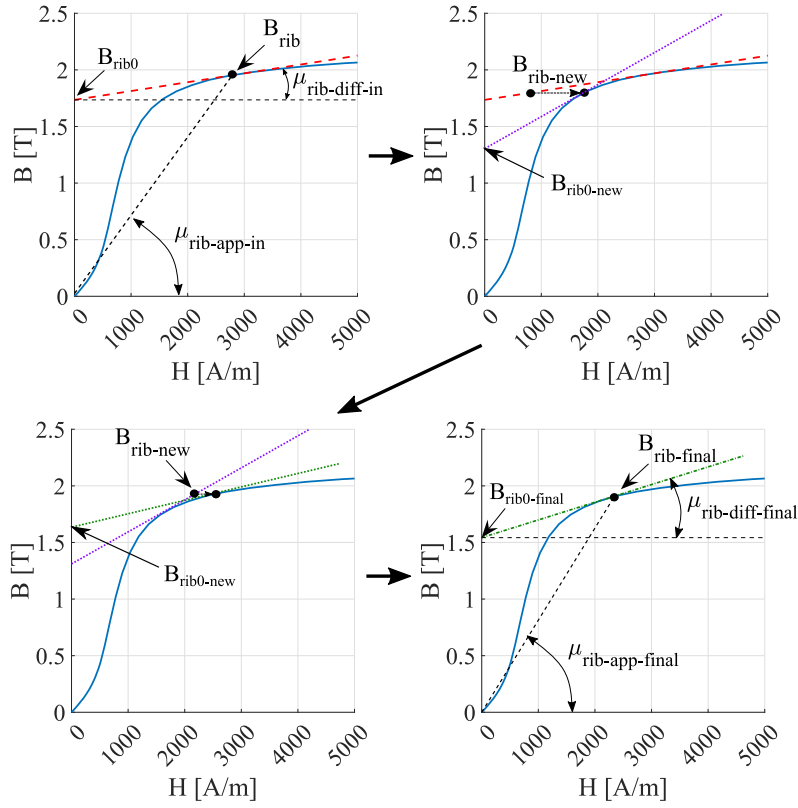


Figure 3.5: Example of  $B_{rib0}$ ,  $\mu_{rib-diff}$  and  $\mu_{rib-app}$  identification for the iron ribs modeling.

circuit.

It is a common practice to consider all the iron ribs equally saturated at a predefined value  $B_{rib}$  whatever operating condition is analyzed. This approximation is acceptable as long as the dimensions of the ribs are relatively small and the shunted flux does not substantially modify the machine performance. Clearly, this assumption loses its validity as the speed increases since the iron ribs dimensions become more important.

In fact, as the speed increases the effective working point  $B_{rib}^i$  considerably deviates from the a-priori defined value; moreover each iron rib may assume different operating points. Consequently, an iterative procedure is required as the speed increases in order to update the parameters defining the iron ribs behaviour, i.e. the flux generators  $\phi_r^i$  and the reluctances  $R_r^i$ . Furthermore, when the PMaSyRM case is considered, these values are also affected by the amount of PM material placed within the rotor slots and their distribution.



### 3.1.3 PM design criteria

The q-axis equivalent magnetic circuit reported in Fig. 3.3a can be simplified applying the Thèvenin theorem; Fig. 3.3b shows the equivalent of one branch of the circuit, where  $R_{eq}^i$  is the parallel between  $R_a^i$ ,  $R_m^i$  and  $R_r^i$ , while  $U_{eq}^i$  can be computed as:

$$U_{eq}^i = R_{eq}^i \cdot l_{fe} \cdot [w_{PM}^i \cdot B_{rem} - w_r^i \cdot B_{rib0}^i] \quad (3.10)$$

Writing the first Kirchhoff's law at the nodes 1, 2 and 3 in Fig. 3.3 and expressing the flux flowing in the connected branches as a function of the m.m.f. related to the PM and ribs ( $\mathbf{U}_{eq}$ ), stator excitation ( $\Delta\mathbf{F}$ ) and rotor reaction ( $\Delta\mathbf{Z}$ ), it is possible to write the following matrix equation:

$$\mathbf{A} \cdot \Delta\mathbf{Z} = \mathbf{B} \cdot \mathbf{U}_{eq} + \mathbf{C} \cdot \Delta\mathbf{F} \quad (3.11)$$

where  $\mathbf{A}$ ,  $\mathbf{B}$  and  $\mathbf{C}$  are matrices defined by the barriers, airgap, magnets and ribs reluctances while the three vectors  $\mathbf{U}_{eq}$ ,  $\Delta\mathbf{Z}$  and  $\Delta\mathbf{F}$  are defined as follows:

$$\mathbf{U}_{eq} = \begin{bmatrix} U_{eq}^1 \\ U_{eq}^2 \\ U_{eq}^3 \end{bmatrix}, \Delta\mathbf{F} = \begin{bmatrix} F^1 \\ F^2 - F^1 \\ F^3 - F^2 \end{bmatrix}, \Delta\mathbf{Z} = \begin{bmatrix} Z^1 \\ Z^2 - Z^1 \\ Z^3 - Z^2 \end{bmatrix} \quad (3.12)$$

As shown in eq. (3.10),  $U_{eq}^i$  depends on the PM widths which have to be identified according to a specific criterion.

Various methodologies can be adopted to size the PM width, according to which performance index is going to be optimized. In particular, the PMs dimension can be identified according to one of the following criteria:

1. *Natural compensation.* This condition is obtained if the PM flux at no-load ( $\lambda_{PM-q}^*$ ) equals the q-axis flux due to the current contribution [68, 115]:

$$\lambda_{PM-q}^* = \lambda_{PM-NC} = L_q I_{max} \quad (3.13)$$

where  $L_q$  is the total q-axis inductance (sum of magnetizing and leakage components).

An elegant way to implement this PM design criterion is to impose the fluxes entering the branches of the stator m.m.f generators (reported in Fig. 3.3a with the symbol  $F^i$ ) equal to zero. In other words, the rotor magnetic potentials ( $Z_i$ ) have to equal the stator ones ( $F_i$ ). Imposing the condition  $\Delta\mathbf{Z} = \Delta\mathbf{F}$  allows to determine the equivalent m.m.f.  $\mathbf{U}_{eq}$ :

$$\mathbf{U}_{eq} = \mathbf{B}^{-1} \cdot (\mathbf{A} - \mathbf{C}) \cdot \Delta\mathbf{F} \quad (3.14)$$

from which the PM widths  $w_{PM-NC}^i$  can be calculated:

$$w_{PM-NC}^i = \frac{1}{B_{rem}} \left[ \frac{U_{eq}^i}{R_{eq}^i \cdot l_{fe}} + w_r^i \cdot B_{rib0}^i \right] \quad (3.15)$$

supposing a certain iron rib dimension  $w_r^i$  and electromagnetic exploitation  $B_{rib}^i$ .

It is worth to underline that adopting this PM sizing approach along with the criterion of designing the rotor flux barriers with equal permeance, allows minimizing also the torque ripple. In fact, when these two criteria are adopted, the matrix  $\mathbf{B}^{-1} \cdot (\mathbf{A} - \mathbf{C})$  is diagonal, which means that the equivalent PM m.m.f. ( $U_{eq}(\alpha)$  in Fig. 3.4) is proportional to the stator m.m.f  $F(\alpha)$ . Therefore the harmonic interaction between these two m.m.f. is minimized.

2. *Target ipf.* The PM widths allowing to achieve a desired internal power factor can be identified by imposing the following constraint:

$$\lambda_{PM-q}^* = L_q i_q - \lambda_d \left\{ \tan \left[ \arctan \left( \frac{i_q}{i_d} \right) - \arcsin(ipf^*) \right] \right\} \quad (3.16)$$

if both cross coupling terms ( $L_{dq}$  and  $\lambda_{PM-d}$ ) are neglected. In (3.16)  $ipf^*$  is the target internal power factor and  $L_q$  is the total q-axis inductance (sum of the magnetizing and leakage components). Since the *Natural compensation* criterion also allows to define the PMs distribution into the flux barriers which guarantees the proportionality between

$\Delta F$  and  $\Delta U_{eq}$ , when the *Target ipf* criterion is adopted it is convenient to scale the PM dimensions obtained with the *Natural compensation* criterion ( $w_{PM-NC}$ ), using eq. (3.17). Indeed, Once the PM flux linkages are known in the natural compensation condition  $\lambda_{PM-NC}$  and in the condition providing a given internal power factor  $\lambda_{PM-q}^*$ , the new PM dimensions can be simply calculated as:

$$\mathbf{w}_{PM}^* = \mathbf{w}_{PM-NC} \frac{\lambda_{PM-q}^*}{\lambda_{PM-NC}} \quad (3.17)$$

3. *Torque maximization*. In this case, each barrier is completely filled by PMs.

Once the PMs widths are defined, the q-axis equivalent magnetic circuit, reported in Fig. 3.3, can be solved to compute the no-load PM flux linkage and the q-axis inductance.

### 3.1.4 Iterative calculation of the q-axis inductance and PM flux

Based on the considerations reported in the previous subsections, the design of the PM dimension and the calculation of the q-axis quantities require an iterative procedure. In fact, the iron rib dimensions ( $w_r^i$ ) structurally depend on the PM width  $w_{PM}^i$  (via the mass  $m_{PM}^i$  in eq. (2.3)), which in turn is electromagnetically affected by the iron ribs width as shown in eq. (3.15). The last equation also proves that the PM dimension is affected by the electromagnetic working point of the respective rib, i.e. from the two parameters  $B_{rib0}^i$  and  $\mu_{rib-diff}^i$  included in  $R_{eq}^i$ . The latter follows from the resolution of the equivalent circuit which clearly depends also on the iron rib widths.

A comprehensive iterative procedure, summarized in the flowchart reported in Fig. 3.6, is here proposed to solve the non-linear q-axis magnetic circuit considering all the above mentioned dependencies between structural and electromagnetic design aspects. The SyRM design is a particular and simpler case of the PMaSyRM one. In particular, the workflow is constituted by the following steps.

1) For each machine defined by the two independent variables  $sr, mr$ , the design of the main

stator and rotor dimensions is carried out (including the barrier height  $h_a^i$  and barrier surface  $S_b^i$ , tooth width  $w_t$  and tooth length  $l_t$ , and yoke length  $l_t$ ) without considering the PM assistance.

- 2) Then, the iron ribs dimension are calculated using eq. (2.3) without considering the PM weights and supposing a certain electromagnetic exploitation of the ribs, i.e.  $B_{rib}^i$  so to be able to determine both  $B_{rib0}^i$  and  $\mu_{rib-diff}^i$  needed to define their circuital representation.
- 3) Consequently, if a PMSyRM is considered, the PM dimensions can be calculated once the PM design criterion is selected. If the max *ipf* criterion is chosen, the q-axis inductance  $L_q$  required to evaluate  $\lambda_{PM-q}^*$  and so the PM widths  $w_{PM}^*$  is estimated at the first iteration using the approximate formulation reported in [27,28] which does not require the resolution of the equivalent circuit. Otherwise (i.e SyRM case), the algorithm proceeds directly to step 5.
- 4) Once the PM widths are known, the iron ribs dimensions are re-calculated taking into account the PMs masses and compared with the previous values. If their difference lies within predefined bounds, the algorithm proceeds to the next step; otherwise, the PM widths are re-calculated considering the updated values of iron ribs  $w_r^i$ .
- 5) Once both PM and ribs dimensions are defined, the magnetic circuit is fully defined and it can be solved calculating the unknown rotor reaction  $\Delta Z$  via the eq. (3.11). The effective saturation level  $B_{rib-new}^i$  in Fig. 3.5 can be evaluated for each iron rib with the following relationship:

$$B_{rib-new}^i = B_{rib0}^i + \frac{\Delta Z^i}{R_r^i} \cdot \frac{1}{w_r^i \cdot l_{fe}} \quad (3.18)$$

The so computed value is then compared with the previous one ( $B_{rib}^i$ ). If their difference is acceptable the algorithm proceeds to the next step; otherwise, the new value  $B_{rib-new}^i$  is used to update the parameters of the tangent line ( $B_{rib0}^i$  and  $\mu_{rib-diff}^i$ ) depicted in Fig. 3.5 and the algorithm restarts from the step 2 in the PMSyRM case (re-calculating the PM dimensions) or step 5 in the SyRM case.

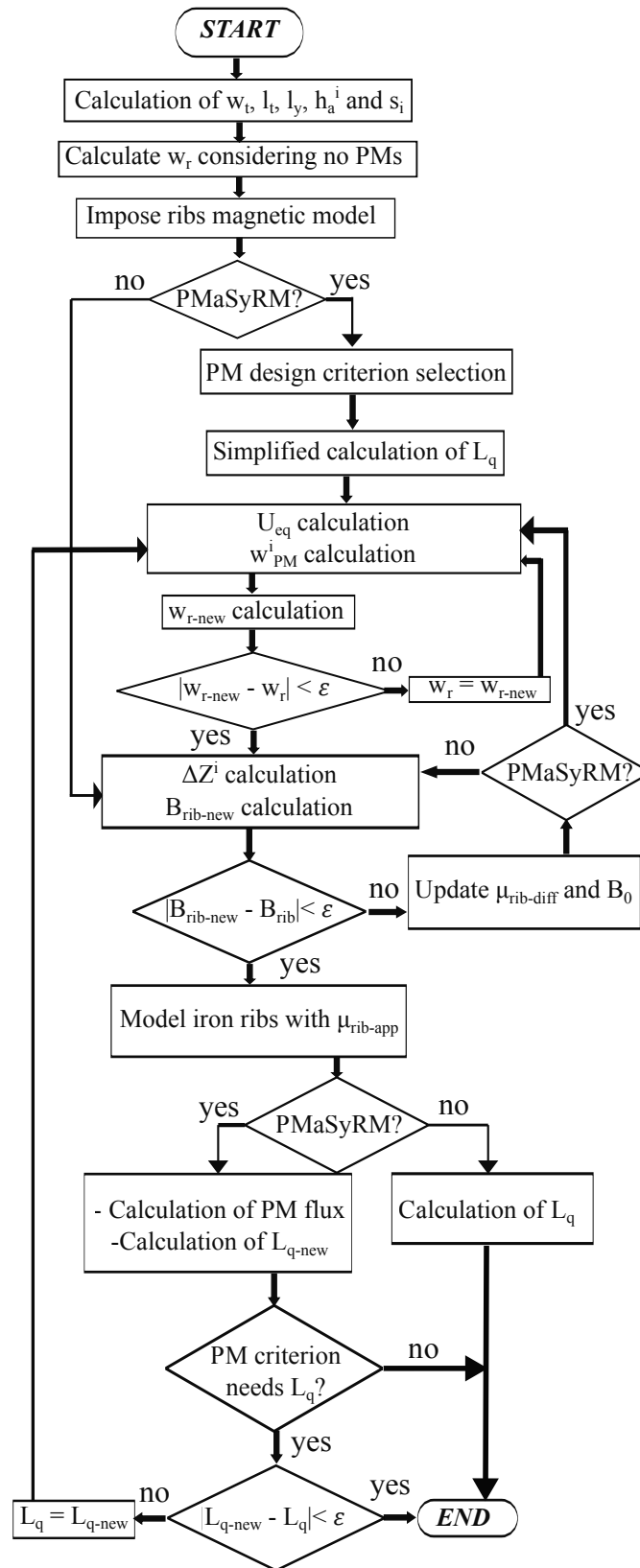


Figure 3.6: Flowchart of the analytical design procedure.

6) Once the saturation level of each rib is correctly evaluated, it is possible to fully define the variables related to the q-axis, i.e. the PM flux linkage and the q-axis inductance, considering either the PM or the stator excitation. If this calculation step is performed still modeling the iron ribs as the parallel between the flux generator  $\phi_r^i$  and the reluctance  $R_r^i$ , then the rib working point ( $B_{rib}^i$ ) would move on the line defined by the parameters ( $B_{rib0-new}^i$  and  $\mu_{rib-diff-new}^i$ ) depicted in Fig. 3.5. However, this approach would lead to incorrect estimation of  $\lambda_{PM}$  and  $L_q$  since the electromagnetic rib working points would differ from the load scenario (when both stator and PM excitations are present). To avoid this issue, the PM flux linkage and the q-axis inductance are calculated modeling the ribs with a single reluctance  $R_{r-app}^i$  defined by the apparent permeability ( $\mu_{rib-app}^i$ ) as shown in Fig. 3.5:

$$R_{r-app}^i = \frac{h_r^i}{\mu_{rib-app}^i \cdot w_r^i \cdot l_{fe}} \quad (3.19)$$

By doing so, the electromagnetic working points of all iron ribs are unequivocally fixed to the one related to the load scenario.

Therefore, the calculation of the q-axis inductance can be performed by modeling the iron ribs only with the apparent reluctances, turning off the PMs m.m.f.  $U_m^i$  and solving the resulting Thévenin magnetic circuit. Indeed, the resolution of such circuit leads to the calculation of the rotor magnetic potentials  $\Delta Z^i$ . From these values it is possible to calculate the airgap flux  $\phi_g^i$  flowing in each airgap branch of the magnetic circuit and, therefore, the airgap flux density  $B_g^i$ . Then, the complete waveform of  $B_g$  can be evaluated by combining all the calculated  $B_g^i$  (three in this case). By integrating the obtained waveform over the pole pitch it is possible to calculate the q-axis flux and the q-axis inductance.

The same workflow can be adopted to calculate the flux per pole due to the PMs, by turning off the stator m.m.f. generators and applying the above procedure for the airgap flux density computation.

7) As last check and only for the PM-assisted machines, the computed  $L_q$  is compared with

the one used to estimate the PM flux linkage needed to achieve the desired internal power factor (eq. (3.16)). If these two values are similar the algorithm ends, otherwise it restarts from step 2.

### 3.2 FE validation of the analytical model

The proposed analytical design approach has been implemented considering a wide range of design variables  $sr - mr$ . Table 3.1 summarizes the main assumptions and constraints. As previously pointed out, the outer envelope is fixed (i.e  $r_s$  and  $l_{fe}$  are given). The airgap thickness

Table 3.1: Design constraints and assumptions

Parameter	Value	Units
Outer stator radius	30	mm
Stack length	30	mm
Pole pairs	2	/
Airgap thickness	0.3	mm
N° of stator slots	24	/
N° of flux barriers per pole	3	/
Shape of flux barriers	U/I-shaped	/
Maximum speed	80000	rpm
Stator/rotor materials	JNHF600/35HXT780T	/
PM material	N42UH	/
Cooling capacity	30	kW/m <sup>2</sup>
Iron flux density	1.4	T

has been selected as a compromise choice between the need of minimizing it (beneficial from the electromagnetic point of view) and practical assembly limits, whereas the selected number of pole pairs allows a lower fundamental frequency beneficial for both control and thermal management. The stator and rotor materials are chosen so to minimize the iron losses and improve the rotor integrity at high-speed (further details about the materials selection can be

found in [116]); the iron flux density is a consequence of the selected iron material for the stator lamination.

The PM dimensions have been designed to achieve an internal power factor  $ipf^*$  equal to 0.9. The estimated performance of each machine of the design plane  $sr - mr$  has been compared with the respective FE analysis with the aim of investigating the accuracy of the analytical approach.

Fig. 3.7 reports a comparison between the analytical ( $an$ ) and FE computation ( $FEA$ ) of d-axis inductance (3.7a), q-axis inductance (3.7b) and PM flux linkage (3.7c). The empty areas of the design plane are due to the presence of unfeasible machines. The FE calculation of

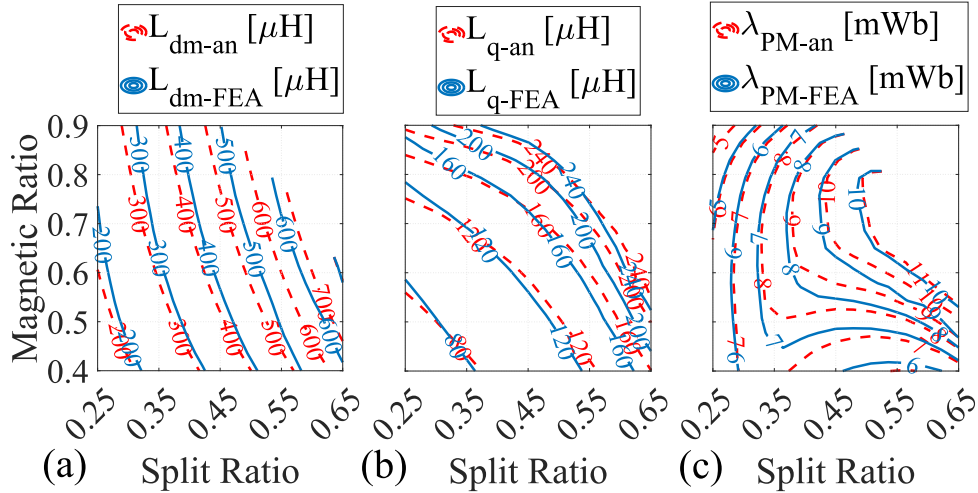


Figure 3.7: Comparison between the analytical estimation and FE-computation of a) d-axis inductance, b) q-axis inductance and c) PM flux linkage at 80 krpm.

these three parameters have been performed with the frozen permeability method [91] in order to capture their values in the load scenario (i.e. when supplying with  $i_d, i_q$  and PM excitation). Analysing Fig. 3.7 it is worth to underline the good estimation of all parameters from a qualitative point of view.

The excellent agreement of both q-axis inductance and PM flux linkage can be ascribed to the good estimation of the iron ribs saturation levels. Fig. 3.8 reports a comparison between the analytical and FE calculations of  $B_{rib}$  of each flux barrier. It is worth to notice that the contour plot of the outermost rib features an additional empty zone (left area of the design plane): the



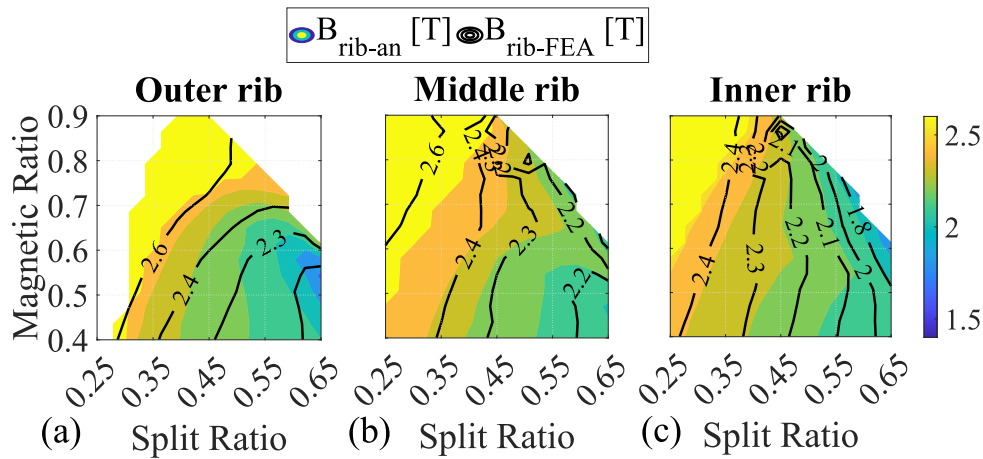


Figure 3.8: Comparison between the analytical and FE calculations of  $B_{rib}$  of the a) outer barrier, b) middle barrier, c) inner barrier.

machine of such zone are still feasible but the respective outermost ribs width is zero or falls within the mechanical tolerance.

Although inductances and PM flux linkage are estimated with a good degree of accuracy, the torque, highlighted in Fig. 3.9a, shows non-negligible discrepancies respect to the FE-computed values. These residual errors are mainly due to the non-linear phenomena not considered in the

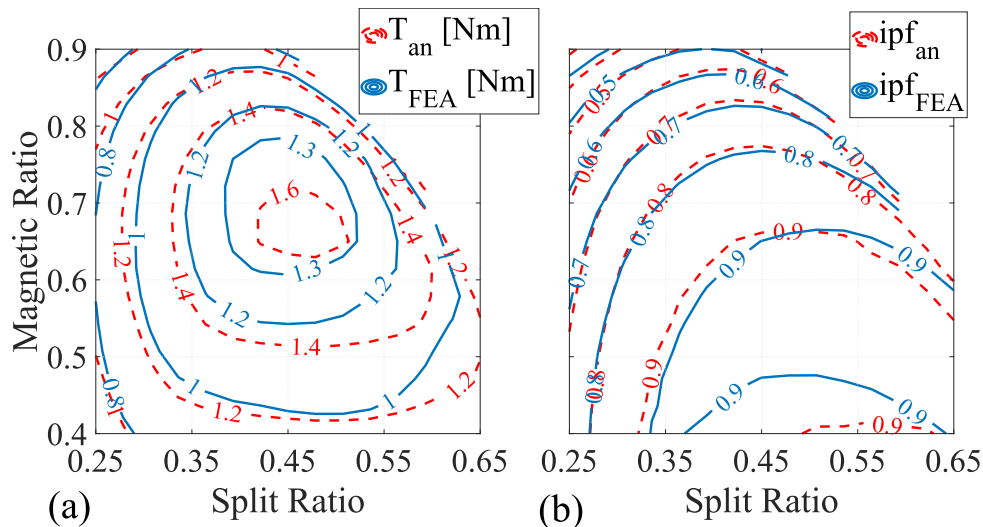


Figure 3.9: Comparison between the analytical estimation and FE-computation of a) torque, b)  $ipf$  at 80krpm.

analytical model, namely the cross-saturation effects (i.e  $L_{dq}$  and  $\lambda_{PM-d}$ ).

Fig. 3.10a reports the percentage rate between the d- and q-axis PM flux linkage (the d-axis

PM flux linkage has been calculated adopting the frozen permeability method), whereas the influence of the cross-coupling contribution is shown in Fig. 3.10b in terms of percentage rate between  $L_{dq}$  and  $L_{dm}$ . The torque contour differs from the FE one mainly in the zone of the  $sr - mr$  plane characterized by large cross-saturation phenomena.

As a consequence, the inclusion of such effects in the design stage is needed to reach an accurate prediction of the electromagnetic performance of both SyRM and PMSyRM. Con-

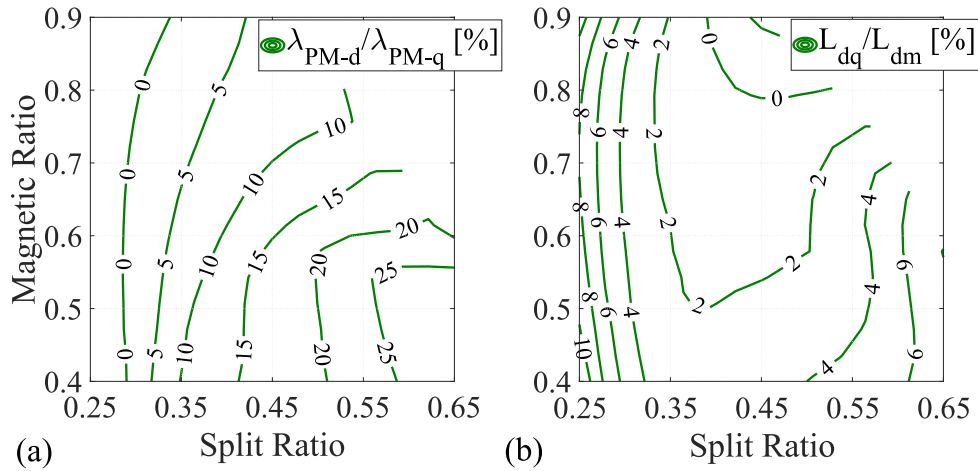


Figure 3.10: Finite element computation of a) rate between the PM flux linkage along the d-axis and q-axis, b) rate between the cross-coupling inductance and the d-axis one.

versely, the analytical  $ipf$  (Fig. 3.9b) contour shows a good agreement with the FE one, both in terms of numerical values and contour shape. It is worth to underline that the obtained internal power factor is not the desired one (i.e. 0.9) over the entire  $sr - mr$  plane. The reason behind this behaviour will be fully investigated.

### 3.3 Enhancing the design approach accuracy

With the aim of improving the performance estimation without sacrificing the fast evaluation characteristic of the pure analytical approach, a hybrid design procedure, proposed in the last chapter for SyRMs, is extended here to the PM-assisted ones.

In particular, once the analytical design is performed for the whole  $sr - mr$  plane, the 4 machines at the corners of the plane are selected and FE-simulated. From the FE-simulation

all inductance ( $L_{dm}$ ,  $L_{qm}$ ,  $L_{dq}$  and  $L_s$ ) and PM flux ( $\lambda_{PM-d}$  and  $\lambda_{PM-q}$ ) contributions can be correctly evaluated adopting the frozen permeability method [91,92]. This allows the calculation of several correction factors defined as the ratio between the finite element (FEA) computed value and the respective analytical ( $an$ ) prediction as:

$$k_x^i = \frac{x_{FEA}^i}{x_{an}^i} \quad (3.20)$$

where  $x$  can be either the d- or q-axis PM flux linkage  $\lambda_{PM-d}$ ,  $\lambda_{PM-q}$ , the magnetizing inductances  $L_{dm}$ ,  $L_{qm}$ , the slot leakage inductance  $L_s$  or the cross coupling inductance  $L_{dq}$  of the  $i^{th}$  corner machine. The so computed correction factors are then extended to the entire design plane  $sr - mr$  using a linear interpolation, allowing the adjustment of the magnetic model. By doing so, the cross-coupling terms ( $L_{dq}$  and  $\lambda_{PM-d}$ ) are taken into account within the design workflow and the mismatches between analytical and FE-computed magnetizing inductances and q-axis PM flux are greatly reduced as shown in Fig. 3.11. The good agreement in terms

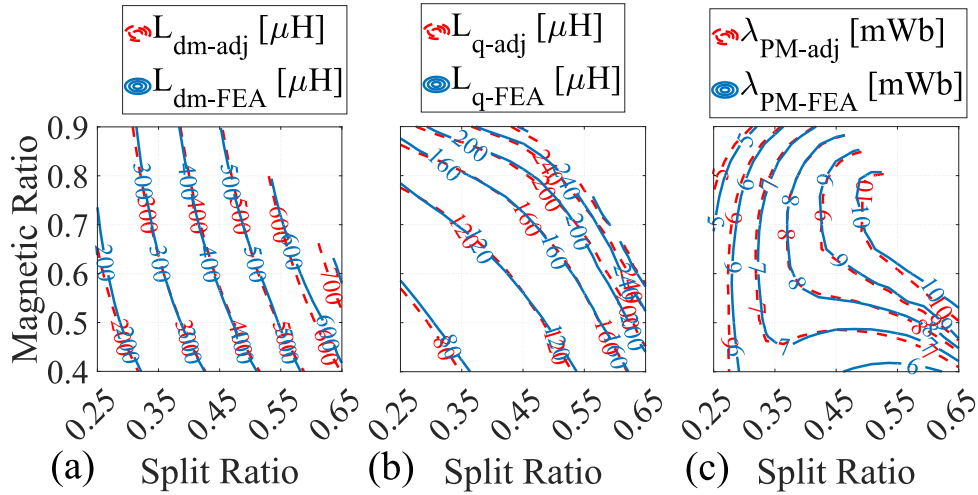


Figure 3.11: Comparison between the adjusted estimation and FE-computation of a) d-axis inductance, b) q-axis inductance and c) PM flux linkage at 80 krpm.

of d- and q-axis inductances and PM flux linkage leads to the excellent matches between the adjusted torque and internal power factor contours shown in Fig. 3.12.

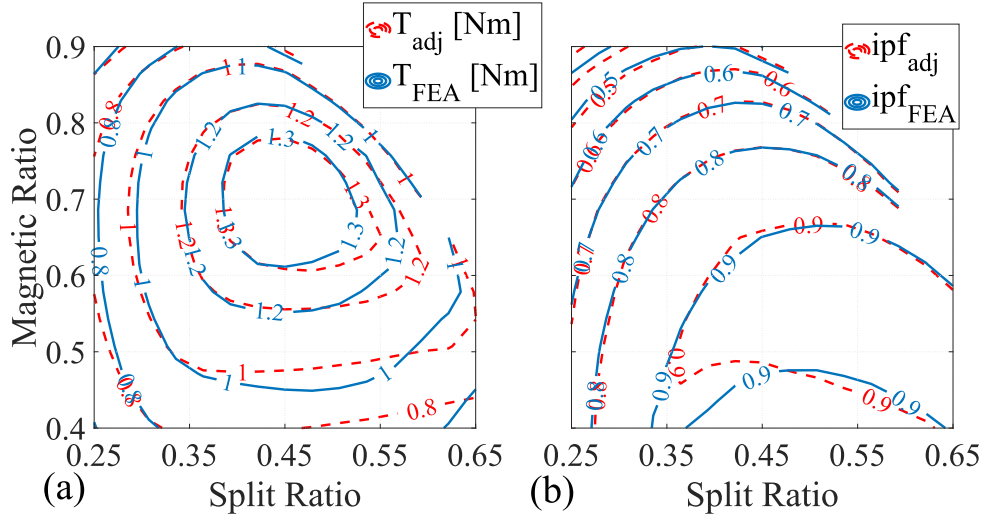


Figure 3.12: Comparison between the adjusted estimation and FE-computation of a) Torque, b)  $ipf$  at 80 krpm.

### 3.4 Preliminary design considerations

The reduction of the design space to only two variables ( $sr$ ,  $mr$ ) and the accurate calculation of torque and power factor as their function greatly reduce the design complexity. Indeed, the selection of the machine to be considered for the final design refinements (needed prior the prototyping) is greatly simplified. The choice of the final design is not univocal and clearly depends on the application requirements, e.g. the performance indexes having the priority (e.g. maximum torque, maximum power factor, minimum PM volume, etc.). In the following, the contours of the variables influencing mostly torque and power factor are analysed in order to infer the different trade-offs involved when designing high speed PMSyR machines.

Fig. 3.13a, b and c report the constant loci in the  $sr - mr$  plane of total torque, PM torque and reluctance torque component, respectively. The total torque contours and so the location of the maximum torque design (showed with the marker ■) depend on the concomitant actions of the reluctance and PM torques. Fig. 3.13d, e and f show the contours of the variables defining the reluctance torque behaviour, namely the d- and q-axis currents and the inductances difference, respectively. It can be seen that the reluctance torque, and the location of the maximum reluctance torque design in the  $sr - mr$  plane, is the compromise between the need of maximizing the magnetizing current ( $i_d$ ), the anisotropy ( $L_d - L_q$ ) and the quadrature current

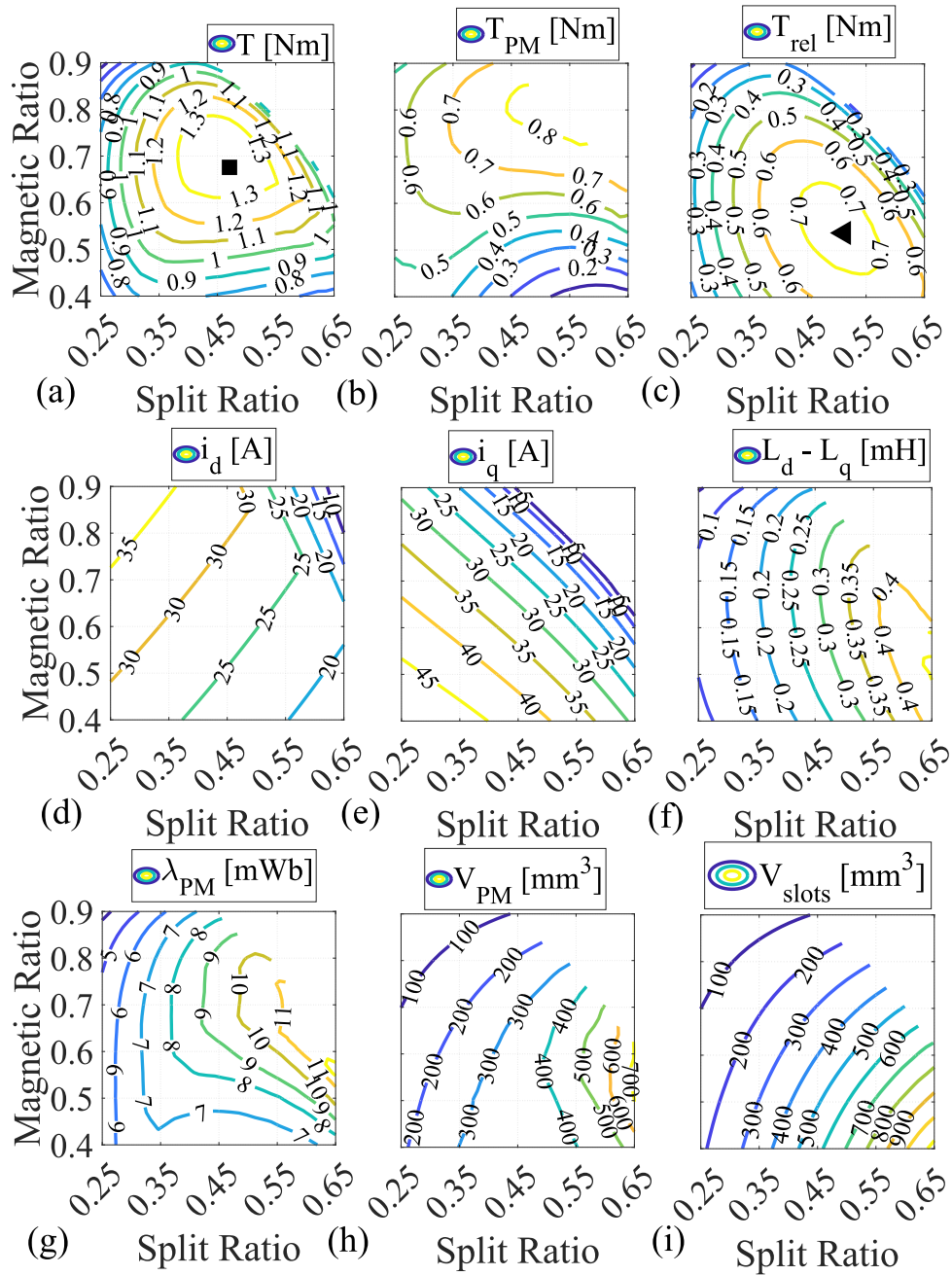


Figure 3.13: Constant loci contour plot of a) total torque, b) PM torque, c) reluctance torque, d)  $i_d$ , e)  $i_q$ , f)  $L_d - L_q$ , g) PM flux, h) PM volume and i) Needed PM volume.

( $i_q$ ) [27, 108].

The shape of the PM torque component contours depends on both d-axis current (Fig. 3.13d) and PM flux linkage (Fig. 3.13g). The latter is heavily affected by the amount of PM material imposed by the selected PM design criterion, as it can be seen comparing subfigures 3.13g and 3.13h. The PM volume  $V_{PM}$  is also affected by the maximum available space within the rotor

flux barriers ( $V_{slots}$ ), shown in Fig. 3.13i.

Fig. 3.14a and 3.14b report the internal power factor of the PMaSyR machine and the respective value obtained without the PM assistance, respectively. Although the PM-assistance greatly improves the internal power factor respect to the pure reluctance machines, only part of the design plane  $sr - mr$  provides the target internal power factor (i.e. 0.9). For some region

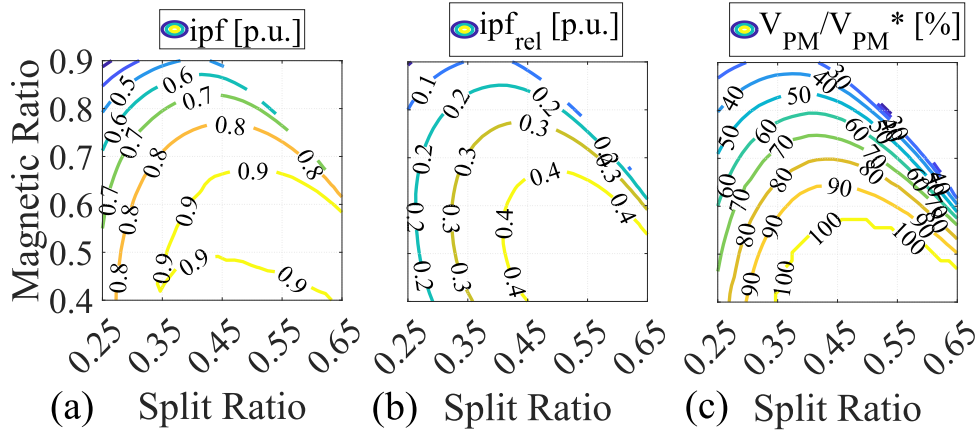


Figure 3.14: Constant loci contour plot of a)  $ipf$  and b)  $ipf_{rel}$  reluctance component and c) ratio between actual PM volume and needed one.

of the design plane, the PM volume required ( $V_{PM}^*$ ) to satisfy the selected design criterion exceeds the available space within the rotor flux barriers. Fig. 3.14c reports the ratio between the effectively used PM volume and the ideally required value justifying this unexpected behaviour. In particular, the  $ipf$  values differ from the target one when designing machines with high magnetic ratio and low split ratio, as shown in Fig. 3.14a. Indeed, higher  $mr$  implies a higher thickness of the flux guides which reduces the flux barriers radial thickness ( $h_a^i$ ) and so the available space for the PMs. Similarly, lower  $sr$  implies a reduction of the rotor diameter and so also of the flux barriers area.

Lastly, Fig. 3.15 shows the percentage difference between the module of the total flux and its d-axis components with respect to the latter. This figure of merit quantifies the approximation related to the assumption of neglecting the PM flux during the design of the stator tooth, yoke and rotor flux guides thicknesses. Analysing this figure, it is straightforward to conclude that the PM effect can be surely neglected during the magnetic design of the stator and rotor laminations.

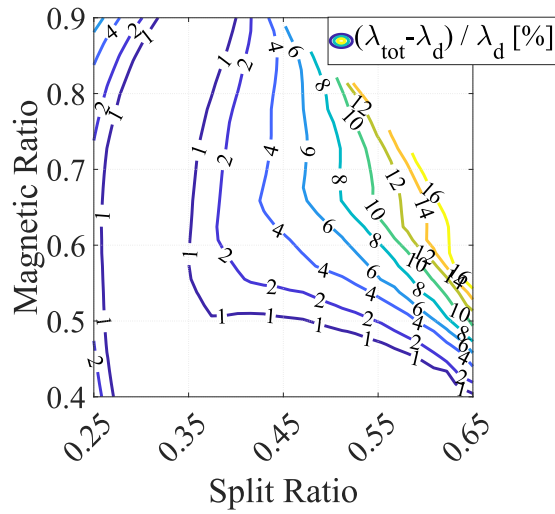


Figure 3.15: Constant loci contour plot of the percentage difference between the module of the total flux and its d-axis components (in p.u. of the total flux).

However, this does not imply that the PM presence should not influence the selection of the final machine. For example, selecting the design providing the maximum reluctance torque (shown with  $\blacktriangle$  in Fig. 3.13c) and adding the PM within the rotor slots (according to a certain criterion) would lead to a sub-optimal design. In fact, the resulting machine would produce a lower torque (1.1 Nm in this case) compared to the maximum torque design calculated considering both PM and reluctance components (1.4 Nm showed with  $\blacksquare$  in Fig. 3.13a).

### 3.5 Effects of PM insertion at increasing speed

The proposed approach has been used to design several PMaSyRMs with increasing maximum speed without and with the permanent magnet assistance. In particular the two most common magnet families have been investigated considering a neodymium-based PM (N42UH) and ferrite one (35H). These three classes of machines will be hereafter called SyR, NDaSyR and FEaSyR, respectively. Table 3.1 lists the main constraints and assumptions of this design exercise, while Table 3.2 reports the main characteristics of the selected PM materials.



Table 3.2: PM characteristics

PM material	Mass Density [kg/m <sup>3</sup> ]	T [deg]	$B_{rem}$ [T]
F35H	4600	100	0.38
N42UH	7500	100	1.22

### 3.5.1 Torque

Fig. 3.16 reports the iso-torque loci ( $T$ ) in the  $sr - mr$  plane for 3 mechanical speeds (40, 80 and 120 krpm) and different PM-assistance. The black markers  $\bullet$ ,  $\blacktriangleright$ ,  $\blacksquare$  represent the locations of the

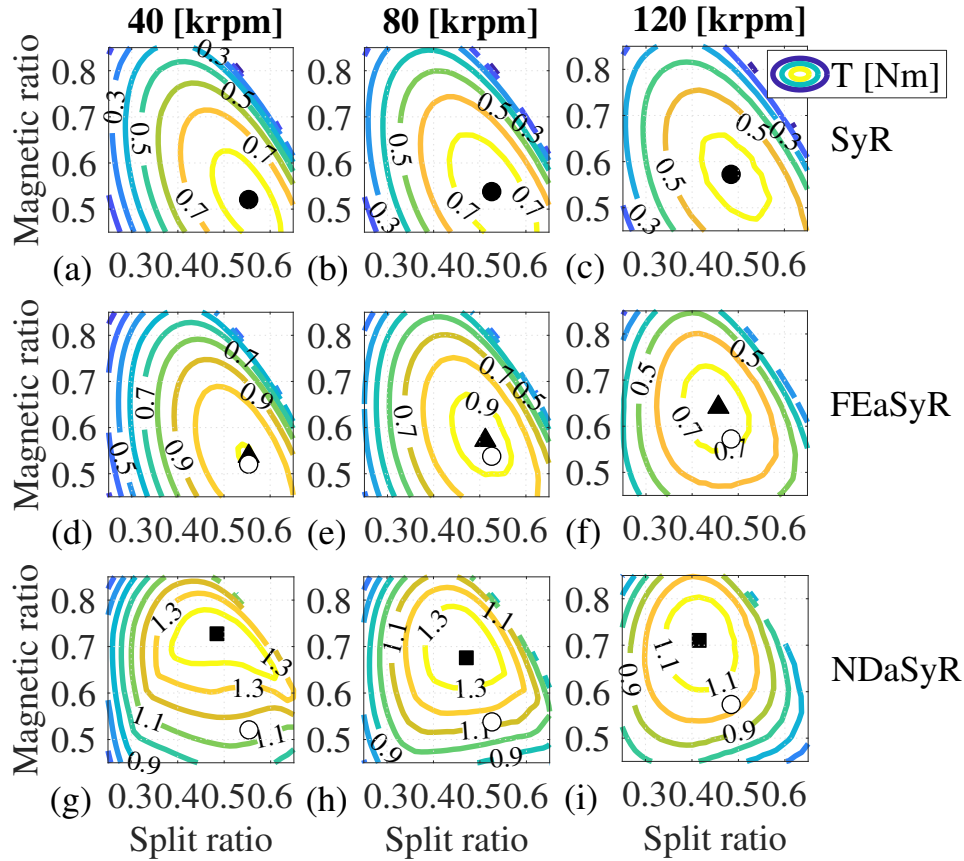


Figure 3.16: Torque function of split and magnetic ratio obtained considering three maximum speeds (40, 80, 120 krpm) for the pure SyRM and for the versions assisted by NdFeB and Ferrite magnets.

maximum torque designs for the SyR, FEaSyR and NDaSyR respectively. The white markers  $\circ$  in the FEaSyR and NDaSyR graphs are the respective maximum reluctance torque designs. For a given maximum speed, the torque contour and so the maximum torque design location



obtained using ferrite magnets do not significantly deviate from the pure SyR one. On the contrary, the constant torque loci of the NDaSyRMs are remarkably different from the respective baseline SyR designs. In particular, the maximum torque designs tend to move towards lower split ratio and higher magnetic ratio with respect to the position of the respective maximum reluctance solutions.

In order to justify this behaviour, the torque components and the main variables affecting their trends are investigated. Fig. 3.17 and Fig. 3.18 depict the reluctance ( $T_{rel}$ ) and the PM torque ( $T_{PM}$ ) contours of FE- and ND-assisted machines along with the location of the maximum PM, reluctance and total torque designs. As expected, both torque components decrease as the speed increases due to the thicker structural ribs. The reluctance torque decreases due

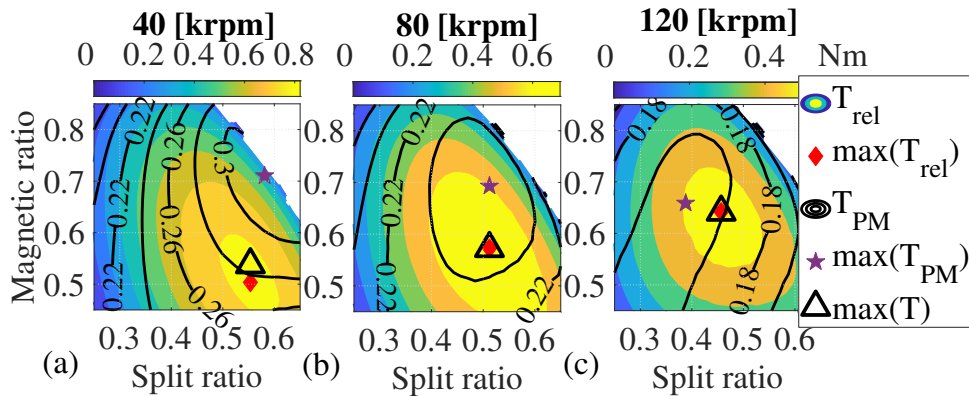


Figure 3.17: Reluctance ( $T_{rel}$ ) and PM ( $T_{PM}$ ) torque components of the FEaSyRMs as function of both design variables for three different speeds and locations of the maximum reluctance, PM and total torque designs.

to the higher q-axis inductance while the PM torque decreases due to the higher rotor PM flux leakage. The rate of these two decrements depends on how the rib dimensions and their saturation levels change with the speed. Both quantities depend on the PM types: the rib dimension are affected by the PM mass density, while the rib saturation is affected by the PM residual flux density. From Fig. 3.17 and 3.18 it can be deduced that the reluctance torque shows the same qualitative trends within the design plane as the maximum speed increases for both PM types. On the contrary, the PM torque component shows a completely different behaviour according to the magnet type. The higher PM torque featured by the NDaSyR machines along

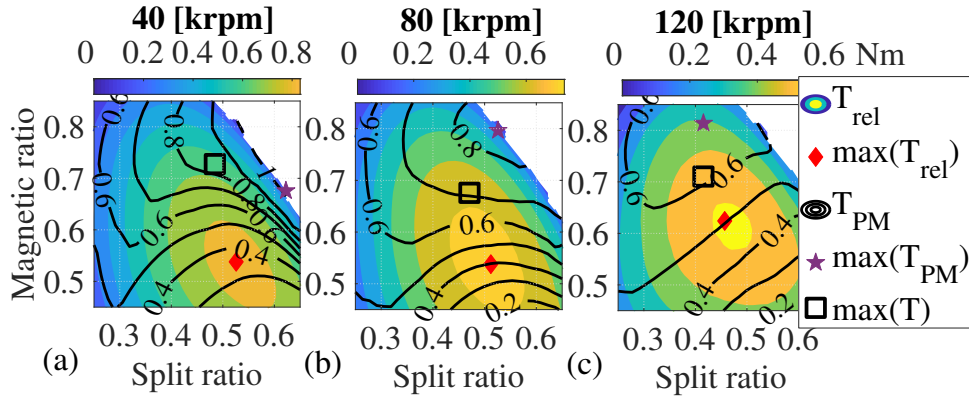


Figure 3.18: Reluctance ( $T_{rel}$ ) and PM ( $T_{PM}$ ) torque components of the NDaSyRMs as function of both design variables for three different speeds and locations of the maximum reluctance, PM and total torque designs.

with its different contour shape compared to the FEaSyR ones make the total torque contour of NDaSyRMs more affected by the PM-assistance. As a consequence, the maximum torque design when adopting high energy density PM differs from the pure reluctance one and is the compromise between these two torque components. This is clearly evident at 80 krpm and 120 krpm (Fig. 3.18) while it is not immediate for the 40 krpm case because the PM torque features almost the same maximum value (1 Nm) for several combination of  $sr$  and  $mr$  of the top right of the design plane.

### 3.5.2 PM torque

The PM torque contours are determined by the d-axis current (independent from the PM material) and by the PM flux linkage ( $\lambda_{PM}$ ). The latter depends on the rotor geometry and PM design criterion which in this case is the achievement of a target internal power factor  $ipf^* = 0.9$ . Adopting this criterion, the PM flux linkage (and so the PM volume  $V_{PM}$ ) is a nonlinear function of both d- and q-axis inductances, current components and target  $ipf^*$  as in (3.16).

The amount of PM ( $V_{PMs}$ ) required to achieve the desired power factor may exceed the available space within the rotor flux barriers ( $V_{slots}$ ) if low energy density magnets are adopted or if the target speed is very high (or both); consequently, in such cases, the PM volume would equal the available rotor barriers volume. Fig. 3.19 reports the PM torque, PM flux linkage, PM

volume and available rotor barriers volume in the design plane  $sr - mr$  when considering a maximum speed of 80 krpm for both PM types. It can be clearly seen that the PM volume of the

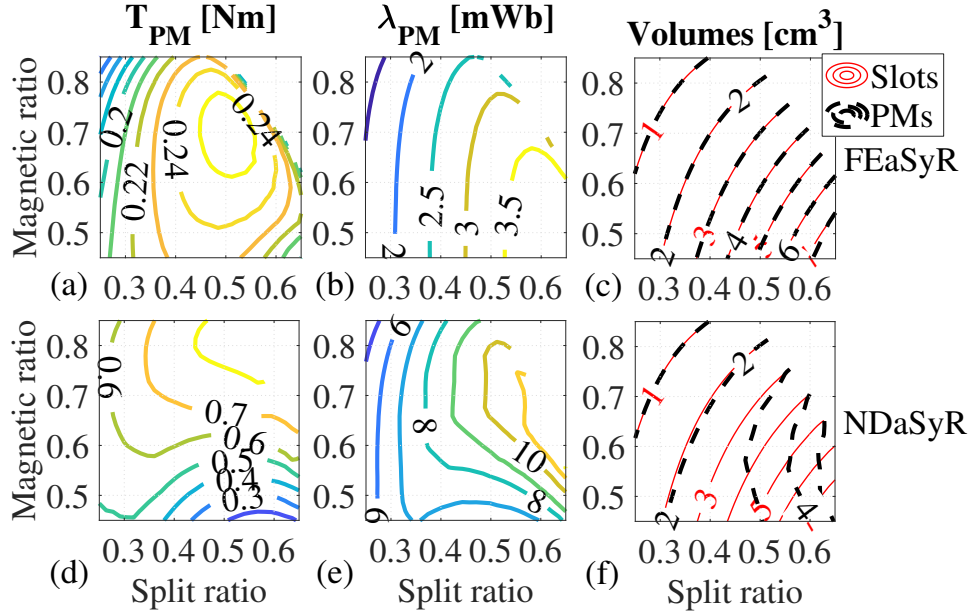


Figure 3.19: PM torque (a, d), PM flux linkage (b, e), PM volume and rotor slot volume (c, f) contours in the  $sr - mr$  plane when the maximum speed is 80 krpm for both FE- and ND-assisted machines.

FEaSyRMs (Fig. 3.19c) equals the available rotor barriers space for the considered maximum speed.

On the contrary, neodymium based PM allows satisfying the power factor target without exceeding the available space for most of the design plane (Fig. 3.19f). This justifies the different behaviour of the PM flux, and PM torque, featured by the FE- and ND-assisted machines in the design plane  $sr - mr$ . Indeed, the PM flux linkage contours of the FEaSyRMs follow the trends imposed by the geometrical constraint of the maximum available space within the rotor barriers, while the NDaSyRMs one follow the trends dictated by the PM design criterion.

### 3.5.3 Reluctance torque

The comparison between the PM-assisted machines and the pure reluctance ones designed for the same maximum speed shows how the adoption of low energy density PM is not convenient

also in terms of reluctance torque. The ratio  $k_{Trel}$  between the reluctance torque of the PM-assisted machines and the torque of the respective SyRMs (i.e. having equal maximum speed and  $sr, mr$ ) is higher when adopting neodymium based PM, as shown in Fig. 3.20a and d for the 80 krpm designs. The reluctance torque ratio between the PM-assisted machines and the pure SyR ones depends on both iron rib dimensions and their saturation levels. The ferrite magnet features a mass density lower than the neodymium one (4600 vs 7500 kg/m<sup>3</sup>) which implies a lower increment of the iron rib dimensions with respect to the pure SyRMs. Indeed, the ratio between the average rib sizes ( $k_{ATR}$ ) of the PMA SyRMs with respect to the SyRMs, shown in Fig. 3.20b, d) is lower for FEaSyR for a given point in the plane  $sr - mr$ . Consequently,

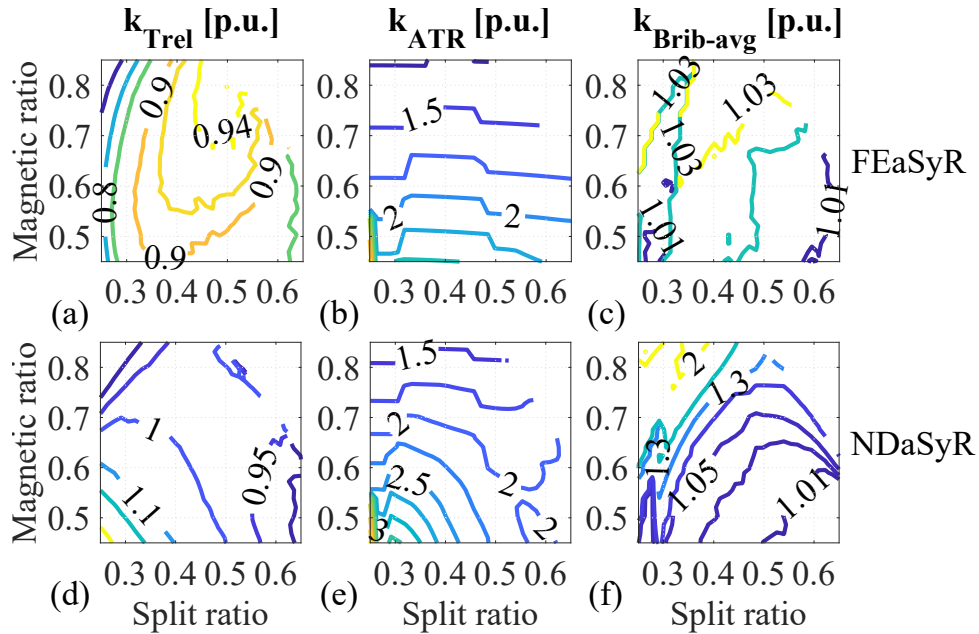


Figure 3.20: Reluctance torque ratio (a, d), average total rib ratio (b, e), average ribs saturation ratio (c, f) contours in the  $sr - mr$  plane when the maximum speed is 80 krpm for both FE- and ND-assisted machines.

one would expect the FEaSyRMs to produce higher reluctance torque being smaller the iron rib dimensions. However, when adopting ferrite magnets, the iron ribs saturation is much lower than the neodymium PM one, as shown in Fig. 3.20c, f) in terms of ratio of the average flux density of the iron ribs. A lower saturation level implies a higher q-axis flux short-circuited by the iron ribs which in turn determines a higher torque drop. It can be concluded that, although the neodymium-based PMs require bigger iron ribs, they allow to achieve higher rib saturation,

therefore the reluctance torque of NDaSyRMs features a lower decrement as the speed increases compared to the FEaSyRMs.

### 3.5.4 Internal power factor

Fig. 3.21 shows the internal power factor contours for the considered designs. The PM assistance allows increasing this performance index but the target value (0.9) is not achieved for all the solutions of the design plane  $sr - mr$ . As the design speed increases, the iron rib dimen-

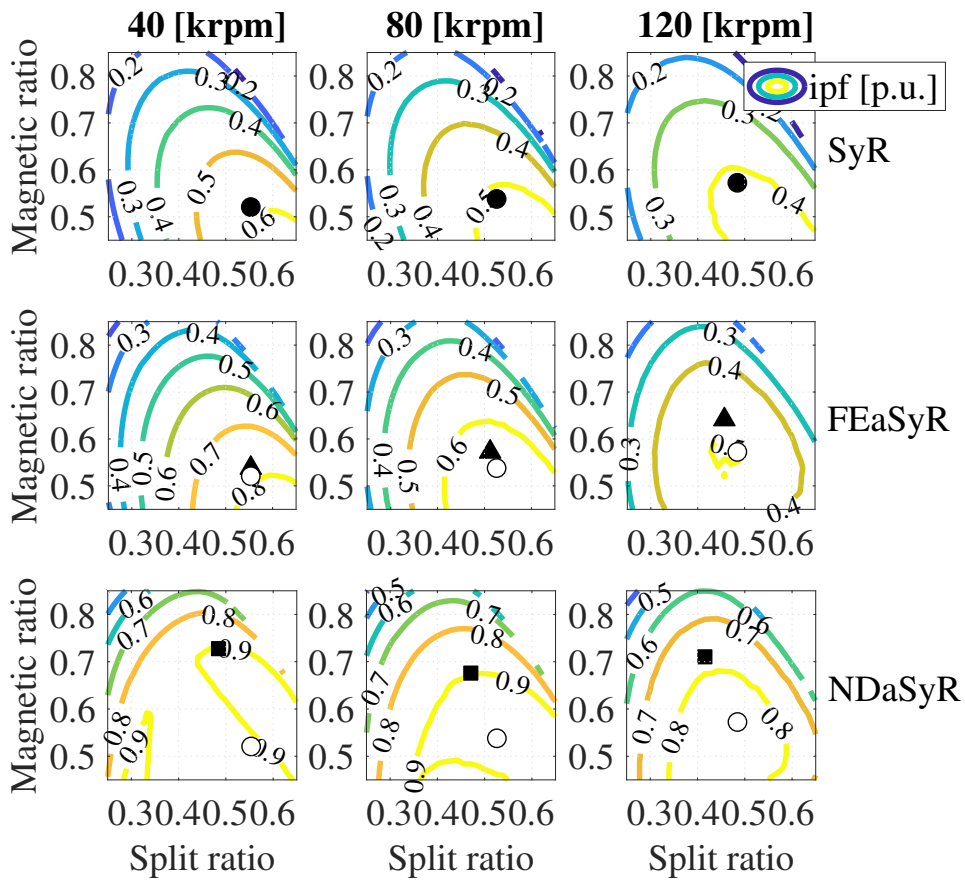


Figure 3.21: Internal power factor contour in the  $sr - mr$  plane for three different maximum speeds (40, 80, 120 krpm) for the pure SyR and the two PM-assisted versions.

sions increase and this has the twofold effect of worsening the q-axis inductance and reducing the rotor flux barriers area that can accommodate the PM material. In turn, the increment of the q-axis inductance implies that more PM volume is needed to achieve the target power factor. Therefore, the required amount of PM increases with the speed while the available space

decreases. When ferrite magnets are adopted, the target  $ipf$  is not reached for none of the considered speeds: in fact, the ratio between the PM volume ( $V_{PM}$ ) and the required one ( $V_{PM}^*$ ), shown in Fig. 3.22, is always lower than one. On the contrary, when using the NdFeB magnets the target power factor is achieved by part of the solutions in the design plane  $sr - mr$ . The

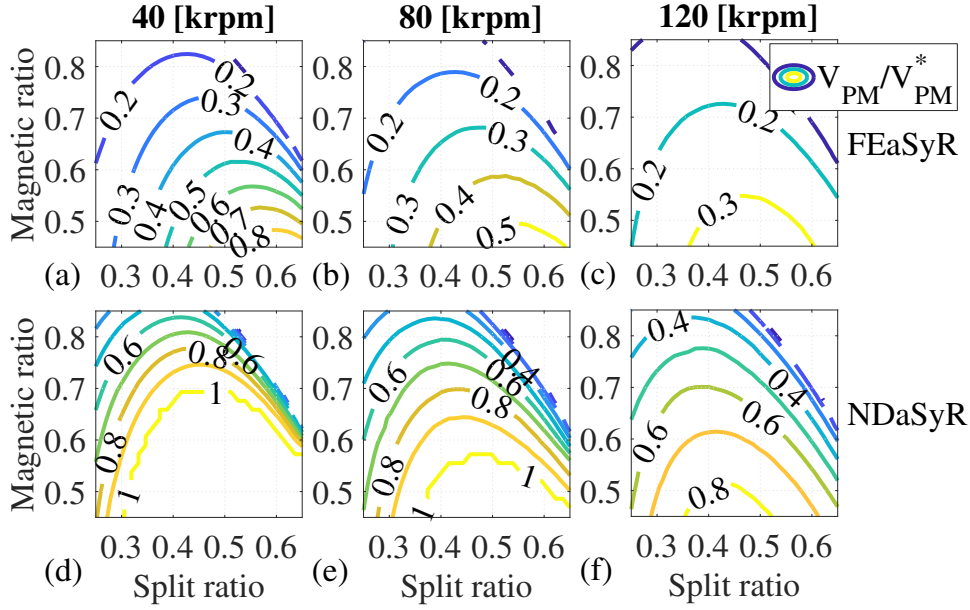


Figure 3.22: Ratio between the PM volume ( $V_{PM}$ ) and its required value ( $V_{PM}^*$ ) as function of both design variables for three different speeds and for both PM materials.

designs featuring an  $ipf = 0.9$  correspond to the solutions having the ratio  $V_{PM}/V_{PM}^* = 1$ . The deviation of the  $ipf$  from the target is proportional to the volume ratio  $V_{PM}/V_{PM}^*$ .

### 3.6 Performance boundaries

Fig. 3.23 reports torque and internal power factor of the maximum torque designs (identified by the black markers in Fig. 3.16 and 3.21) as a function of the speed obtained after accurate FEA. As expected, the PM-assistance enhances both performance indexes and the biggest improvement is obtained using high energy density PMs. With neodymium based magnets, the target  $ipf$  (0.9) can be achieved up to a certain speed (80 krpm in this case) above which it rapidly decreases reaching 0.7 at 140 krpm. The  $ipf$  of the optimal FEaSyRMs is relatively high at low speed ( $\approx 0.8$ ) and constantly decreases with the speed until it reaches a value similar to the one

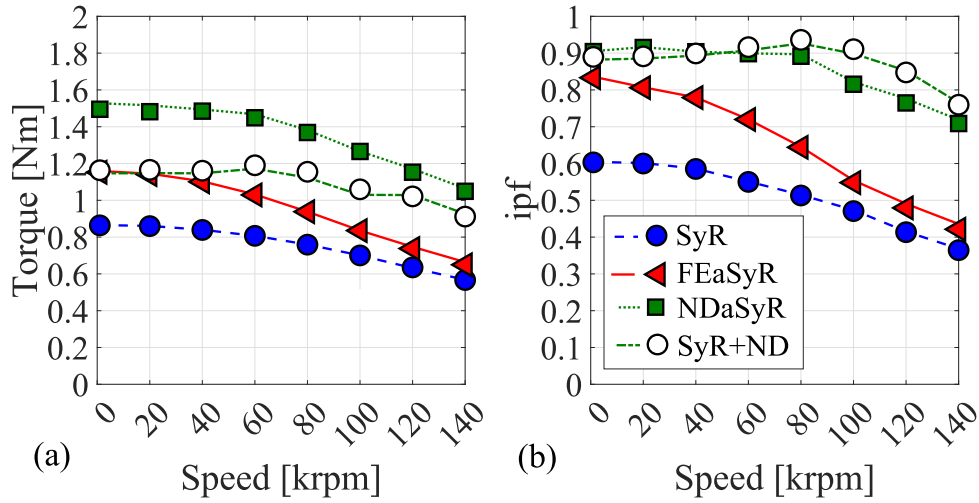


Figure 3.23: Torque (a) and internal power factor (b) as a function of the speed of the selected designs.

featured by the optimal SyR design ( $\approx 0.4$ ) at 140 krpm.

With the adopted PM design criterion, the NDaSyR machines feature an almost doubled torque with respect to the SyRMs for all the considered speed values. Instead, the FEaSyRMs show a lower torque improvement, e.g. around 30% at low speed and 5% at maximum speed, as reported in Fig. 3.23a.

Along with the pure SyR designs and both PM-assisted variants, Fig. 3.23 also shows the performance of the PMSyR machines obtained adding the neodymium based-PM to the maximum reluctance torque design (shown with the white markers  $\circ$  in Fig. 3.16 and 3.21). These sub-optimal designs, hereafter called SyR+ND, feature power factors similar to those obtained by the optimal NDaSyRMs but with a considerable lower torque (30% lower for the lowest speed design and 5% for the highest one).

Fig. 3.24 depicts the torque components of all the considered designs as function of the speed. While the PM torque ( $T_{PM}$ ) of optimal FEaSyR and NDaSyR machines decreases with the speed, their reluctance torque ( $T_{rel}$ ) shows a different behaviour. Indeed, the reluctance torque component of all PMSyRMs is lower than the torque of the optimal SyRM designed for the same speed. In particular,  $T_{rel}$  decreases with the speed for FEaSyRMs whereas, for NDaSyRMs it is almost constant up to 80 krpm and then reduces reaching 0.45 Nm at 140



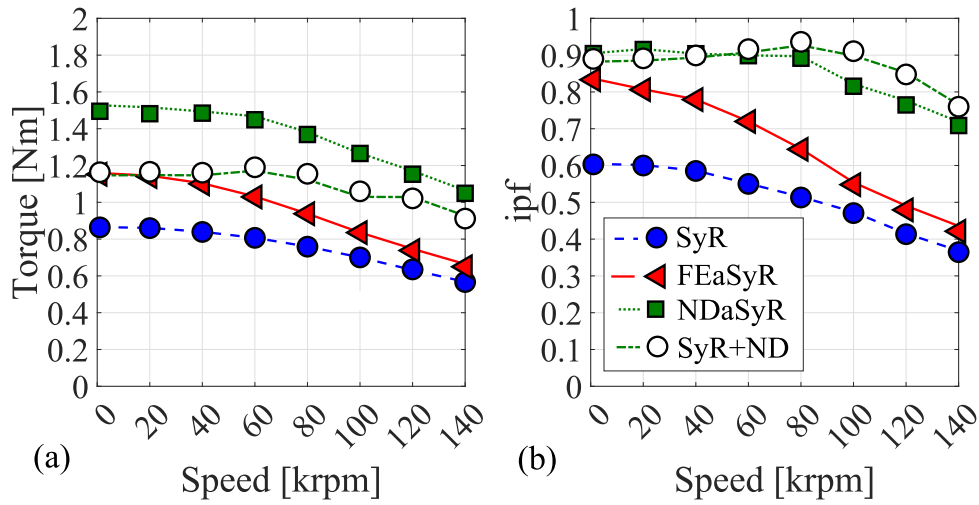


Figure 3.24: Permanent magnets (a) and reluctance (b) torque components of the selected machines as function of the speed.

krpm. This behaviour is due to two effects: the lower reluctance torque reduction with the speed of the NDaSyRMs as explained in Section III-C and the fact that the distance between the maximum total torque design and reluctance torque design decreases as the speed increases (see markers in Fig. 3.16g,h,i). It is worth highlighting that the sub-optimal designs SyR+ND feature a higher  $T_{rel}$  and a lower  $T_{PM}$  compared to the optimal NDaSyRMs.

Fig. 3.25 reports the mechanical power of all the considered optimal and sub-optimal solutions as function of the maximum design speed. Along with the previous considerations, it is worth to underline that the insertion of PMs within the rotor flux barrier is always beneficial within the considered speed range.

### 3.7 Analysis of the optimal machines

Fig. 3.26 shows the trends of  $sr$  and  $mr$  of the optimal SyR, FEaSyR, NDaSyR designs as function of the speed. The design variables of the sub-optimal SyR+ND solutions are also reported and obviously they correspond to SyRMs ones; in fact, their geometries differ from the pure SyR designs only in terms of rib dimensions and PMs. Fig. 3.27 reports the cross sections of these four classes of machines at 40, 80 and 120 krpm. The optimal split ratio always decreases with the speed with and without PM assistance and whatever type of PM. Indeed, the



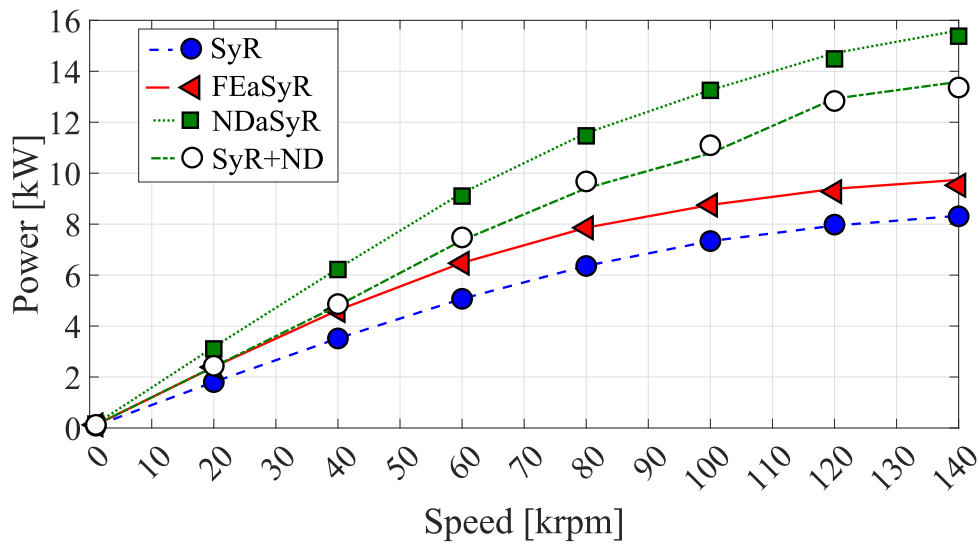


Figure 3.25: Power as a function of the speed of the selected designs.

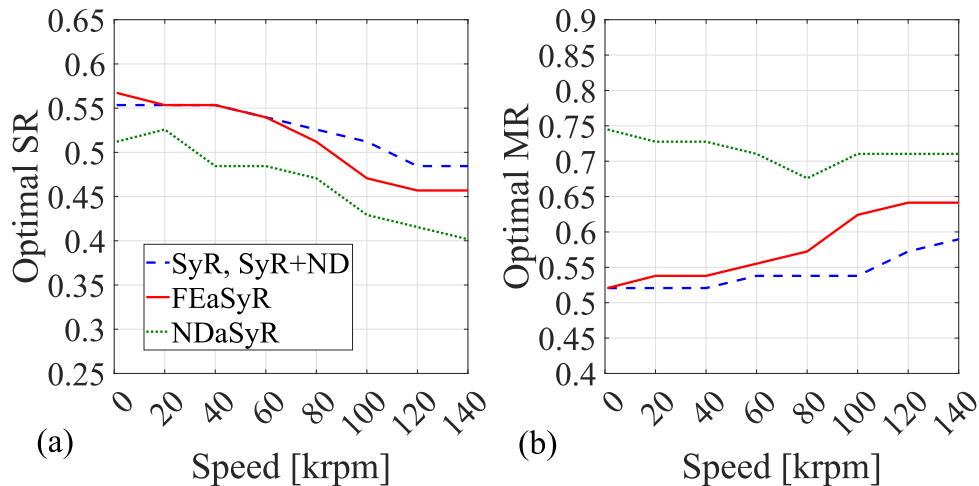


Figure 3.26: Design variables  $sr$  (a) and  $mr$  (b) of the optimal SyR, FEaSyR and NDaSyR machines as function of the speed.

designs showing the highest PM and reluctance torques (markers  $\star$ ,  $\blacklozenge$  in Fig. 3.19, 3.20) have a decreasing split ratio as the speed increases. Lower  $sr$  implies lower centrifugal force which in turn reduces the iron ribs increment and so the reluctance torque drop. Although lower  $sr$  implies lower PM flux linkage (due to the lower PM amount, see Fig. 3.19), the PM torque component increases because the d-axis current increases in the same direction. Another interesting point to underline is that the optimal NDaSyRMs have a lower rotor diameter with respect to SyR and FEaSyRMs. This is due to both higher mass density of the neodymium compared to the ferrite and different contour shapes of the PM torque component for NDaSyRMs and

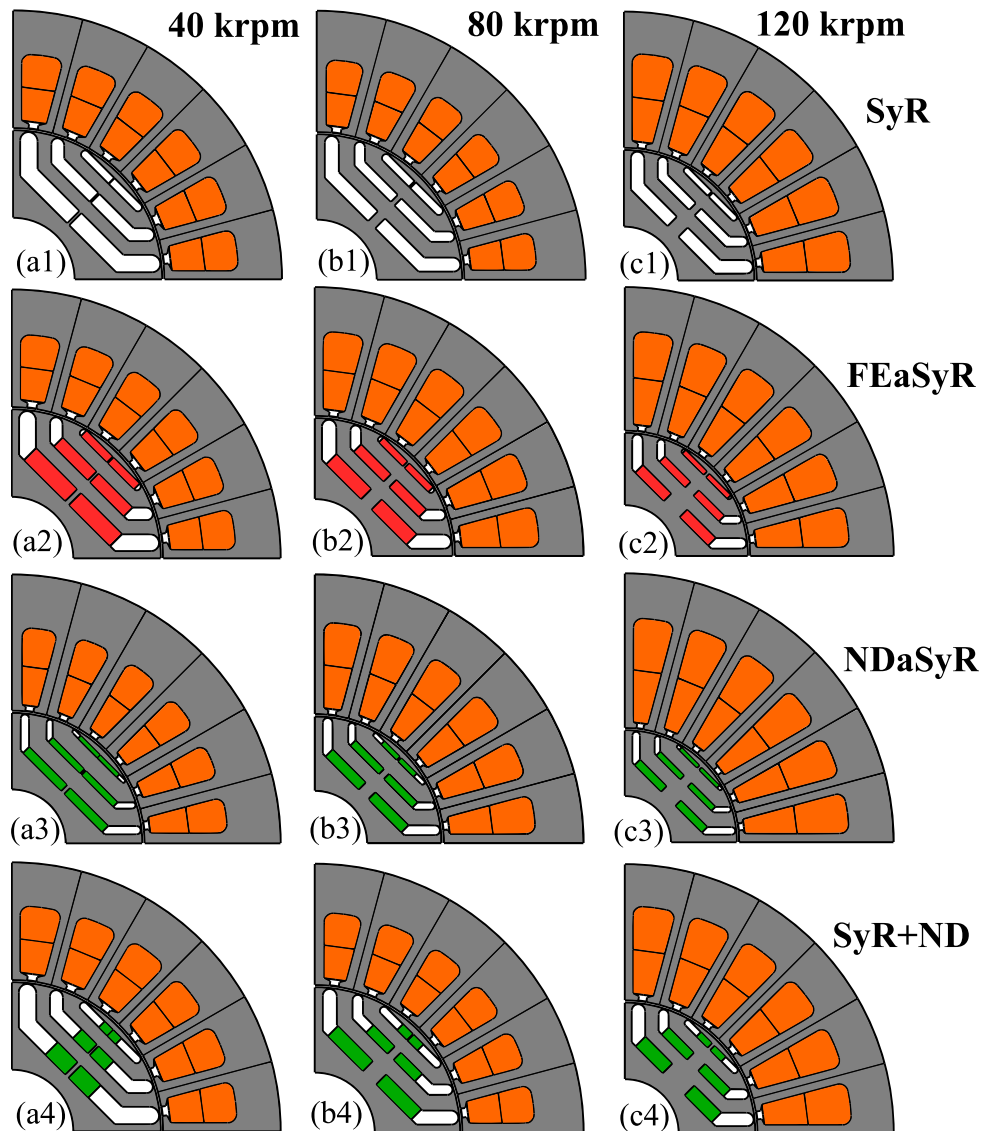


Figure 3.27: Cross section of the optimal SyR, FEaSyR and NDaSyR machines and sub-optimal SyR+ND designs at 40, 80 and 120 krpm.

FEaSyRMs.

The optimal magnetic ratio of the SyR and FEaSyR designs tends to increase with the speed because the reluctance torque, which is the main component, increases in the same direction (as shown in Fig. 3.17). On the contrary, the NDaSyRMs feature an almost constant trend of  $mr$  (higher than the FEaSyR one) because the PM torque (which increases with  $mr$ ) plays a major role in defining the overall torque (Fig. 3.18). It is then possible to conclude that the optimal NDaSyRMs feature a lower rotor diameter and bigger stator tooth, stator back iron and rotor

flux guides with respect to FEaSyRMs, as it can be seen from Fig. 3.27. Finally, it is worth noticing that above a certain speed (40krpm in this case), the sub-optimal designs SyR+ND make use of more PM material compared to the optimal NDaSyRMs, as shown in Table 3.3.

It is worth to underline that also the manufacturing issues and the demagnetization risk, which have not been considered within the analysis, could constitute a criterion of selection of the "optimal design" to be prototyped.

Table 3.3: PM volume ( $V_{mag}^*$ ) of the selected designs [ $\text{cm}^3$ ]

Speed [krpm]	FEaSyR	NDaSyR	SyR+ND
<b>40</b>	5.8	2.6	2.6
<b>80</b>	4.3	2.6	3.4
<b>120</b>	2.7	1.8	3.2

### 3.8 Insight: PM design criteria comparison

In the last sections, only the *ipf target* criterion has been investigated. In this section, the tool is used to compare the aforementioned PM sizing approaches considering a wide range of operating speed. Particular attention will be posed to the implications of each design criterion in terms of performance and machines geometries.

#### 3.8.1 Performance vs speed analysis

The aforementioned procedure is applied to design PMaSyRMs with operating speeds in the range [1 - 120] krpm considering the three design criteria: *Natural compensation*, *Target ipf* and *Maximum torque*. The goal of this design exercise is to compare the optimal results in terms of performance and geometries. In particular, the workflow of the last section has been adopted and it is here briefly re-called:

1. for each considered speed and PM insertion criterion, the proposed hybrid design routine is applied and the torque and ipf contours in the plane  $sr - mr$  are evaluated;

2. the average torque is chosen as main performance index and the maximum torque solution is selected from the design plane  $sr - mr$ ;
3. once point 1 and 2 have been performed for each speed, the three different PM design criteria are compared in terms of output power, torque and power factor, optimal design variables and optimal geometries versus the rotational speed.

Fig. 3.28 reports the torque (a) and the internal power factor (b) as a function of the speed for the *Natural compensation* (solid line), *Target ipf* ( $ipf^* = 0.8$  dashed line) and *Torque maximization* (dotted line) cases.

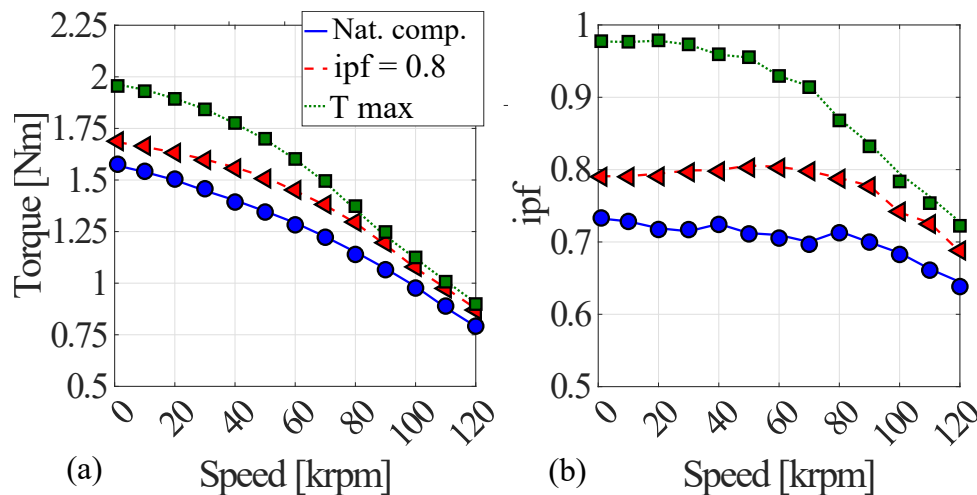


Figure 3.28: Torque (a) and ipf (b) versus speed of the maximum torque designs

As expected, the adoption of the *Torque maximisation* criterion provides the highest torque and power factor up to 80 krpm. Indeed, above these speeds the *Target ipf* criterion basically provides the same results. This behaviour can be explained by geometrical considerations: the available space for the PMs placement decreases with speed due to the iron ribs increment; it follows that the amount of PMs required to reach a predefined  $ipf$  will coincide with the full barrier dimensions as for the *Torque maximization* criterion. The *Natural compensation* criterion leads to the lowest performance. The considerations regarding the torque trends can be fully extended to the power ones, as in Fig. 3.29 which reports the power as function of the speed. Although the 3 criteria lead to different performances, they share the value of threshold

speed (i.e. 100 krpm) above which the output power cannot be enhanced by further increasing the speed.

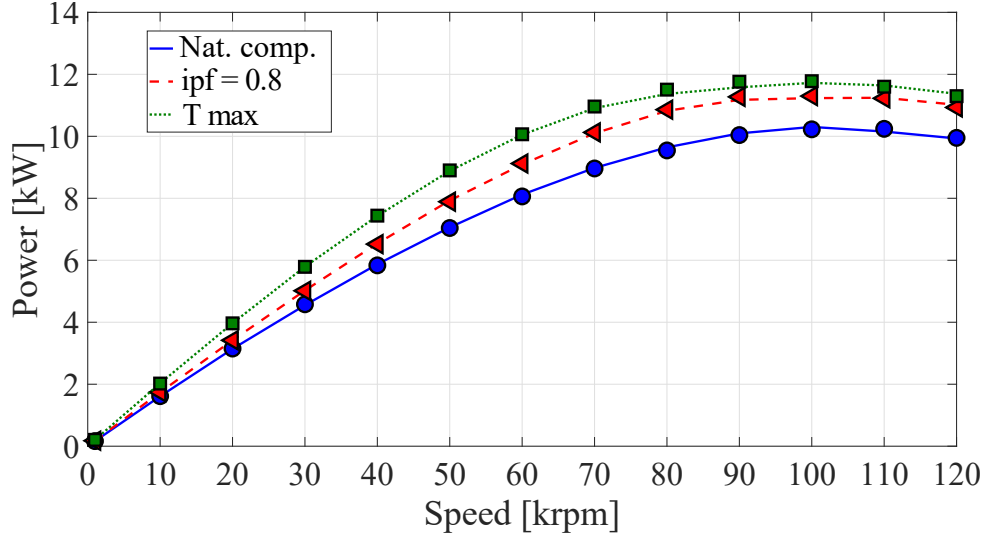


Figure 3.29: Maximum power as function of the speed.

The above performances are clearly influenced by the selected criterion which in turn modifies the shape of the torque contour plot in  $sr - mr$  plane. It follows that the position in such plane of the machine which maximizes the torque for a given design speed will change according to the amount of PMs inserted within the rotor barriers. Fig. 3.30a,b show the trends of the optimal (torque wise) design variables  $sr$  and  $mr$  as function of the speed for the 3 considered scenarios. When the *Natural compensation* or the *Target ipf* criteria are adopted, the optimal split ratio does not change significantly with the speed (solid blue and dashed red lines) while it decreases when the flux barriers are filled by PMs (dotted green line). In a dual way, the optimal magnetic ratio of the *Torque maximization* criterion remains almost constant with the speed whereas the other two cases feature an optimal  $mr$  which clearly reduces as the speed increases.

The trends of the optimal  $sr$  and  $mr$  lead to the machine cross-sections reported in Fig. 3.30c,d,e. Since the magnetic ratio in the *Natural compensation* and *Target ipf* criteria decreases with the speed, the respective rotor designs are characterized by increasing flux barriers height while the teeth width decreases with the speed. Conversely, the *Torque maximization* criterion

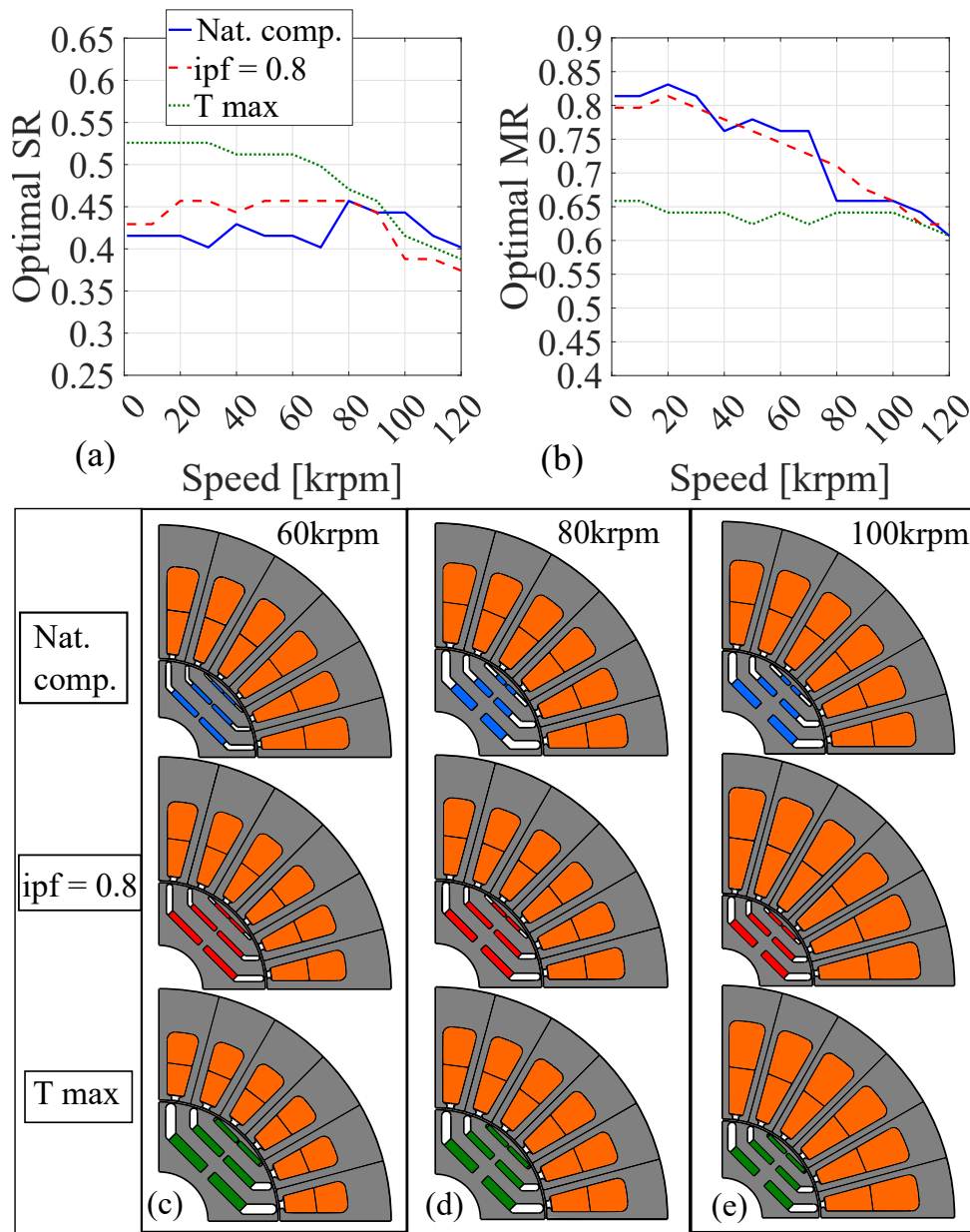


Figure 3.30: Optimal split (a) and magnetic (b) ratios as function of the speed; cross sections of the optimal machines at 60 krpm (c), 80 krpm (d) and 100 krpm (e) for the 3 considered scenarios.

allows to obtain almost the same flux barriers height and teeth width whatever speed value is considered.

### 3.8.2 sr-mr plane considerations

The reason behind the different trends of  $sr$  and  $mr$  which modify the machine geometry can be partially explained analysing the torque components contours in the design plane for a given

operating speed. Fig. 3.31 reports the total torque along with its PM and reluctance components for the three considered design criteria at 60 krpm; the following considerations can be drawn.

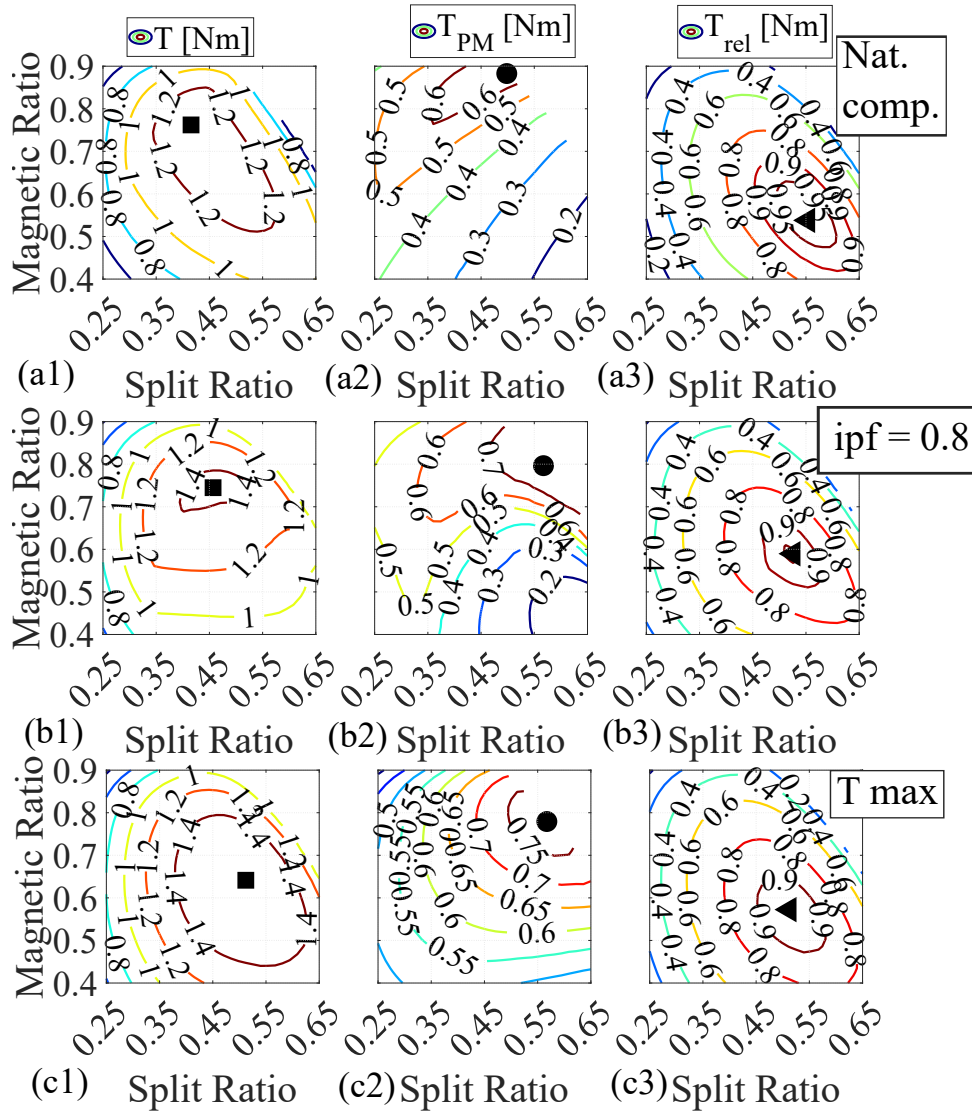


Figure 3.31: Total torque (a), PM torque (b) and reluctance torque (c) for Natural compensation (1), Target ipf (2) and Torque maximization (3) design criteria at 60 krpm.

- The reluctance torque  $T_{rel}$  (shown in Fig. 3.31a3, 3.31b3 and 3.31c3) is poorly affected by the adopted PM design criterion. Its contour shapes are similar in the three cases and the maximum of this torque component is obtained for low values of  $mr$  and high values of  $sr$  (according to the chosen boundaries). However, from a numerical point of view,  $T_{rel}$  is slightly higher moving from the *Natural compensation* criterion to the *Torque*

*maximization* one. Although it is not so appreciable, this torque reduction is due to the increment of the structural iron ribs when increasing the PM mass in the *Target ipf* and *Torque maximization* design scenarios, as also shown in Fig. 3.32a3, 3.32b3 and 3.32c3 which report the average width of the iron ribs in the  $sr - mr$  plane at 60krpm in the 3 cases. Indeed, the higher flux short-circuited via iron ribs implies an increment of the q-axis inductance which in turn determines a more significant torque drop.

- Differently from the reluctance torque component, the shape of the PM torque contours (shown in Fig. 3.31a2, 3.31b2 and 3.31c2) is greatly affected by the amount of PMs which changes according to the adopted design criterion.
  - In the *Torque maximization* scenario, the required PM volume  $V_{PM}$  is equal to the available space within the flux barriers  $V_{slots}$ , as shown in Fig. 3.32c1.
  - On the contrary, for the *Target ipf* criterion, the PM flux (eq. (3.16)) is a non-linear function of the current components, ribs saturation, desired *ipf* and it is also proportional to the product  $L_q \cdot i_q$  which depends on the above parameters. Therefore, the PM flux contours shown in Fig. 3.32b2 differ from the fully filled barriers case and the PM torque contours (Fig. 3.31b2) change accordingly. It is worth to notice that for high  $mr$  and low  $sr$  the required PM exceeds the available space  $V_{slots}$  therefore the PM flux contours resemble those obtained with the *Torque maximization* approach.
  - With the *Natural compensation* criterion, the PM flux is directly proportional to the product  $L_q \cdot I_{max}$ , therefore also the PM torque behaviour in the  $sr - mr$  design plane will follow the one of such product as in Fig. 3.32a2 except for the regions where the required PM volume exceeds the available space as shown in Fig. 3.32a1.
- The concomitant action of the reluctance and PM torque components leads to the total torque contour plots reported in Fig. 3.31a1, 3.31b1 and 3.31c1. The shape of these contours and the position of the machine providing the maximum torque are therefore



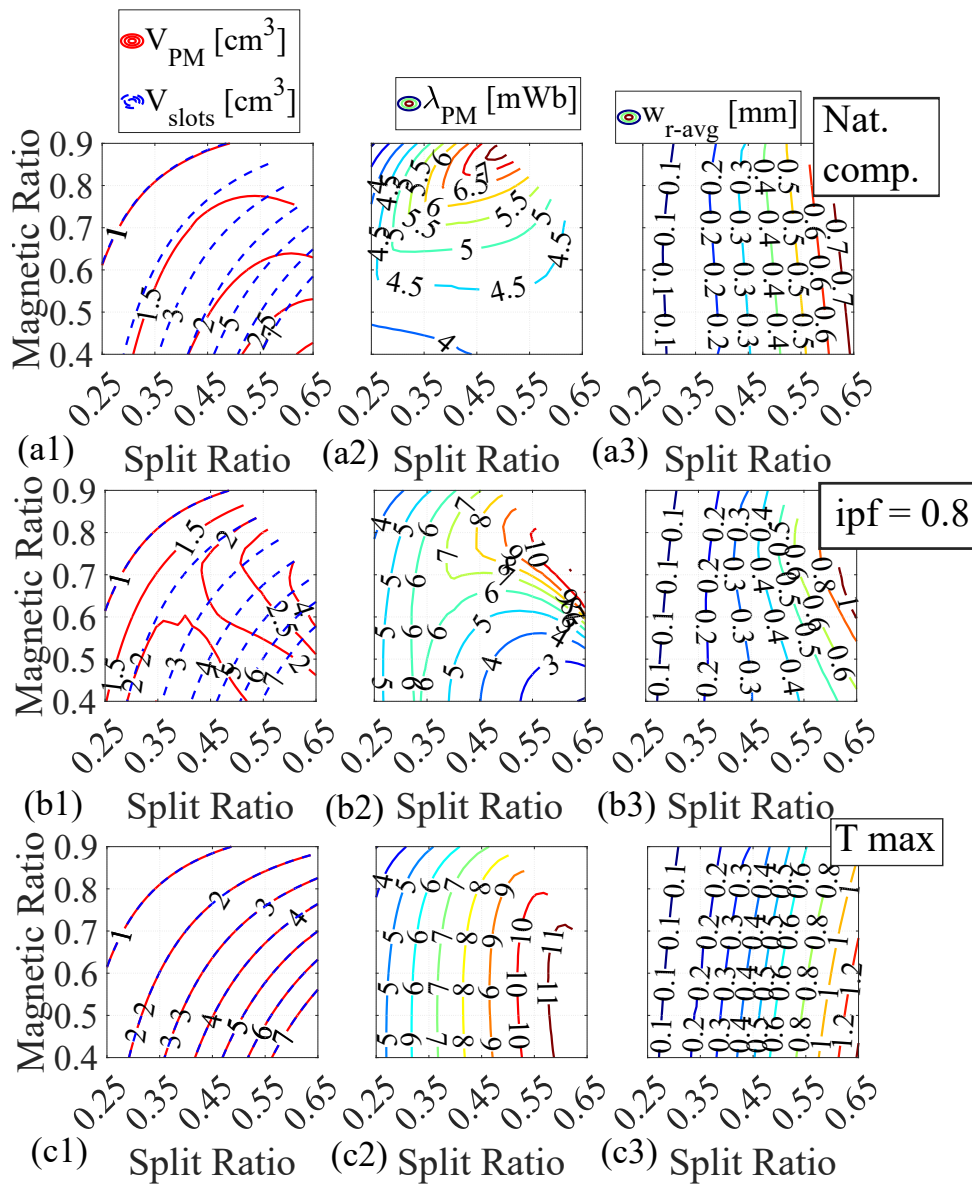


Figure 3.32: PM volume / available barrier volume (a), PM flux (b), average width of the rotor ribs (c) for Natural compensation (1), Target  $ipf$  (2) and Torque maximization (3) design criteria at 60 krpm.

mainly affected by the PM torque component. Indeed, the PM torque non-linearly increases moving from the bottom right to the top of the design plane when adopting the *Natural compensation* approach, therefore the total torque contour will be shifted to the top-left of the design plane with respect to the pure reluctance one. This consideration can be partially extended to the *Target ipf* scenario although in such case the total torque features a higher split ratio since the maximum of the PM component is shifted to the

right of the design plane. Differently, the adoption of the *Torque maximization* approach leads to a PM torque increasing from the bottom left to the top right of the  $sr - mr$  plane, thus the maximum value of the total torque is obtained for higher split ratio and lower magnetic ratio if compared to the other two criteria.

All these considerations can be fully extended to the other operating speeds, ranging from 0 to 70 krpm. Above the latter speed, the differences between the 3 approaches become less evident both in terms of performance and optimal machine location in the  $sr - mr$  plane (especially in terms of magnetic ratio).

## 3.9 Publications

Some results presented in this chapter have been published by the author in [117–119].

# Chapter 4

## Surface Permanent Magnet synchronous Machines

In this chapter, the methodology adopted for SyRMs and PMSyRM is extended to the surface-mounted permanent magnet synchronous motors design.

Although the design philosophy is the same as it is always based on the definition of the two independent design variables, the rotor design drastically changes both from electromagnetic and structural points of view.

Indeed, neither flux barriers nor structural iron bridges are present, while the permanent magnets are located on a solid rotor surface. The structural integrity at high-speed is preserved by designing, for each machine of the design plane, the so-called "retaining sleeve".

The other design assumptions and choices do not change with respect to the other two chapters: a distributed single-layer winding and a number of pole pairs equal to 2 is considered.

The aim of this chapter is to propose a comprehensive design procedure able of considering all the main aspects involved during the design of high speed PMSMs when a metallic sleeve is adopted.

The proposed design approach is used to assess the maximum power capability of PMSMs for given stator losses as the maximum design speed increases. The main aim is to assess the effects of the performance limiting factors on both optimal torque and related machine geometry. In

---

addition, the influence of the airgap thickness is also investigated in terms of trade-off between torque and rotor losses, as well as optimal geometries.

## 4.1 Analytical design procedure

The design approach resembles the one adopted for SyRMs and PMaSyRMs. Therefore, both performance and geometry of a surface PMSM can be defined by two independent design variables: the split ratio  $sr$  and the magnetic ratio  $mr$ .

The following assumptions and constraints are also re-called for the sake of clarity:

- the external dimensions (i.e external radius  $r_s$  and active axial length  $l_{fe}$ ) are imposed;
- the flux density  $B_{fe}$  within the stator yoke and teeth is preliminary fixed (generally close to the knee point of the  $B - H$  curve of the stator core material);
- the cooling system capability is chosen in terms of total stator losses that can be extracted via the outer stator surface.

The torque can be expressed as in (4.1):

$$T = \frac{3}{2} \cdot p(\lambda_d i_q - \lambda_q i_d) \quad (4.1)$$

where  $\lambda_d$  and  $\lambda_q$  can be expressed as function of current components, inductance and PM flux as in (4.2) and (4.3).

$$\lambda_d = (L_{dm} + L_s)i_d + L_{dq}i_q + \lambda_{PM-d} \quad (4.2)$$

$$\lambda_q = L_{dq}i_d + (L_{qm} + L_s)i_q + \lambda_{PM-q} \quad (4.3)$$

where all these magnetic quantities have been already defined in the last chapters.

It is well known that a surface-mounted PMSM is an isotropic machine which in turn means that the flux paths due to the d and q-axis currents are basically the same. It follows that the d-axis inductance is equal to the q-axis one.

Furthermore, the cross-coupling effects are negligible dealing with SPMSM, therefore both the  $L_{dq}$  and  $\lambda_{PM-q}$  can be neglected in the fluxes equations.

Therefore, the torque produced by an isotropic synchronous PM machine can be simplified as follows:

$$T = \frac{3}{2} \cdot p \cdot \lambda_{PM} \cdot i_q \quad (4.4)$$

$$ipf = \sin \left[ \frac{\pi}{2} - \arctan \left( \frac{L \cdot i_q}{\lambda_{PM}} \right) \right] \quad (4.5)$$

where  $\lambda_{PM}$  is equal the no-load PM flux linkage on the d-axis and  $L$  is the machine inductance. In the following, each geometric parameter, depicted in Fig. 4.1, as well as the stator current, flux linkage and so the torque are expressed as function of both  $sr$  and  $mr$ . All these electric and magnetic quantities are heavily affected by the machine geometry which in turn is defined by the combination of the design variables  $sr - mr$  and by the initial constraints and assumptions.

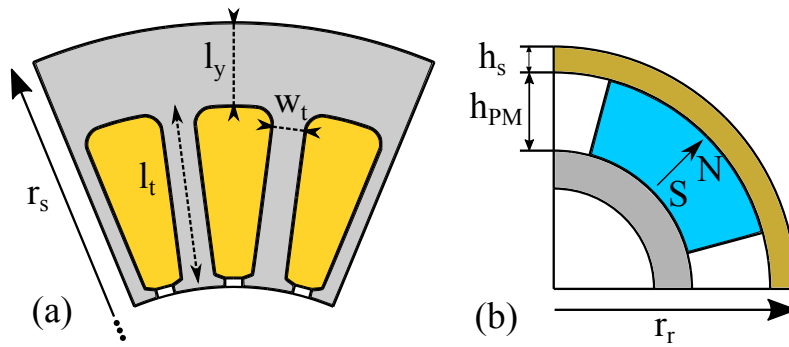


Figure 4.1: Stator (a) and rotor (b) parametrization.

### 4.1.1 Stator design

The stator main parameters are the tooth width  $w_t$ , the yoke thickness  $l_y$  and the tooth length  $l_t$ . The first one can be determined imposing the flux entering the tooth to be equal to the integral of the airgap flux density over the slot pitch, whereas the second can be calculated imposing the flux within the stator yoke to be equal to half of the flux per pole, thus obtaining the following relationships [82]:

$$w_t = \frac{2 \cdot \pi \cdot r_s}{6 \cdot p \cdot q} \cdot \frac{B_{g-max}}{B_g} \cdot sr \cdot mr \cdot k_t \quad (4.6)$$

$$l_y = \frac{\alpha_{PM} \cdot \pi \cdot r_s}{2 \cdot p} \cdot \frac{B_{g-max}}{B_g} \cdot sr \cdot mr \quad (4.7)$$

where  $B_{g-max}$  is the peak value of the airgap flux density (assuming a rectangular shape of the no-load airgap flux density) and  $\alpha_{PM}$  is the PM angular span.

### 4.1.2 Maximum current calculation

The q-axis current can be considered equal to the maximum available current  $I_{max}$  if only the operation in the maximum torque per ampere condition is envisaged. As the cooling capacity is preliminary chosen (through the factor  $k_{cool}$  equal to the ratio between the total losses and the external surface of the stator), the maximum current can be calculated imposing that the sum of Joule and iron losses  $P_{fe}$  equal to the maximum capability of the cooling system as in (2.30).

### 4.1.3 Rotor design: magnetic equivalent circuit

Neglecting the tangential component of the airgap flux density, the PM height can be calculated by solving the magnetic circuit reported in Fig. 4.2 preliminary choosing the angular span of the PM over the pole pitch. Indeed, the peak value of the total magnetic voltage has to be equal to the current linkage  $H_c h_{PM}$ , as in (4.8):

$$2 \cdot U_g + 2 \cdot U_{st} + U_{sy} + U_{ry} + 2 \cdot U_{PM} = 2 \cdot H_c \cdot h_{PM} \quad (4.8)$$

where  $U_g$ ,  $U_{sy}$ ,  $U_{ry}$ ,  $U_{st}$  and  $U_{PM}$  are the airgap, stator yoke, rotor yoke, stator teeth and PM magnetic voltage drops. It is worth to notice that  $U_{PM}$  is also function of the PM height:

$$U_{PM} = \frac{H_c}{B_r} \cdot B_{g-max} \cdot h_{PM} \quad (4.9)$$

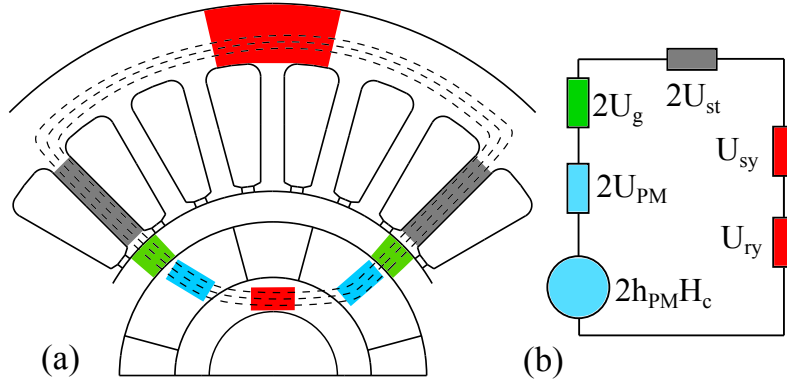


Figure 4.2: a) Flux path due to PMs; b) magnetic equivalent circuit.

where  $H_c$  and  $B_r$  are the coercive field and residual flux density of the PM. By combining (4.8) and (4.9), the PM height can be finally computed as:

$$h_{PM} = \frac{2 \cdot U_g + 2 \cdot U_{st} + U_{sy} + U_{ry}}{2 \cdot H_c \cdot \left(1 - \frac{B_{g-max}}{B_r}\right)} \quad (4.10)$$

The stator yoke, rotor yoke and stator teeth magnetic voltage drops do not depend on the sleeve thickness since the magnetic load  $B_{fe}$  is imposed. Conversely, as reported in (4.11),  $U_g$  is affected by the sleeve dimension, since it is a function of the equivalent magnetic airgap (which is the sum of the mechanical one  $g$  and the sleeve thickness  $h_s$ ):

$$U_g = \frac{B_{g-max}}{\mu_0} \cdot (g + h_s) \quad (4.11)$$

#### 4.1.4 Sleeve computation

The retaining sleeve role is twofold: secure the PMs at high speed and exert the proper pressure on the magnets and consequently on the shaft in order to transfer the machine maximum torque. These functionalities need to be guaranteed in any thermal operating condition. Super-alloys are usually used when considering metallic sleeves as they feature high mechanical strength and robust behaviour at high temperatures. Therefore, a suitable sleeve thickness should be selected to make sure the sleeve can bear the mechanical and thermal loads.



So, in order to achieve the proper size, sleeve's stress should be analyzed. Generally, there are two approaches to calculate the stress for this case: the analytical method and finite element modelling. 2D or 3D finite element modelling is a precise method that can provide an accurate stress distribution over the geometry but at the design level that different geometries need to be tried and the mechanical analysis needs to be coupled to the electromagnetic analysis it could be computationally expensive. From a conceptual point of view, sleeve, magnets and shaft can be all considered as cylinders that interact with each other through the pressure at their boundaries. Several analytical approaches have been proposed in literature to analyse the stress in concentric cylinders [120,121]. Among these formulations, the plane stress in thick cylinder, also known as Lamé formula, is a good approach as not only covers both the mechanical and thermal effects but also has an exact solution for this particular application. In order to derive the equilibrium equations, the 2D cross-sections of the shaft, magnets, and sleeve are considered as three cylinders, as shown in Fig. 4.3. Three set of radial and circumferential displacement

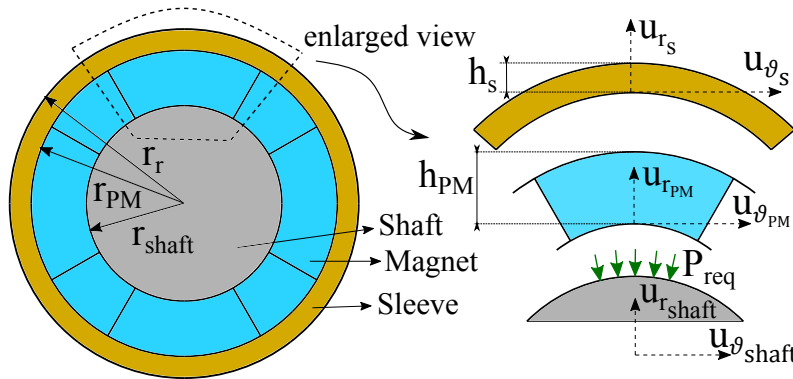


Figure 4.3: Sleeve stress schematic view with coordinate system.

vectors  $(U_{r_{sh}}, U_{\theta_{sh}})$ ,  $(U_{r_m}, U_{\theta_m})$ , and  $(U_{r_{sl}}, U_{\theta_{sl}})$  have been considered for the shaft, magnet, and sleeve, respectively. For sake of complexity, the edging stress effect between the magnets is neglected at this stage as it is negligible and can be considered in the final detail design. The static equilibrium equation for the isotropic thick cylinder under centrifugal body force and

temperature gradient is:

$$\frac{E_l}{1 - \nu_l^2} \left( \frac{d^2 u_l}{dr^2} + \frac{1}{r} \frac{du_l}{dr} - \frac{u_l}{r^2} - \beta_l(1 + \nu_l) \frac{d\Delta T_l}{dr} \right) + \rho_l r \Omega^2 = 0 \quad (4.12)$$

where  $r$  is the radial coordinate,  $E$  is the module of elasticity,  $\nu$  is the Poisson ratio,  $\beta$  is the coefficient of thermal expansion,  $\Delta T$  is the temperature variation function in the radial direction,  $\rho$  is the density,  $\Omega$  is the rotational speed, while the subscript  $l = sh, pm, s$  stands for shaft, magnet and sleeve, respectively. These three ordinary differential equations have a homogeneous and a particular solution:

$$u_{r_l} = C_{1_l} r + \frac{C_{2_l}}{r} + \beta_l(1 + \nu_l) \frac{1}{r} \int_{r_{in}}^r \Delta T_l r dr + \frac{\rho_l \Omega^2 (1 - \nu_l^2) r^3}{8E_l} \quad (4.13)$$

where  $u_r$  is the displacement as a function of radial position, and  $C_1$  and  $C_2$  are the unknown constants that are determined by imposing the boundary conditions. As the displacement functions are three, one for the shaft, magnet and sleeve, there are six unknowns that need to be determined. Based on the interaction at the boundaries of these parts, the following boundary conditions have been applied to find these six unknown coefficients:

$$\begin{aligned} \sigma_{r_{sh}} &\neq \infty @ (r = 0), \\ \sigma_{r_{sh}} &= \sigma_{r_{pm}} @ (r = r_{sh}), \\ u_{r_{pm}} - u_{r_{sh}} &= \delta_{sh-pm} @ (r = r_{sh}), \\ \sigma_{r_{pm}} &= \sigma_{r_s} @ (r = r_{pm}), \\ u_{r_s} - u_{r_{pm}} &= \delta_{pm-s} @ (r = r_{pm}), \\ \sigma_{r_s} &= 0 @ (r = r_s), \end{aligned} \quad (4.14)$$

Four of the above equations impose conditions on the radial stress while two set the interference

needed at the interfaces between shaft-magnet and magnet-sleeve. Since the radial stress is required to impose the boundary conditions, displacement-strain and stress-strain relations (for isotropic material) need to be expressed:

$$\epsilon_{r_l} = \frac{du_l}{dr}, \epsilon_{\theta_l} = \frac{u_{r_l}}{r}, \quad (4.15)$$

$$\begin{aligned} \epsilon_{r_l} &= \frac{1}{E_l}(\sigma_{r_l} - \nu\sigma_{\theta_l}) + \beta_l\Delta T_l, \\ \epsilon_{\theta_l} &= \frac{1}{E_l}(\sigma_{\theta_l} - \nu\sigma_{r_l}) + \beta_l\Delta T_l, \end{aligned} \quad (4.16)$$

where  $\epsilon_r$  and  $\epsilon_\theta$  are strain in radial and circumferential directions, respectively. By replacing the displacement expression (4.13) into the strain relations (4.15) and (4.16), the stress expression in radial direction can be obtained. By setting geometrical constraints, operating speed, material properties and required interference values, a set of six algebraic linear equations is obtained whose solution provides the six unknown constants.

The previous system of equations allows obtaining the radial and circumferential displacements and stresses in all components as function of the radius for a given rotor structure (defined by the external rotor radius  $r_r$ , sleeve and PM thicknesses  $h_s, h_{pm}$ , and interferences  $\delta_{sh-pm}, \delta_{pm-s}$ ). In order to verify if the geometry under consideration represents a functional and a reliable design, the following conditions need to be met:

1. the compressive radial stress between shaft and magnet should be more than the value required to transmit the maximum torque;
2. the interference between magnets and sleeve should be less than 0.2mm as a higher value would cause practical problems during the shrink fitting of the sleeve;
3. the maximum Von Mises stress in the PM should not exceed its ultimate strength and the radial stress should be compressive rather than tensional as PM materials feature low tensile strength;
4. the maximum Von Mises stress  $\sigma_{sl}^{VM}$  in the sleeve should be less than the material yield

strength to avoid any plastic deformation and subsequent failure.

Fig. 4.4 shows the maximum Von Mises stress in the sleeve for a wide range of rotor geometries featuring a given outer radius and several magnet and sleeve thicknesses when the conditions 1)-3) are satisfied.

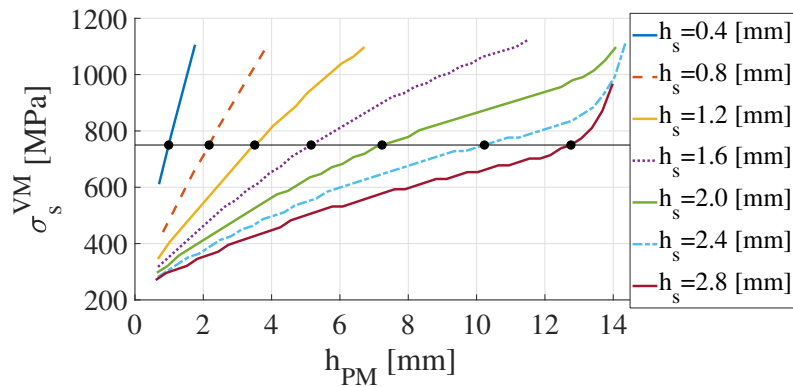


Figure 4.4: Maximum Von Mises stress in the sleeve as function of magnet and sleeve thicknesses at 80 krpm for a given outer rotor radius  $r_r=18$  mm.

In this case study, the maximum Von Mises stress in the sleeve has been set to 750 MPa and the black markers identify the maximum permanent magnet dimensions ( $h_{PM,max}$ ) that a given sleeve thickness can support without exceeding any limits. Repeating such parametric study for several rotor outer radii, it is possible to derive the maximum magnet thickness as function of the sleeve dimensions for several rotor outer radii as shown in Fig. 4.5.

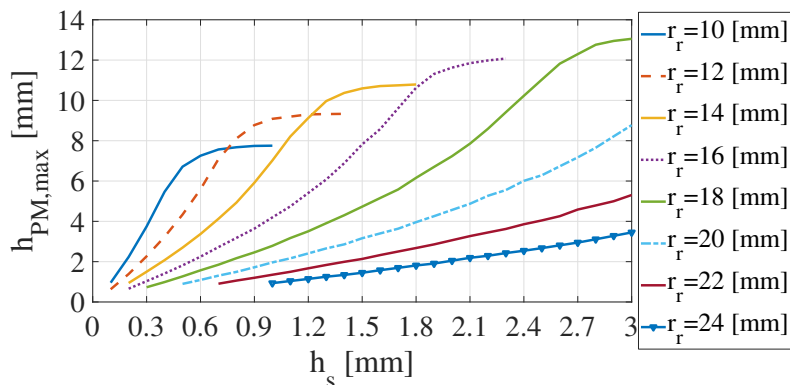


Figure 4.5: Maximum PM thickness as function of the sleeve thickness for different outer rotor radii at 80 krpm.

### 4.1.5 Iterative calculation of PM and sleeve thicknesses

Analysing eq. (4.10) and (4.11) follows that the sleeve and the PM thicknesses can not be independently calculated as the sleeve presence affects the magnetic performance and the PM dimensions influence the sleeve dimensions. As a consequence, an iterative procedure (summarized in the flowchart shown in Fig. 4.6) is required to identify these two parameters. In particular, first the  $h_{PM}$  is calculated by (4.10) considering  $h_s = 0$  in (4.11). Then, the sleeve

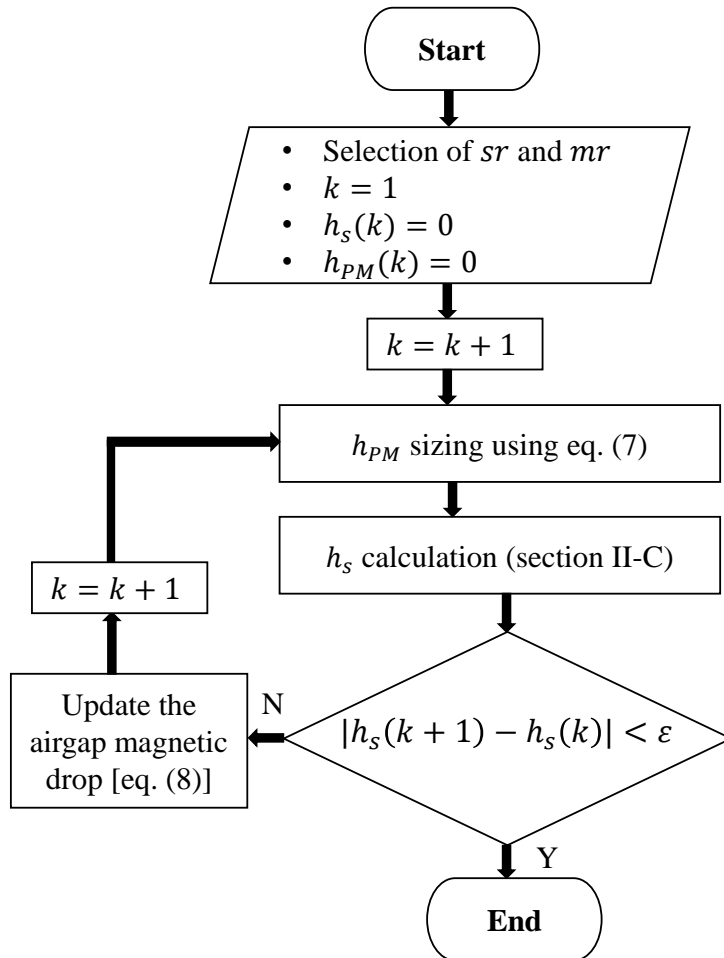


Figure 4.6: Iterative computation of PM height and sleeve thickness.

calculation procedure of section II-D is applied so to determine the value of  $h_s$  required to sustain the above computed  $h_{PM}$  for the considered rotor radius and maximum speed. The obtained  $h_s$  is then used to update the airgap magnetic voltage drop in (4.11) leading to the computation of a new  $h_{PM}$  still using (4.10). This iterative procedure ends when the absolute error between

the values of  $h_s$  for two consecutive iterations becomes lower than a predefined threshold.

## 4.2 Design approach validation and adjustment

The proposed analytical procedure permits a fast prediction of the electromagnetic performance for a wide range of  $sr - mr$  combinations thus allowing to compare different geometries for a given set of design assumptions. The just described analytical procedure has been applied to design and analyze machines starting from the constraints and assumptions reported in Table 4.1 and a maximum speed of 40 krpm.

Table 4.1: Design constraints and assumptions

Parameter	Value	Units
Outer stator radius	30	mm
Stack length	30	mm
Pole pairs	2	/
N° of stator slots	24	/
Maximum speed	40000	rpm
PM material	Recoma 28	/
Stator material	10JNHF600	/
Rotor material	17/4 ph	/
Sleeve material	Inconel 718	/
PM remanence	1.06	T
Iron flux density	1.4	T
Cooling capability	23	$kW/m^2$
PM angular span	60	mech. deg

Fig. 4.7c reports the torque contours in the  $sr - mr$  design plane evaluated with the just described analytical model and those obtained by FEA. The visible mismatch between the results is mainly due to the inaccuracy of the analytical model in predicting the iron losses and the PM flux linkage as shown in Fig. 4.10a, b.

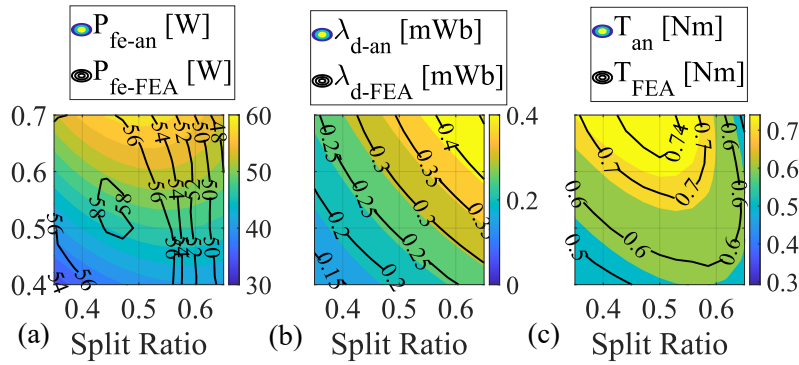


Figure 4.7: Comparison between analytical results and FE ones: a) iron losses; b) d-axis flux and c) electromagnetic torque.

The reasons behind the iron losses mismatches can be split into two causes:

- major cause: an actual non-uniform distribution of the flux density over the  $sr - mr$  plane (i.e. the actual peak value of the flux density in yoke and teeth ( $B_{fe}$ ) is not constant in the  $sr - mr$  plane)
- minor cause: the influence of the harmonic iron losses.

Indeed, the imposed  $B_{fe}$  during the design exercise refers to a no-load condition (i.e.  $i_q = 0$ ), since the magnetic equivalent circuit and the calculation of the stator tooth and yokes is performed only considering the PM contribution as it is common procedure for PMSMs [82]: indeed, considering both the PM contribution and the q-axis magnetomotive force at the same time is a challenging from an analytical point of view (it would need several iterations and divergence problems can arise).

It follows that the actual peak value of the flux density with yoke and teeth will be different in the load operating condition. For the sake of clarity, Fig. 4.8 reports the FE-computed peak value of flux density within yoke (a,c) and teeth (b,d) at no-load (a,b) and load conditions (c,d) over the  $sr - mr$  plane for a 40 krpm case.

It is worth to notice that the FE no-load  $B_{fe}$  is actually quasi-constant over the  $sr - mr$  plane as imposed during the design exercise for both the yoke and teeth (a tooth factor  $k_t = 0.9$  is applied therefore the flux density within the tooth is imposed to be about 10 % higher than the yoke one), despite the numerical values are slightly lower since the tooth and yoke widths have

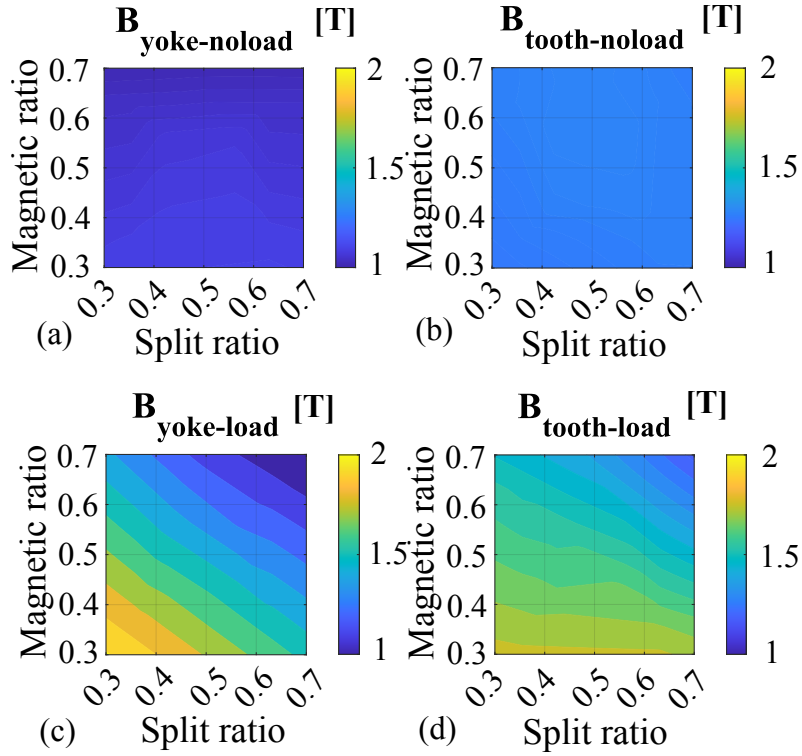


Figure 4.8: No load (a,b) and load (c,d) peak value of the flux density within stator yoke (a,c) and stator tooth (b,d) in the  $sr - mr$  plane

been slightly oversized during the design routine to avoid over-saturation in load and over-load scenarios.

Differently, in the load scenario the effects of the stator magnetomotive force due to the  $i_q$  contribution lead to a non-uniform distribution of the flux density.

This non-uniform distribution of  $B_{fe}$  is the main reason behind the qualitative iron losses mismatches. Indeed, the analytical iron losses shown in Fig. 4.9a clearly match those computed using the peak value of the no-load flux density of Fig. 4.9b from a qualitative point of view (the numerical differences are due to the oversized tooth and yoke).

On the contrary, when the peak value of the FE-computed  $B_{fe}$  is used in the Steintmetz equation, the stator iron losses contour clearly has a different shape which in turn resembles the one of the actual FE-computed iron losses; it can be concluded that the non-uniform distribution in the  $sr - mr$  of  $B_{fe}$  within yoke and teeth is identified as the main cause of the iron losses discrepancies; the residual mismatches are due to the minor cause (i.e. the harmonic iron



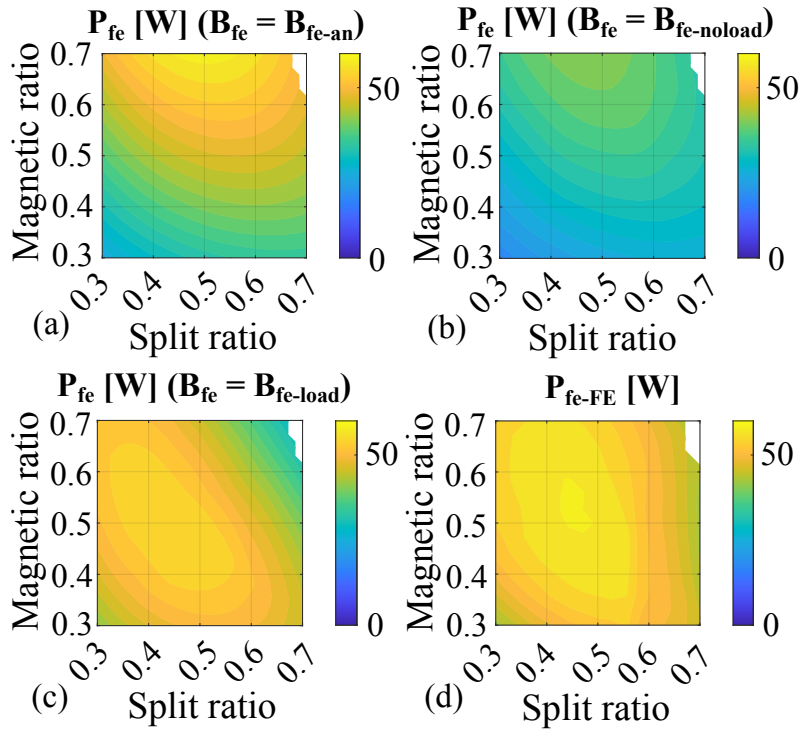


Figure 4.9: Analytical stator iron losses (a); stator iron losses calculated using the peak value of FE-computed  $B_{fe}$  at no-load (b) and load (c) conditions; actual FE iron losses (d).

losses).

With the aim of tackling the above issues, the FE-adjustment procedure reported in [108] for synchronous reluctance machines is here extended to include the PMSM design scenario. In particular, the machines at the corners of the design plane  $sr - mr$  are FE-simulated in order to accurately evaluate their iron losses and so the ratio between the FE and analytical losses. Such iron loss correction factor is then extended to the overall design plane using a linear interpolation. The analytical design is then re-carried out by updating the stator current (eq. (2.30)) until the iron losses error becomes negligible.

Once the iron losses of the corner machines have been identified and so their maximum currents, the correction factors for the d- and q-axis fluxes are FE calculated. The extension of these correction factors to the overall design plane leads to the adjustment of the magnetic model. The comparison between the adjusted torques and the FE ones shown in Fig. 4.10b3 is excellent as expected and it is due to a more reliable estimation of iron losses and d-axis flux reported in Fig. 4.10b1 and b2 respectively. It is worth to underline that the corrected torque

average error is about 2% highlighting the accuracy of the proposed approach. In addition, the maximum error is always located away from the maximum torque region, which is the area of final interest.

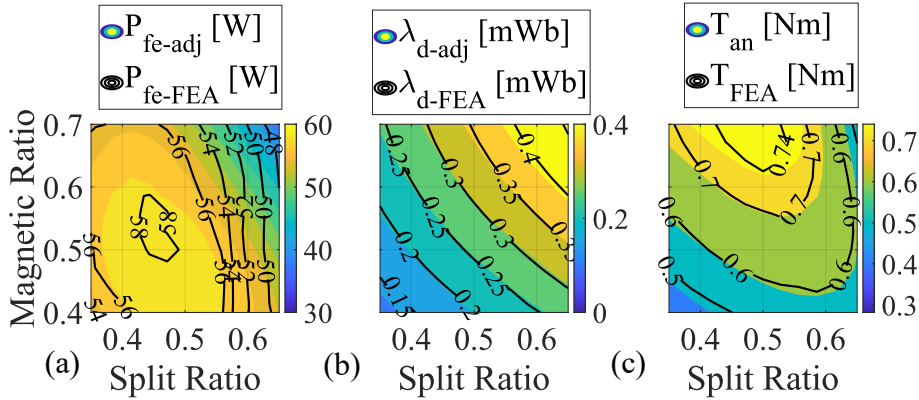


Figure 4.10: Comparison between analytical adjusted results and FE ones: a) iron losses; b) d-axis flux and c) electromagnetic torque.

#### 4.2.1 Thermal performance validation

The constant stator losses design criteria, used throughout the proposed comparative design exercise, is meant to lead to thermal performance that do not substantially differ from one machine to another. This statement is based on the strong assumption that the temperature distribution within the machine mainly depend from the overall losses while their distribution (between iron and copper) plays a minor role. Fig. 4.11a reports the winding temperature in the  $sr - mr$  plane considering a design speed of 40krpm and an airgap thickness of 1 mm. The thermal performance have been estimated using the commercial software [94] adopting a spiral water jacket as cooling system whose details will be reported in the experimental section. The winding temperature is almost constant within the design plane and the difference between the highest and lower temperature is around 15°C (when excluding extreme machine designs at the border of the design plane). The winding temperature contour clearly resembles the constant loci of the ratio between iron and copper stator losses shown in Fig. 4.11b. As expected, the winding temperature is lower in the regions of the design plane characterized by higher iron losses and lower copper losses.

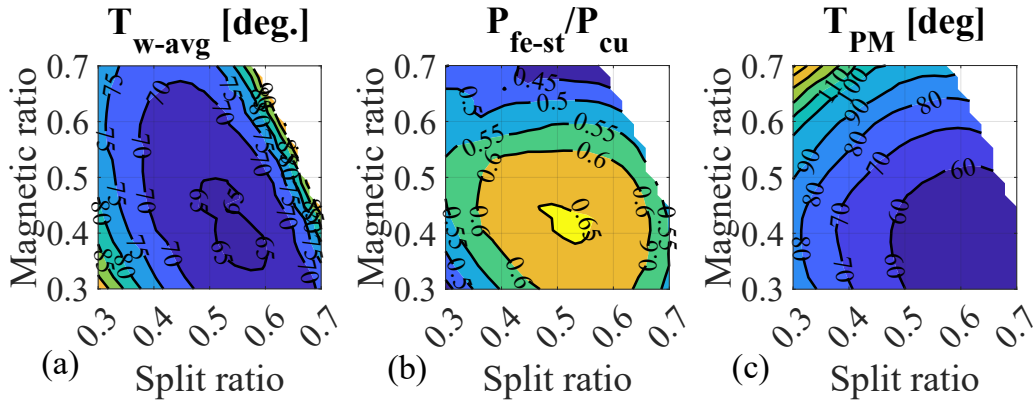


Figure 4.11: (a) Estimated winding average temperature, (b) ratio between iron and copper stator losses and (c) PM temperatures in the  $sr - mr$  plane at 40krpm.

Dealing with SPM, also the PM temperature  $T_{PM}$  plays a major role since it influences the PM magnetic characteristic and, therefore, the average torque. Fig. 4.11 shows  $T_{PM}$  in the  $sr - mr$  at 40 krpm. The maximum value is around 120 degrees. This is an acceptable value which in turn does not modifies significantly the B-H curve of the PM material.

It can be concluded that the constant stator losses design criteria constitutes a valid approach as it leads to machine designs with comparable thermal performance without directly evaluating the latter within the design workflow.

### 4.3 High speed designs

The proposed design procedure is hereafter used to investigate the influence of the maximum speed and the airgap thickness on the machine performance. The parameters which do not change within all the analysis are those listed in Table 4.1; the remaining ones are calculated for each  $sr - mr$  combination according to the procedure described in section II. Fig. 4.12 reports the constant torque loci in the  $sr - mr$  plane for different rotational speeds (40, 60 and 80 krpm) and airgap thickness (0.5, 1, 1.5 and 2 mm), along with a marker highlighting the maximum torque design (hereafter called optimal design). As expected, the torque is negatively affected by the speed and airgap increase. This is mainly due to the increment of the iron losses (affecting the stator current) and to the sleeve thickness which widens the equivalent magnetic

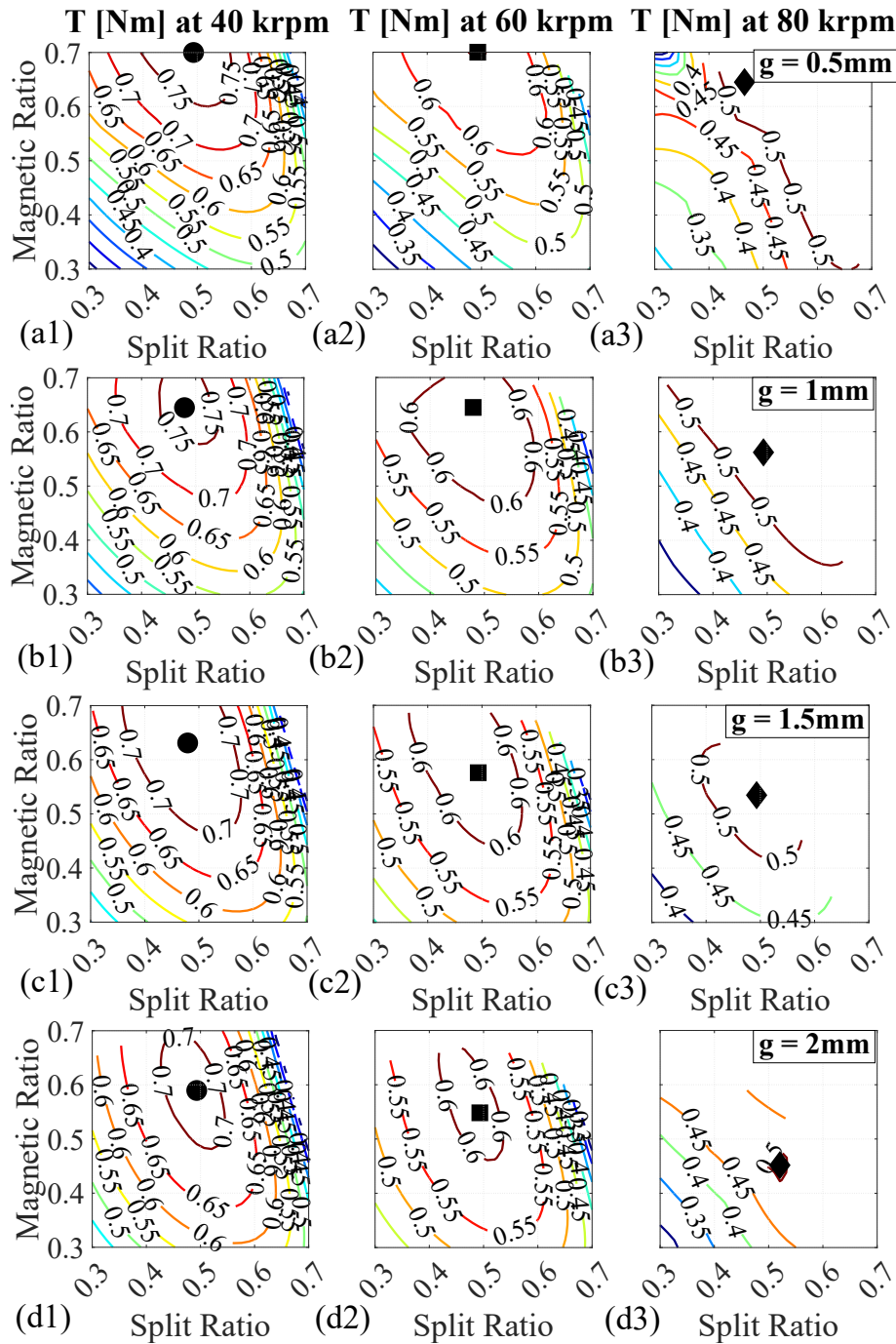


Figure 4.12: Torque constant loci contour plot in the  $sr - mr$  plane at (1) 40krpm, (2) 60krpm and (3) 80krpm when the airgap thickness is a) 0.5 mm, b) 1 mm, c) 1.5 mm and d) 2 mm

airgap, leading to a higher flux leakage for a given combination of  $sr$  and  $mr$ . As the speed increases, for a given airgap thickness, the optimal design moves towards lower magnetic ratios while the split ratio remains almost constant; the same trend is observed moving from small to large airgap, for a given maximum speed. In the following two subsections, the reasons behind

such behaviours are investigated.

### 4.3.1 Airgap thickness effects

The torque trend with respect to the airgap thickness can be explained analyzing eq. (4.4) and Fig. 4.13 which reports the PM flux and the q-axis current at 60 krpm for three different airgap thicknesses. Indeed the torque contour and so the maximum torque location are defined by these

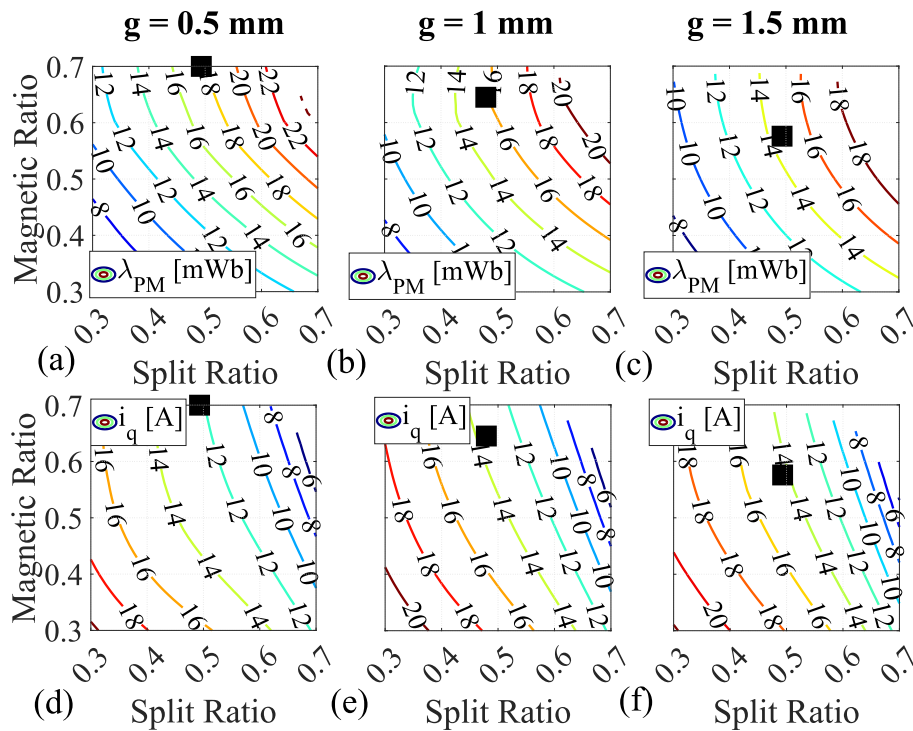


Figure 4.13: Contour plot of PM flux (a, b, c) and q-axis current (d, e, f) when the airgap thickness is 0.5 mm (a, d), 1 mm (b, e) and 1.5 mm (c, f) at 60 krpm.

two quantities which present different shapes in the  $sr - mr$  plane. In particular, the maximum current is located at the bottom-left of the design plane, whereas the PM flux shows an opposite trend. For a given couple of design variables  $sr - mr$ , the PM flux decreases with the airgap while the current increases. The first behavior can be explained considering that a wider airgap implies higher flux leakages, therefore a lower PM flux linkage for a given first harmonic of the airgap flux density. For the same reason, iron losses decrease when the airgap is higher and, as a consequence, the current increases.

According to the above considerations, for a small airgap the PM flux has a major influence on the maximum torque location, whereas the stator current contribution is more significant when the airgap is increased. As a consequence, the maximum torque is located at high  $mr$  when considering low airgap thickness and moves towards lower magnetic ratio for a thicker airgap, as the role of the current contribution becomes more significant. Differently, the optimal  $sr$  remains constant for different airgap levels because PM flux linkage and q-axis current have opposite trends when moving horizontally in the design plane.

### 4.3.2 Maximum speed effects

The reasons behind the trend of the electromagnetic torque with respect to the speed, for a given airgap thickness, can be inferred by analyzing the contours of the PM flux linkage and the q-axis current shown in Fig. 4.14 for 40, 60 and 80 krpm.

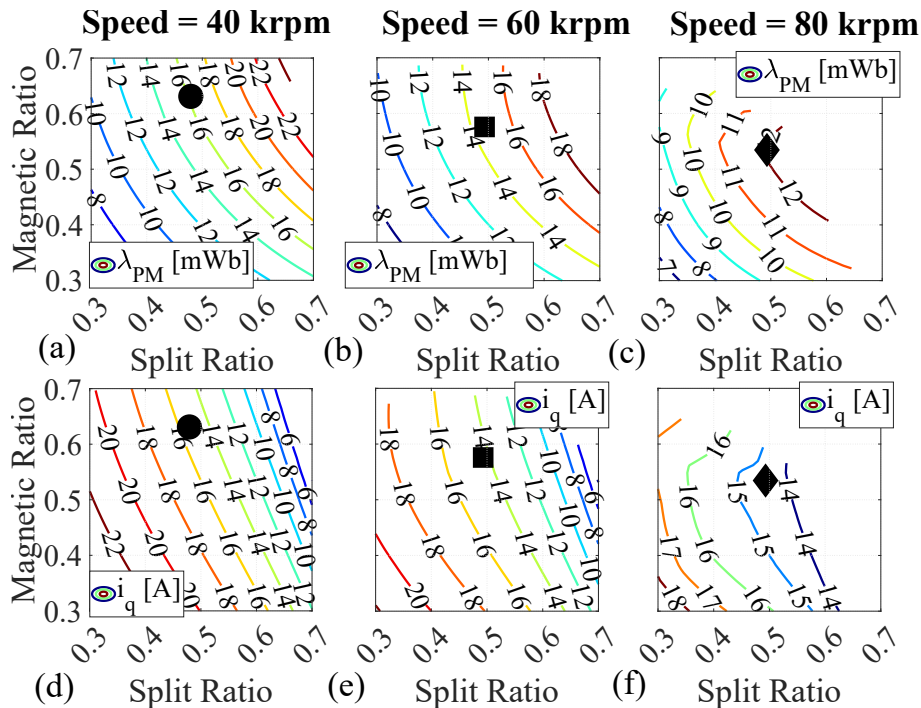


Figure 4.14: Contour plot of PM flux (a, b, c) and q-axis current (d, e, f), when the speed is 40 krpm (a, d), 60 krpm (b, e) and 80 krpm (c, f) for an airgap thickness equal to 1.5 mm.

Higher rotational speeds imply a reduction of both PM flux and stator current. The first one decreases due to the higher leakage flux caused by the increment of the magnetic equivalent

airgap; the latter due to the higher iron losses, which reduce the allowable maximum current. The maximum torque design features lower magnetic ratio as the speed increases since the rate of decrement (with the speed) of the PM flux is lower than that of the q-axis current. Also in this case, the split ratio of the optimal design remains constant as the speed increases due to the opposite trends of the PM flux and q-axis current when moving horizontally in the design plane.

### 4.3.3 Independent assessment of the high speed limiting factors

In this section the effects of the structural and loss limitations are separately analyzed. In particular, for a given airgap (e.g. 1.5 mm), the design exercise in the  $sr - mr$  plane is performed first neglecting the influence of the stator iron losses in the stator current calculation and then neglecting the sleeve increment as the speed increases. Although the superimposition principle is not applicable since the non-linear behavior of the machine does not allow such approximation, this analysis could give some qualitative insights about the trends of the design variables.

Fig. 4.15 reports the optimal split ratio (a) and magnetic ratio (b) as function of the operating speed when only the structural limitations (solid line), loss ones (dash line) or both of them (dot line) are considered within the design workflow.

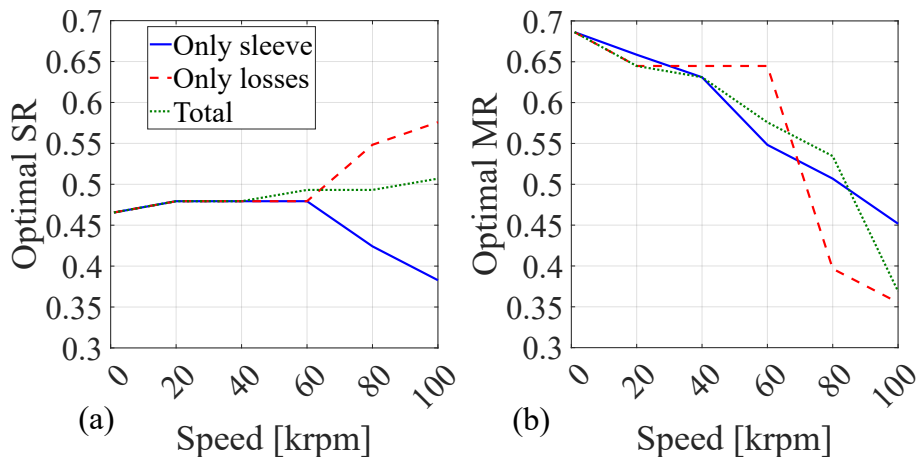


Figure 4.15: Optimal split (a) and magnetic (b) ratios as function of the speed.

It is worth to notice that the optimal split ratio tends to decrease when only the structural limitations are considered, while it increases when the design exercise only accounts for the



iron losses increment. On the contrary, sleeve or iron losses increase leads to a reduction of the optimal magnetic ratio as the maximum speed increases.

The reason behind the decrement of the split ratio when only the structural limitation are considered above 60 krpm can be explained considering the sleeve thickness influence and Fig. 4.16 which shows the PM flux (a,b,c) and sleeve thickness (d,e,f) contours in the  $sr - mr$  plane at 40 (a,d), 60 (b,e) and 80 (c,f) krpm. On one hand, a higher split ratio implies a higher

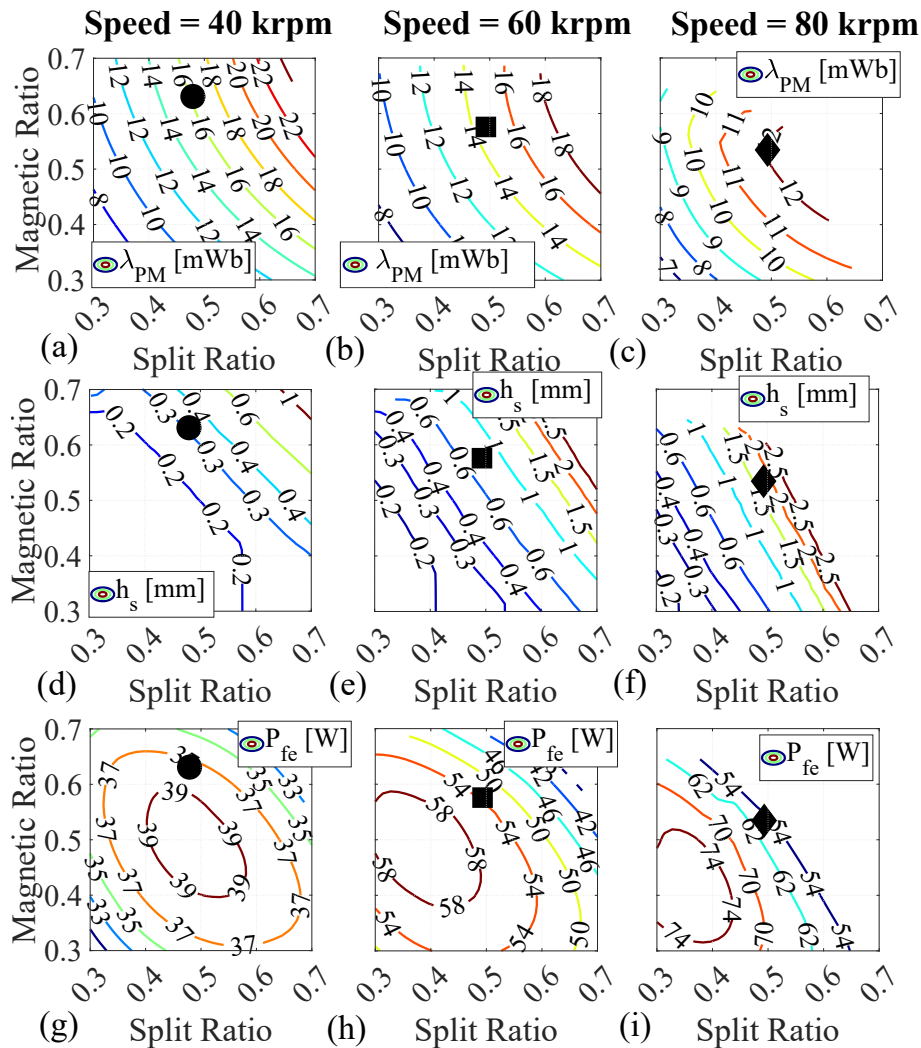


Figure 4.16: Costant loci contour plot of PM flux (a, b, c), sleeve thickness (d, e, f) and stator iron losses (g, h, i) when the speed is 40 krpm (a, d, g), 60 krpm (b, e, h) and 80 krpm (c, f, i) and for an airgap thickness equal to 1.5 mm.

rotor radius which in turn leads to an increment of the sleeve thickness. The sleeve thickness increment implies an increment of the PM height  $h_{PM}$  to reach the same airgap flux density  $B_g$ .



On the other hand, lower split ratios result in lower PM flux (since the pole pitch in meters is reduced). Until 60 krpm none of these two competitive behaviors is preponderant with respect to the other one and the split ratio basically remains constant. Differently, above 60 krpm, the influence of the sleeve increment plays a major role and therefore the optimal split ratio tends to decrease.

Differently, when only the iron losses are considered, the optimal split ratio above 60 krpm increases since in that direction the iron losses tend to decrease as shown in Fig. 4.16g, h and i. The optimal magnetic ratio always tends to decrease whatever the limitation (structural, thermal or both) is considered. The reason behind such decrement has been explained in section IV-B: indeed, the rate of the decrement of the PM flux with the speed is lower than the one of the q-axis current (see Fig. 4.14).

It can be concluded that the trends of the optimal split and magnetic ratio depend on concurrent needs of the structural and iron losses effects. In other words, they depend on the sleeve and soft magnetic material affecting the rate of increment of the sleeve and iron losses with the speed.

## 4.4 Optimal designs

### 4.4.1 Performance

The trend of the optimal designs in terms of torque and output power as function of the speed are shown in Fig. 4.17a and 4.17b. The markers in the same figure represent the FE-evaluated performance, confirming an excellent agreement with the prediction of the proposed method.

As previously pointed out, the torque always decreases with the speed due to the increment of iron losses and sleeve thickness. This trend is more pronounced at low speed, when the magnetic equivalent airgap almost coincides with the mechanical one. At high speed, the sleeve thickness plays a major role in the definition of the magnetic airgap, therefore the maximum torque designs tend to provide similar performance regardless the airgap thickness.

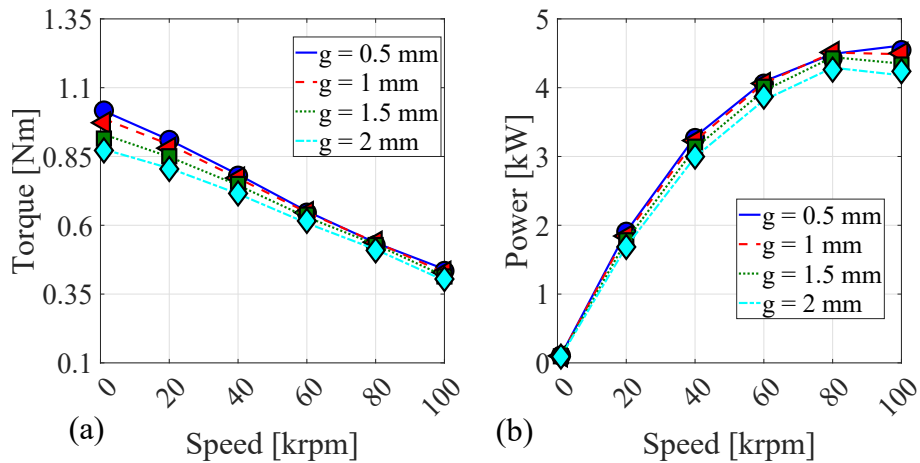


Figure 4.17: Torque (a) and power (b) as function of the speed.

Regarding the power, the speed increase is beneficial up to 80 krpm for this particular case study whose details are defined in Table 4.1. Beyond this speed the power reaches a plateau or starts to decrease depending on the considered airgap thickness. The improvement of the output power as the maximum speed increases and the airgap decreases comes at the cost of higher rotor losses. Indeed, Fig. 4.18 shows the sleeve and PM losses evaluated with FEAs. As expected, the rotor losses increase with the speed and decrease with the airgap. On one

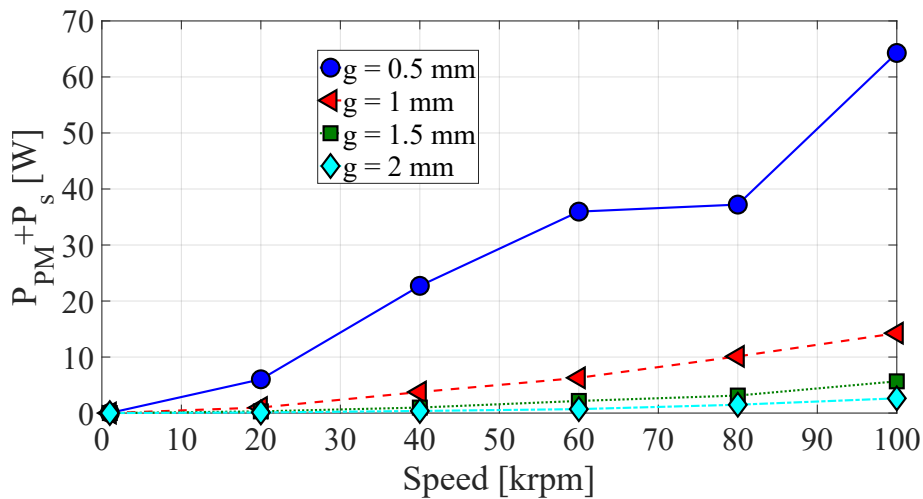


Figure 4.18: Rotor losses of the optimal designs as function of the speed.

hand, the rotor losses increase with the speed, due to the higher fundamental frequency of the flux density. On the other hand, the increment of the sleeve thickness drastically increases the magnetic equivalent airgap which in turn determines a reduction of the eddy currents in the

rotor components.

#### 4.4.2 Machine geometries

The trends of the magnetic and split ratio of the maximum torque designs reported in Fig. 4.12 and justified in the previous section are confirmed by the respective machine cross sections shown in Fig. 4.19 and whose main parameters are also reported in Table 4.2. Obviously, the

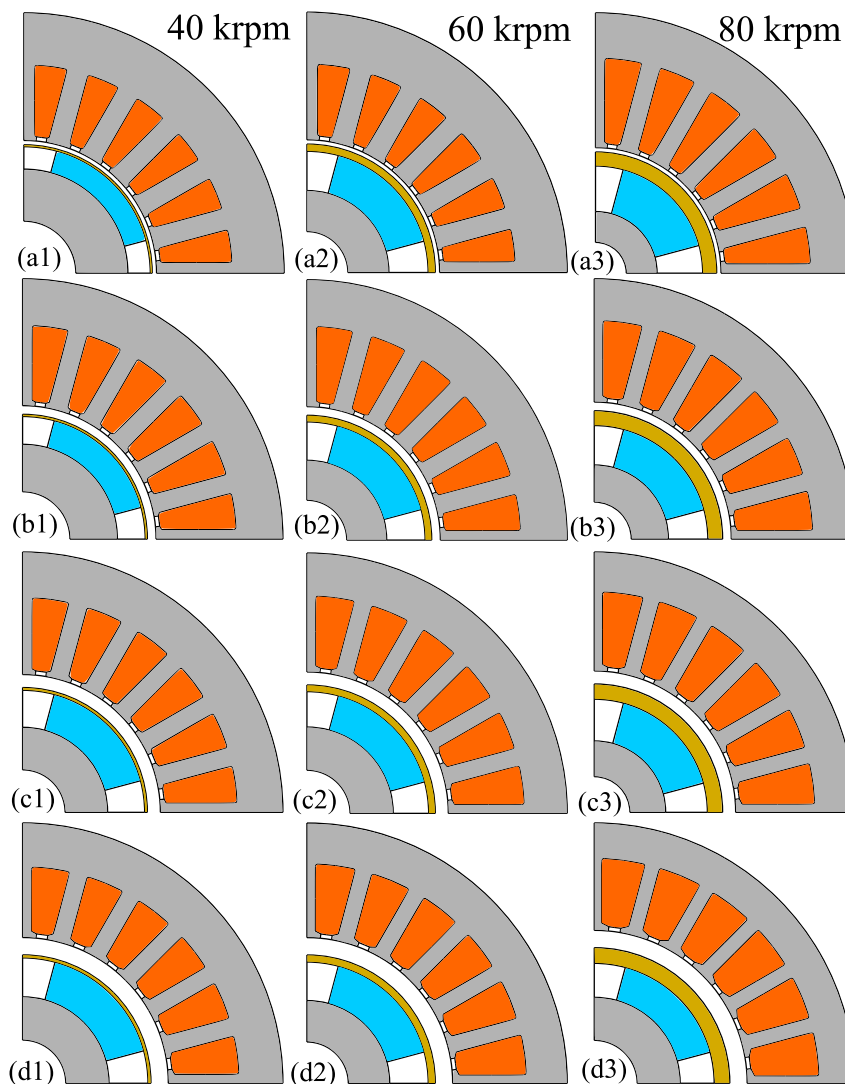


Figure 4.19: Cross section of the optimal machines at (1) 40krpm, (2) 60krpm and (3) 80krpm when the airgap thickness is a) 0.5 mm, b) 1 mm, c) 1.5 mm and d) 2 mm

optimal machines share the same rotor radius and feature decreasing tooth and yoke dimensions as the magnetic ratio decreases (with both speed and airgap increment).

Table 4.2: Optimal machine geometrical parameters (in mm)

Design	Variable	g=0.5mm	g=1mm	g=1.5mm	g=2mm
<b>40krpm</b>	$w_t$	2.44	2.18	2.14	2.05
	$l_y$	5.96	5.34	5.23	5.02
	$h_{PM}$	2.58	3.21	4.27	4.50
	$h_s$	0.22	0.25	0.31	0.35
<b>60krpm</b>	$w_t$	2.44	2.18	2.00	1.91
	$l_y$	5.96	5.34	4.91	4.67
	$h_{PM}$	4.55	4.45	4.09	4.46
	$h_s$	0.83	0.76	0.76	0.81
<b>80krpm</b>	$w_t$	2.12	1.96	1.86	1.66
	$l_y$	5.18	4.79	4.55	4.06
	$h_{PM}$	5.31	4.56	4.84	3.95
	$h_s$	1.63	1.71	1.76	1.81

The trend of PM height with the speed depends on selected airgap thickness. Indeed,  $h_{PM}$  tends to increase with the speed for  $g$  up to 1 mm, whereas it remains almost constant when  $g = 1.5$  mm and it tends to decrease when  $g = 2$ mm. The reason of these behaviours can be inferred considering (4.10) and (4.11). The magnet dimension  $h_{PM}$  is directly proportional to the magnetic voltage drop in the airgap  $U_g$ ; the latter is in turn proportional to both the equivalent magnetic airgap thickness (sum of the mechanical airgap and sleeve thicknesses) and the airgap flux density  $B_g$ . As a consequence, as the speed increases, the magnet thickness is defined by the tradeoff between the decrement of the airgap flux density and the increment of the sleeve thickness. In fact, when the mechanical airgap thickness is small, the sleeve thickness increment has a major effect on  $U_g$ , therefore  $h_{PM}$  increases. On the contrary, when the mechanical airgap thickness is higher, the sleeve thickness influence on  $U_g$  is less pronounced (i.e. even at 100 krpm  $g$  is comparable with  $h_s$ ), thus the reduction of  $B_g$  plays a major role and  $h_{PM}$  tends to decrease.

### 4.4.3 Thermal performance

The comparative design exercise among different airgap thicknesses and design speeds has been carried out considering the same stator losses. As shown in Fig. 4.11, the thermal behavior of the machine in the  $sr - mr$  plane is approximately the same. This consideration is also valid as the speed increases as shown in Fig. 4.20a which reports the winding temperatures of the optimal designs. As expected, higher design speed implies a reduction of the Joule losses, therefore

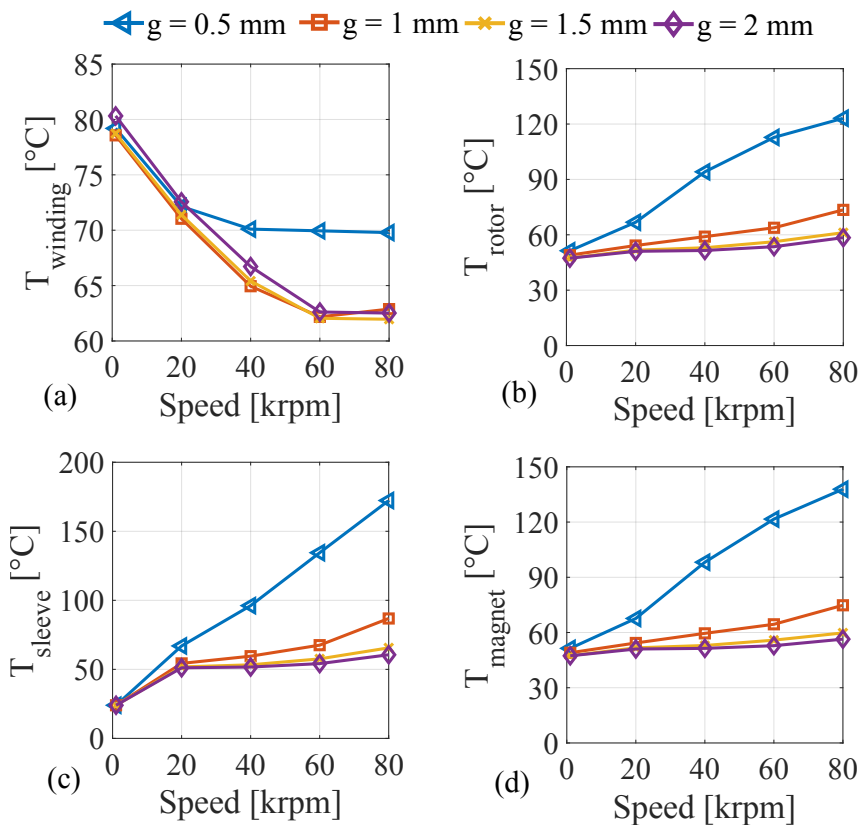


Figure 4.20: Winding (a), rotor (b), sleeve (c) and magnet (d) temperatures of the optimal designs at rated conditions.

the winding temperature tends to decrease with the speed as the iron losses are easier to be dissipated.

It is worth to underline that the rotor losses are not considered within the design process, therefore the temperature of the rotor components need to be verified in a second stage. Fig. 4.20b,c and d reports the rotor, sleeve and magnet temperatures of the optimal designs. As expected, the temperatures of those rotor components tend to increases with the speed and decreases with

the airgap thickness. Except for the lower airgap thickness (i.e. 0.5 mm), such temperature lie within a small range.

## **4.5 Publications**

Some results presented in this chapter have been published by the author in [122].

# Chapter 5

## Comparison among technologies

In this chapter a final comparison among three machine topologies (SyR, PMaSyR and SPM) is presented. The comparison is carried out considering the following assumptions, constraints and choices.

- The outer envelope and the axial length are both fixed to 30 mm.
- The magnetic load is fixed to the knee value of the stator material BH curve.
- A laminated rotor is selected for the SyRM and PMaSyRM cases, while a solid one is adopted in the SPM scenario.
- The three machine topologies share the stator material (10JHNF600).
- A single layer distributed winding featuring a number of slot equal to 24 is adopted and the number of pole pairs is 2 for all the designs.
- The number of flux barriers is set to 3 for the SyR and PMaSyR designs.
- The acceptable temperature is below 150 degrees for the winding and the PMs.
- In the PM-assisted scenario, the PM are sized using the natural compensation criterion and the adopted PM material is NdFeB-40, featuring a residual flux density equal to 1.22 T for the considered temperature range.

- The PM material adopted for the SPM case is SmCo28, featuring a residual flux density equal to 1.06 T for the considered temperature range.

According to the above specifications, the comparison is carried out considering different airgap thickness and cooling system capability so to infer the influence of these two parameters on the machine performance.

The methodology resembles the one of the last 3 chapters:

- for each machine topology, design speed, cooling system and airgap thickness, the hybrid analytical procedure is applied and the torque and power factor in the split ratio/magnetic ratio plane are evaluated;
- from the design plane, the maximum torque solution is selected and all the machine candidates are compared in terms of torque, power factor, power and geometry.

## 5.1 Overview on the design process

The design methodology is here briefly re-called. It starts with the definition of two independent design variables, namely split and magnetic ratios.

For a given outer envelope (i.e.  $r_s$  and the active axial length  $l_{fe}$  are fixed) and for a given magnetic load  $B_{fe}$  the combination of  $sr - mr$  defines the complete stator and rotor geometry reported in Fig. 5.1. Indeed, the stator can be defined by 3 main parameters: the tooth width, yoke thickness and tooth length. The first two parameters can be easily determined as follows:

$$w_t = \frac{2 \cdot \pi \cdot sr \cdot r_s}{6 \cdot p \cdot q} \cdot \frac{B_{g-max}}{B_{fe}} \quad (5.1)$$

$$l_y = \frac{1}{2} \cdot \frac{2\pi \cdot sr \cdot r_s}{p} \cdot \frac{B_{g-avg}}{B_{fe}} \quad (5.2)$$

where the formulation of  $B_{g-max}$  and  $B_{g-avg}$  changes according to the machine type. In SyR or PMAyR cases, the airgap flux density is due to d-axis magnetizing current, therefore it



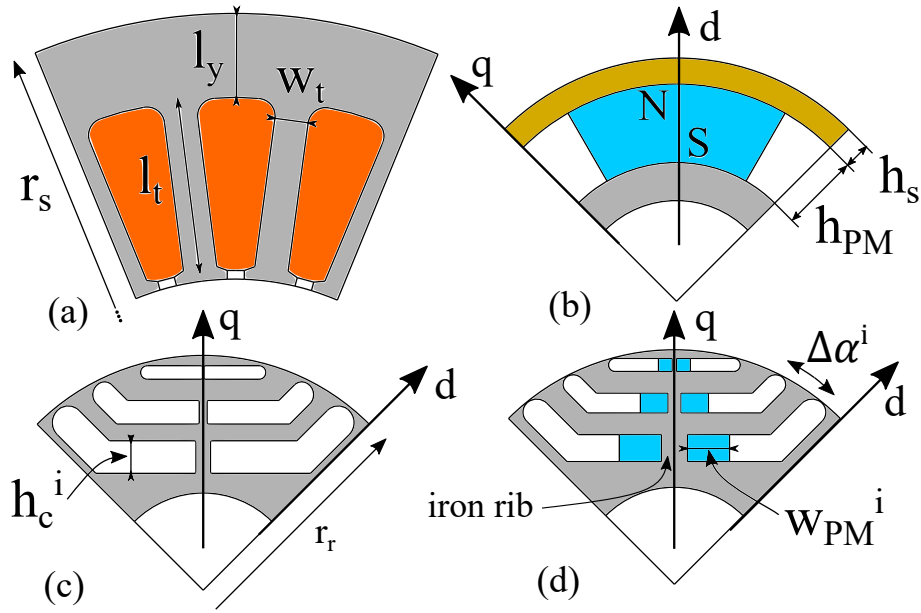


Figure 5.1: Stator (a) and rotor (b,c,d) parametrizations.

is assumed to be sinusoidal and its average value can be calculated as follows:

$$B_{g-avg} = \frac{2}{\pi} \cdot B_g = \frac{2}{\pi} \cdot mr \cdot B_{fe} \quad (5.3)$$

while its maximum value  $B_{g-max}$  coincides with  $B_g$ .

Differently, in the SPM case, the no-load airgap flux density can be approximated with a rectangular shape and its average value calculated as follows:

$$B_{g-avg} = \alpha_{PM} \cdot B_{g-max} \quad (5.4)$$

where  $B_{g-max}$  is the peak value of the rectangular waveform:

$$\begin{aligned} B_{g-max} &= \alpha_{PM} \cdot \frac{\pi}{4 \cdot \cos \left[ \frac{\pi \cdot (1 - \alpha_{PM})}{2} \right]} \cdot B_g = \\ &= \alpha_{PM} \cdot \frac{\pi}{4 \cdot \cos \left[ \frac{\pi \cdot (1 - \alpha_{PM})}{2} \right]} \cdot mr \cdot B_{fe} \end{aligned} \quad (5.5)$$

### 5.1.1 Rotor design

The main difference between SyR based machines and SPM ones is related to the rotor design. In the first case, the rotor design include the flux barriers, iron ribs and, possibly, the PM within the rotor slots as reported in chapters 2 and 3; the magnetic circuit reported in Fig. 5.2 is often used to properly design the PMs according to a specified criterion (PMAyRMs case) and compute the q-axis flux (SyRM and PMAyRM cases). Differently, a SPM rotor can be

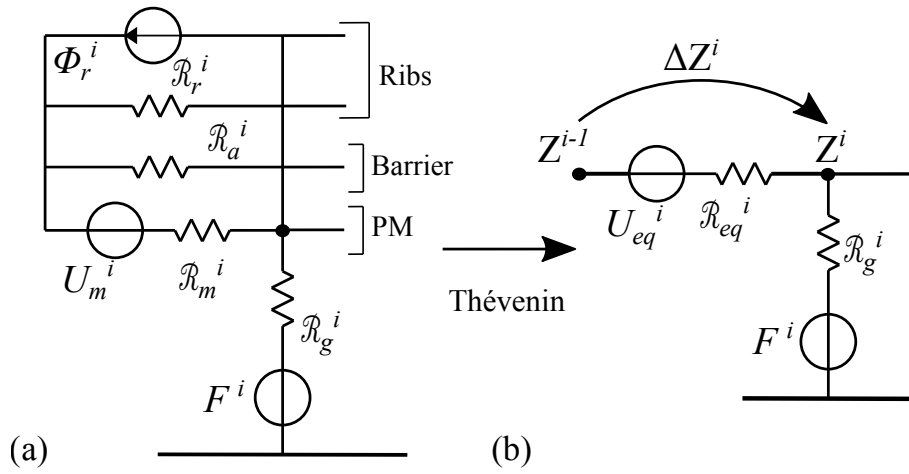


Figure 5.2: q-axis magnetic equivalent circuit before (a) and after (b) the Thévenin transformation.

described by the PM radial thickness and span over the pole pitch and by the sleeve thickness as well explained in chapter 4; the PM and sleeve thicknesses design can be performed adopting an iterative procedure which includes both the electromagnetic (i.e. the needed airgap flux density at no-load) and structural (i.e. centrifugal forces and thermal expansion) issues.

The following rules for the rotor design are briefly re-called for the sake of clarity.

- The SyR and PMAyR rotors are designed so to obtain an uniform distribution of the equivalent rotor slots and flux barriers sharing the same permeance; the iron ribs are sized according to a simplified formulation which accounts for the steady-state centrifugal forces.
- The PMs design in the PMAyR case is performed adopting the *Natural compensation* criterion.

- The PMs in the SPM case are designed so to reach the desired flux density for each combination of  $sr - mr$  in the design plane; in particular, the angular span is fixed while the only variable is the PM radial thickness  $h_{PM}$ .

### 5.1.2 Comparison setup

The comparison between the three machine topologies is performed in terms of design speed, airgap thickness and cooling system capability. It is worth to underline that a constant stator losses scenario is hereafter considered, therefore the maximum current is computed as in (5.6).

$$I_{max} = \frac{1}{3N_s} \sqrt{\frac{k_{fill} A_{slots}}{2\rho_{cu}(l_{fe} + l_{ew})} (2\pi r_s l_{fe} k_{cool} - P_{fe-st})} \quad (5.6)$$

where all the variables and parameters have been defined in the last chapters.

In particular, the following workflow is adopted:

- for each machine type, airgap thickness, design speed and  $k_{cool}$  the main performance in the  $sr - mr$  plane are evaluated and the maximum torque solution is selected; an example is reported in Fig. 5.3.

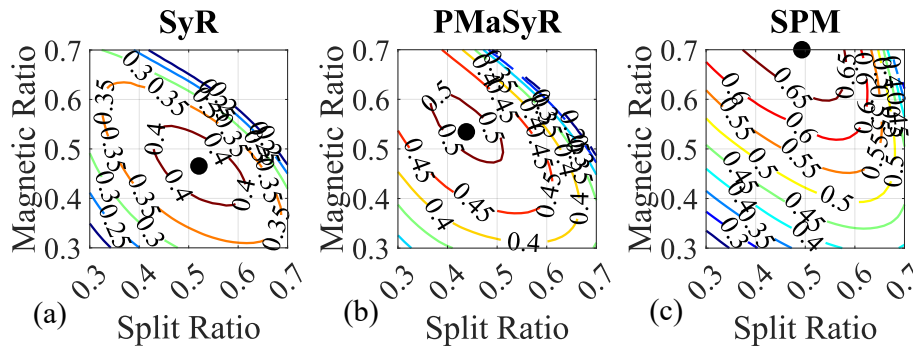


Figure 5.3: Example of torque in  $sr - mr$  plane for SyR (a), PMaSyR (b) and SPM cases (c).

- by doing so, it is possible to compare the three machine technologies in terms of:
  - maximum torque/power as function of the speed for a given airgap thickness and cooling system;

- evaluate the influence of the cooling capability and the airgap thickness with respect to the machine type;
- analyze how the optimal design variables  $sr$  and  $mr$  change with respect to the machine type, cooling system, speed and airgap thickness.

## 5.2 Performance vs speed

Fig. 5.4 shows the power of the optimal (torque wise) designs as a function of the speed, for the three different machine topologies. The lowest power, and therefore also the lowest power density since the outer envelope is fixed, is provided by the SyR machine, whereas the highest one is given by the SPM machine type. This expected result does not depend either on the airgap thickness or the cooling system. Differently, the rate of the power improvement is actually affected by airgap thickness: lower  $g$  implies more comparable results between the three cases, while SPMs clearly outcompete the other two machine types for higher  $g$ . It can be also noticed that the higher airgap thickness values do not result in power decrements only when considering the SPM case, while SyR and PMAyR performance are greatly affected by  $g$ .

This behavior can be explained by electromagnetic and geometrical considerations.

- In the SyR case, for a given  $sr - mr$  combination (i.e. given stator and rotor design) the increment of the airgap thickness leads to an increment of the  $i_d$  current since  $B_g$  (imposed by the magnetic ratio) is inversely proportional to  $g$ ; this behavior can be observed in Fig. 5.5 where the d-axis current in the  $sr - mr$  plane is reported for three different airgap thickness. In such figure of merit, the cooling system and the speed are given and are equal to  $50\text{kW/m}^2$  and  $40\text{krpm}$ . Clearly,  $i_d$  increases moving from  $0.3\text{ mm}$  (Fig. 5.5a) to  $1\text{ mm}$  (Fig. 5.5b) and  $1.5\text{ mm}$  (Fig. 5.5c) and the rate of such increment is almost inversely proportional to the  $g$  one.

However, increasing the d-axis current implies a reduction of the q-axis one (since the

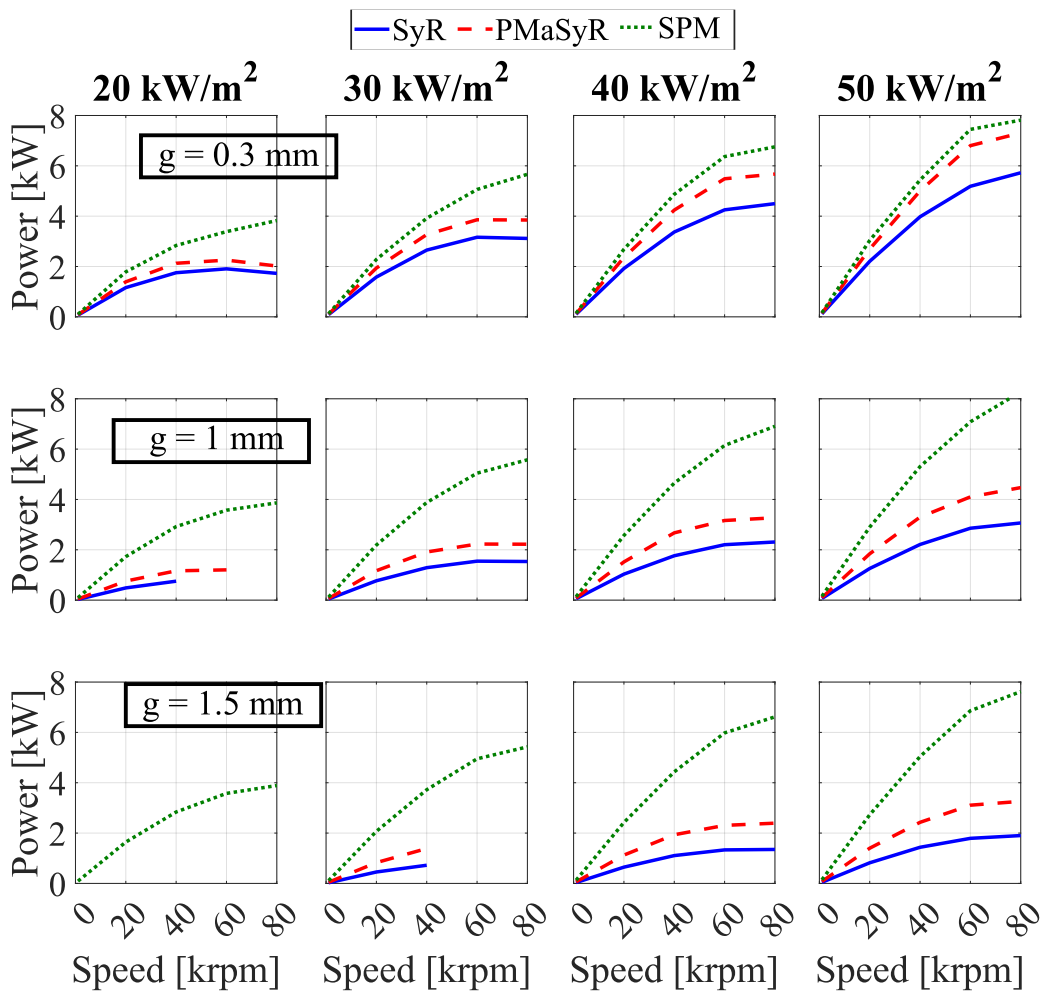


Figure 5.4: Power of the optimal (torque wise) designs vs speed for different airgap thicknesses and cooling system capabilities.

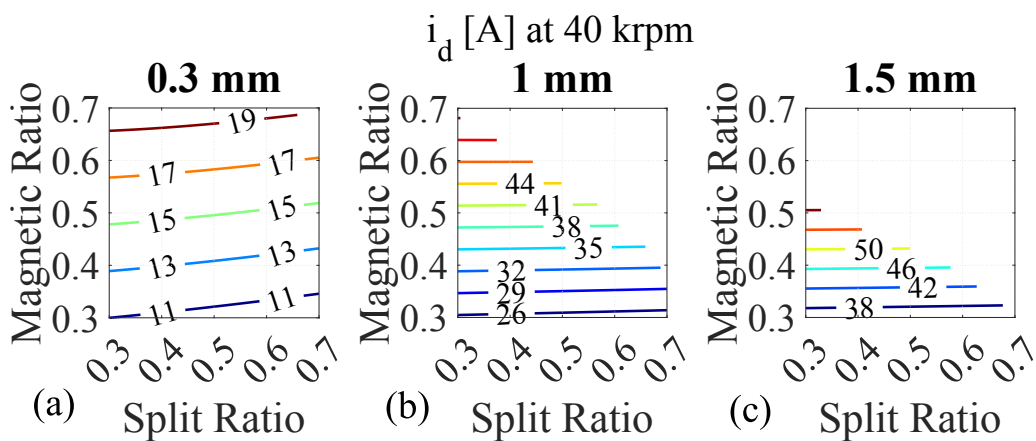


Figure 5.5: SyRM  $i_d$  in the  $sr - mr$  plane for a given speed (40 krpm) and cooling system capability (50 kW/m<sup>2</sup>) when considering an airgap thickness equal to (a) 0.3 mm, (b) 1 mm and (c) 1.5 mm

cooling system capability is fixed), thus "compensating" the d-axis current increment, as shown in Fig. 5.6 which shows the  $i_q$  constant loci in the  $sr - mr$  for a given cooling system and design speed, when considering an airgap equal to 0.3 mm (Fig. 5.6a), 1 mm (Fig. 5.6b) and 1.5 mm (Fig. 5.6c).

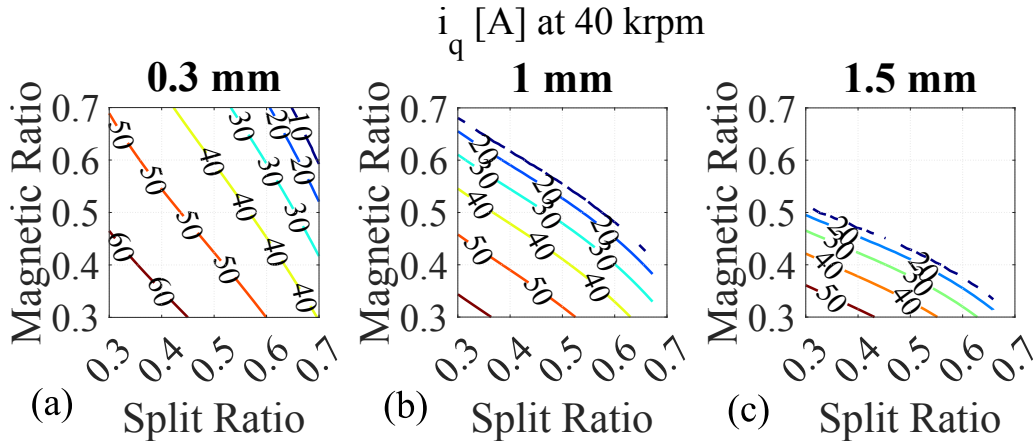


Figure 5.6: SyRM  $i_q$  in the  $sr - mr$  plane for a given speed (40 krpm) and cooling system capability ( $50 \text{ kW/m}^2$ ) when considering an airgap thickness equal to (a) 0.3 mm, (b) 1 mm and (c) 1.5 mm

However, the saliency ratio ( $L_{dm}/L_{qm}$ ) decreases with the airgap thickness, as shown in Fig. 5.7 which reports the saliency ratio over the  $sr - mr$  for a given speed and cooling system capability in the three airgap cases. Such reduction of the saliency ratio is given by the decrement of the d-axis inductance (Fig. 5.8) whereas the q-axis one remains almost constant (Fig. 5.9). The decrement of the d-axis inductance with the airgap thickness is due to the fact that, since the  $B_g$  is imposed for a given  $sr - mr$  combination, also the d-axis flux does not change with  $g$ ; it follows that, since the d-axis current increases with  $g$ , the d-axis inductance, given by (5.7), has to decrease.

$$L_{dm} = \frac{\lambda_{dm}}{i_d} \quad (5.7)$$

In 5.7,  $\lambda_{dm}$  is the magnetizing flux (which does not include the leakage fluxes) and it is independent by  $g$  for a given  $sr - mr$  combination.

Conversely, the q-axis inductance remains almost constant since the reduction of the q-

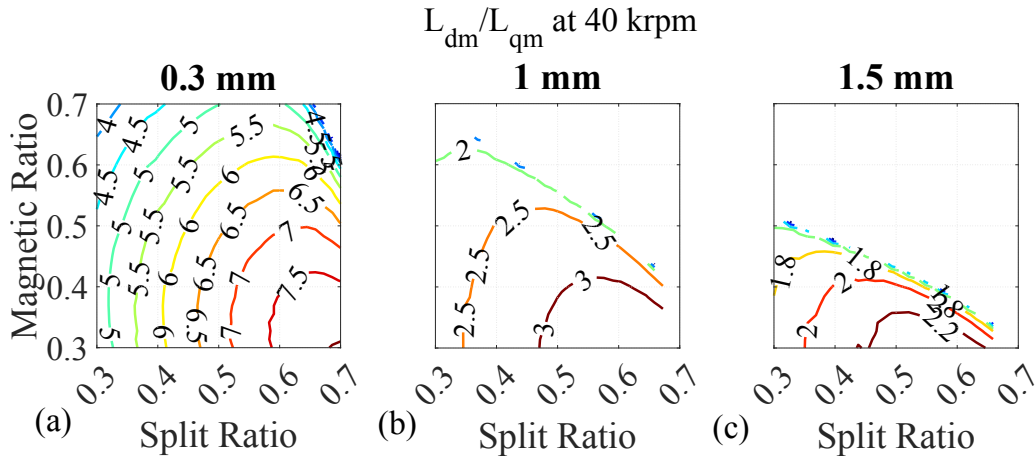


Figure 5.7: SyRM saliency ratio in the  $sr - mr$  plane for a given speed (40 krpm) and cooling system capability ( $50 \text{ kW/m}^2$ ) when considering an airgap thickness equal to (a) 0.3 mm, (b) 1 mm and (c) 1.5 mm

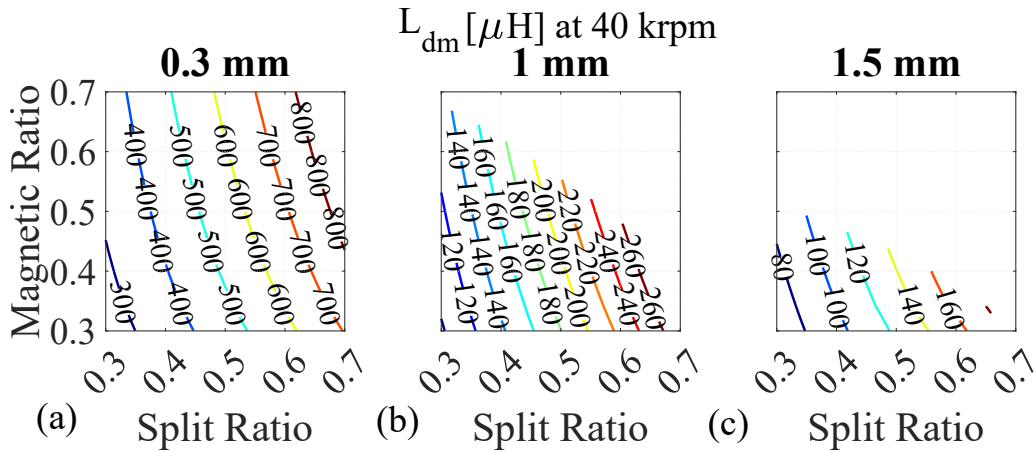


Figure 5.8: SyRM d-axis magnetizing inductance in the  $sr - mr$  plane for a given speed (40 krpm) and cooling system capability ( $50 \text{ kW/m}^2$ ) when considering an airgap thickness equal to (a) 0.3 mm, (b) 1 mm and (c) 1.5 mm

axis current leads to a proportional decrement of the q-axis flux (being the q-axis airgap flux density not imposed). Clearly, since higher  $g$  implies higher flux leakages, the reduction of the q-axis flux is slightly higher than the q-axis current one, therefore also  $L_{qm}$  tends to slightly decrease with the airgap.

- The above point also applies to the PMaSyRM case, but in this case the presence of the PMs always leads to a power improvement with respect to the SyRM case; however, the power density achievable with a PM assisted machine is clearly affected by the PM inser-

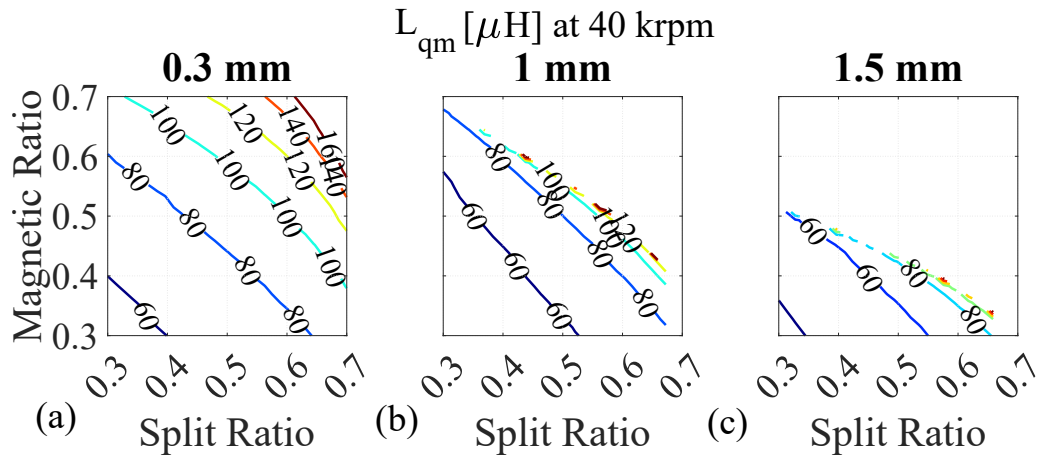


Figure 5.9: SyRM d-axis magnetizing inductance in the  $sr - mr$  plane for a given speed (40 krpm) and cooling system capability ( $50 \text{ kW/m}^2$ ) when considering an airgap thickness equal to (a) 0.3 mm, (b) 1 mm and (c) 1.5 mm

tion design criterion (see chapter 3 for more details). Adopting the *natural compensation* criterion allows to increase the constant power speed range (CSPR) but not the maximum torque (which could be reached by filling the flux barriers with PMs).

- Differently, when considering the SPM case, there is not a magnetizing current ( $i_d = 0$ ), therefore for a given  $sr - mr$  combination increasing  $g$  leads to an increment of the PM height, without affecting the q-axis current thus keeping almost unchanged the output power. Clearly, the increment of the leakage fluxes and the impact of the geometrical constraints (e.g. shaft radius) result in a slightly power reduction as  $g$  increases also in the SPM case.
- Finally, while in the SPM case there are always feasible machines in the considered range of  $k_{cool}$  and  $g$ , SyRM and PMSyRMs do not provide any possible machine geometry for lower values of the cooling system capability and higher values of the airgap thickness. This is to the fact that high  $g$  and low  $k_{cool}$  lead to an increment of the d-axis current and a reduction of the maximum one, thus greatly reducing the q-axis component of the stator current.

Fig. 5.10 reports the internal power factor of the optimal (torque wise) designs as a function of the speed, for the three different machine topologies. The following considerations can be



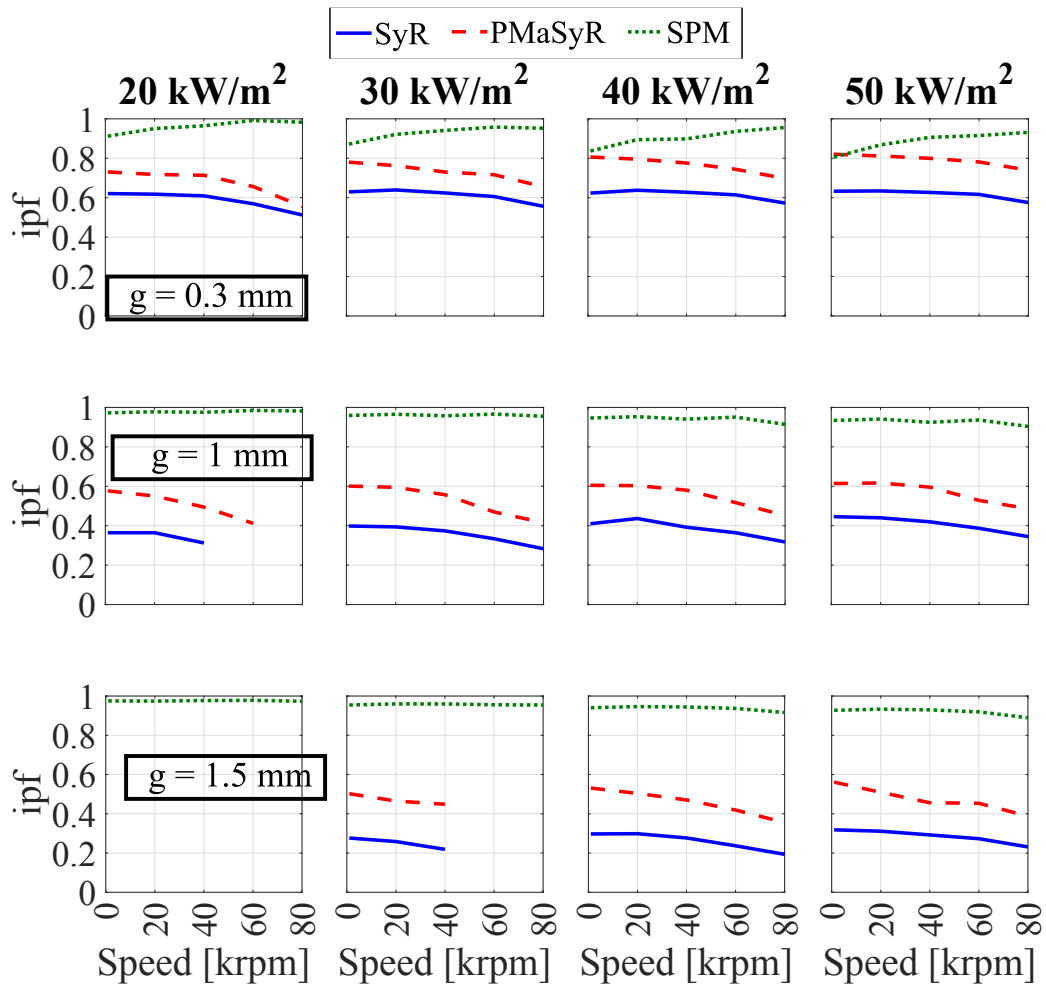


Figure 5.10: Internal power factor of the optimal (torque wise) designs vs speed for different airgap thicknesses and cooling system capabilities.

deduced:

- the highest  $ipf$  is always provided by the SPM case, regardless the airgap thickness or the cooling system capability. Higher  $g$  emphasizes such behavior. Indeed, the  $ipf$  formulation for an isotropic machine with  $i_d = 0$  can be written as follows:

$$ipf = \frac{\lambda_{PM}}{\sqrt{\lambda_{PM}^2 + (L \cdot i_q)^2}} \quad (5.8)$$

where  $\lambda_{PM}$  is the PM flux and  $L$  is the inductance. The increment of  $g$  leads to an inductance decrement, thus allowing a power factor improvement. From the same figure, one can notice that, as the speed increases, the  $ipf$  tends to increase only when consider-

ing the lowest airgap thickness, while it remains almost constant or starts to decrease for higher airgap thicknesses.

The first behavior can be explained according to the previous inductance consideration: increasing the design speed implies a wider sleeve thickness which in turn increases the equivalent magnetic airgap and therefore an inductance decrement is detected; differently,  $\lambda_{PM}$  does not change since a more demanding structural need results in a higher PM radial thickness keeping unchanged the airgap flux density  $B_g$ .

This kind of reasoning is clearly valid as long as the increment of the sleeve thickness does not imply geometrical issues: indeed, higher mechanical airgap thickness leads to wider PMs height which in turn increases the sleeve thickness; if the latter becomes large enough, the available space for the PM placement could be reduced thus leading to a  $\lambda_{PM}$  decrement and, as a consequence, also the power factor starts to decrease.

Differently, for a given design speed and airgap thickness, the  $ipf$  tends to slightly decrease with the cooling system capability  $k_{cool}$ ; also this behavior can be explained using eq. (5.8): higher  $k_{cool}$  implies higher q-axis current, thus reducing the power factor.

- In the SyR and PMaSyR cases, the  $ipf$  present similar trends, despite the adoption of the PM-assisted technology clearly allows to increase its absolute value. The latter tends to decrease with the design speed and with the airgap thickness. Although not immediate, the reason behind such trend can be explained according to the classical  $ipf$  formulation:

$$ipf = \sin \left[ \arctan \left( \frac{i_q}{i_d} \right) - \arctan \left( \frac{\lambda_q}{\lambda_d} \right) \right] \quad (5.9)$$

where  $\lambda_q$  and  $\lambda_d$  are the current and flux components in the d-q reference frame. The latter depends either on the inductance and, in the PMaSyR case, also on the PM flux:

$$\lambda_d = (L_{dm} + L_s)i_d \quad (5.10)$$

$$\lambda_d = (L_{qm} + L_s + L_{rib})i_q - \lambda_{PM} \quad (5.11)$$

if the cross-coupling influence is neglected. As the speed increases,  $L_{rib}$  increases thus leading to increment of the q-axis flux which in turn determines a flux angle increment since the d-axis flux does not change with the speed. Furthermore, the maximum current decreases with the speed according to eq. (2.30) while its d-axis component remains constant, thus leading to a q-axis current decrement. It follows that the current phase angle tends to decrease for a given  $sr - mr$  combination as the speed increases. The above two trends (flux and current phase angles increment and decrement) clearly reduce the internal power factor according to eq. (5.9).

A similar consideration can be extended to  $ipf$  trend with respect to the airgap thickness. Indeed, higher  $g$  imply lower current angle ( $i_d$  increases while  $i_q$  slightly decreases as in Fig. 5.5 and Fig. 5.6) while the flux one does not change significantly.

Dealing with PMSyR designed using the *natural compensation* criterion, the above reasoning can be still applied. Indeed, the PM contribution only increase the absolute value of the  $ipf$ , while its trends basically resemble the SyRM case ones.

Differently from the SPM case, both in the SyRM and PMSyRM ones, the  $ipf$  tends to slightly increase with the cooling system capability for a given design speed and airgap thickness. This trend can be explained considering that the increment of  $k_{cool}$  leads to a  $i_q$  increment too which in turn determines an higher current phase angle in eq. (5.9); however, the flux phase angle tends to slightly increase according to the  $i_q$  increment (such increment is mitigated by the reduction of the q-axis inductance caused by the saturation): it follows that the difference between the current and flux phase angle remains almost constant or slightly decreases according to trade-off between current and flux phase angle increments.

### 5.3 Optimal machines analysis

The optimal designs, i.e. the ones providing the maximum torque in the design plane, can clearly feature different geometries since the combination  $sr - mr$  which maximizes the torque

for a given airgap thickness, cooling system and maximum speed is the result of several compromises among structural, thermal and electromagnetic needs.

Different  $sr - mr$  combinations imply different stator and rotor geometries. Indeed, the  $sr$  mainly influences the rotor radius and structural parameters (iron ribs and sleeve) whereas the  $mr$  basically defines the iron parts, including the teeth and yokes width. Higher  $mr$  leads to higher iron parts width, and viceversa.

The rotor radius of the optimal designs as a function of the speed, for the three different machine topologies, is shown in Fig. 5.11, whereas Fig. 5.12 reports the tooth width of the same designs.

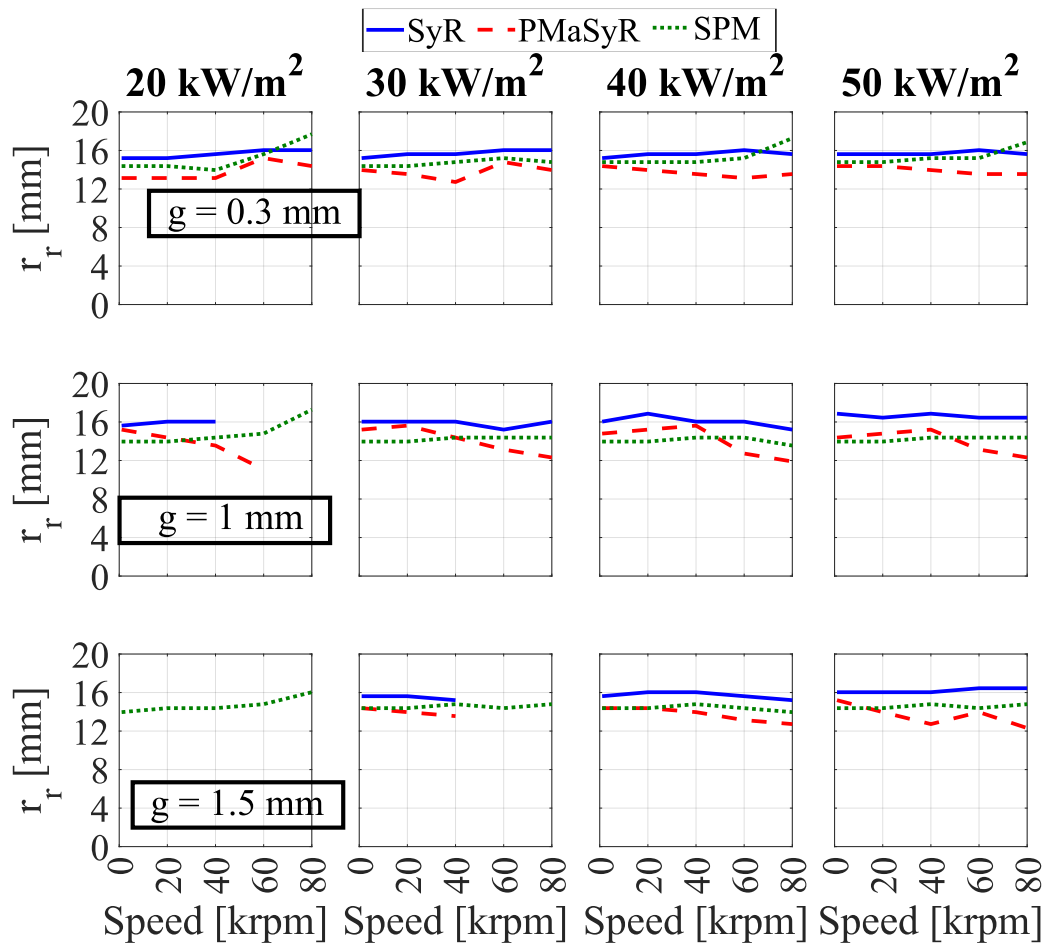


Figure 5.11: Rotor radius of the optimal (torque wise) designs vs speed for different airgap thicknesses and cooling system capabilities.

The rotor radius tends to remain constant or slightly increases with the speed, when the

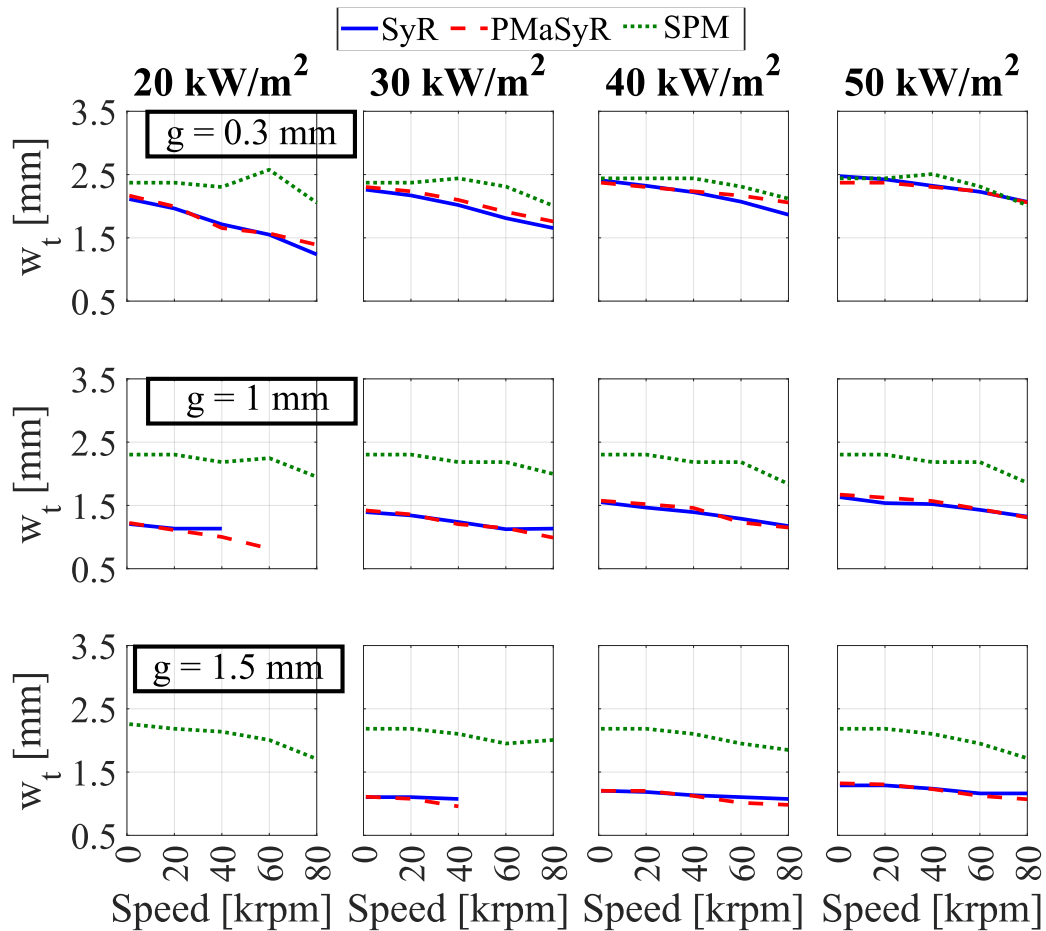


Figure 5.12: Tooth width of the optimal (torque wise) designs vs speed for different airgap thicknesses and cooling system capabilities.

airgap thickness is equal to 0.3 mm, regardless the machine topology or the cooling system. Such trends also apply to the other airgap thicknesses when considering the SyR and SPM cases. Differently,  $r_r$  slightly decreases with the speed in the PMAyR case.

Conversely, the tooth width decreases with the speed for all the machine topologies, cooling system capabilities and airgap thicknesses.

The reason behind such trends have been deeply analyzed in the last chapters for the three machine topologies.

Fig. 5.13, 5.14 and 5.15 reports the cross-sections of the above optimal machines thus visually confirming the rotor radius and tooth width considerations. It is worth to underline that the optimal machines' shapes of PMAyR resemble the ones of the SyR case. This behavior is heavily affected by the adopted PM design criterion: indeed, the *Natural compensation ap-*

proach leads to rotor configurations with low amount of PM within the rotor slots. It follows that the PM torque does not influence substantially the total torque in the  $sr - mr$  plane, therefore the maximum torque solution is near to the one providing by the pure SyRM machine.

The tooth width, yoke and flux guide thicknesses clearly decrease as both the airgap thickness and maximum speed increase but, while the rate of decrement with the speed is similar for the three machine topologies, the decrement with the airgap thickness is less pronounced in the SPM case. This is due to the less strict limits for the SPM rotor design, whose PM height can be increased to reach a higher magnetic ratio and therefore a higher torque too.

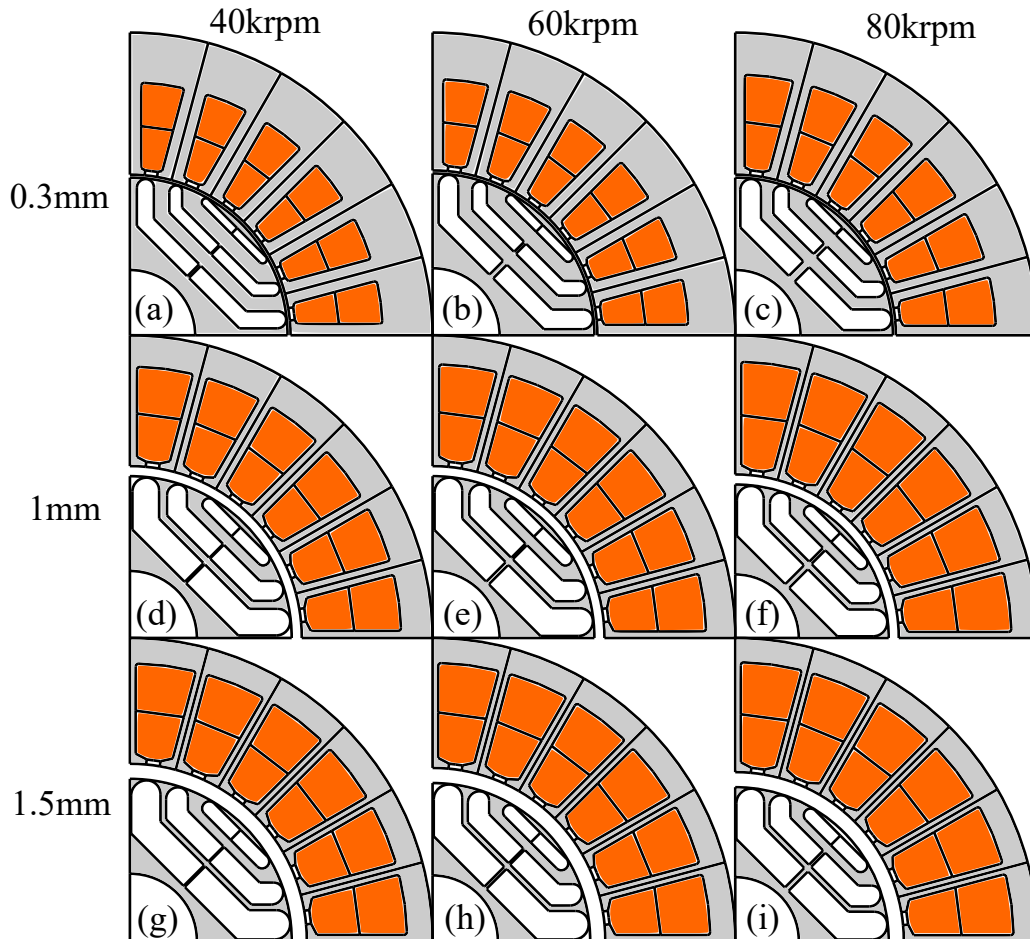


Figure 5.13: Cross sections of the optimal SyR machines at (a,d,g) 40 krpm, (b,e,h) 60 krpm and (c,f,i) 80 krpm when the airgap thickness is (a,b,c) 0.3 mm, (d,e,f) 1 mm, (g,h,i) 1.5 mm and d) 2 mm for a cooling system capability equal to  $40 \text{ kW/m}^2$ .

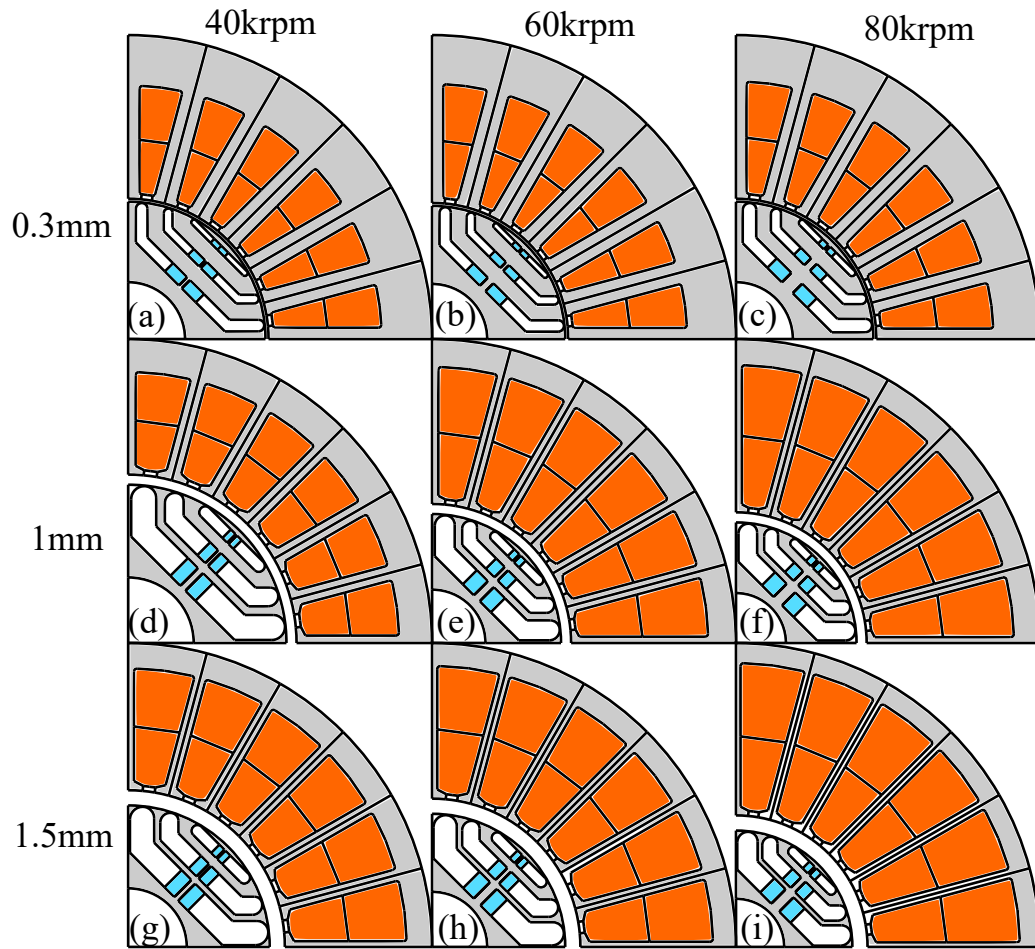


Figure 5.14: Cross sections of the optimal PMSyR machines at (a,d,g) 40 krpm, (b,e,h) 60 krpm and (c,f,i) 80 krpm when the airgap thickness is (a,b,c) 0.3 mm, (d,e,f) 1 mm, (g,h,i) 1.5 mm and d) 2 mm for a cooling system capability equal to  $40 \text{ kW/m}^2$ .

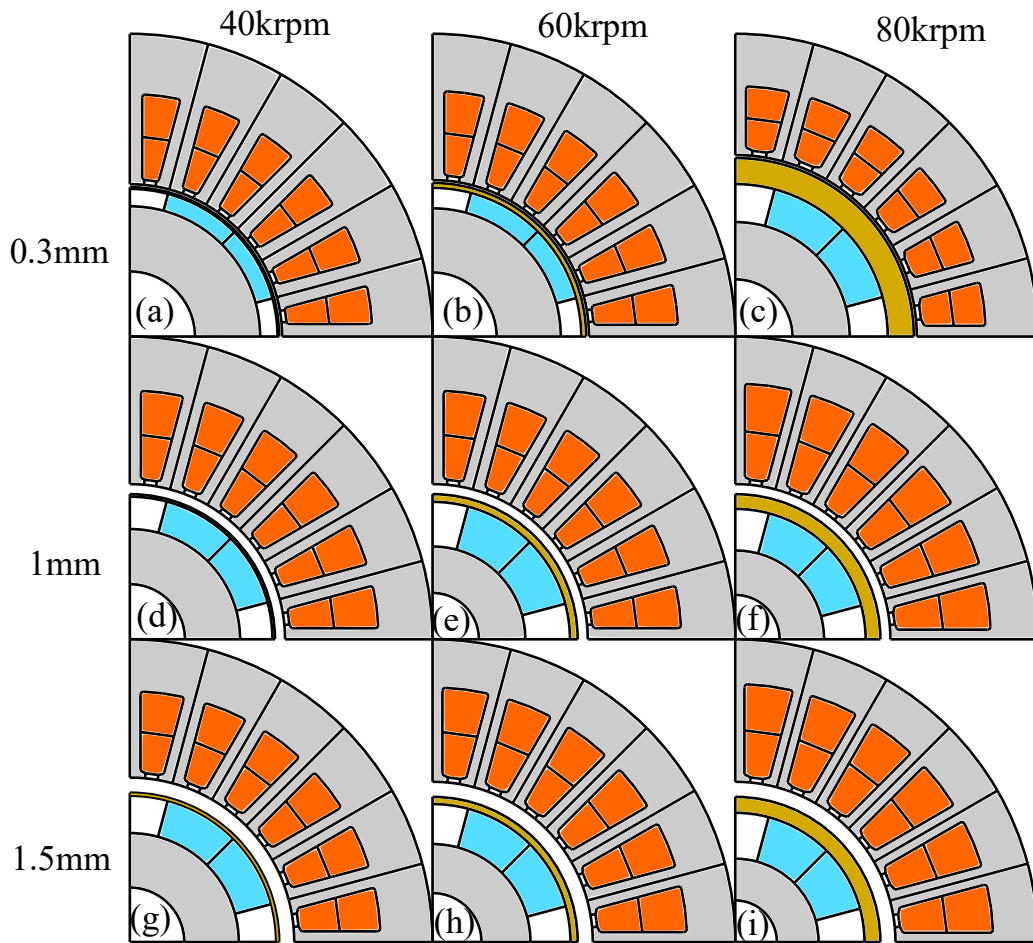


Figure 5.15: Cross sections of the optimal SPM machines at (a,d,g) 40 krpm, (b,e,h) 60 krpm and (c,f,i) 80 krpm when the airgap thickness is (a,b,c) 0.3 mm, (d,e,f) 1 mm, (g,h,i) 1.5 mm and d) 2 mm for a cooling system capability equal to  $40 \text{ kW/m}^2$ .



# Chapter 6

## Experimental results

This chapter describes the experiment tests performed on four different machine prototypes.

In particular, the proposed hybrid design approach and subsequent considerations have been validated with experimental tests on two SyRM prototypes:

- the first one is based on the constraints, assumptions and choices reported in Table 2.1 and whose stator and rotor laminations are composed by a CoFe alloy (Vacodur 49), whose first variant was presented in [31];
- the second one is based on the constraints, assumptions and choices reported in Table 2.4 and whose stator and rotor laminations are made of a SiFe alloys (10JNHF600 for the stator and 35HXT780T for the rotor, i.e. the best material combinations of the section 2.6 at 80krpm).

The two machines present different maximum speeds: 50krpm and 80krpm respectively. Several tests will be shown, aiming at fully characterizing the machine behavior under different operating conditions.

Then, the extension of the design methodology to the PM-assisted scenario has been validated by the selection of a particular machine from the optimal results of chapter 3. Then, after a more in depth description of a design refinement stage, which includes the re-distribution of the PMs and the structural iron ribs optimization, the machine has been tested so to identify its

---

magnetic model and to evaluate its high-speed behavior.

Finally, the design considerations about the SPM case have been validated against experimental findings on a 4.2 kW prototype.

## 6.1 SyRM

### 6.1.1 CoFe machine

The 5kW-50krpm machine was designed with a multi-objective optimization algorithm targeting the average torque and the torque ripple using different lamination materials. Fig. 6.1 reports a comparison between the optimal designed machine (c3 machine of Fig. 2.25) and the prototype, in terms of position in the  $sr - mr$  plane (6.1a) and overall geometry (6.1b). The

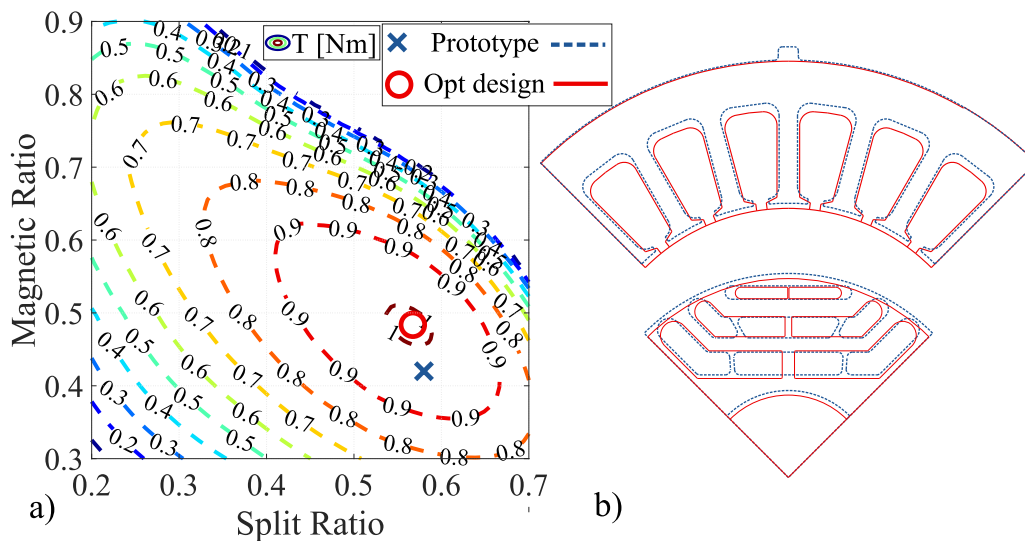


Figure 6.1: Comparison between optimal designed machine and actual prototype.

prototype has a split ratio and magnetic ratio of 0.58 and 0.42, respectively, while the optimal design has  $sr = 0.56$  and  $mr = 0.48$ . Although not identical, these two machines are very similar, and for this reason the existing prototype has been used to validate the presented design methodology.

The rotor structural design, i.e. the positioning of the iron ribs, was performed via a structural sensitivity FEA and the cross section of the manufactured machine is reported in Fig. 6.2d. In particular, an electromagnetic optimization of the rotor geometry was performed according to [123].

The optimization routine is performed so to maximize the average torque and minimize the torque ripple, by varying the barriers' thicknesses shape, position and orientation at the airgap,

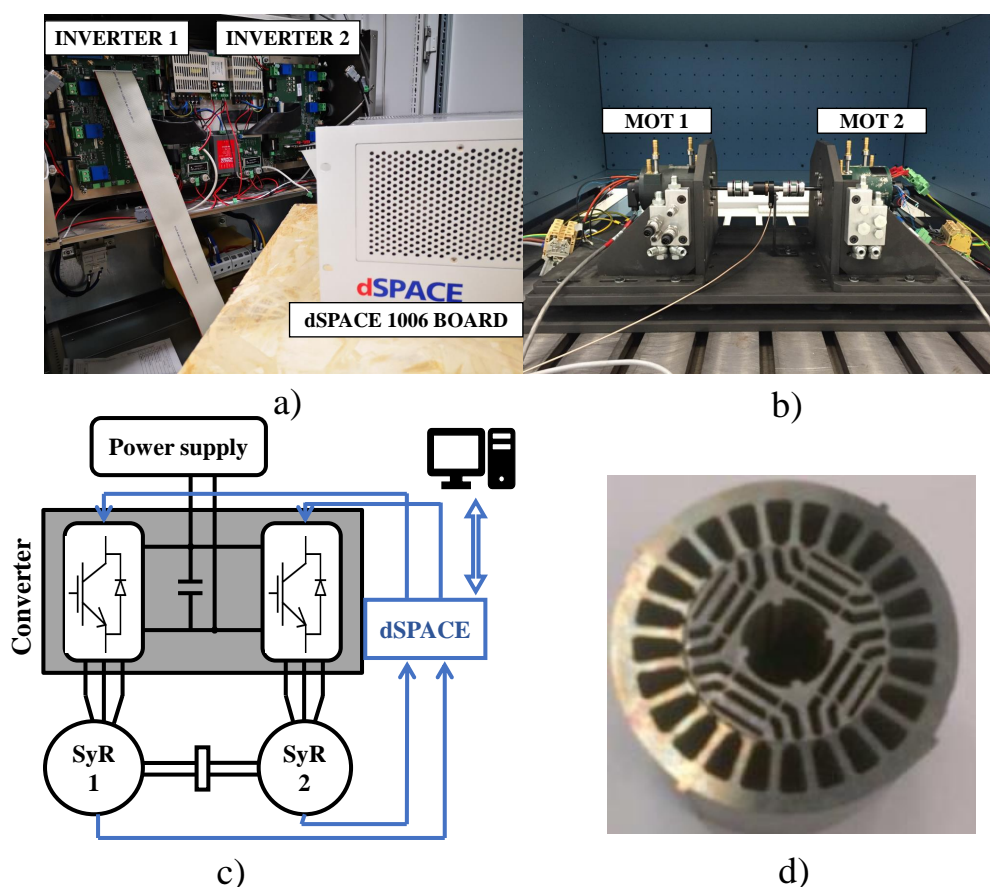


Figure 6.2: a) Inverter and dSpace board , b) Back-to-back motors, c) Experimental set-up layout, d) Top view of the laminations stack.

considering one operating condition (i.e. the rated one) and by also optimizing the current phase angle to easily evaluate the MTPA without further simulations. Such design optimization procedure and its effectiveness have been deeply investigated and validated in [124].

The total rib thicknesses per barrier are equal to the ones calculated with the proposed analytical approach (since it was designed using the same analytical mechanical formulation). In particular the outermost barrier shows higher tangential iron ribs with respect to the designed one, in order to avoid the manufacturing of the respective radial rib (whose width is too close to the mechanical tolerances). The final radial iron ribs of the middle and innermost barrier are rotated and splitted in two as shown in Fig. 6.1b.

Fig. 6.2c shows the experimental test set-up consisting of two identical SyR motors mechanically coupled (Fig. 6.2b) whose cross-section of the laminations stack is shown in Fig. 6.2d, a

20-kHz back-to-back IGBT 2-level converter fed by a dc voltage source (270V) and a dSPACE 1006 board (Fig. 6.2a) where the vector control strategy is implemented. Two different experiments have been performed, the first one aimed at identifying the flux-current relationship with the method presented in [125]. while the second aimed at verifying the dynamic behaviour of the system at the maximum speed. In the former, several combinations of  $i_d$  and  $i_q$  have been considered.

During the magnetic model identification test, one machine is speed controlled, whereas the other one, whose model has to be identified, is torque controlled. Indeed, this experimental identification technique does not rely on the stator resistance knowledge (which changes with the temperature), does not make use of the voltage measurements, and does not need any inverter non-linearities compensation. It allows the identifications of the fluxes for every point in the d-q axis current plane via a sequence of two tests carried at constant speed in motoring mode ( $-m$ ) and generating mode ( $-g$ ). Imposing two complex conjugate current vectors, the machine produces two complex conjugate flux linkage vectors; manipulating the vector voltage equations in these two operating conditions allows estimating the flux components:

$$\lambda_d = \frac{v_{q-m} + v_{q-g}}{2 \cdot w} \quad \lambda_q = -\frac{v_{d-m} - v_{d-g}}{2 \cdot w} \quad (6.1)$$

where the  $w$  is the test electrical speed. Figure 6.3 shows currents, voltages, speed and torque recorded with the control platform during the experimental identification of one point of the d-q current plane.

The variables used to estimate the flux linkages have been averaged over the time window (mechanical period) placed in the last part of each operating mode in order to consider only the fundamental harmonics.

The identification tests performed on the prototype machine have shown a non-negligible mismatch between the experimental and FE-computed fluxes leading to an electromagnetic torque lower (0.7 Nm) with respect to the FE one (0.99 Nm), as reported in Fig. 6.4a. The experimental torque has been measured with a torque-meter and also estimated by the crossing

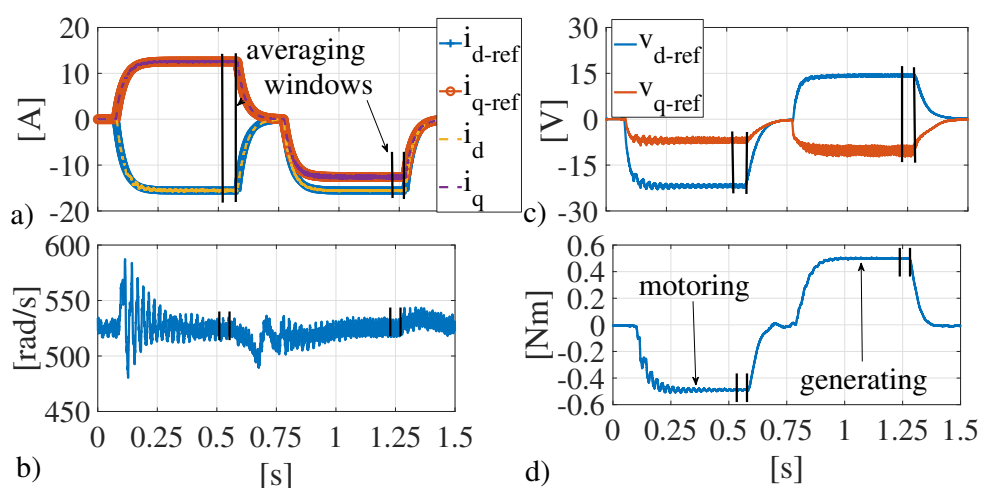


Figure 6.3: a) Reference and measured currents, b) measured speed, c) reference voltages, and d) measured torque transients during the experimental identification test of one d-q current combination.

product between current and fluxes. This latter value have been used for the comparison. This discrepancy can be mainly ascribed to the manufacturing tolerances. In fact, when simulating a rotor geometry considering the worst case scenario in terms of manufacturing tolerances (iron ribs increases of 0.05mm), then the error becomes much smaller, as reported in Fig. 6.4c and 6.4d. These sub-figures highlight a good agreement between the measured d- and q-axis fluxes and the ones FE-calculated when considering the manufacturing tolerances. Consequently, a good match is also achieved in terms of average torque as reported in Fig. 6.4b. The remaining mismatch between FE and experimental q-axis flux, which leads to the torque mismatch reported in Fig. 6.4b, can be ascribed to several reasons, e.g. the residual geometric differences between the prototype and the FE model, different magnetic behaviour (in terms of BH curve) of the material. Re-evaluating the performance with the analytical model leads to a torque of 0.79 Nm compared to the FE one of 0.75 Nm and the experimental one of 0.7 Nm, as reported in the inset of Fig. 6.4b. In the same operating condition, the FE-computed internal power factor is 0.41 whereas the experimental one is 0.40. Fig. 6.5a shows the result of an acceleration test from zero to 50 krpm without load torque, whereas Fig. 6.5b reports the reference voltages during the same test.

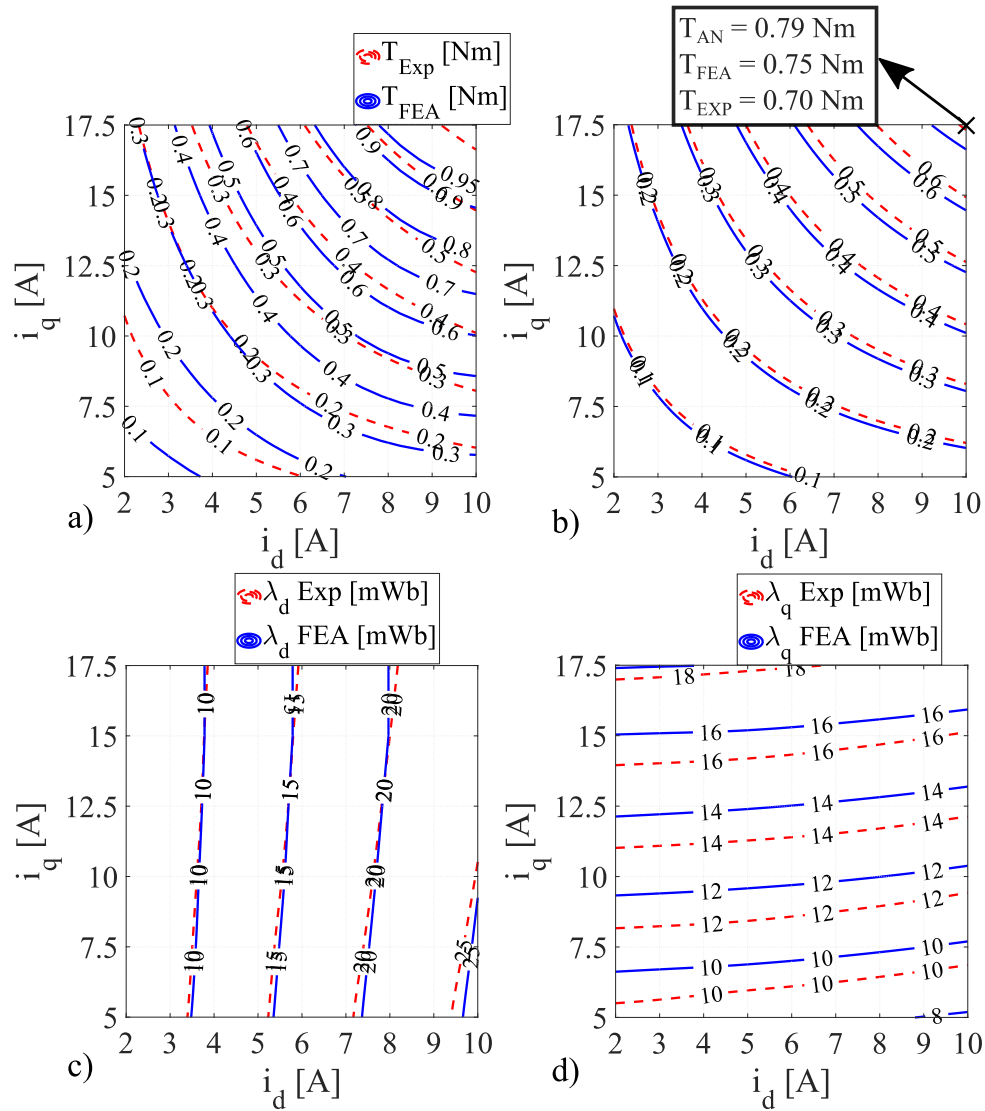


Figure 6.4: (a,b) FE-computed torque vs experimental one a) neglecting the mechanical tolerances b) considering the mechanical tolerances; (c,d) Magnetic identification in the  $i_d - i_q$  plane (a,b).

### 6.1.2 SiFe machine

To validate the proposed design approach and the considerations regarding the soft magnetic material selection, a prototype of the optimal machine at 80 krpm with the material combination M3 of section 2.6 has been developed and tested. Before commencing the manufacturing, the rotor optimal geometry needs a structural FE refinement. In fact, the proposed design approach allows restricting the range of promising solutions, but once a geometry is chosen, its rotor needs to be structurally optimized. Indeed, the distribution of the iron ribs along the barriers

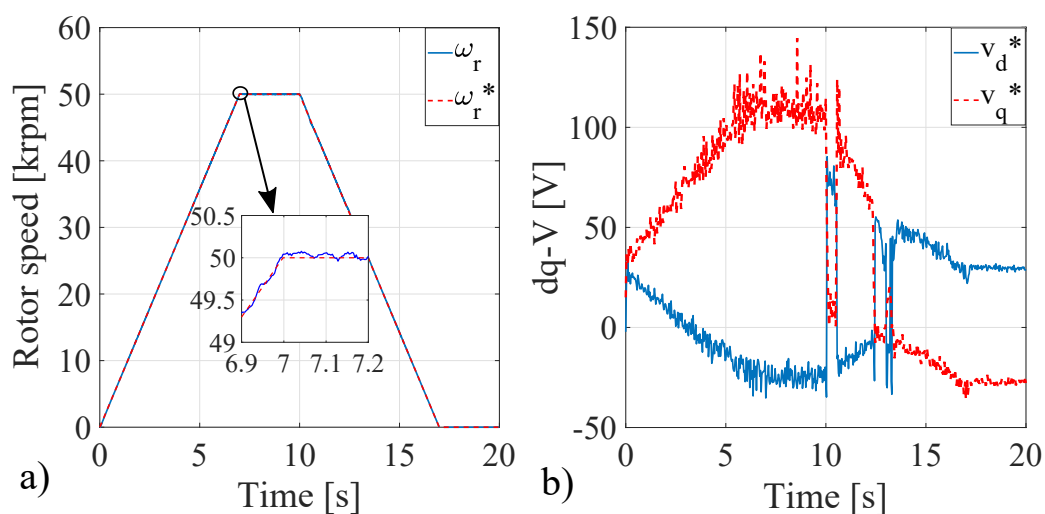


Figure 6.5: Experimental speed test: a) reference speed and rotor speed; b) dq reference voltages.

have to be optimized trying to keep the total iron bridge thickness per barrier as close as possible to the analytical estimated values. By doing so, the average torque would not change being not affected by the ribs position along the barrier but mainly by their thickness. A comprehensive description of the adopted structural design procedure is reported in [93], while Fig. 6.6 reports the Von Mises stress distribution of the final rotor geometry along with the photo of the EDM manufactured rotor lamination stack prior the shaft and end-caps assembly.

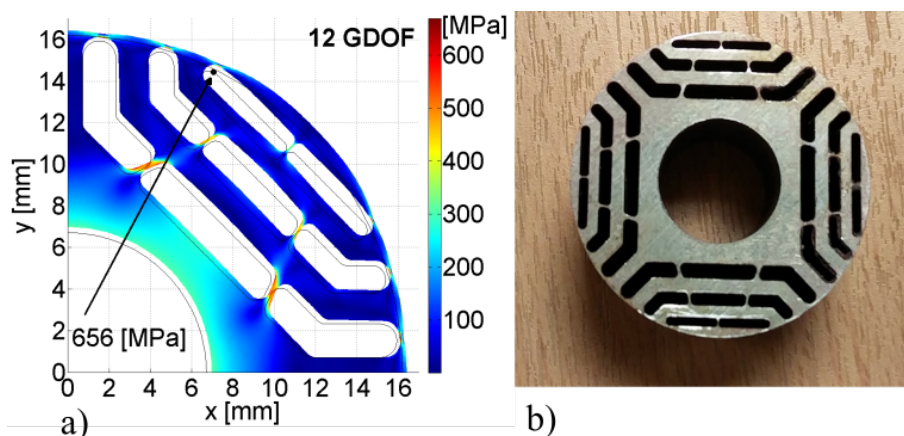


Figure 6.6: a) Von Mises stress distribution of the final rotor design, b) rotor stack prior the shaft assembly.

Fig. 6.7 shows a section view of the overall prototype highlighting the main components along with a photo of the assembled system. The cooling system consists in a single spiral water



jacket covering the whole stator axial length with a rated flow rate of 20 litre/min [126]. The same figure also depicts the bearing housing featuring inlet and outlet channels for the air-oil mist lubrication of the selected bearings.

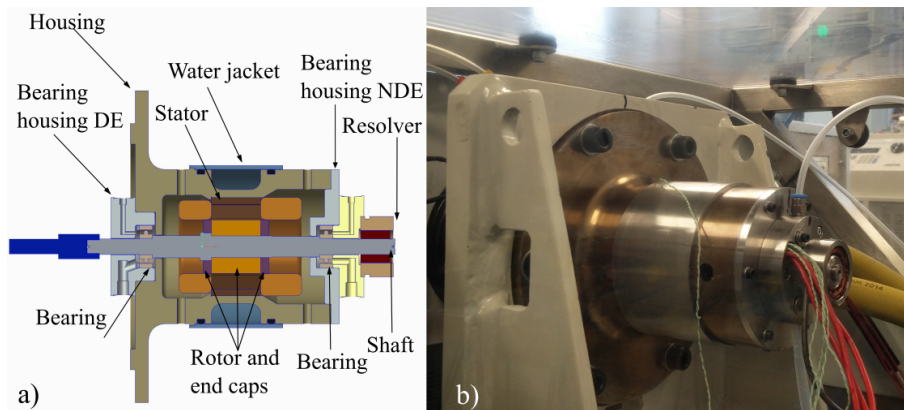


Figure 6.7: a) Section drawing of the built prototype showing the most important components, b) side view of the complete machine mounted on the bracket of the test rig.

The prototyped SyR machine was coupled, via a gearbox (ratio 1:5.975) and a 3.5 Nm torque sensor, to a load motor (37 kW - 20 krpm IM) supplied with a four-quadrant regenerative drive. An in-house designed three-phase full-bridge converter featuring SiC power modules has been used to supply the machine under test. The control platform used to implement the control algorithm is based on a Xilinx Zynq7020 SoC. A high ratio between the switching and the fundamental frequency was guaranteed setting the switching frequency to 40 kHz.

To confirm the FE-calculated performance and implement an accurate vector control, the flux-current relationships of the SyR prototype have been identified adopting the procedure presented in [125]. Fig. 6.8 reports the results of this experimental identification over the entire d-q current plane with a satisfactory agreement with the FE prediction.

After measuring the d- and q-axis fluxes, it is possible to derive the torque and inductances along the maximum torque per ampere trajectory needed to tune and implement the standard vector control scheme. After some preliminary tests, several motoring no-load tests have been performed imposing a trapezoidal speed reference with increasing maximum values. Fig. 6.9 reports the measured and the reference speed, d- and q-axis currents and reference voltages during a no-load test up to 35 krpm. After verifying the safe operations up to a certain speed, an

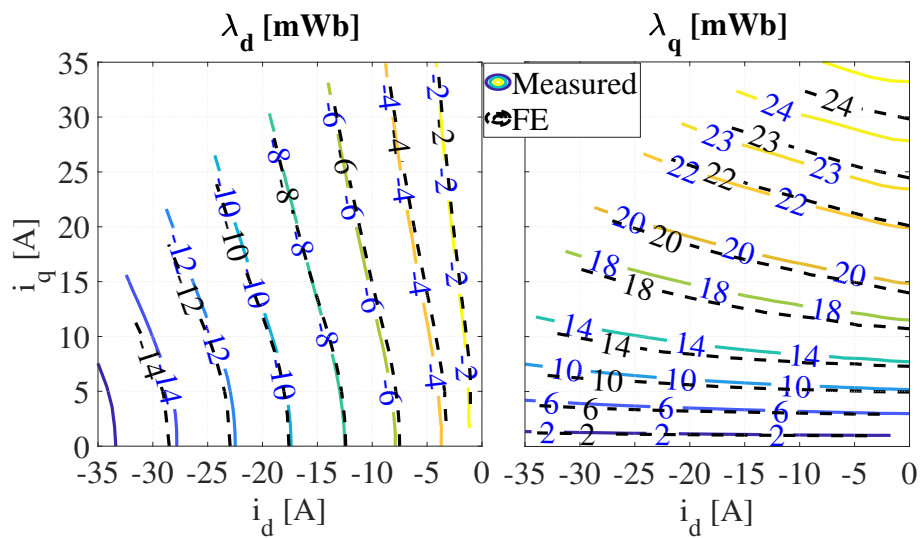


Figure 6.8: Comparison between measured and FE d- and q-axis fluxes in the d-q current plane.

extensive campaign of generating load tests has been performed at different speeds and loads.

For every considered speed and load (up to 30 krpm at full load, 28A), the tests were carried

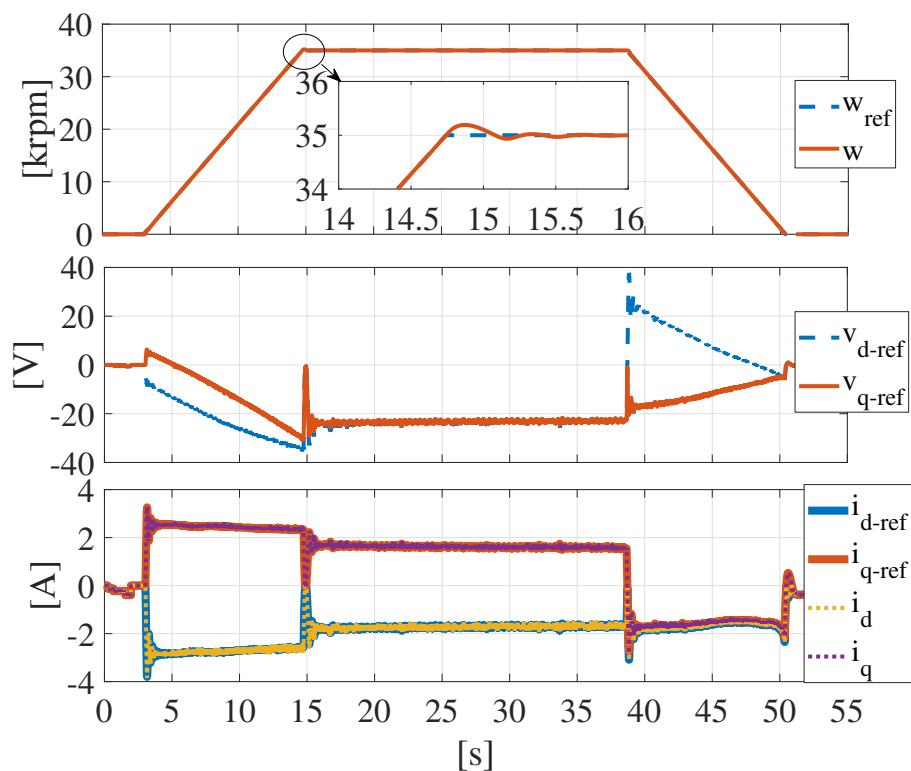


Figure 6.9: Measured and reference speeds, voltage reference and measured and reference currents during a motoring no-load test.

out reaching the thermal steady state and acquiring several electrical, mechanical and thermal

variables. Fig. 6.10 shows the transient behaviour of the speed, torque, voltage and currents (in the d-q reference frame) during the current step between 21 and 28 A at 30 krpm. The same figure also reports the steady state phase currents, dc link voltage, duty cycles and torque. This condition correspond to the machine producing the rated torque ( $T_{rated} = 0.77 \text{ Nm}$ ). Above

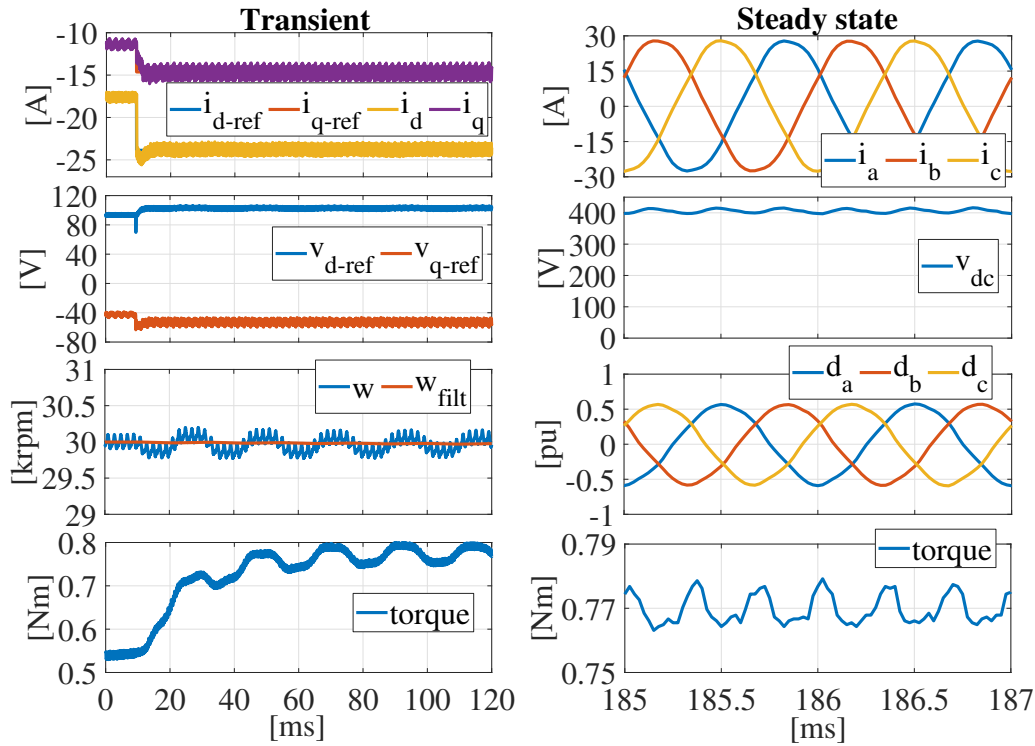


Figure 6.10: Transient and steady state acquisitions during the load test at 30 krpm in which the current module increases from 21 to 28 A.

30krpm (at load) and 35krpm (at no load), the measured vibrations exceeds the acceptable limits and, for the sake of safety, tests at higher speed have not been performed. An in depth analysis of the vibration spectrum at the different rotating speeds leads to the conclusion that a shaft misalignment (or a non-perfect alignment of the bearings within their housings) is the most probable cause of this behaviour.

The last figure (Fig. 6.11) outlines the measured temperatures experienced by the winding during the load tests (with torques from  $1/4T_{rated}$  to the rated value with a step of  $1/4T_{rated}$ ) at 30 krpm. The thermal model used during the comparative design exercise has been used to estimate the thermal performance of the prototyped machines at 30 krpm and the rated torque.

The average winding temperature predictions, also shown in Fig. 6.11, are underestimated (about 10%) with respect to the measured ones.

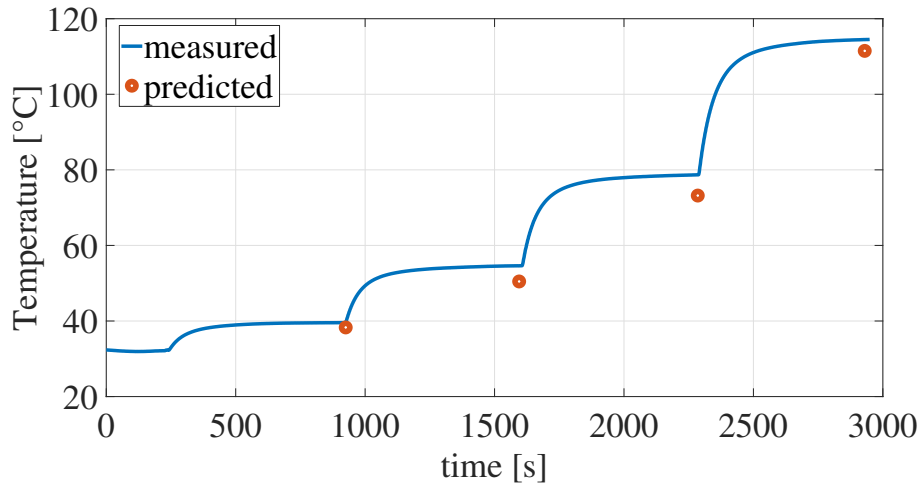


Figure 6.11: Measured winding temperature during the load tests at 30 krpm compared with the estimated ones at steady state.

## 6.2 PMA SyRM

The design approach and outlined general design insights for PMA SyRMs have been experimentally validated prototyping and testing an 80 krpm machine. Although designing a PMA SyRM first optimizing the reluctance torque and then adding high energy density permanent magnets leads to a sub-optimal design (see chapter 3), the solution SyR+ND, shown in Fig. 3.27b4, has been selected as final candidate to be manufactured and tested. This design solution produces less torque using more magnet material, but it eases the manufacturing of the rotor. Indeed, the optimal NDA SyRM at 80 krpm features rotor flux barrier thicknesses lower than 1 mm. This makes the cutting of the rotor lamination a challenging task when considering standard manufacturing techniques commonly used for low-volume production, e.g electrical discharge machining (EDM) or laser cutting. On the contrary, the sub-optimal SyR+ND design have bigger flux barrier dimensions, therefore the lamination cutting, the PMs manufacturing and their insertion into the rotor are all simplified. It is worth to underline that this manufacturing challenge is due to the small outer diameter required by the specific application under consideration.

## 6.2.1 Design refinement

This section describes the design refinements carried out on the selected solution before its manufacturing. In particular, first the structural optimization of the rotor iron ribs distribution is detailed and then the PMs are redistributed within the rotor flux barriers in order to minimize the torque ripple.

### a. Structural optimization

The proposed design approach allows fully defining the stator and rotor geometries except for the iron ribs distribution. Indeed, the simplified mechanical formulation, used in the analytical design, estimates only the radial iron rib dimensions and not their distributions along the respective flux barriers. Given the complexity of the rotor structural behaviour, the ribs allocations can only be defined via a structural FE-based study, i.e. either a sensitivity analysis or an optimization. The structural integrity of a PMaSyR is guaranteed only if the rotor maximum von Mises stress  $\sigma_{vm}^{max}$  at the maximum speed is below the yield strength of the lamination material ( $\sigma_y = 822$  MPa for the considered rotor material). Unfortunately, this condition is satisfied by several iron rib dimensions and distributions. As a consequence, another criterion needs to be defined in order to select the most performing geometry. A possible solution, first reported in [32] and then in [33], consists in minimizing the iron rib dimensions subject to the constraint on the maximum von Mises stress experienced by the rotor at the highest speed. In this case, a FE-based optimization has been carried out solving the following problem:

$$\begin{aligned} \min \quad & ATR \\ \text{s.t.} \quad & \sigma_{vm}^{max} \leq k_s \cdot \sigma_y \end{aligned} \tag{6.2}$$

where  $k_s$  is a safety factor (0.8), while  $ATR$ :

$$ATR = \frac{1}{n} \sum_{i=1}^n (2 \cdot TR^i + 2 \cdot LR^i + CR^i) \tag{6.3}$$

is the average total rib of the  $n$  flux barriers, being  $TR^i$ ,  $CR^i$  and  $LR^i$  the tangential, central and lateral rib sizes, all depicted in Fig. 6.12a. It is worth to underline that during the structural FE optimization the flux barrier heights  $h_a^i$  and their angular positions at the airgap  $\Delta\alpha^i$ , reported in red in Fig. 6.12a, are kept constant to the respective values obtained with the proposed hybrid design procedure. Solving this constrained one-objective optimization problem (6.2), involving

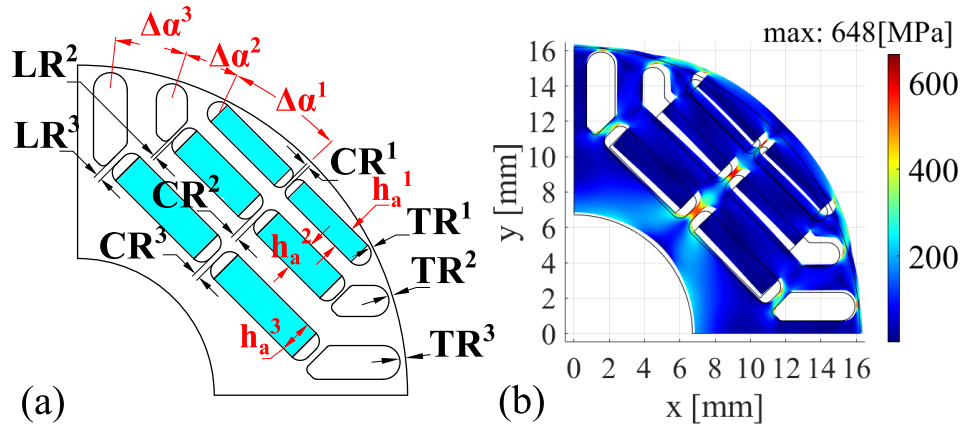


Figure 6.12: a) Full rotor parametrization, b) Von Mises stress distribution of the optimal at 80krpm.

8 geometrical variables to identify, indirectly leads to the solution featuring the highest possible torque for a given stress limit ( $k_s \cdot \sigma_y$ ). The adoption of this structural design approach lies on two hypotheses:

- the decrement of the average torque caused by the increment of an iron rib has to be independent from its position (which can be either on the tangential, lateral, or central rib);
- the iron rib dimensions and their distribution should have a negligible effect on the torque ripple.

Although the first hypothesis can be considered always verified, the second is definitely a strong assumption and needs to be verified case by case. Both these two aspects will be investigated in the following.

The problem (6.2) has been solved using a stochastic optimization algorithm (differential evolution) with 80 elements evolving for 150 generations. In order to obtain the most conserva-

tive design, the structural optimization has been carried out considering the flux barriers fully filled of PMs, even though the initial solution (Fig. 3.27b4) has lower PM material in the two outermost rotor slots. A minimum rib thickness of 0.1 mm has been considered during the optimization as manufacturing constraint; both central and lateral ribs are not drawn if their optimal values fall below this threshold.

Fig. 6.12b reports the Von Mises stress distribution of the optimal rotor geometry while Table 6.1 lists its iron rib dimensions. As expected, the optimal geometry features increasing central ribs from the outermost to the innermost barrier. However, this does not hold true for the tangential ribs as the optimal geometry does not have the lateral ribs on the middle barrier. It is worth underlining that the total rib per flux barrier along with their average obtained with the structural FE optimization are similar to the respective values analytically estimated with the proposed design methodology as reported in Table 6.1, thus indirectly validating the iron ribs design approach.

Table 6.1: Iron ribs dimensions of the optimal design [mm]

<b>Flux barrier</b>	<b>TR</b>	<b>CR</b>	<b>LR</b>	<b>total</b>	<b>total analytical</b>
<b>1</b>	0.33	0.20	-	0.86	0.43
<b>2</b>	0.57	0.37	-	1.51	1.3
<b>3</b>	0.30	0.51	0.55	2.21	2.4
<b>ATR</b>				1.52	1.38

### b. PM redistribution analysis

The average total ribs (*ATR*) obtained with the structural optimization is slightly higher than the expected one as shown in Table 6.1. As a consequence, the average torque of the mechanical optimized design is lower than the expected value albeit it is less than 5% at the MTPA (Maximum torque per Ampere) condition as shown in Fig. 6.13a. This figure reports both average torque and torque ripple for the rated current as function of the current phase angle. The torque oscillation of both analytical design and structural optimized one is above 20%. This is caused by several phenomena not included in the design workflow such as the local saturation effects

and the influence of having different tangential ribs thicknesses. With the aim of reducing the torque pulsation, an electromagnetic FE sensitivity analysis has been performed redistributing the PMs within the rotor flux barriers keeping unchanged the overall PM volume (equal to the optimal value  $V_{mag}^*$  analytically obtained and reported in Table 3.3).

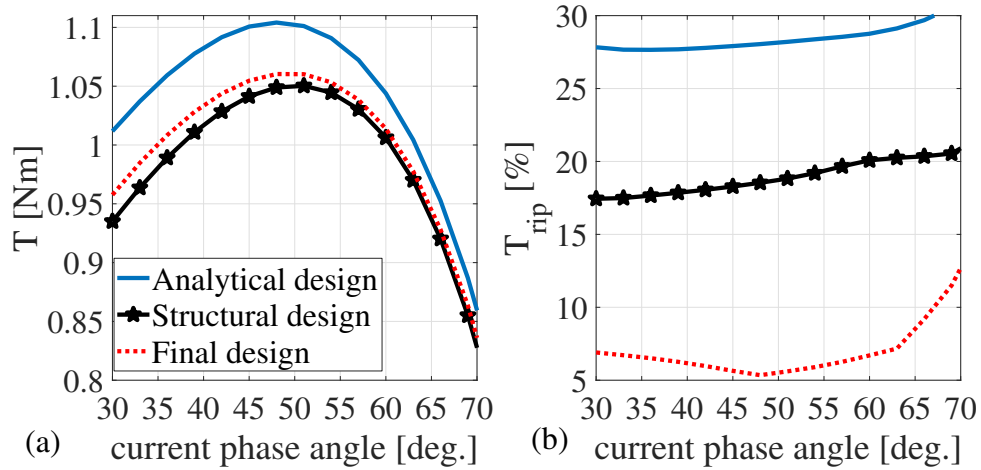


Figure 6.13: Average torque and torque ripple as function of the current phase angle for the electromagnetic optimum geometry, the structural one, and the final prototype.

Fig. 6.14 reports the results of such analysis in terms of PM volume placed in the outermost barrier ( $V_{mag1}$ ), average torque and torque ripple as function of the PM volumes placed in the two innermost rotor barriers ( $V_{mag2}$ ,  $V_{mag3}$ ). The PM volumes are expressed in per unit of the respective maximum volumes. Obviously, as both  $V_{mag2}$ ,  $V_{mag3}$  increase,  $V_{mag1}$  (Fig. 6.14a) decreases until it reaches zero when  $V_{mag2} = V_{mag3} = 1$  since  $V_{mag1} + V_{mag2} + V_{mag3} = V_{mag}^*$ . As expected, the average torque maximum variation is less than 3% being the total PM volume kept constant during the analysis (Fig. 6.14b). On the contrary, the torque ripple changes significantly with the PM distributions (Fig. 6.14c) and the maximum range of variation is about 20%. In particular, the structural optimized solution (shown with the marker ★) features a torque ripple at the rated MTPA condition of 20% while the minimum torque ripple PM distribution is about 5.2% (red marker ○). The performance of the solution featuring the lowest torque ripple are also reported in Fig. 6.13 (labeled as Final design). While the average torque variation between the optimal structural design and the final one is negligible, the torque ripple is significantly improved over a wide range of current phase angle and not only at the MTPA



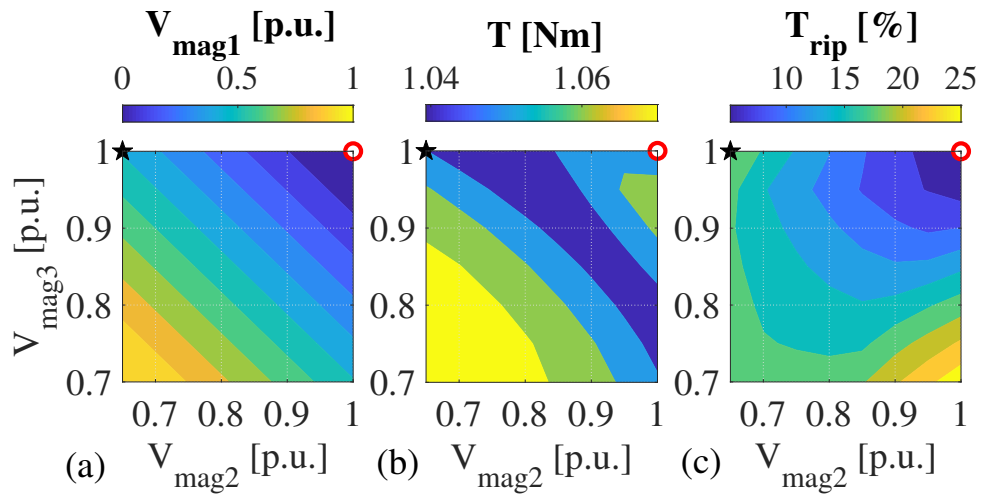


Figure 6.14: PM re-distribution FE analysis: a) PM volume of the outermost PM, b) average torque, and c) torque ripple as function of the per unit PM volumes placed in the two innermost flux barriers.

condition. The optimal PM distribution is characterized by an empty outermost barrier and two fully filled innermost barriers. This PM allocation further facilitates their insertion being the outermost slot the smallest one. For the sake of clarity, Fig. 6.15 shows the rotor geometries and PM distributions obtained with the proposed analytical design methodology (a), after the FE structural optimization (b) and after the PM redistribution FE sensitivity analysis (c).

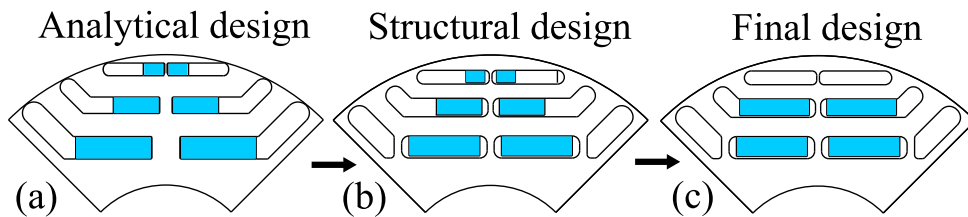


Figure 6.15: Design refinement evolution.

## 6.2.2 Experimental findings

The final design obtained as described in the previous sections has been prototyped and tested on an instrumented test rig.

### a. Prototype and test rig setup

Both stator and rotor were manufactured by EDM and Fig. 6.16 shows two top view photos of the rotor lamination stack before and after the magnets and shaft insertion. The stator and rotor were assembled into custom designed housing featuring a single spiral water jacket and the inlet and outlet channels for the air-oil mist bearings lubrication, as can be seen on the right side of Fig. 6.17.

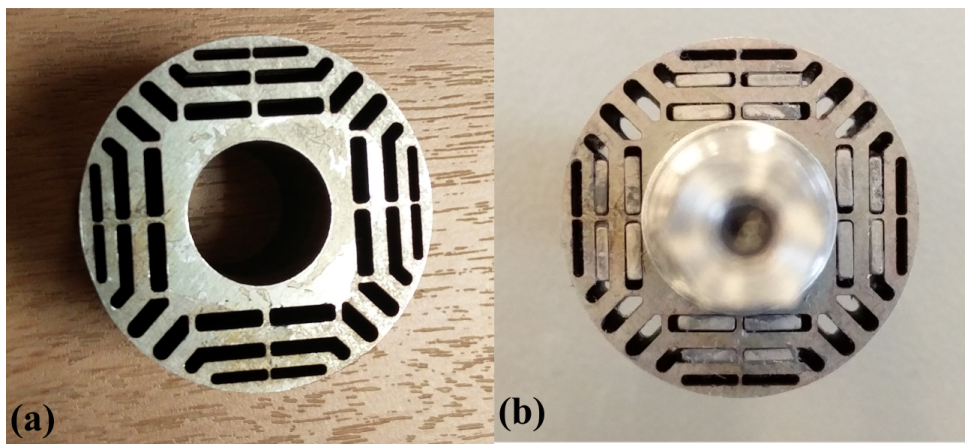


Figure 6.16: Top view of the rotor lamination stack before (a) and after (b) magnets and shaft insertion.

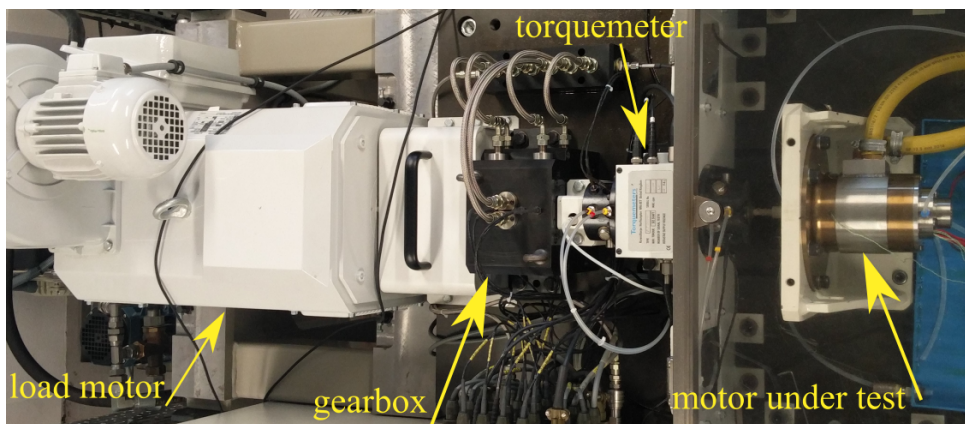


Figure 6.17: Experimental setup layout.

The test rig configuration is the same of the last section and include the prototyped machine coupled to a load motor via a gearbox, as also shown in Fig. 6.17. An in-house designed three-phase full-bridge converter featuring SiC power modules was adopted to supply the machine

under test [127]. The control platform used to implement the control algorithm is based on a Xilinx Zynq7020 SoC [128].

### b. Test results

The first experiment carried out on the prototype is a series of generating no load tests at various speeds aimed at measuring the back electromotive force (bemf). Fig. 6.18 reports a screenshot of the scope during the no-load voltage test at 24 krpm while Fig. 6.19 compares the measured and FE-predicted bemf profiles. A good match is evident although small discrepancies are present mainly due to the different behaviour of the tangential iron ribs. Indeed, a small variation of their sizes due to the manufacturing tolerances causes a different saturation levels and so a discrepancy between the expected and measured voltage profiles.

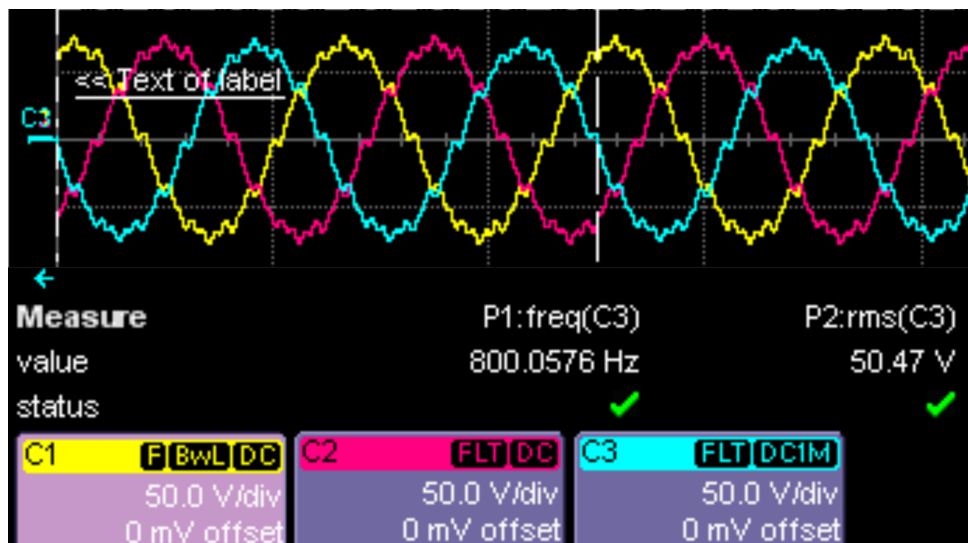


Figure 6.18: Scope capture while measuring the phase-to-phase voltages during the no-load test at 24 krpm.

To confirm the FE-calculated performance, the torque and the internal power factor have been measured implementing the procedure presented in [125]. Fig. 6.20 reports the results of this series of experimental tests carried out for several current modules and current phase angles. A satisfactory agreement with the FE prediction is clearly visible, although the measured torque is 5% lower when considering a light overload at MTPA condition (i.e. current amplitude 30 A in Fig. 6.20). Also the internal power factor at the rated MTPA operating point is slightly lower

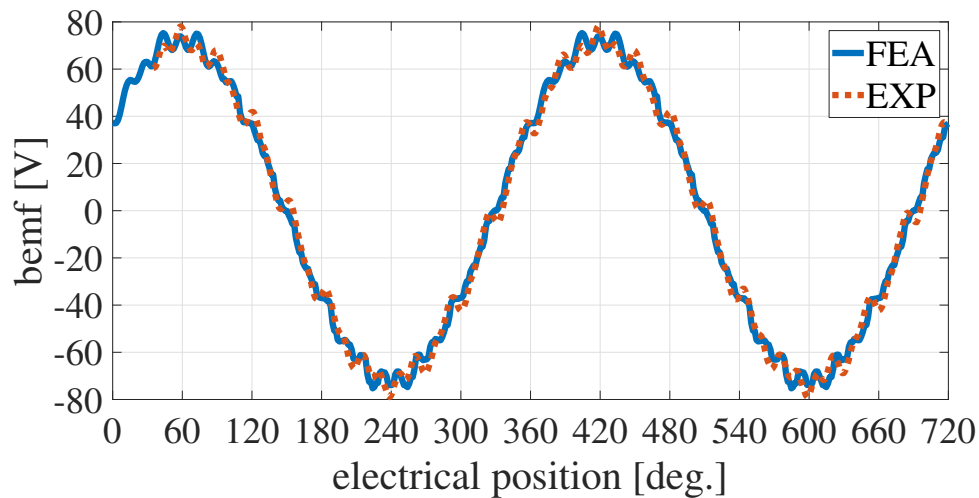


Figure 6.19: Comparison between measured and FE phase-to-phase no-load voltages at 24 kprm.

than expected, i.e. 0.8 instead of 0.845. These small discrepancies can be ascribed to the effects that the manufacturing tolerances have on the performance of a small scale prototype.

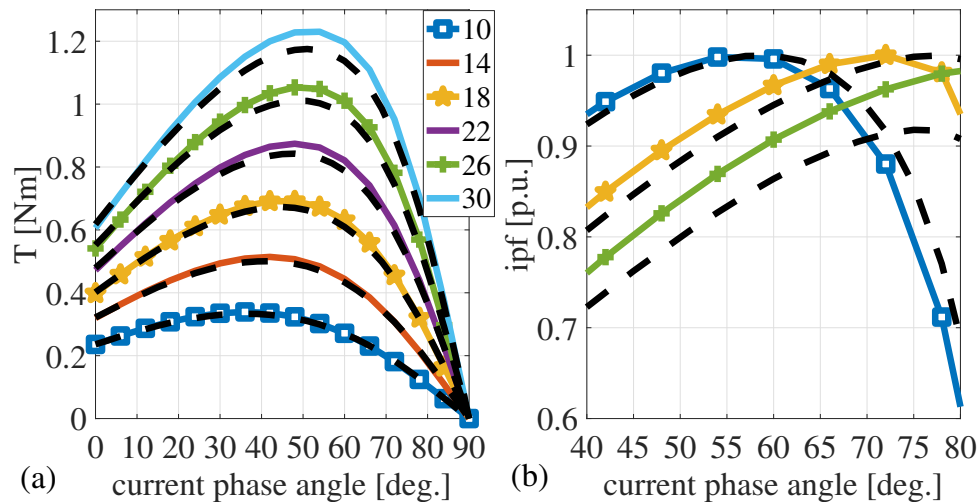


Figure 6.20: Comparison between estimated (colored lines) and measured (dashed black lines) average torque (a) and internal power factor (b) as function of the current phase angle and for different peak current amplitudes.

After measuring the torque and inductances along the maximum torque per ampere trajectory, the PI regulators of a standard vector control scheme [129] can be tuned. After some preliminary tests, several motoring no-load tests have been performed imposing a trapezoidal speed reference with increasing maximum values. Fig. 6.21 reports the measured and the refer-

ence speed, d- and q-axis currents and reference voltages during a no-load test up to 50 krpm.

After verifying the safe operations up to a certain speed, several load tests have been per-

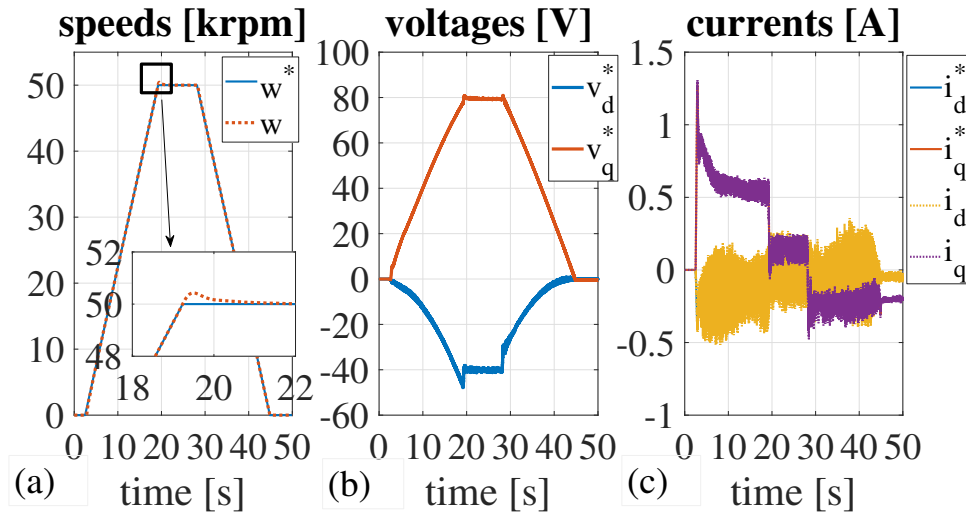


Figure 6.21: Motoring no load test up to 50 krpm: a) speed, b) voltages, c) currents.

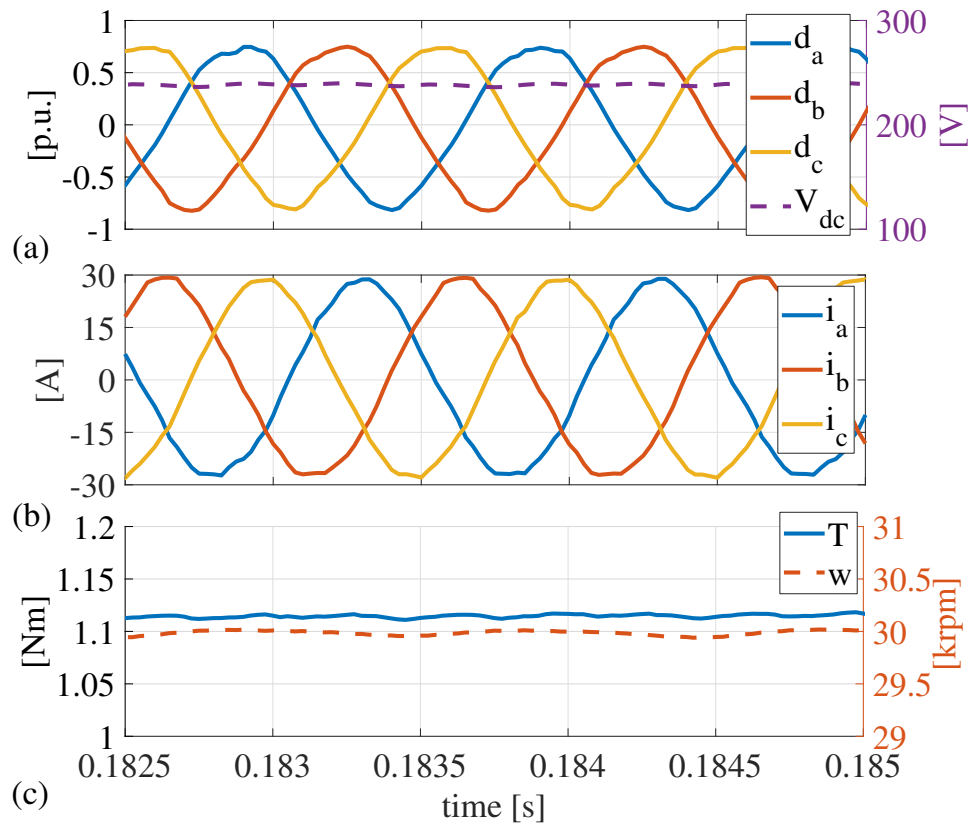


Figure 6.22: Load test at 30 krpm and the rated torque: a) duty cycles and dc-link voltage, b) phase currents, and c) torque and speed, all acquired with the control platform at 40 kHz.

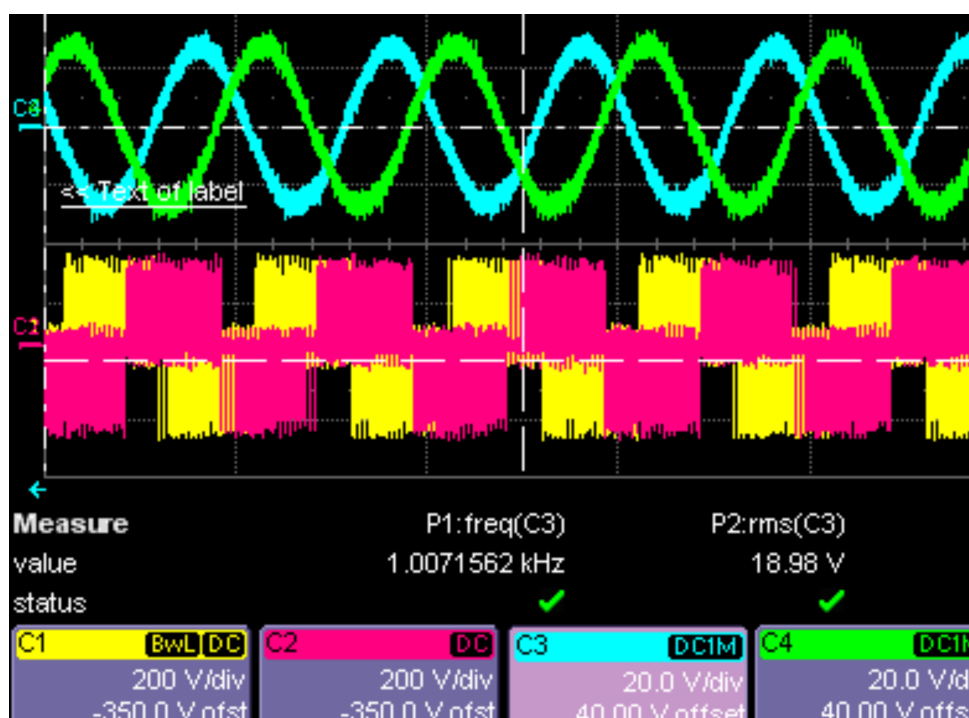


Figure 6.23: Scope capture while measuring the phase-to-phase voltages and phase currents during the rated load test at 30 krpm.

formed and Fig. 6.22 shows the duty cycles, dc-link voltage, speed, torque and phase currents all acquired with the control platform during the test at the rated torque at 30 krpm. The phase currents and phase-to-phase voltage profiles captured with the scope during the same test are shown in Fig. 6.23.

Above 50 and 30 krpm at no load and load respectively, the measured vibrations exceed the acceptable limits and, for the sake of safety, tests at higher speed have not been performed. The reason behind such vibrations is the same of the SiFe SyRM test rig: a shaft misalignment (or a non-perfect bearings assembly within their housings).

## 6.3 SPMM

### 6.3.1 Selection of the final design

For the considered assumptions listed in Table 4.1, the speed maximizing the power density is either 80 or 100 krpm depending on the airgap thickness. The selection of the latter has been

carried out considering the rotor losses. Fig. 6.24a and 6.24b show the output power and the rotor losses at 80 and 100 krpm as function of the airgap thickness. It can be seen that the

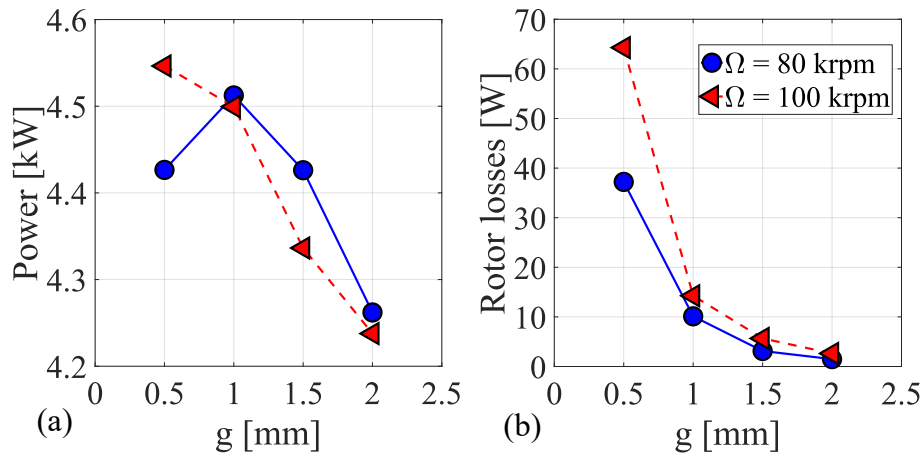


Figure 6.24: Power (a) and rotor losses (b) as function of the airgap thickness at 80 and 100 krpm.

reduction of the airgap thickness (from 2 to 0.5mm) produces a power improvement (circa 7%) as well as a significant increment of the rotor losses (circa 2000%). Although it does not feature the highest power density, the machine with an airgap thickness of 1.5 mm has been selected as final candidate. Indeed, it provides a higher output power with respect to the design reaching 100 krpm guaranteeing also low rotor losses.

The permanent magnet array of the final design has been re-arranged prior the prototyping stage. In particular, a quasi-Halbach configuration featuring the same airgap flux density of the optimal design has been adopted which also allow to decrease the used magnet volume. This change has been done in order to avoid filling inter-polar spaces between the magnets of the standard array to ease the assembly process.

### 6.3.2 Experimental findings

The final 4.2kW-80krpm design described in the previous section has been prototyped and tested on an instrumented test rig.



### a. Test layout and setup

A view of the main components together with the assembled rotor is reported in Fig. 6.25, while the stator lamination with and without the winding is shown in Fig. 6.26.

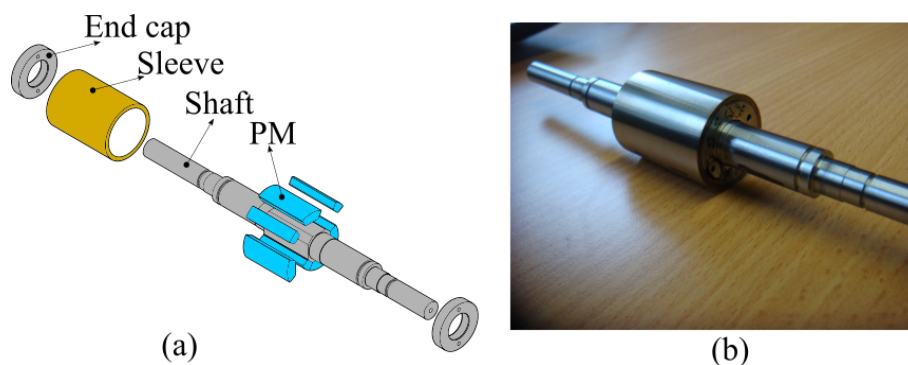


Figure 6.25: (a) Rotor assembly process; b) assembled rotor.

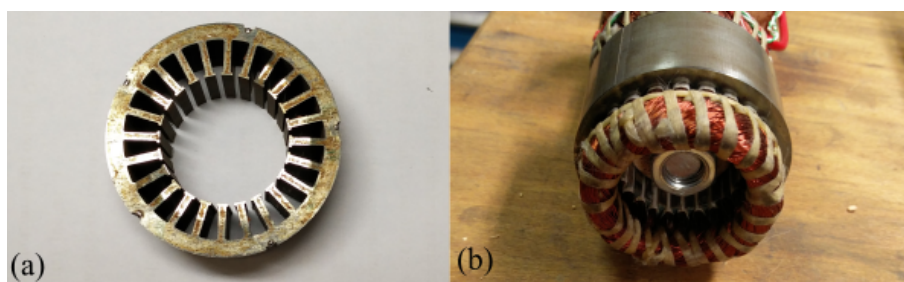


Figure 6.26: a) Top view of the stator laminations; b) stator after the winding assembly.

As for the latter two experimental cases, the SPM manufactured stator and rotor have been encapsulated within a custom designed housing featuring a single spiral water jacket as shown in Fig. 6.27 and the inlet and outlet channels for the air-oil mist bearings lubrication, as can be seen in Fig. 6.27. The latter also reports the complete test rig. It can be seen that the prototype is connected to a load motor via a gearbox (ratio 1:5.975) and a 3.5 Nm torque sensor.

Also the adopted power electronic converter is the same of the SiFe SyR and PMSyR test rigs.

### b. Test results

Several tests have been performed to fully characterize the machine behavior under different operating conditions.



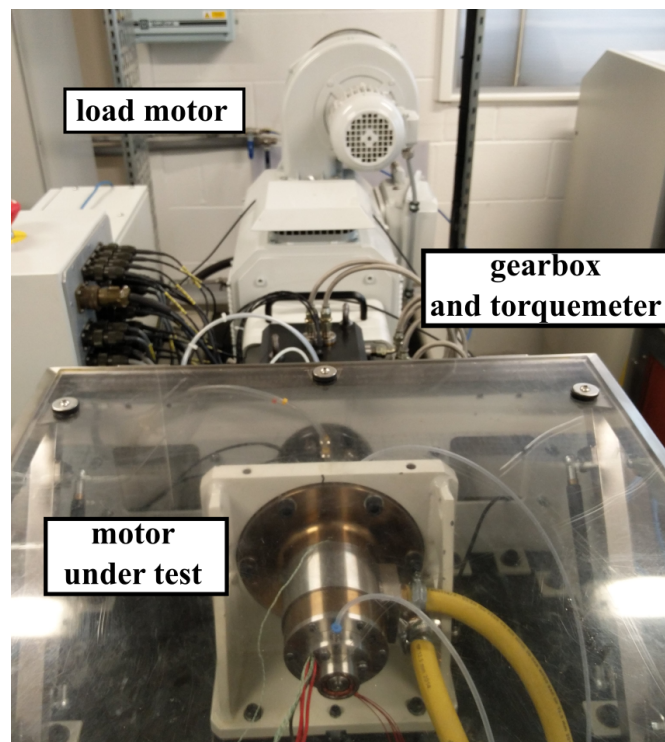


Figure 6.27: Experimental setup layout.

First, the back electromotive force has been measured by a series of no-load tests. Fig. 6.28a shows the phase to phase voltage measured at 30 krpm, whereas the excellent comparison between the FE-computed and measured profiles is reported in Fig. 6.28b. Fig. 6.29 reports the measured torque compared to the FE-one for several current amplitudes (up to 2 times the rated one). A good agreement can be observed. The maximum error is about 3% and it can be mainly ascribed to the impact of the manufacturing tolerances which can play a significant role in the final performance indicators when designing high-speed small-size machines. Fig. 6.30a shows the comparison between the FE-computed and measured internal power factor at MTPA condition, while the efficiency map in the speed-current plane is reported in Fig. 6.30b. Both power factor and efficiency have been measured using a power analyzer. It is worth to notice that both power factor and efficiency are in good agreement with FE estimations. Indeed, the maximum error is about 1.4% for the power factor, while the average efficiency error is 1.5% (the maximum error is about 15%); these mismatches can be ascribed to several factors including the manufacturing tolerances and the behavior of the magnetic materials [130].

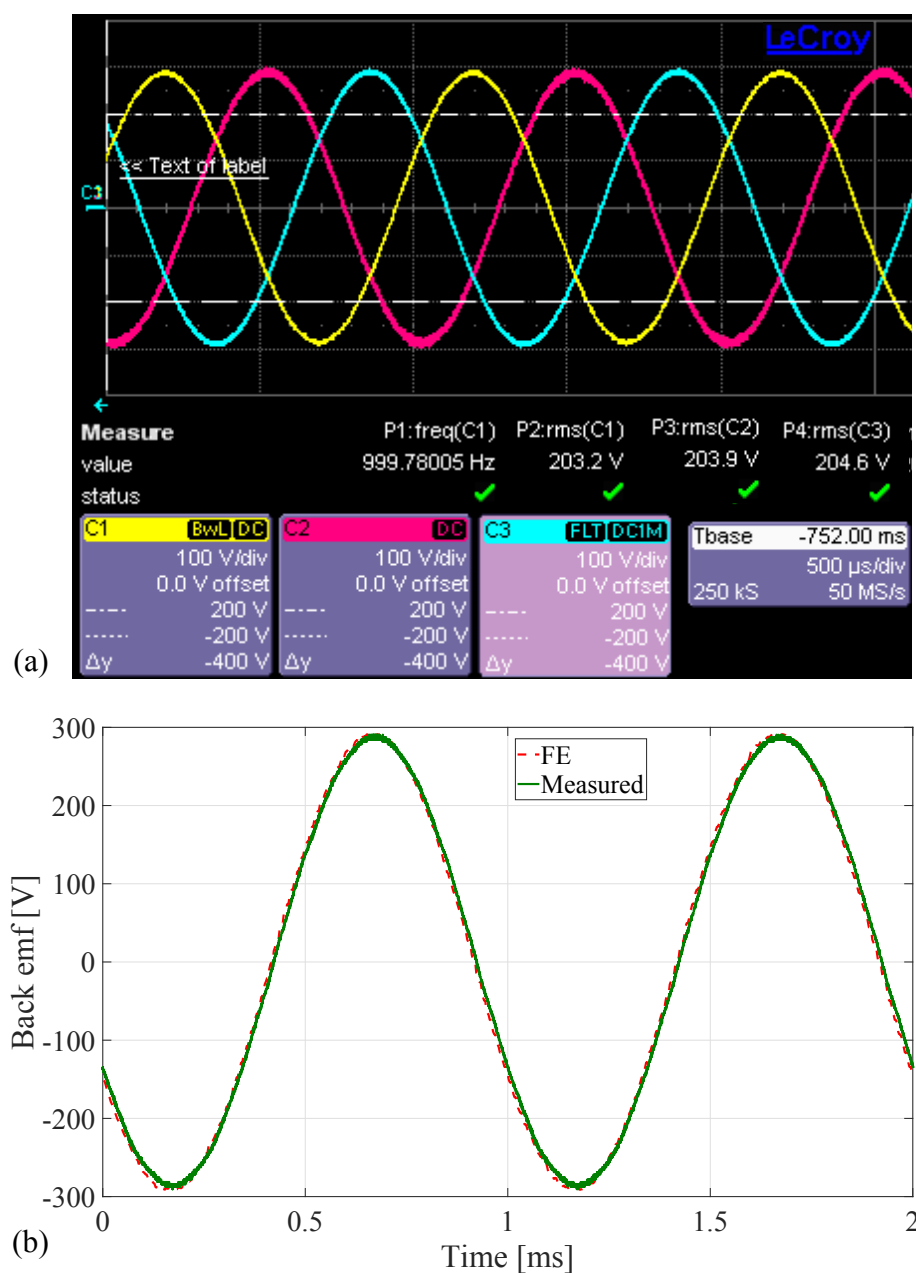


Figure 6.28: back emf test at 30 krpm: (a) scope capture showing the the phase-to-phase voltages during the no-load test; (b) comparison between measured and FE phase-to-phase no-load voltages.

Fig. 6.31a reports an acceleration test at no-load up to 38 krpm, while Fig. 6.31b shows the d- and q-axis voltages during the same test. Above 38 krpm, the measured vibrations exceeded the safety limits, therefore tests at higher speed have not been performed; by analysing the vibration spectrum, a non-perfect alignment of the bearings within the housing has been identified as the most probable cause of such vibrations, which are neither related to the final design nor

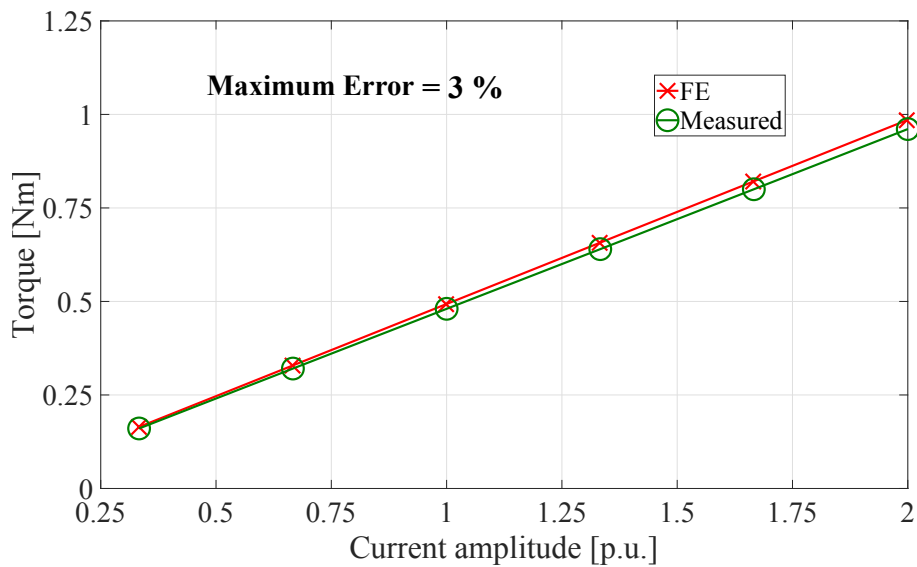


Figure 6.29: Comparison between FE computed and measured torque at MTPA condition.

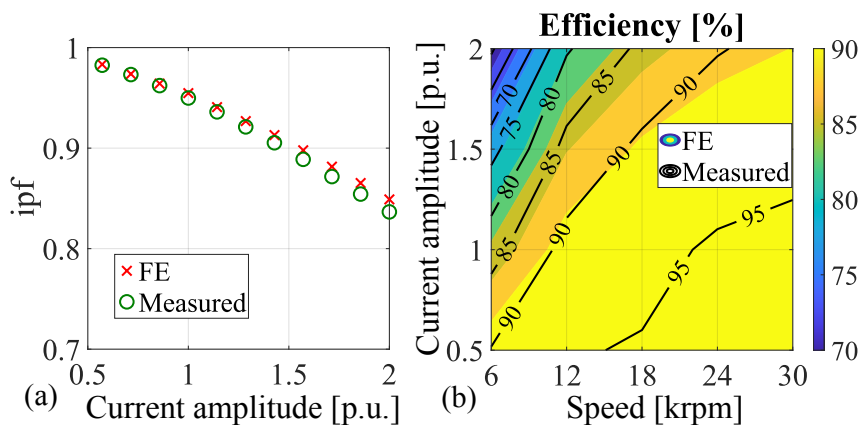


Figure 6.30: Comparison between (a) FE computed and measured power factor at MTPA condition and (b) FE computed and measured efficiency in the speed-current plane.

to the test rig.

Finally, the thermal behavior of the machine at rated conditions and for different operating speed is shown in Table 6.2, where the measured winding maximum temperature is compared to the one estimated using a commercial solver [94]. A good match can be observed for all the considered operating points.

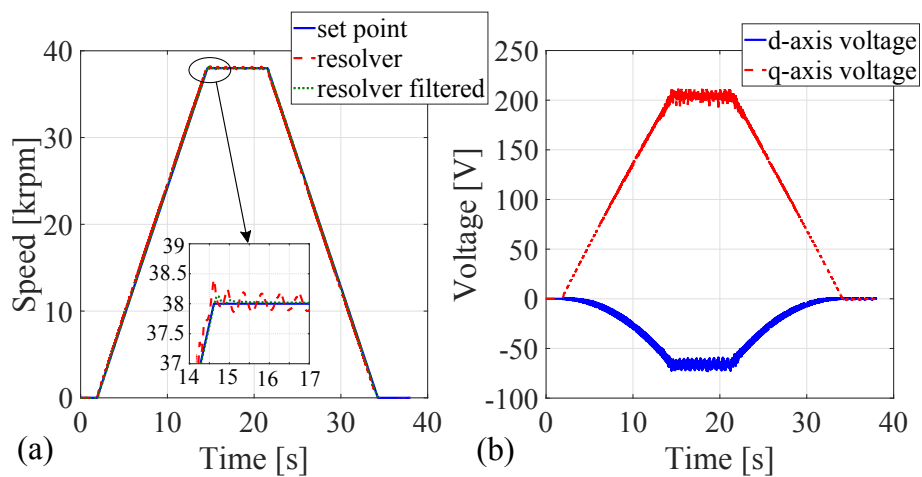


Figure 6.31: Speed test: (a) reference speed against the measured and measured-filtered ones; b) d- and q-axis voltages.

Table 6.2: Comparison between measured and FE average winding temperatures.

	Temperatures [deg.]				
	6krpm	12krpm	18krpm	24krpm	30krpm
FE	55	56	56	57	58
EXP	47	50	52	52	56

# Chapter 7

## Conclusions and future work

In this thesis an improved design approach for high speed synchronous reluctance machines with and without permanent magnet assistance and surface mounted permanent magnet synchronous machines, based on an analytical model, has been proposed. This is able to fully consider the high speed limiting design factors, i.e. the increasing structural limitation and iron losses. The accuracy of the analytical model has been compared with the FE results and a detail analysis of the roots of their mismatch has been investigated at both low and high speeds. In the SyR and PMSyR cases, the saturation of the d-axis flux path, the cross-saturation, the iron losses and the non-linear behavior of the q-axis magnetic circuit have been identified to be the main causes of inaccuracy in the analytical performance estimation. A new computational efficient approach has been then proposed in order to adjust the identified pitfalls of the analytical model. Indeed, by FE-simulating a subset of design solutions it is possible to correct the mismatch between analytical and FE performance for the whole set of design solutions.

### 7.1 Results' summary

In the second chapter and after the full FE validation, the proposed design method has been used to study the limiting phenomena taking place as the operating speed increases when considering a pure synchronous reluctance machine case. It has been shown that both iron ribs

and iron losses increments limit the maximum power that can be achieved by increasing the speed. Indeed, above a certain value is definitely not convenient to further increase the speed. This speed threshold is higher if only the structural limitations are considered letting the overall losses increase (implicitly assuming an increment of the cooling capability with the speed). Considering the maximum torque design the trends of torque, internal power factor, optimum split and magnetic ratio as function of the speed depend on the selected lamination material. However, mainly the rate of decrement of the optimal performance is affected by the materials. Therefore, several general conclusions regarding the worsening of the maximum torque design solution as the speed increases can be drawn.

- The iron ribs affect more the q-axis inductance and so the power factor rather than the torque.
- The iron losses increment heavily influences the maximum current and so the torque capability for a certain level of the total losses, and slightly improves the power factor.

For the first considered lamination material (a cobalt-iron alloy with good magnetic performance and standard structural characteristic), the optimal split ratio tends to remain almost constant as the speed increases while the optimal magnetic ratio tends to decrease. Clearly this behavior is highly dependent on the lamination material and so the balance between the iron losses and iron ribs effects.

Indeed, an in-dept analysis on the material selection showed that adopting CoFe alloys leads to machines that outperform the SiFe counterpart up to a certain speed, which for the considered case study is about 60 krpm. Above this speed, machines with SiFe provide better performance. In the lower speed range, the effect of the higher saturation flux density of the CoFe alloys allows achieving better performance. On the contrary, for higher design speeds, the higher iron losses and low yield strength of the CoFe materials outweigh the advantage of the higher saturation level and make the SiFe adoption more convenient. Using materials (either SiFe or CoFe) with a higher yield strength for the rotor, always leads to better performance despite their higher iron losses. The analysis of the optimal machines showed that the split ratio and

magnetic loads decrease as the speed increases with a higher decrement rate when adopting materials with low yield strength for the rotor.

The thermal analysis of the same set of machines has confirmed the validity of the implemented design approach. In particular, keeping invariant the total machine losses for all the design speeds allows a comparison on a fair basis, i.e. with the same cooling system. Although the distribution of the losses varies as the design speed increases, the maximum winding temperatures of all designs lie within an acceptable range, indeed.

It has been found that the magnetic exploitation of the lamination materials (especially when considering CoFe alloys) has to be selected according to the maximum operating speed of the machine. Indeed, when designing machines in the low-medium speed range, the optimal performance are obtained when selecting the magnetic load close to the knee point of the material  $B - H$  curve. At low speeds, the iron losses influence on the overall losses is negligible and it is more convenient to maximize the magnetic load in order to increase the saliency ratio. On the contrary, when designing high speed SyR machines, it is better to reduce the magnetic exploitation of the adopted soft magnetic materials. In fact, the rate of the torque decrement associated with the maximum current reduction (needed to keep constant the overall losses) is higher than the rate of the torque decrement due to the saliency ratio reduction (associated with the lower magnetic load).

In the third chapter the analysis has been extended to the PM assisted design scenario. In particular, the resolution of the q-axis equivalent magnetic circuit has been proposed to calculate both q-axis inductance and PM flux linkage taking into account the non-linear behavior of the rotor iron ribs. Then, an iterative procedure has been proposed to design the PM dimensions, to achieve a pre-defined performance index (e.g. the power factor, the torque, the CPSR), and to calculate the q-axis performance taking into account the electromagnetic non-linear behavior of the iron ribs which are sized also considering the mechanical effect of the additional weight of the PMs. After FE validating the analytically predicted torque and power factor, a computational efficient FE-based approach has been implemented in order to enhance the accuracy of the analytical performance estimation.

The proposed hybrid analytical-FE design approach has been then applied to a specific case study to draw some preliminary design considerations. It has been shown how the PM-assistance can be neglected during the magnetic design of the stator and rotor laminations, and how this heavily affects the selection of the optimal machine.

It has been shown that, for a given maximum speed, the maximum torque solution when adopting ferrite PM is geometrically similar to the maximum reluctance torque design. On the contrary, adopting high energy density PM, the maximum total torque design differs from the maximum reluctance one. This difference is mainly due to the bigger PM torque component obtained with neodymium-based PMs and its different behavior in terms of split and magnetic ratio dependencies.

As a consequence, if neodymium-based PMs are chosen, the selection of the optimal design (torque-wise) should consider both PM and reluctance torque components. In other words, the design procedure of adding neodymium-PM to the maximum reluctance torque design leads to a sub-optimal solution (i.e. 30% lower output power in the considered case study).

The four chapter has investigated the surface mounted PM synchronous machine case. Also in this case, the rise of the iron losses and sleeve thickness limit the maximum power that can be achieved increasing the speed. Indeed, there is a speed value above which the power density does not increases anymore. Such threshold speed is slightly reduced when considering thicker airgap thickness. The increment of the latter also leads to a torque decrement since a wider airgap implies higher flux leakages.

As the speed or airgap thickness increases the maximum torque design moves towards lower magnetic ratios, since in that direction there is the optimal compromise between the competitive needs of maximizing the PM flux linkage and the q-axis current which are the variables affecting the torque behavior. On the contrary, the optimal split ratio is neither affected by the speed nor by the airgap thickness; indeed, it remains almost constant. Such behavior is determined by the competitive needs of the sleeve increment (which would lead to a lower rotor radius) and the iron losses increment (which would lead to higher radius). In conclusion, the change with the speed of the machine geometry featuring the highest torque depends on the selected soft magnetic and



sleeve materials which define the rate of change of iron losses and sleeve thickness.

A final comparison among technologies has been reported in chapter 5, where the three machine topologies have been compared in terms of power, *ipf* and optimal geometries considering a wide range of maximum speed, cooling system capability and airgap thickness, thus obtaining some insights about the different trends.

In order to validate the design considerations, experimental measurements 4 different prototypes have been provided in chapter 6.

First the design considerations about the SyR scenario have been validated against experimental results on two different SyR prototypes, whose stator and rotor laminations are made of CoFe and SiFe alloys respectively.

Then, an 8.5kW-80krpm NdFeB-PM-assisted synchronous reluctance machine has been prototyped and tested. Both structural and electromagnetic design refinement stages prior the manufacturing have been fully detailed justifying all the design choices. The prototype has been fully tested up to 50 krpm at no load and up to 30 krpm at load in both generating and motoring operating modes. No-load voltage profile at a fixed speed, average torque and internal power factor as function of current module and phase angle have all been compared to the respective predicted values. Such comparison shows an acceptable agreement endorsing both design methodology and general considerations.

Finally, the design approach and considerations of the chapter 4 have been validated by manufacturing a 4.2kW-80krpm surface permanent magnet synchronous machine. The rationale behind the selection of the final design have been discussed including the influence of the rotor eddy current losses. Several experimental tests have been reported including no-load voltage profile at a fixed speed, average torque as function of current module. The comparison of such variables with the respective predicted values shows an acceptable agreement endorsing both design methodology and general considerations.

## 7.2 Outlook

The proposed method has been validated for three machine topologies and it is suitable to be used as a general approach to perform an initial design stage of a high-speed synchronous machine. The method is capable of taking into account all the non-linearities involved during the machine operations and can be considered as a multi-physics approach since it deals with both the electromagnetic, thermal and structural needs.

Therefore, this thesis opens the possibility of performing several further investigations, which can be summarized as follows.

- Inclusion of the high-frequency copper losses within the design workflow: indeed, the increment of the Joule losses with the speed due to the skin effect and circulating current phenomena has not been investigated in this thesis. The inclusion of such phenomena within the design routine is a challenging task but could allow to compare different types of winding such as Hairpin, Litz wire or random wound ones, both from a thermal and electromagnetic points of view. Analytical and/or FE procedures could be adopted.
- Extension of the above procedure to traction applications, where selection of the number of poles, winding layout, a large constant power speed range and PM demagnetization issues play a major role.
- The analytical magnetic model can be improved so to better consider the saturation of the d- and q-axis flux paths, especially dealing with SyRMs and PMaSyRMs. Indeed, a better magnetic model would allow to better calculate the machine performance at overload conditions, including the PM demagnetization and the short-circuit current effects. The latter concepts are of paramount importance in traction applications.

# Bibliography

- [1] Jacek F Gieras. *Advancements in electric machines*. Springer Science & Business Media, 2008.
- [2] A. Binder and T. Schneider. High-speed inverter-fed ac drives. In *2007 International Aegean Conference on Electrical Machines and Power Electronics*, pages 9–16, 2007.
- [3] B. Sarlioglu and C. T. Morris. More electric aircraft: Review, challenges, and opportunities for commercial transport aircraft. *IEEE Transactions on Transportation Electrification*, 1(1):54–64, 2015.
- [4] David Gerada, Abdeslam Mebarki, Neil L. Brown, Chris Gerada, Andrea Cavagnino, and Aldo Boglietti. High-speed electrical machines: Technologies, trends, and developments. *IEEE Transactions on Industrial Electronics*, 61(6):2946–2959, 2014.
- [5] Dmitry Golovanov, Zeyuan Xu, David Gerada, Michele Degano, Gaurang Vakil, and Chris Gerada. The influence of stator material on the power density and iron loss of a high-performance starter-generator for more electric aircraft. In *2018 21st International Conference on Electrical Machines and Systems (ICEMS)*, pages 169–173, 2018.
- [6] Christof Zwyssig, Johann W. Kolar, and Simon D. Round. Megaspeed drive systems: Pushing beyond 1 million r/min. *IEEE/ASME Transactions on Mechatronics*, 14(5):564–574, 2009.
- [7] "NK automation". Accessed: Jan. 11, 2022. [Online]. Available: <https://www.nkautomations.com/>.

- [8] R. Lateb, J. Enon, and L. Durantay. High speed, high power electrical induction motor technologies for integrated compressors. In *2009 International Conference on Electrical Machines and Systems*, pages 1–5, 2009.
- [9] Perry Tsao, M. Senesky, and S.R. Sanders. An integrated flywheel energy storage system with homopolar inductor motor/generator and high-frequency drive. *IEEE Transactions on Industry Applications*, 39(6):1710–1725, 2003.
- [10] A. T. de Almeida, F. J. T. E. Ferreira, and G. Baoming. Beyond induction motors—technology trends to move up efficiency. *IEEE Transactions on Industry Applications*, 50(3):2103–2114, May 2014.
- [11] K. Lang, A. Muetze, R. Bauer, and S. Pircher. Comparison of induction and synchronous reluctance machine based actuators for elevated temperature environments. *IEEE Transactions on Energy Conversion*, 31(3):1012–1022, 2016.
- [12] R. Moghaddam, F. Magnussen, and C. Sadarangani. Novel rotor design optimization of synchronous reluctance machine for low torque ripple. In *2012 XXth International Conference on Electrical Machines*, pages 720–724, 2012.
- [13] M. Sanada, K. Hiramoto, S. Morimoto, and Y. Takeda. Torque ripple improvement for synchronous reluctance motor using an asymmetric flux barrier arrangement. *IEEE Transactions on Industry Applications*, 40(4):1076–1082, 2004.
- [14] J. H. Lee. Optimum design criteria for maximum torque density and minimum torque ripple of synrm according to the rated wattage using response surface methodology. *IEEE Transactions on Magnetics*, 45(3):1578–1581, 2009.
- [15] E. Howard, M. J. Kamper, and S. Gerber. Asymmetric flux barrier and skew design optimization of reluctance synchronous machines. *IEEE Transactions on Industry Applications*, 51(5):3751–3760, 2015.

- [16] D.A. Staton, T.J.E. Miller, and S.E. Wood. Maximising the saliency ratio of the synchronous reluctance motor. *Electric Power Applications, IEE Proceedings B*, 140(4):249–259, July 1993.
- [17] Nicola Bianchi. Synchronous reluctance and interior permanent magnet motors. In *2013 IEEE Workshop on Electrical Machines Design, Control and Diagnosis (WEMDCD)*, pages 75–84, 2013.
- [18] M. Ferrari, N. Bianchi, A. Doria, and E. Fornasiero. Design of synchronous reluctance motor for hybrid electric vehicles. *IEEE Transactions on Industry Applications*, 51(4):3030–3040, 2015.
- [19] M. Ferrari, N. Bianchi, and E. Fornasiero. Analysis of rotor saturation in synchronous reluctance and pm-assisted reluctance motors. *Industry Applications, IEEE Transactions on*, 51(1):169–177, 2015.
- [20] A. Tassarolo. Modeling and analysis of synchronous reluctance machines with circular flux barriers through conformal mapping. *Magnetics, IEEE Transactions on*, 51(4):1–11, April 2015.
- [21] M. Murataliyev, M. Degano, and M. Galea. A novel sizing approach for synchronous reluctance machines. *IEEE Transactions on Industrial Electronics*, 68(3):2083–2095, 2021.
- [22] A. Vagati, M. Pastorelli, F. Scapino, and G. Franceschini. Impact of cross saturation in synchronous reluctance motors of the transverse-laminated type. *Industry Applications, IEEE Trans on*, 36(4):1039–1046, 2000.
- [23] A. Vagati, M. Pastorelli, and G. Franceschini. High-performance control of synchronous reluctance motors. *Industry Applications, IEEE Transactions on*, 33(4):983–991, 1997.
- [24] G. Bacco, N. Bianchi, and H. Mahmoud. A nonlinear analytical model for the rapid prediction of the torque of synchronous reluctance machines. *IEEE Transactions on Energy Conversion*, 33(3):1539–1546, 2018.

- [25] H. Mahmoud and N. Bianchi. Non-linear analytical model of eccentric synchronous reluctance machines considering the iron saturation and slotting effect. *IEEE Transactions on Industry Applications*, 53(3):2007–2015, 2017.
- [26] A. Vagati. The synchronous reluctance solution: a new alternative in ac drives. In *Proceedings of IECON'94 - 20th Annual Conference of IEEE Industrial Electronics*, volume 1, pages 1–13 vol.1, 1994.
- [27] A. Vagati, G. Franceschini, I. Marongiu, and G.P. Trogli. Design criteria of high performance synchronous reluctance motors. In *Conference Record of the 1992 IEEE Industry Applications Society Annual Meeting*, pages 66–73 vol.1, 1992.
- [28] S. Ferrari and G. Pellegrino. Feafix: Fea refinement of design equations for synchronous reluctance machines. *IEEE Transactions on Industry Applications*, 56(1):256–266, 2020.
- [29] M. Di Nardo, M. Galea, C. Gerada, M. Palmieri, F. Cupertino, and S. Mebarki. Comparison of multi-physics optimization methods for high speed synchronous reluctance machines. In *Industrial Electronics Society, IECON 2015 - 41st Annual Conference of the IEEE*, pages 002771–002776, Nov 2015.
- [30] M. Di Nardo, M. Galea, C. Gerada, M. Palmieri, and F. Cupertino. Multi-physics optimization strategies for high speed synchronous reluctance machines. In *2015 IEEE Energy Conversion Congress and Exposition (ECCE)*, pages 2813–2820, 2015.
- [31] M. Palmieri, M. Perta, and F. Cupertino. Design of a 50.000-r/min synchronous reluctance machine for an aeronautic diesel engine compressor. *IEEE Transactions on Industry Applications*, 52(5):3831–3838, Sept 2016.
- [32] M. D. Nardo, G. L. Calzo, M. Galea, and C. Gerada. Design optimization of a high-speed synchronous reluctance machine. *IEEE Transactions on Industry Applications*, 54(1):233–243, 2018.

- [33] A. Credo, G. Fabri, M. Villani, and M. Popescu. Adopting the topology optimization in the design of high-speed synchronous reluctance motors for electric vehicles. *IEEE Transactions on Industry Applications*, 56(5):5429–5438, 2020.
- [34] C. Babetto, G. Bacco, and N. Bianchi. Analytical power limits curves of high-speed synchronous reluctance machines. *IEEE Transactions on Industry Applications*, 55(2):1342–1350, 2019.
- [35] A. Krings, A. Boglietti, A. Cavagnino, and S. Sprague. Soft magnetic material status and trends in electric machines. *IEEE Transactions on Industrial Electronics*, 64(3):2405–2414, 2017.
- [36] N. Fernando, G. Vakil, P. Arumugam, E. Amankwah, C. Gerada, and S. Bozhko. Impact of soft magnetic material on design of high-speed permanent-magnet machines. *IEEE Transactions on Industrial Electronics*, 64(3):2415–2423, 2017.
- [37] D. Golovanov, D. Gerada, G. Sala, M. Degano, A. Trentin, P. H. Connor, Z. Xu, A. La Rocca, A. Galassini, L. Tarisciotti, C. N. Eastwick, S. J. Pickering, P. Wheeler, J. C. Clare, M. Filipenko, and C. Gerada. 4mw class high power density generator for future hybrid-electric aircraft. *IEEE Transactions on Transportation Electrification*, pages 1–1, 2021.
- [38] L. Shao, A. E. H. Karci, D. Tavernini, A. Sorniotti, and M. Cheng. Design approaches and control strategies for energy-efficient electric machines for electric vehicles—a review. *IEEE Access*, 8:116900–116913, 2020.
- [39] A. Krings, M. Cossale, A. Tenconi, J. Soulard, A. Cavagnino, and A. Boglietti. Magnetic materials used in electrical machines: A comparison and selection guide for early machine design. *IEEE Industry Applications Magazine*, 23(6):21–28, 2017.
- [40] M. Cossale, A. Krings, J. Soulard, A. Boglietti, and A. Cavagnino. Practical investigations on cobalt–iron laminations for electrical machines. *IEEE Transactions on Industry Applications*, 51(4):2933–2939, 2015.

- [41] O. Bottauscio, G. Serra, M. Zucca, and M. Chiampi. Role of magnetic materials in a novel electrical motogenerator for the more electric aircraft. *IEEE Transactions on Magnetics*, 50(4):1–4, 2014.
- [42] M. A. Prabhu, J. Y. Loh, S. C. Joshi, V. Viswanathan, S. Ramakrishna, C. J. Gajanayake, and A. K. Gupta. Magnetic loading of soft magnetic material selection implications for embedded machines in more electric engines. *IEEE Transactions on Magnetics*, 52(5):1–6, 2016.
- [43] M. Centner and U. Schafer. Optimized design of high-speed induction motors in respect of the electrical steel grade. *IEEE Transactions on Industrial Electronics*, 57(1):288–295, 2010.
- [44] E. C. Lovelace, T. M. Jahns, T. A. Keim, and J. H. Lang. Mechanical design considerations for conventionally laminated, high-speed, interior pm synchronous machine rotors. *IEEE Transactions on Industry Applications*, 40(3):806–812, 2004.
- [45] A. Credo and P. Pescetto. Design optimization of a synchronous reluctance motor based on operating cycle. In *2020 International Conference on Electrical Machines (ICEM)*, volume 1, pages 2486–2492, 2020.
- [46] M. Salameh, I. P. Brown, and M. Krishnamurthy. Fundamental evaluation of data clustering approaches for driving cycle-based machine design optimization. *IEEE Transactions on Transportation Electrification*, 5(4):1395–1405, 2019.
- [47] Shafigh Nategh, Aldo Boglietti, Yujing Liu, Daniel Barber, Ron Brammer, David Lindberg, and Ola Aglen. A review on different aspects of traction motor design for railway applications. *IEEE Transactions on Industry Applications*, 56(3):2148–2157, 2020.
- [48] H. Fujimura R. Hirayama K. Wajima S. Yamazaki. Non-oriented electrical steel sheet and its application technology for the traction motors of hybrid/electrical vehicles. *Nipponn Steel Technical Report No. 122 November 2019*, Nov 2019.



- [49] Yi Wang, Dan M. Ionel, and David Staton. Ultrafast steady-state multiphysics model for pm and synchronous reluctance machines. *IEEE Transactions on Industry Applications*, 51(5):3639–3646, 2015.
- [50] Seyed Morteza Taghavi and Pragasen Pillay. A mechanically robust rotor with transverse laminations for a wide-speed-range synchronous reluctance traction motor. *IEEE Transactions on Industry Applications*, 51(6):4404–4414, 2015.
- [51] M. N. Ibrahim, Peter Sergeant, and E. M. Rashad. Synchronous reluctance motor performance based on different electrical steel grades. *IEEE Transactions on Magnetics*, 51(11):1–4, 2015.
- [52] M. Palmieri, M. Perta, F. Cupertino, and G. Pellegrino. High-speed scalability of synchronous reluctance machines considering different lamination materials. In *IECON 2014 - 40th Annual Conference of the IEEE Industrial Electronics Society*, pages 614–620, 2014.
- [53] Michele Degano, Mukhammed Murataliyev, Wang Shuo, Davide Barater, Giampaolo Buticchi, Werner Jara, Nicola Bianchi, Michael Galea, and Chris Gerada. Optimised design of permanent magnet assisted synchronous reluctance machines for household appliances. *IEEE Transactions on Energy Conversion*, 36(4):3084–3095, 2021.
- [54] Won-Ho Kim, Kwang-Soo Kim, Seung-Joo Kim, Dong-Woo Kang, Sung-Chul Go, Yon-Do Chun, and J. Lee. Optimal pm design of pma-synrm for wide constant-power operation and torque ripple reduction. *IEEE Transactions on Magnetics*, 45(10):4660–4663, 2009.
- [55] S. Morimoto, M. Sanada, and Y. Takeda. Performance of pm-assisted synchronous reluctance motor for high-efficiency and wide constant-power operation. *IEEE Transactions on Industry Applications*, 37(5):1234–1240, 2001.
- [56] N. Bianchi, E. Fornasiero, and Soong Wen. Selection of pm flux linkage for maximum low-speed torque rating in a pm-assisted synchronous reluctance machine. *Industry Applications, IEEE Transactions on*, 51(5):3600–3608, 2015.

- [57] Haiwei Cai, Bo Guan, and Longya Xu. Low-cost ferrite pm-assisted synchronous reluctance machine for electric vehicles. *IEEE Transactions on Industrial Electronics*, 61(10):5741–5748, 2014.
- [58] Thanh Anh Huynh and Min-Fu Hsieh. Comparative study of pm-assisted synrm and ipmsm on constant power speed range for ev applications. *IEEE Transactions on Magnetics*, 53(11):1–6, 2017.
- [59] G. Pellegrino, A. Vagati, B. Boazzo, and P. Guglielmi. Comparison of induction and pm synchronous motor drives for ev application including design examples. *Industry Applications, IEEE Transactions on*, 48(6):2322–2332, 2012.
- [60] Chao Lu, Simone Ferrari, and Gianmario Pellegrino. Two design procedures for pm synchronous machines for electric powertrains. *IEEE Transactions on Transportation Electrification*, 3(1):98–107, 2017.
- [61] N. Bianchi and H. Mahmoud. An analytical approach to design the pm in pmarel motors robust toward the demagnetization. *IEEE Transactions on Energy Conversion*, 31(2):800–809, 2016.
- [62] G. Pellegrino, A. Vagati, and P. Guglielmi. Design tradeoffs between constant power speed range, uncontrolled generator operation, and rated current of ipm motor drives. *Industry Applications, IEEE Transactions on*, 47(5):1995–2003, 2011.
- [63] Iman Kleilat, Khadija El Kadri Benkara, Guy Friedrich, Stéphane Vivier, Nazih Moubayed, and Rabih Dib. Comparison of two analytical methods for calculating the maximum mechanical stress in the rotor of high-speed-assisted synchronous reluctance machines. *IEEE Transactions on Industry Applications*, 57(2):1344–1353, 2021.
- [64] Md. Zakirul Islam, Akm Arafat, Sai Sudheer Reddy Bonthu, and Seungdeog Choi. Design of a robust five-phase ferrite-assisted synchronous reluctance motor with low demagnetiza-

- tion and mechanical deformation. *IEEE Transactions on Energy Conversion*, 34(2):722–730, 2019.
- [65] Nicola Bianchi and Hanafy Mahmoud. An analytical approach to design the pm in pmarel motors robust toward the demagnetization. *IEEE Transactions on Energy Conversion*, 31(2):800–809, 2016.
- [66] Yawei Wang, Giacomo Bacco, and Nicola Bianchi. Geometry analysis and optimization of pm-assisted reluctance motors. *IEEE Transactions on Industry Applications*, 53(5):4338–4347, 2017.
- [67] M. Barcaro, N. Bianchi, and F. Magnussen. Permanent-magnet optimization in permanent-magnet-assisted synchronous reluctance motor for a wide constant-power speed range. *Industrial Electronics, IEEE Transactions on*, 59(6):2495–2502, 2012.
- [68] A. Vagati, B. Boazzo, P. Guglielmi, and G. Pellegrino. Design of ferrite-assisted synchronous reluctance machines robust toward demagnetization. *IEEE Transactions on Industry Applications*, 50(3):1768–1779, 2014.
- [69] Barbara Boazzo. *Reduced-cost Permanent Magnet motor drives: a comprehensive design procedure and a universal approach to the magnetic model identification and control*. PhD thesis, Politecnico di Torino, IT, 2014.
- [70] N. Bianchi, M. Degano, and E. Fornasiero. Sensitivity analysis of torque ripple reduction of synchronous reluctance and interior pm motors. *Industry Applications, IEEE Transactions on*, 51(1):187–195, 2015.
- [71] Yi Wang, Dan M. Ionel, Minjie Jiang, and Steven J. Stretz. Establishing the relative merits of synchronous reluctance and pm-assisted technology through systematic design optimization. *IEEE Transactions on Industry Applications*, 52(4):2971–2978, 2016.

- [72] Nicola Bianchi, Hanafy Mahmoud, and Silverio Bolognani. Fast synthesis of permanent magnet assisted synchronous reluctance motors. *IET Electric Power Applications*, 10(5):312–318, 2016.
- [73] Hanafy Mahmoud, Nicola Bianchi, Giacomo Bacco, and Nicola Chiodetto. Nonlinear analytical computation of the magnetic field in reluctance synchronous machines. *IEEE Transactions on Industry Applications*, 53(6):5373–5382, 2017.
- [74] J. Cekani, F. G. Capponi, G. De Donato, and F. Caricchi. Mechanical flux weakening methods for the achievement of a very wide constant power speed range in automotive applications. *IEEE Journal of Emerging and Selected Topics in Power Electronics*, pages 1–1, 2021.
- [75] Lu Wang, Z.Q. Zhu, Hong Bin, and L. M. Gong. Recent developments of high speed electrical machine drive systems. In *2021 Sixteenth International Conference on Ecological Vehicles and Renewable Energies (EVER)*, pages 1–10, 2021.
- [76] Jing Ou, Yingzhen Liu, and Martin Doppelbauer. Comparison study of a surface-mounted pm rotor and an interior pm rotor made from amorphous metal of high-speed motors. *IEEE Transactions on Industrial Electronics*, 68(10):9148–9159, 2021.
- [77] Gianmario Pellegrino, Alfredo Vagati, Barbara Boazzo, and Paolo Guglielmi. Comparison of induction and pm synchronous motor drives for ev application including design examples. *IEEE Transactions on Industry Applications*, 48(6):2322–2332, 2012.
- [78] Zhi Yang, Fei Shang, Ian P. Brown, and Mahesh Krishnamurthy. Comparative study of interior permanent magnet, induction, and switched reluctance motor drives for ev and hev applications. *IEEE Transactions on Transportation Electrification*, 1(3):245–254, 2015.
- [79] Tae-Woo Lee and Do-Kwan Hong. Rotor design, analysis and experimental validation of a high-speed permanent magnet synchronous motor for electric turbocharger. *IEEE Access*, 10:21955–21969, 2022.

- [80] Fengge Zhang, Guanghui Du, Tianyu Wang, Guangwei Liu, and Wenping Cao. Rotor retaining sleeve design for a 1.12-mw high-speed pm machine. *IEEE Transactions on Industry Applications*, 51(5):3675–3685, 2015.
- [81] D.C. Hanselman. *Brushless Permanent Magnet Motor Design*. Magna Physics Publishing, 2006.
- [82] Tapani Jokinen, Valeria Hrabovcova, and Juha Pyrhonen. *Design of rotating electrical machines*. John Wiley & Sons, 2013.
- [83] Dong-Hoon Jung, Jae-Kwang Lee, Jun-Young Kim, Ik Sang Jang, Ju Lee, and Ho-Joon Lee. Design method of an ultrahigh speed pm motor/generator for electric-turbo compounding system. *IEEE Transactions on Applied Superconductivity*, 28(3):1–4, 2018.
- [84] Yu Wang, Zi-Qiang Zhu, Jianghua Feng, Shuying Guo, Yifeng Li, and Yu Wang. Rotor stress analysis of high-speed permanent magnet machines with segmented magnets retained by carbon-fibre sleeve. *IEEE Transactions on Energy Conversion*, 36(2):971–983, 2021.
- [85] Haiyang Fang, Dawei Li, Ronghai Qu, Jian Li, Cong Wang, and Bao Song. Rotor design and eddy-current loss suppression for high-speed machines with a solid-pm rotor. *IEEE Transactions on Industry Applications*, 55(1):448–457, 2019.
- [86] A. Binder, T. Schneider, and M. Klohr. Fixation of buried and surface-mounted magnets in high-speed permanent-magnet synchronous machines. *IEEE Transactions on Industry Applications*, 42(4):1031–1037, 2006.
- [87] Ji-Hun Ahn, Jang-Young Choi, Cheol Hoon Park, Cheol Han, Chang-Woo Kim, and Tae-Gwang Yoon. Correlation between rotor vibration and mechanical stress in ultra-high-speed permanent magnet synchronous motors. *IEEE Transactions on Magnetics*, 53(11):1–6, 2017.

- [88] Hamid Ali Khan, Faisal Khan, Surat Khan, Naseer Ahmad, Jahangeer Badar Soomro, and Irfan Sami. Design and performance investigation of 3-slot/2-pole high speed permanent magnet machine. *IEEE Access*, 9:41603–41614, 2021.
- [89] Guanghui Du, Na Huang, Hucheng He, Gang Lei, and Jianguo Zhu. Parameter design for a high-speed permanent magnet machine under multiphysics constraints. *IEEE Transactions on Energy Conversion*, 35(4):2025–2035, 2020.
- [90] C. Babetto, G. Bacco, and N. Bianchi. Synchronous reluctance machine optimization for high-speed applications. *IEEE Transactions on Energy Conversion*, 33(3):1266–1273, 2018.
- [91] W. Q. Chu and Z. Q. Zhu. Average torque separation in permanent magnet synchronous machines using frozen permeability. *IEEE Transactions on Magnetics*, 49(3):1202–1210, 2013.
- [92] J. A. Walker, D. G. Dorrell, and C. Cossar. Flux-linkage calculation in permanent-magnet motors using the frozen permeabilities method. *IEEE Transactions on Magnetics*, 41(10):3946–3948, 2005.
- [93] M. Di Nardo, G. L. Calzo, M. Galea, and C. Gerada. Structural design optimization of a high speed synchronous reluctance machine. In *2016 XXII International Conference on Electrical Machines (ICEM)*, pages 2073–2079, Sept 2016.
- [94] "Motor-CAD". Accessed: Jan. 11, 2021. [Online]. Available: <https://www.motor-design.com>.
- [95] James Borg Bartolo, He Zhang, David Gerada, Liliana De Lillo, and Chris Gerada. High speed electrical generators, application, materials and design. In *2013 IEEE Workshop on Electrical Machines Design, Control and Diagnosis (WEMDCD)*, pages 47–59, 2013.
- [96] S. Sprague. Emerf lamination steels (3rd ed.). [cd-rom]. Motion Control and Motor, Ann Arbor, MI, 2009.

- [97] "VAC Vacuumschmelze". Accessed: Feb. 22, 2021. [Online]. Available: <https://www.vacuumschmelze.com>.
- [98] "JFE Steel Corporation". Accessed: Feb. 22, 2021. [Online]. Available: <https://www.jfe-steel.co.jp/enm>.
- [99] "Nippon Steel and Sumitomo Metal". Accessed: Feb. 22, 2021. [Online]. Available: <https://www.nssmc.com>.
- [100] D. Gerada, A. Mebarki, N. L. Brown, C. Gerada, A. Cavagnino, and A. Boglietti. High-speed electrical machines: Technologies, trends, and developments. *Industrial Electronics, IEEE Transactions on*, 61(6):2946–2959, 2014.
- [101] Darja Steiner Petrovic. Non-oriented electrical steel sheets. *Materials and Technologies*, 44:317–325, 11 2010.
- [102] Yoshihiko Oda, Masaaki Kohno, and Atsuhito Honda. Recent development of non-oriented electrical steel sheet for automobile electrical devices. *Journal of Magnetism and Magnetic Materials*, 320(20):2430–2435, 2008. Proceedings of the 18th International Symposium on Soft Magnetic Materials.
- [103] Kim Verbeken, Ivone Infante Danzo, J Barros-Lorenzo, Jürgen Schneider, and Yvan Houbaert. Innovative processing for improved electrical steel properties. *Revista de Metalurgia*, 46(5):458–468, 2010.
- [104] Senda Kunihiro Namikawa Misao Hayakawa Yasuyuki. Electrical steels for advanced automobiles—core materials for motors, generators, and high-frequency reactors. *Jfe Technical Report No. 4 (Nov. 2004)*, Nov 2004.
- [105] I. Tanaka and H. Yashiki. Magnetic and mechanical properties of newly developed high-strength nonoriented electrical steel. *IEEE Transactions on Magnetics*, 46(2):290–293, 2010.

- [106] K. Bourchas, A. Stening, J. Soulard, A. Broddefalk, M. Lindenmo, M. Dahlén, and F. Gyllensten. Quantifying effects of cutting and welding on magnetic properties of electrical steels. *IEEE Transactions on Industry Applications*, 53(5):4269–4278, 2017.
- [107] A. Boglietti, A. Cavagnino, L. Ferraris, and M. Lazzari. The annealing influence onto the magnetic and energetic properties in soft magnetic material after punching process. In *IEEE International Electric Machines and Drives Conference, 2003. IEMDC'03.*, volume 1, pages 503–508 vol.1, 2003.
- [108] G. Gallicchio, M. Di Nardo, M. Palmieri, A. Marfoli, M. Degano, C. Gerada, and F. Cupertino. High speed synchronous reluctance machines: Modeling, design and limits. *IEEE Transactions on Energy Conversion*, 37(1):585–597, 2022.
- [109] M. Di Nardo, G. Gallicchio, M. Palmieri, A. Marfoli, G. Lo Calzo, M. Degano, C. Gerada, and F. Cupertino. High-speed synchronous reluctance machines: Materials selection and performance boundaries. *IEEE Transactions on Transportation Electrification*, 8(1):1228–1241, 2022.
- [110] Gianvito Gallicchio, Marco Palmieri, Francesco Cupertino, Mauro Di Nardo, Michele Degano, and Chris Gerada. Influence of the magnetic load on high speed synchronous reluctance machines design. In *IECON 2021 – 47th Annual Conference of the IEEE Industrial Electronics Society*, pages 1–6, 2021.
- [111] G. Gallicchio, M. Palmieri, F. Cupertino, M. Di Nardo, M. Degano, and C. Gerada. Design methodologies of high speed synchronous reluctance machines. In *2022 International Conference on Electrical Machines (ICEM)*, pages 448–454, 2022.
- [112] O. Korman, M. Di Nardo, M. Degano, C. Gerada, G. Gallicchio, and F. Cupertino. On the pole pair selection of synchronous reluctance machines for traction applications. In *2022 International Conference on Electrical Machines (ICEM)*, pages 2114–2120, 2022.



- [113] G. Pellegrino, P. Guglielmi, A. Vagati, and F. Villata. Core losses and torque ripple in ipm machines: Dedicated modeling and design tradeoff. *Industry Applications, IEEE Transactions on*, 46(6):2381–2391, 2010.
- [114] I. Boldea and S.A. Nasar. *The Induction Machine Handbook*. Electric Power Engineering Series. CRC Press, 2010.
- [115] P. Guglielmi, B. Boazzo, E. Armando, G. Pellegrino, and A. Vagati. Permanent-magnet minimization in pm-assisted synchronous reluctance motors for wide speed range. *Industry Applications, IEEE Transactions on*, 49(1):31–41, 2013.
- [116] M. Di Nardo, G. Gallicchio, M. Palmieri, A. Marfoli, G. Lo Calzo, M. Degano, C. Gerada, and F. Cupertino. High speed synchronous reluctance machines: Materials selection and performance boundaries. *IEEE Transactions on Transportation Electrification*, pages 1–1, 2021.
- [117] Gianvito Gallicchio, Mauro Di Nardo, Marco Palmieri, Alessandro Marfoli, Michele Degano, Chris Gerada, and Francesco Cupertino. High speed permanent magnet assisted synchronous reluctance machines - part i: A general design approach. *IEEE Transactions on Energy Conversion*, pages 1–1, 2022.
- [118] Mauro Di Nardo, Gianvito Gallicchio, Marco Palmieri, Alessandro Marfoli, Michele Degano, Chris Gerada, and Francesco Cupertino. High speed permanent magnet assisted synchronous reluctance machine - part ii: Performance boundaries. *IEEE Transactions on Energy Conversion*, pages 1–1, 2022.
- [119] Gianvito Gallicchio, Marco Palmieri, Francesco Cupertino, Mauro Di Nardo, Michele Degano, and Chris Gerada. Permanent magnets assistance design methods of high-speed synchronous reluctance machines. In *2022 IEEE Energy Conversion Congress and Exposition (ECCE)*, pages 1–8, 2022.

- [120] Junuthula Narasimha Reddy. *Mechanics of laminated composite plates and shells: theory and analysis*. CRC press, 2003.
- [121] Wilhelm Flügge. *Stresses in shells*. Springer Science & Business Media, 2013.
- [122] Gianvito Gallicchio, Mauro Di Nardo, Marco Palmieri, Mohammad Reza Ilkhani, Michele Degano, Chris Gerada, and Francesco Cupertino. Surface permanent magnet synchronous machines: High speed design and limits. *IEEE Transactions on Energy Conversion*, pages 1–14, 2022.
- [123] F. Cupertino, G. Pellegrino, and C. Gerada. Design of synchronous reluctance motors with multiobjective optimization algorithms. *IEEE Transactions on Industry Applications*, 50(6):3617–3627, 2014.
- [124] Gianmario Pellegrino, Francesco Cupertino, and Chris Gerada. Automatic design of synchronous reluctance motors focusing on barrier shape optimization. *IEEE Transactions on Industry Applications*, 51(2):1465–1474, 2015.
- [125] E. Armando, R. I. Bojoi, P. Guglielmi, G. Pellegrino, and M. Pastorelli. Experimental identification of the magnetic model of synchronous machines. *Industry Applications, IEEE Transactions on*, 49(5):2116–2125, 2013.
- [126] Mauro Di Nardo. *Design of High Speed Synchronous Reluctance Machine*. PhD thesis, University of Nottingham, UK, 2017.
- [127] G. L. Calzo, P. Zanchetta, C. Gerada, A. Gaeta, and F. Crescimbeni. Converter topologies comparison for more electric aircrafts high speed starter/generator application. In *2015 IEEE Energy Conversion Congress and Exposition (ECCE)*, pages 3659–3666, Sept 2015.
- [128] A. Galassini, G. Lo Calzo, A. Formentini, C. Gerada, P. Zanchetta, and A. Costabeber. ucube: Control platform for power electronics. In *2017 IEEE Workshop on Electrical Machines Design, Control and Diagnosis (WEMDCD)*, pages 216–221, 2017.

- [129] T. M. Jahns, G. B. Kliman, and Thomas W. Neumann. Interior permanent-magnet synchronous motors for adjustable-speed drives. *Industry Applications, IEEE Transactions on*, IA-22(4):738–747, 1986.
- [130] Andrea Credo, Ilya Petrov, Juha Pyrhönen, and Marco Villani. Impact of manufacturing stresses on multiple-rib synchronous reluctance motor performance. *IEEE Transactions on Industry Applications*, pages 1–10, 2022.